Håkon Ivarssønn Røst

Novel Approaches for Exploring Electron Interactions in Reduced Dimensions

Doctoral thesis

NTNU
Norwegian University of
Science and Technology

Håkon Ivarssønn Røst

Novel Approaches for Exploring Electron Interactions in Reduced Dimensions

Thesis for the Degree of Philosophiae Doctor

Trondheim, September 2022

Norwegian University of Science and Technology
Faculty of Natural Sciences
Department of Physics

NTNU
Norwegian University of
Science and Technology

Abstract

Arguably, some of the most intriguing phenomena in contemporary condensed matter research can be observed in systems of 'reduced' dimensions. In cases where electrons are not allowed to propagate freely in all three spatial directions, a newfound interplay with other electrons and other collective excitations can often be observed. The confinement of the electrons can thus lead to altered electronic properties or, in extreme cases, completely different phase behavior. For instance, the results can range from electronic states with massless Dirac fermions to potent pairing mechanisms for unconventional superconductivity. Ultimately, the implications of said 'confinement' would depend on the material the electrons propagate in and the other degrees of freedom it enables and inhabits.

This thesis is concerned with forming and studying such systems of 'reduced' dimensions and the physical phenomena they exhibit. The work is based on six research papers covering various topics, materials, and experimental techniques. Three papers examine the physical structure of state-of-the-art quantum materials and pathways to modify and control their behavior and quality. The remaining three focus on electron interactions with collective modes of excitation, both in van der Waals materials and in ferromagnetic and antiferromagnetic structures and heterostructures.

Preface

This thesis is submitted in partial fulfillment of the requirements for the degree of Philosophiae Doctor (Ph.D.) at the Norwegian University of Science and Technology (NTNU) in Trondheim, Norway. The work is based on six manuscripts, where three have been published and the remaining three are currently in progress. An additional three manuscripts – where the candidate has had a less important contribution, have also been included in the appendices for completeness. These, however, serve primarily as additional reference literature and are not part of the main thesis work.

The research was conducted at the Department of Physics (IFY) from September 2018 to May 2022, supervised by Professor Justin W. Wells (NTNU, UiO). Dr. Simon P. Cooil (UiO) and Dr. Lars Thomsen (Australian Synchrotron) have served as co-supervisors. The experimental work has been performed using both in-house instrumentation at NTNU, at the University of Bristol, and at several international synchrotron facilities. Lab-based measurements have primarily been performed using NanoESCA II and III instruments, available at the Bristol NanoESCA Facility and the SFF Center of Excellence 'QuSpin' at NTNU, respectively. Synchrotron-based measurements have been performed at – in no particular order: The Australian Synchrotron (Melbourne, Australia), ASTRID-2 (Aarhus, Denmark), BESSY II (Berlin, Germany), Elettra (Trieste, Italy), and NSLS-II (NY, USA).

Håkon Ivarssønn Røst
Trondheim, Norway
July 2022

Acknowledgements

Throughout my Ph.D., I have had the pleasure of interacting and collaborating with numerous bright minds – and equally important, fantastic and friendly human beings. I want to use this opportunity to express my appreciation to them.

First of all, I would like to thank my supervisor: Professor Justin W. Wells. For your ever-encouraging, steadfast scientific guidance and friendship over the last couple of years. This thesis would not have come through without your invaluable scientific insight, your leadership, and the many 'refreshments' that we have drawn from your basement and enjoyed together.

To Dr. Simon P. Cooil: thank you for your scientific guidance, for serving as my co-supervisor, and for our incredible collaborations and late-night synchrotron beamtime shifts. And equally important: thank you for your friendship, your kindness, your wit, and for teaching me the true meaning of a Fermi surface.

A big thank you also to Dr. Lars Thomsen for serving as my second co-supervisor and assisting me with remote, mid-pandemic NEXAFS measurements from 'down under', as well as subsequent data interpretation. And a special thank you to Dr. Federico Mazzola: for our fruitful scientific interactions, for sharing your insights on many-body ARPES analysis, and for your contagious passion for science, coffee, and life in general.

Next, I want to thank some of my colleagues at the Department of Physics. Thank you, Rajesh, for your guidance, patience, and support, and for sharing your love for spicy food with everyone. Thank you, Frode, for our interactions at work and outside, our fun trips abroad, and (too) many espresso shots. Thank you, Anna Cecilie, for your cheerful demeanor, for being my 'little sister' in the lab, and for your unexpected and inventive pronunciation of dairy products. Thanks, Matthias, for serving me many dumplings, fixing my vacuum leaks, and (sometimes) appreciating my car music playlists. Thanks, Alex, for your help with XPS analysis, and for our

debates on the cultural significance of the Star Wars sequel trilogy. Thanks, Jinbang, for figuring out the NanoESCA together with me, and for showing us all inventive new ways and places to sleep. Thanks to Johannes, for his beamtime companionship and DFT number crunching; to Even, for his keen enthusiasm for tight-binding calculations, 2D materials, and our extended coffee breaks; to Asle, for our lively discussions, and for always borrowing my chair in the office. To my office mates: Atousa, Eirik, and Håvard, for our never-ending 'crunch time' together in E5-145. Thanks to Lina, Payel, Verena, and Karen-Elisabeth, for always keeping me company in the lunch room – even when I decide to sit down and eat the moment everyone else is leaving to get back to work.

I would also like to show my appreciation to all the beamline scientists and staff that have contributed to the scientific work in this thesis. Thank you, Zheshen Li, Marco Bianchi, Craig Polley, Anton Tadich, Bruce Cowie, Thomas Schmidt, Mauricio Prieto, Liviu Tănase, Lucas de Souza Caldas, Silvano Lizzit, Paolo Lacovig, Ezequiel Tosi and Jurek Sadowski.

Finally, I would like to give a special thank you to my close friends and family. I appreciate all of your support, and for staying sane – despite my occasional frustrations with ambiguous experimental results and lab malfunctions. A tip o' the sombrero to my string-swinging mariachi compadres: for our lively cabin trips, musical endeavors, and live performances. To my Mother and Father, for their everlasting patience and kindness. To my older sister Lisa, for our many dinners, adventures, and heartfelt conversations. And to my Ingrid, for our companionship, your support, your silliness, and for sharing numerous memorable moments and dabs of hot sauce with me.

List of Publications

Publications relevant for this thesis

Paper 1

H. I. Røst, R. K. Chellappan, F. S. Strand, A. Grubišić-Čabo, B. P. Reed, M. J. Prieto, L. C. Tănase, L. de Souza Caldas, T. Wongpinij, C. Euaruksakul, T. Schmidt, A. Tadich, B. C. C. Cowie, Z. Li, S. P. Cooil, J. W. Wells. *Low-Temperature Growth of Graphene on a Semiconductor.* J. Phys. Chem. C 125 (7), 4243-4252, 2021. [1]

Paper 2

H. I. Røst, B. P. Reed, F. S. Strand, J. A. Durk, D. A. Evans, A. Grubišić-Čabo, G. Wan, M. Cattelan, M. J. Prieto, D. M. Gottlob, L. C. Tănase, L. de Souza Caldas, T. Schmidt, A. Tadich, B. C. C. Cowie, R. K. Chellappan, J. W. Wells, S. P. Cooil. *A Simplified Method for Patterning Graphene on Dielectric Layers.* ACS Appl. Mater. Interfaces 13 (31), 37510-37516, 2021. [2]

Paper 3

H. I. Røst, S. P. Cooil, A. C. Åsland, A. Ali, B. D. Belle, J. Hu, J. T. Sadowski, F. Mazzola, J. W. Wells *Phonon-Induced Mass Enhancements in a Wide Bandgap Material.* In manuscript. [3]

Paper 4

H. I. Røst, E. Tosi, F. S. Strand, A. C. Åsland, P. Lacovig, S. Lizzit, J. W. Wells. *Probing the Atomic Arrangement of Sub-Surface Dopants in a Silicon Quantum Device Platform.* In manuscript. [4]

Paper 5

H. I. Røst, F. Mazzola, J. Bakkelund, A. C. Åsland, J. Hu, S. P. Cooil, C. M. Polley, J. W. Wells. *Disentangling Electron-Boson Interactions on the Surface of a Familiar Ferromagnet.* In manuscript. [5]

Paper 6

K. Mæland, H. I. Røst, J. W. Wells, A. Sudbø. *Electron-Magnon Coupling and Quasiparticle Lifetimes on the Surface of a Topological Insulator.* Phys. Rev. B 104 (12), 125125, 2021. [6]

Other publications

Paper 7

L. Michels, A. Richter, R. K. Chellappan, H. I. Røst, A. Behsen, K. H. Wells, L. Leal, V. Santana, R. Blawid, G. J. da Silva, S. P. Cooil, J. W. Wells, S. Blawid. *Electronic and Structural Properties of the Natural Dyes Curcumin, Bixin and Indigo.* RSC Adv. 11 (23), 14169-14177, 2021. [7]

Paper 8

A. C. Åsland, J. Bakkelund, E. Thingstad, H. I. Røst, S. P. Cooil, J. Hu, I. Vobornik, J. Fujii, A. Sudbø, J. W. Wells, F. Mazzola. *One-Dimensional Spin-Polarised Surface States – A Comparison of Bi(112) with Other Vicinal Bismuth Surfaces.* In manuscript. [8]

Paper 9

D. Mamedov, A. C. Åsland, S. P. Cooil, H. I. Røst, J. Bakkelund, J. W. Wells, S. Karazhanov. *Enhanced Hydrophobicity of CeO_2 Thin Films by Surface Engineering.* ChemRxiv preprint, 2022. [9]

Contents

Chapter 1

Introduction

Perhaps some of the most exotic phenomena in condensed matter physics originate from the interplay of electrons at surfaces, across interfaces, or with different collective modes of excitation within a material. The picture of the solitary electron that paves its way along the periodic energy potentials of a perfectly ordered system can serve as an excellent tool for understanding the fundamental properties of many solids. However, a multitude of other – and arguably more exciting, behavior can be explained if the idea of these lone striders is abandoned, and the company of other electrons, or perhaps even bosons, crystal imperfections, or dopants, gets thrown into the mix.

When the idea of 'packets' of light and the explanation of the photoelectric effect was introduced in 1905 [10], Albert Einstein enabled a range of later technological developments that all utilize or exploit the fundamental property of light energy quantization. Additionally, his newfound understanding of said phenomenon inspired the idea of using light to test another contemporary hypothesis: quantized energy states in solid materials. Technological developments of suitable instrumentation soon followed, and by the mid-1960s, *electron spectroscopy* had developed into a fully-fledged tool for analyzing chemical states [11].

Since then, further advances in instrumentation have allowed interactions between electrons and several of the mentioned degrees of freedom to be studied with unprecedented detail. Electron spectroscopies can now resolve a photoexcited electron by both its energy and momentum – properties which can be linked back to its behavior in a material before photoexcitation. As an interacting electron will get 'dressed' by the signatures of its particle-particle interactions, comparing its measured behavior to that of an ideal,

non-interacting electron allows many-body interactions to be observed from experimentally measured energy bands. With the proper analytical methodology, specific interactions can also be disentangled from one another and quantified.

The work presented in this thesis concerns the interactions of electrons in solid state systems, with a particular emphasis on those observed in quantum systems of 'reduced' dimensions. In Papers [1] and [2], a new, novel, and viable approach to producing and patterning a benchmark quantum material is presented. In Paper [3] unexpected, and exotic many-body interactions are observed at high binding energies in a wide bandgap insulator. In Paper [4], the previously ambiguous and debated geometric distribution of dopant atoms in a silicon quantum device platform is established once and for all. Finally, the interplay of conducting electrons with collective magnetic excitations, both within the same material and across material interfaces, are studied in Papers [5] and [6], respectively.

Reading the Thesis

The work presented is sectioned by topic, with the idea that the necessary information and motivation are presented directly before reading each of the papers [1–6]. With this approach, I hope to give the reader the relevant tools where and when necessary and avoid repeating too much information throughout the text. By priming the reader sufficiently when needed, I aspire to make the reading of each paper a bit less challenging – particularly for those not versed with all the intricacies of experimental surface science.

First, the principles of light-matter interactions and some of the most typical electron spectroscopies are discussed in Chapter 2, as these are needed for reading and understanding all six papers. Next, Chapter 3 considers the detection of photoelectrons and some of the practical implications of the techniques discussed in Chapter 2. In Chapters 4-7, each Paper is presented by topic. Starting with Papers [1] and [2] in Chapter 4, then Paper [3] in Chapter 5, Paper [4] in Chapter 6, and ending with Papers [5] and [6] in Chapter 7. Finally, a few conclusive remarks about each paper and outlooks on further work are presented in Chapter 8.

Chapter 2

The Principles of Photoexcitation

This Chapter outlines the foundations of photoexcitation, -absorption, and -emission. The principles presented here should provide an introduction to the relevant experimental techniques, sufficient to interpret the scientific work that will be presented in subsequent Chapters. More elaborate and rigorous theoretical treatments of photoabsorption and -emission can be found in standard texts on experimental condensed matter physics. See, for instance, Hufner [12] for a general picture, and Kevan [13] and Stöhr [14] for extensions on angle-resolved photoemission spectroscopy (ARPES) and near-edge X-ray absorption fine structure (NEXAFS), respectively. A thorough review of X-Ray photoelectron diffraction (XPD) has been provided by Woodruff [15].

2.1 Foundations

At the heart of the scientific work presented in this thesis, particularly that of Refs. [1–5], is the utilization of light-matter interactions to obtain meaningful and valuable information about the materials in question. In this Section, the interactions of bound electrons with electromagnetic radiation are discussed, either exciting them to unoccupied states within their parent material(s) or removing them entirely by ejection into a vacuum. The discussion is based on the principles of light-matter interactions outlined in Chapters 1 and 4 of Refs. [12] and [16], respectively. A few key points from Damascelli's review article on photoemission are also included [17].

2.1.1 Fermi's Golden Rule for Photoexcitation

Perhaps one of the most studied phenomenons in solid state physics is the interaction between light (i.e., electromagnetic radiation) and bound electrons in well-defined energy states. Due to their negative charge, electrons will experience a time-dependent, oscillating force from the electric field $\mathcal{E}_0$ carried by the incident light. In some cases, the electrons can absorb the light energy and assume new, unoccupied states of higher energy. This process is known as *photoexcitation*.

Light with energy E_{ph} in the ultraviolet to soft X-ray regime (i.e., $30\,eV$ - $6\,keV$ [18]) will have a wavelength λ that typically is greater than the diameter of most common elemental atoms. Hence for an electron residing near an atom, e.g., in a molecule or a solid, the local electric field carried by ultraviolet light or soft X-rays can be regarded as constant in space but oscillating in time[1] with frequency $\nu = E_{ph}/h$, where h is Planck's constant. This is known as the *dipole approximation* [12]. Furthermore, suppose the interaction between the electron and the incoming radiation is weak. In that case, the oscillating electric field $\mathcal{E}$ can be regarded as a time-dependent perturbation to the electron's ground state energy. The light-electron interaction problem can thus be treated using time-dependent perturbation theory [16].

The rate $\mathcal{W}_{i \to f}$ at which electrons get excited from an initial state $|\psi_i\rangle$ of energy E_i to a final state $|\psi_f\rangle$ of energy E_f, by absorbing 'packets' of light – or *photons*, with energy $E_{ph} = h\nu$ is given by *Fermi's golden rule* [12, 16]:

$$\mathcal{W}_{i \to f} = \frac{2\pi}{\hbar} \left| \langle \psi_f | \, \hat{H}_{int}(\mathbf{p}) \, |\psi_i\rangle \right|^2 \delta(E_f - E_i - h\nu). \tag{2.1}$$

Here, $\hat{H}_{int}(\mathbf{p}) = -\mathcal{E}_0 \cdot \mathbf{p}$ is the Hamiltonian of the light-matter perturbation, with $\mathbf{p} = q\mathbf{r}$ being the dipole vector of the oscillating electric field of amplitude $\mathcal{E}_0$. The Kronecker delta $\delta(E_f - E_i - h\nu)$ ensures that only excitations where $E_f = E_i + E_{ph}$ are permitted, i.e., the system's energy is conserved.

Eq. 2.1 states that the rate at which light will promote electrons is highly dependent on the energy and functional form of the final state. It is, therefore, natural to think that excitations to final states with different energies and wavefunctions can have drastically different excitation probabilities and rates. This principle is strategically exploited in several experimental works presented in Refs. [1–5], and discussed in the subsequent chapters.

---

[1] All light energies used in this work are in the lower end of the range ($< 2\,keV$), with wavelengths equal to tens or hundreds of atomic diameters for most elements.

2.1.2 Many-Particle Electronic States

So far, we have not assessed the nature of the initial and final electron states. In the simplest picture, $|\psi_i\rangle$ and $|\psi_f\rangle$ can be regarded as one-particle wavefunctions that are comprised of linear combinations of atomic orbitals $|\phi_j\rangle$ [19]:

$$\left|\psi_{i(f)}\right\rangle = \sum_j c_j \left|\phi_j\right\rangle, \tag{2.2}$$

where c_j are complex – and in some cases time-dependent, coefficients satisfying $\sum_j |c_j|^2 = 1$.

If a more sophisticated (and realistic) model is applied, the $|\psi_i\rangle$ and $|\psi_f\rangle$ of the material should both be many-particle wavefunctions. In a system of N electrons, the light absorption and subsequent excitation of one electron from an initial state $|\psi_i^N\rangle$ to a final state $|\psi_f^N\rangle$ will not only involve an added energy $\Delta E = h\nu$, but also a relaxation of the many-particle final state as to minimize the overall energy of the N-electron system [17].

In situations where the excited electron is freed from the system and emitted into a vacuum, the problem can be simplified slightly by invoking the so-called *sudden approximation*[2]. Here, the photoexcited electron is assumed not to interact with the remaining $N-1$ electrons of the system, and the light absorption and excitation process is *sudden* so that the system does not have time to relax [12, 17]. Then the N-electron initial and final states can be factored as

$$\left|\psi_i^N\right\rangle = \hat{\mathcal{C}}|\phi_i^{\mathbf{k}}\rangle|\psi_i^{N-1}\rangle, \qquad \left|\psi_f^N\right\rangle = \hat{\mathcal{C}}|\phi_f^{\mathbf{k}}\rangle|\psi_m^{N-1}\rangle. \tag{2.3}$$

Here, $|\phi_i^{\mathbf{k}}\rangle$ and $|\phi_f^{\mathbf{k}}\rangle$ are one-electron orbitals of the photoexcited electron's initial and final states, respectively. The wave vector $\mathbf{k}$ of the initial one-electron state is assumed not to change with photon absorption. Furthermore, $|\psi_i^{N-1}\rangle$ and $|\psi_m^{N-1}\rangle$ are wavefunctions of the remaining $N-1$ electrons, where m is a label for the possible final states. Finally, $\hat{\mathcal{C}}$ is an anti-symmetrization operator, ensuring that Pauli's exclusion principle is satisfied.

---

[2]The sudden approximation is in principle only valid when the excited electron is assumed to be a free particle, sufficient in kinetic energy to leave the system before the remaining particles have time to respond. If the kinetic energy of the electron is insufficient, screening of the excited electron and the photohole left behind has to be taken into account. This is known as the *adiabatic limit* of the excitation process [17].

If the expressions of Eq. 2.3 are inserted into Fermi's golden rule, the inner product term of Eq. 2.1 becomes

$$\langle \psi_{\mathrm{f}} | \, \hat{H}_{\mathrm{int}}(\mathbf{p}) \, |\psi_{\mathrm{i}}\rangle = \langle \phi_{\mathrm{f}}^{\mathbf{k}} | \hat{H}_{\mathrm{int}}(\mathbf{p}) | \phi_{\mathrm{i}}^{\mathbf{k}}\rangle \langle \psi_m^{N-1} | \psi_{\mathrm{i}}^{N-1}\rangle. \tag{2.4}$$

Here, we have used the Hermitian nature of the anti-symmetrization operator: $\hat{\mathcal{C}}^\dagger \hat{H}_{\mathrm{int}} \hat{\mathcal{C}} = \hat{\mathcal{C}}^\dagger \hat{\mathcal{C}} \hat{H}_{\mathrm{int}} = \hat{H}_{\mathrm{int}}$. Notice that since only a single electron is being excited, the initial and final states of the remaining $N-1$ electrons are left unaffected by the perturbation operator $\hat{H}_{\mathrm{int}}$. The term $\langle \phi_{\mathrm{f}}^{\mathbf{k}} | \hat{H}_{\mathrm{int}} | \phi_{\mathrm{i}}^{\mathbf{k}}\rangle \equiv \mathcal{M}_{\mathrm{i,f}}^{\mathbf{k}}$ is thus a single-electron-state matrix element of the dipole operator, while $\langle \psi_m^{N-1} | \psi_{\mathrm{i}}^{N-1}\rangle$ describes the overlap integral between the many-particle initial and final states.

To arrive at the total rate of excitation $\mathcal{W}_{\mathrm{i}\to\mathrm{f}}$, all possible final states that satisfy $\delta(E_{\mathrm{f}} - E_{\mathrm{i}} - h\nu)$ must be accounted for. A sum over m is therefore introduced, and Eq. 2.1 becomes

$$\mathcal{W}_{\mathrm{i}\to\mathrm{f}} = \frac{2\pi}{\hbar} \left| \mathcal{M}_{\mathrm{i,f}}^{\mathbf{k}} \right|^2 \sum_m \left| \langle \psi_m^{N-1} | \psi_{\mathrm{i}}^{N-1}\rangle \right|^2 \delta(E_{\mathrm{f}} - E_{\mathrm{i}} - h\nu), \tag{2.5}$$

where $|\langle \psi_m^{N-1} | \psi_{\mathrm{i}}^{N-1}\rangle|^2 = |c_m|^2$ are coefficients that describe the probability the photon absorption will leave the remaining $N-1$ electrons in an excited state $|\psi_m^{N-1}\rangle$.

While the re-written expression for the golden rule in Eq. 2.5 contains several simplifying assumptions, it holds up reasonably well in many cases and is commonly used when describing and quantifying photoemission signals. The following two sections will outline the basic principles of the experimental techniques used in this thesis. All of these are related to Fermi's golden rule either in the general form (Eq. 2.1) or under the sudden approximation (Eq. 2.5).

2.2 Probing Electronic Core States

In this section, some of the main techniques for probing photoexcitations from sharply defined, 'core level' electronic states are outlined and discussed. Understanding these techniques and their applications in surface science will be particularly relevant for interpreting Papers [1], [2] and [4].

2.2.1 X-Ray Photoelectron Spectroscopy (XPS)

In X-ray photoelectron spectroscopy (XPS), soft X-rays are used to excite electrons into a vacuum from the atomic orbitals most tightly bound by
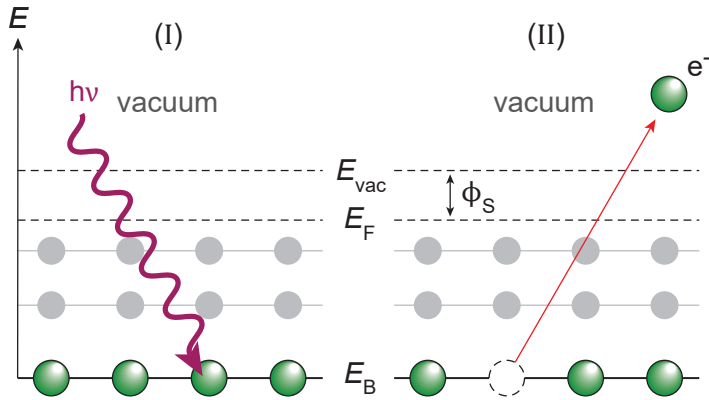
Figure 2.1: An illustration of electron emission by the photoelectric effect. An incident photon is absorbed by an electron occupying a well-defined state with binding energy E_B below the Fermi level E_F in a material (I). If the energy $h\nu$ of the absorbed photon is greater than the sum of E_B and the surface work function ϕ_S, the electron can overcome the surface potential energy barrier and escape the material with a finite kinetic energy E_K (II).

the atomic nuclei[3]. XPS relies on the photoelectric effect, which was first explained by A. Einstein in 1905 [10]. In Einstein's description, electromagnetic radiation that is incident on a material can, if the energy $h\nu$ of the impinging photons is sufficiently high, excite bound electrons from the sample into its surrounding environment with finite kinetic energy E_K. An illustration of the photoelectric effect is given in Fig. 2.1.

By collecting these electrons, separating them based on their kinetic energies, and quantifying their signal intensities, one can obtain information about the initial states in the material before the photoexcitation. This is because bound 'core level' electrons tend to have sharply defined energies, characteristic of both their atomic origin and the local bonding environment in the material they inhabit. Therefore, XPS is particularly useful for studying what atomic species are present in a material, their local chemical environment, and the material stoichiometry [20].

---

[3]Typical atomic orbitals probed by XPS are $1s$ to $3d$.

Energy Conservation

As mentioned, energy conservation must be considered when describing photoexcitation. The same applies to the process of photoemission. The so-called 'three-step model' can provide a conceptually simple and intuitive description of photoemission where energy is conserved. While it fails to capture the many-particle nature of the problem (see Section 2.1.2), it serves as an excellent tool for understanding the evolution of the electron's energy from photon absorption until it escapes its parent material. A summary is therefore given here, based on Chapter 6 of Ref. [12].

In the *first step*, an impinging photon of energy $h\nu$ is absorbed by an electron of binding energy E_B, ripping it free from its parent atom and providing it with a finite kinetic energy E_K^*. In the *second step*, the electron propagates through the material towards the surface. If E_K^* is sufficient, the electron can overcome the surface potential energy barrier ϕ_S and escape the material with a reduced kinetic energy $E_K = E_K^* - \phi_S$. This is the *third step*, after which the electron is captured and detected. This is usually done using an electron analyzer with work function ϕ_A that is placed in electrical contact with the sample material. A common ground causes their Fermi levels to align so that an additional contact potential energy $U = (\phi_A - \phi_S)$ is added to the measured kinetic energy of the photoelectron.

From the three-step model, the total energy of the system can thus be described as

$$h\nu = E_B + \phi_S + E_K. \tag{2.6}$$

According to Eq. 2.6, the binding energy E_B of occupied states in a material can be linked to the E_K of photoelectrons that get excited by light with a well-defined energy $h\nu$, if the surface work function ϕ_S is known. Usually, knowing ϕ_S will require additional measurements of the sample material [21]. However, due to the contact potential U induced by the analyzer, the *measured* kinetic energies becomes

$$E_K^{\text{meas}} = h\nu - E_B - \phi_S + U$$
$$= h\nu - E_B - \phi_A. \tag{2.7}$$

It is therefore sufficient to know ϕ_A, which can be established from calibration measurements of the Fermi level using noble metal samples [21]. The expressions in Eqs. 2.6 and 2.7 are also valid assumptions for the other photoemission techniques that will be discussed in subsequent sections of this Chapter.

Photoemission Signal Intensity

Let us return to Fermi's golden rule under the sudden approximation (Eq. 2.5) to define the measured photoemission intensity. The expression for the rate $\mathcal{W}_{i \to f}$ established so far accounts for both energy conservation in the photoemission process and the availability of final states. Additionally, the intensity of photoemitted electrons from a given initial state $|\psi_i^N\rangle$ is scaled by the Fermi-Dirac function $f_D(E_i, T)$, which describes the probability that the chosen initial state is occupied. The photoemission intensity $I_{i \to f}$ from $|\psi_i^N\rangle$ is then proportional to

$$I_{i \to f}(\nu, T) \propto \mathcal{W}_{i \to f} \cdot f_D(E_i, T)$$
$$= \left| \mathcal{M}_{i,f}^{\mathbf{k}} \right|^2 \sum_m \left| \langle \psi_m^{N-1} | \psi_i^{N-1} \rangle \right|^2 \delta(E_f - E_i - h\nu) f_D(E_i, T). \qquad (2.8)$$

The total photoemission intensity can be obtained by also summing over all possible initial states that satisfy $\delta(E_f - E_i - h\nu)$.

We note here that the magnitude of the one-electron dipole matrix element $\mathcal{M}_{i,f}^{\mathbf{k}} = \langle \phi_f^{\mathbf{k}} | \hat{H}_{int} | \phi_i^{\mathbf{k}} \rangle$ depends on the energy, polarization, and incidence angle of the incoming light relative to the orientation of the single electron atomic orbitals $|\phi_i^{\mathbf{k}}\rangle$ and $|\phi_i^{\mathbf{k}}\rangle$ [12]. Hence changing any of these will lead to modulations in the photoemission intensity, and in certain cases, the signal can be completely suppressed. Although such 'matrix element effects' in many cases can be hard to interpret, they can also contain useful information about the initial states' geometry and orbital nature. Carefully measuring the modulation of $\mathcal{M}_{i,f}^{\mathbf{k}}$ as a function of, e.g., light incidence angle or polarization can therefore help ascertain additional features of the material in question. In the next section, it is discussed how the $\mathcal{M}_{i,f}^{\mathbf{k}}$ modulation of XPS measurements can be used to determine chemically specific atomic positions in a material.

2.2.2 X-Ray Photoelectron Diffraction (XPD)

X-Ray Photoelectron Diffraction (XPD) is a technique that is particularly well suited for obtaining chemically specific information about the structural distribution of atoms on or near solid surfaces. With XPD, the information available through XPS is extended by considering the coherent interference of directly emitted and elastically scattered photoelectrons. This situation is illustrated in Fig. 2.2a. With incoming light, a primary beam of unscattered core level photoelectrons is excited from a material, alongside beams
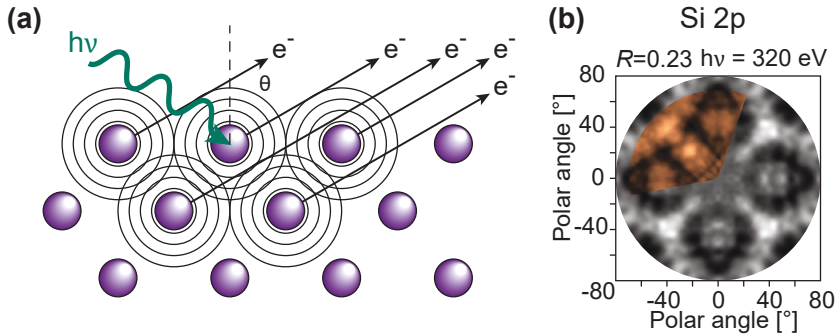
Figure 2.2: Illustation of X-ray Photoelectron Diffraction (XPD). **(a)**: Schematic illustrating the interference of primary (unscattered) and secondary (elastically scattered) electrons in an XPD experiment. **(b)**: Polar angle plot of measured XPD from Si 2p (orange), overlaid on a simulation (grey) of XPD from the bulk Si structure using EDAC [22]. The simulations are the courtesy of Ezequiel Tosi, 2022.

of secondary electrons that have scattered elastically from a finite cluster of neighboring atomic sites. The different outgoing beams will interfere, leading to a measurable modulation in the photoelectron intensity, varying with the solid angle of detection [12].

XPD is typically measured by performing XPS from a core level using fixed photoexcitation energy and recording the resultant photoemission signal over a large range of azimuthal (φ) and polar (θ) angles relative to the sample plane and surface normal direction. The measured intensities $I(\theta, \varphi)$ of each constituent peak component can then be used to obtain polar plots of their modulation functions χ, defined as

$$\chi = \frac{I(\theta, \varphi) - I_0(\theta)}{I_0(\theta)}, \tag{2.9}$$

where $I_0(\theta)$ is the average intensity for a given θ across all measured φ [15]. An example of a measured XPD polar plot is shown as an orange 'pizza slice' in Fig. 2.2b.

To obtain structural information from XPD, the measured intensity modulations χ are typically compared with simulated photoelectron interference from models of the same system. Such simulations will typically consider multiple scattering events from a finite cluster of neighboring atoms around the emitter, i.e., the main interference contributions from the dominating

scattering mechanisms [15]. The agreement between simulated and measured XPD intensity modulations, χ_{sim} and χ_{exp}, can be quantified by calculating a reliability factor R

$$R = \frac{\sum_i \left(\chi_{\text{sim},i} - \chi_{\text{exp},i}\right)^2}{\sum_i \left(\chi_{\text{sim},i}^2 + \chi_{\text{exp},i}^2\right)}, \tag{2.10}$$

where the sums run over the modulation functions obtained for the i different polar angles θ [23]. From Eq. 2.10, $R = 0$ signifies perfect agreement, $R = 1$ indicates no correlation and $R = 2$ anti-correlation between the measurements and simulations [15]. To reach the correct material structure as indicated by the measured XPD, the parameters of each simulation (e.g., the relative atomic positions) are iteratively adjusted and compared to the measurements to minimize R. Typically, $R < 0.3$ indicates a good agreement between simulation and measurement [24, 25]. For the work presented in this thesis, simulations were performed using the program package for electron diffraction of atomic clusters (EDAC) [22].

Chemically Specific Surface Diffraction

Compared to other diffractive techniques commonly used in condensed matter physics, XPD has a few exciting and distinct properties. Firstly, its fundamental excitation process is photo-*emission*, meaning the incoming beam is different than the outgoing beam: incoming photons (bosons) excite outgoing electrons (fermions) of finite kinetic energy. This means that the primary beam of the diffraction problem is an outgoing one: unscattered electrons are generated 'in' the sample and will interfere constructively and destructively with other beams of outgoing electrons. Compared to other diffractive techniques, where one also has to consider interference with the incoming beam(s), this simplifies the scattering problem somewhat for energies of a few hundred eV [12].

The different nature of the incoming and outgoing beams also means that the intensity of the measured diffraction signal is primarily limited by the finite escape depth of the outgoing photoelectrons [26]. The surface sensitivity can thus be tuned by adjusting the photoexcitation energy, and XPD is typically performed with photon energies yielding an escape depth of a few nanometers. This makes XPD moderately surface sensitive compared to, e.g., electron diffraction and helium scattering with sensitivities down to a few atomic layers [27, 28]. Note, however, that despite its ability to

capture some bulk properties from the host material, XPD is not to be considered a bulk-sensitive technique per se when compared to, e.g., X-ray diffraction, where the incoming and outgoing photon beams can penetrate several hundred micrometers [29].

The second and perhaps even more important property of XPD is the chemical sensitivity achieved by the photoemission process. When probing electrons excited from atomic core levels with well-defined energies, elemental specificity and the ability to study different bonding stoichiometries can be achieved [24, 25]. Combined with the tunable depth sensitivity provided by a source of variable photon energy, XPD can offer many new insights that are not available from other techniques used for surface structure determination.

2.2.3   Near-Edge X-Ray Absorption Spectroscopy (NEXAFS)

As opposed to techniques that rely on photo-*emission*, i.e., the promotion of bound electrons into free electron states above the vacuum level E_{vac}, X-ray absorption spectroscopy (XAS) techniques will promote electrons to unoccupied, bound states between E_{vac} and the Fermi level (E_{F}). The XAS process is sketched in Fig. 2.3, along with some of the photoemission techniques discussed in Chapter.

Amongst the different XAS techniques available, Near-edge X-ray absorption fine structure (NEXAFS) measurements are particularly suitable for studying the structural properties of low-Z (i.e., atomic number) molecules on surfaces [30]. In NEXAFS, transitions are probed between tightly bound atomic states, e.g., the $1s$ and $2p$ states, and unoccupied, near-energy intra- or extra-molecular orbitals. This is done by subjecting the atomic species of interest to light of variable photon energy $h\nu$, typically using a synchrotron light source, and observing the rate of light absorption[4] when $h\nu$ assumes the characteristic energies of the transition(s) between the initial and final states.

---

[4]The light absorption as a function of energy is measured from the by-products generated when deep core level electrons transition into unoccupied states, e.g., fluorescent light, Auger electrons, or other secondary electrons from the cascade of scattering processes following the excitation(s) [30].
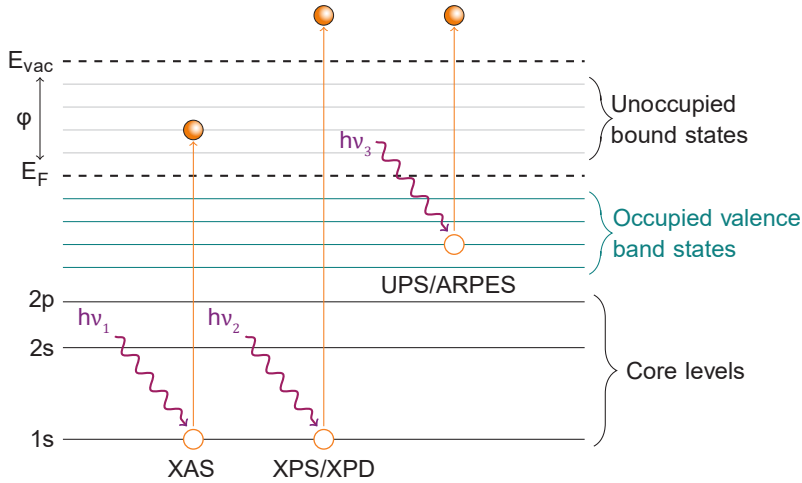
Figure 2.3: Sketch of photoexcitation processes outlining the differences between photo-*emission* and -*absorption*. In the former case, e.g., when measuring XPS, XPD, UPS or ARPES, electrons are excited from bound states below the Fermi level (E_F) and into the continuum of free electron vacuum states ($E_\mathrm{final} > E_\mathrm{vac}$). In contrast XAS techniques excite electrons to the unoccupied, bound electronic states, (i.e. with energies $E_\mathrm{F} < E_\mathrm{final} < E_\mathrm{vac}$).

Carbon K-edge NEXAFS

NEXAFS has several applications but is particularly useful for verifying the presence of, and secondly, determining the molecular orientation of low-dimensional, sp^2-hybridized carbon materials on surfaces [31]. In such cases, the intensity of excitations from the $1s$ atomic level into the unoccupied π^* antibonding orbital as a function of light incidence angle θ relative to the sample plane is exploited. In aromatic carbon compounds, the lowest unoccupied molecular orbital (LUMO) π^* states are comprised of highly directional $2p_\mathrm{z}$ atomic orbitals that are oriented perpendicular to the molecular plane(s) (see Fig. 2.4a). When linearly polarized light with a well-defined electric field vector $\mathcal{E}$ is incident, $1s \rightarrow \pi^*$ excitations are amplified (*i*) at resonant photon energy $h\nu \approx E_{\pi^*} - E_{1s}$ and (*ii*) when $\mathcal{E}$ is aligned with the direction of the $2p_\mathrm{z}$ orbitals [32]. Hence, by measuring with photon energy around that of the $1s \rightarrow \pi^*$ resonance and simultaneously varying the light angle of incidence θ (Fig. 2.4b), the plane orientation of the aromatic
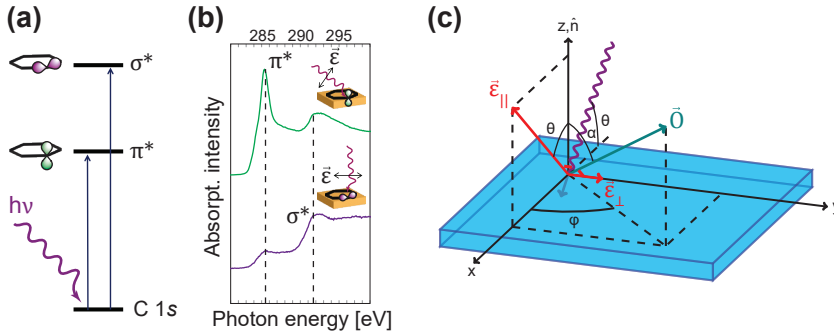
Figure 2.4: Carbon K-edge NEXAFS measurements. **(a)**: Sketch of molecular orbitals in sp^2-hybridized carbon compound undergoing photoabsorption. The lowest unoccupied molecular orbital (LUMO) that electrons can be excited to is the π^* state, which is comprised of out-of-plane $2p_z$ orbitals. **(b)**: Example C $1s$ K-edge NEXAFS from few-layer graphene. When the linearly polarized electric field $\mathcal{E}$ aligns with the direction of the $2p_z$ orbitals, maximal photoabsorption from the $1s \rightarrow \pi^*$ transition is achieved. **(c)**: Coordinate system and characteristic angles and vectors for a NEXAFS experiment. The angles θ and α correspond to those appearing in Eq. 2.11.

rings can be ascertained from the θ that yields the maximum, out-of-plane NEXAFS intensity [31, 32].

The coordinate system of a typical NEXAFS experiment probing aromatic carbon compounds is sketched in Fig. 2.4c. Here, the vector **O** represents the direction of the $2p_z$ orbitals that make up the LUMO π^*. **O** is at an angle α to the surface normal $\hat{\mathbf{n}}$, and projects onto the substrate xy-plane with azimuthal angle φ. The incident, linearly polarized light has a dominant electric field vector $\mathcal{E}_{||}$ at an angle[5] θ to $\hat{\mathbf{n}}$, and a minority component $\mathcal{E}_\perp$ in-plane with the substrate.

For threefold-symmetric aromatic carbon rings, the φ dependence vanishes, and the NEXAFS resonance intensities reduce to [32]:

$$I \propto PI^{||} + (1-P)I^\perp = P \cdot A \left(\cos^2\theta \cos^2\alpha + \frac{1}{2}\sin^2\theta \sin^2\alpha \right)$$
$$+ (1-P) \cdot A \sin^2\alpha, \qquad (2.11)$$

---

[5] Note that since $\mathcal{E}_{||}$ is normal to the wave vector **k** of the incoming light, the angle $\mathcal{E}_{||}$ makes with $\hat{\mathbf{n}}$ is the same as the light angle of incidence relative to the substrate plane.

where P is the fractional polarization of the dominant electric field $\mathcal{E}_{||}$, and A is the angle integrated cross-section of the photoabsorption. Typically, $P \geq 0.9$ and thus the $I^{||}$ contribution dominates. To ascertain the orientation of aromatic carbon plane(s), The $C1s \to \pi^*$ NEXAFS intensity is measured as a function of θ, and compared to the 'theoretical' expression in Eq. 2.11 to determine the corresponding α [1, 31].

2.3 Probing Valence Band Electrons

To access information about electrons closer to the Fermi level, it is common to perform photoemission experiments with lower photoexcitation energies than needed to access the more tightly bound core levels, e.g., in XPS experiments. Furthermore, since the electrons near E_F occupy states with both well-defined binding energy and momentum, one can obtain a complete map of their occupied bandstructure if both parameters are measured from the photoexcited electrons. The following subsection concerns the basic properties of measured valence band photoemission signals.

2.3.1 Angle-Resolved Photoemission Spectroscopy (ARPES)

In angle-resolved photoemission spectroscopy (ARPES), lightly bound photo-emitted electrons are measured as a function of their kinetic energy E_K, and polar θ and azimuthal φ angles when leaving a photoexcited sample. The measured signal as a function of E_K, θ and φ can then be used to reconstruct the energy dispersion relations of the states the electrons occupied before their light excitation.

Like in XPS experiments, measured ARPES signals satisfy the same energy conservation law (Eq. 2.6). However, when ejecting into a vacuum, the electrons' momenta will diminish in the direction parallel to the surface normal from working against the electrostatic forces generated by surface charges. Consequently, all outgoing electrons will be refracted as they overcome the potential energy barrier at the surface, and only the in-plane momentum $\hbar\mathbf{k}_{||}$ of the electrons will be conserved in the process, as shown in Fig. 2.5. The specifics of how $\mathbf{k}_{||}$ relates to the geometry (i.e., the emission angles) of an ARPES experiment will be explained in the next Chapter (3.1) on photoemission signal detection.

Quasi-Particles and Many-Body Interactions

Commonly, the electrons in a solid will interact with each other, as well as different degrees of freedom, such as bosonic excitations. These interactions will renormalize the electron energy and momenta, altering their effective masses m^* and the finite lifetimes τ that they will have in their pre-occupied states [33]. In actual photoemission experiments, the signal received is, therefore, from *quasi-particles* of electrons that are 'dressed' by the interactions that they experience before exciting from the solid [12, 17].

   Returning to the expression for photoemission intensity defined previously, we seek to explore how many-body interactions manifest themselves in measured ARPES. By also accounting for the conservation of in-plane electron momentum during the photoemission process, Eq. 2.8 becomes

$$I\left(\nu, \mathbf{k}_{||}, T\right) \propto \left|\mathcal{M}_{\mathrm{i,f}}^{\mathbf{k}}\right|^2 \sum_m \left|\langle \psi_m^{N-1} | \psi_\mathrm{i}^{N-1} \rangle\right|^2 \delta(E_\mathrm{f} - E_\mathrm{i} - h\nu)$$

$$\cdot \delta(\mathbf{k}_\mathrm{f}^{||} - \mathbf{k}_\mathrm{i}^{||} - \mathbf{G}^{||}) f_\mathrm{D}(E_\mathrm{i}, T). \tag{2.12}$$

Here, $\mathbf{G}^{||}$ is merely an in-plane reciprocal lattice vector that connects $\mathbf{k}_\mathrm{i}^{||}$ and $\mathbf{k}_\mathrm{f}^{||}$. Any information about the energy renormalizations of the initial, many-particle state is likely to be embedded in $|\psi_\mathrm{i}^{N-1}\rangle$. Furthermore, it should be related to the initial energy E_i of the system and also the momentum ($\propto \mathbf{k}$) of the electron being photoemitted and detected.

   From Eq. 2.12, the so-called *spectral function* of the photohole left behind at wave vector $\mathbf{k}$ by the emission process can be defined as [17]:

$$\mathcal{A}(\mathbf{k}, \nu) = \sum_m \left|\langle \psi_m^{N-1} | \psi_\mathrm{i}^{N-1} \rangle\right|^2 \delta(E_\mathrm{f} - E_\mathrm{i}(\mathbf{k}) - h\nu). \tag{2.13}$$

Within the framework of Green's function formalism, $\mathcal{A}$ is proportional to the imaginary part of the complex, one-particle Green's function G of the photoemitted electron. Specifically, $\mathcal{A}$ describes the probability of removing an electron with energy E_i (relative to E_F) from the interacting N-electron system. It also contains information about the energy renormalizations caused by the many-body interactions present in the system [12].

   In the energy-momentum representation, $\mathcal{A}$ takes the form of a Lorentzian:

$$\mathcal{A}(\mathbf{k}, \omega) = -\frac{1}{\pi} G(\mathbf{k}, \omega) = \frac{\pi^{-1} \operatorname{Im} \Sigma(\mathbf{k}, \omega)}{\left[\hbar\omega - \varepsilon(\mathbf{k}) - \operatorname{Re} \Sigma(\mathbf{k}, \omega)\right]^2 + \left[\operatorname{Im} \Sigma(\mathbf{k}, \omega)\right]^2}. \tag{2.14}$$
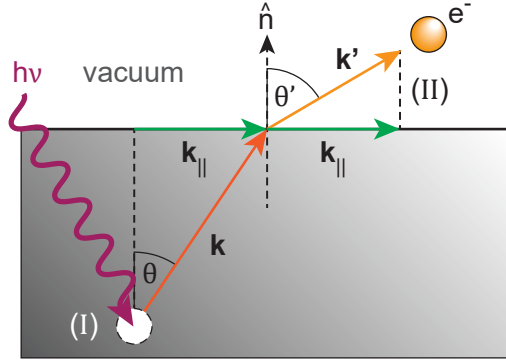
Figure 2.5: A sketch of the surface refraction experienced by a photoelectron leaving a metal sample. In the simplified picture (i.e., the *three-step model*) where $h\nu > E_B$, a photoexcited electron is freed from its bound state with a finite kinetic energy E_K^* and momentum $\hbar\mathbf{k}$, at an angle θ relative to the surface normal $\hat{\mathbf{n}}$ (I). If $E_K^* > \phi_S$ the electron will overcome the surface potential energy barrier, and eject into vacuum with non-zero kinetic energy E_K. In the process, momentum $\hbar\mathbf{k}_\perp$ parallel to $\hat{\mathbf{n}}$ will be lost, and the overall momentum will reduce to $\hbar\mathbf{k}'$ so that the angle θ increases to θ' (II). Note how the momentum $\hbar\mathbf{k}_\parallel$ parallel to the surface is conserved throughout the photoemission process.

Here, $\varepsilon(\mathbf{k})$ is a non-interacting energy band dispersion of electronic states, while $\mathrm{Re}\,\Sigma$ and $\mathrm{Im}\,\Sigma$ are components of the complex self-energy Σ that describes the many-body interactions [34]. In later Chapters, Eq. 2.14 will be used to quantify and disentangle the effects of different types of interactions that can be measured using ARPES, particularly those related to electron-phonon and electron-magnon couplings.

Chapter 3

Photoelectron Detection

In this Chapter, the detection of photoelectrons is discussed, with a particular emphasis on instrument-related and practical considerations. In Sections 3.1 and 3.2, one conventional and one more recent setup for detecting and resolving photoemission signals are presented, respectively. Finally, a few practical considerations for achieving selective, layer-resolved photodetection are discussed in Section 3.3.

3.1   Photodetection with Hemispherical Analyzers

To resolve occupied states from which electrons are excited in a photoemission experiment, outgoing photoelectrons need to be distinguished from one another based on their kinetic energy and momentum. To do so, the electrons are (*i*) focused through a set of optics comprised of electromagnetic lenses and (*ii*) dispersed from one another based on their kinetic energy and emission angle. Finally, (*iii*) the electrons are collected and counted. While different techniques for photoelectron filtering and detection exist (see, e.g., Refs. [35, 36]), it is today most common to use a *hemispherical analyzer* (HA) equipped with an electron detector.

A typical photoemission setup with a HA is shown in Fig. 3.1. In the presence of incoming light from the ultraviolet to soft X-ray regime [18], electrons can be excited from an irradiated sample into the surrounding vacuum. A column of electrostatic lenses then collects and focuses a small solid angle of the emitted photoelectrons through a HA *entrance slit* of width s_1. The HA itself consists of two concentric hemispheres with different radii, i.e., R_1 and R_2, and the two are biased at different electrostatic potentials. A
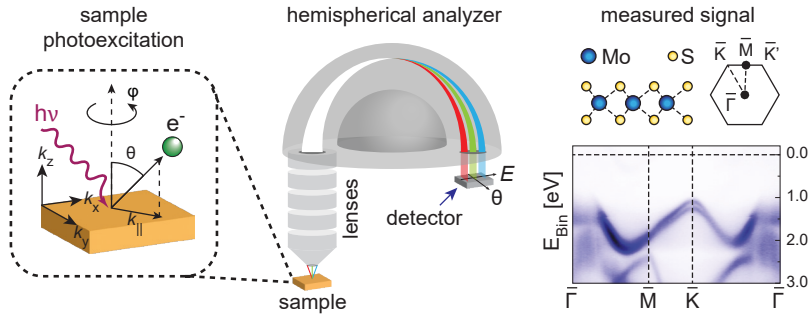
Figure 3.1: A typical photoemission experiment. When subject to light of energy $h\nu$, electrons are excited from the sample and into a vacuum with finite kinetic energy. In-plane momentum ($\propto \mathbf{k}_\|$) is conserved in the process. The excited photoelectrons are collected and filtered in energy and angle using a hemispherical analyzer (HA). The detected signal can be transformed into energy-dispersive (E vs. $\mathbf{k}_\|$) ARPES plots. The example data shown has been collected from exfoliated, multilayer MoS_2.

radial electric field is thus established between the two, and electrons entering through the slit with different linear momentum and kinetic energy will deflect differently on their way through the HA. The two concentric hemispheres, therefore, act as an energy bandpass filter: by tuning the potential between the two, electrons of different energies can be selected.

At the other end of the HA, an *exit slit* of finite width s_2 will limit the range of trajectories – and thus also the kinetic energies allowed to leave the hemispheres and reach the electron detector. An electron that makes a perfect half-circular trajectory from the center of the entrance slit, through the HA, and into the center of the exit slit should have an energy

$$E_{\mathrm{P}} = q\Delta V \cdot \left[\frac{R_1 R_2}{R_1^2 - R_2^2} \right]. \tag{3.1}$$

Here, R_1 and R_2 are the radii of the larger and smaller hemisphere, respectively, ΔV is the potential difference between the two, and q is the elementary charge [37, 38]. E_{P} is commonly referred to as the *pass energy* of the system and will, together with the sizes of the entrance and exit slits, define the overall energy resolution as

$$\Delta E = \frac{E_{\mathrm{P}}}{2} \left[\frac{s_1 + s_2}{R_1 + R_2} + \alpha_{\max}^2 \right], \tag{3.2}$$

where α_{max} is the maximum angle of acceptance through the entrance slit, relative to the entrance normal [38]. In most setups, this acceptance angle can be made quite small, and thus the term α_{max}^2 is commonly neglected from Eq. 3.2.

While the width of the exit slit s_2 in the *energy-dispersive* direction will limit the ΔE accepted through to the detector, the dimensions of the same slit in the orthogonal direction should limit the magnitude of *angular acceptance* (i.e., θ, see Fig. 3.1) of photoelectrons passing through the HA. For practical purposes, however, the angular acceptance of photoelectrons is commonly selected using the electrostatic lenses upstream from the HA.

In ARPES experiments, the measured photoemission signal from electrons ejected with azimuthal and polar photoemission angles φ and θ from a sample can be used to determine the in-plane momentum $\hbar\mathbf{k}_{||}$ that the electrons had before leaving the solid[1]. Here, the theoretical relation between the mentioned quantities is merely stated, and we refer to Damascelli's review for details [17]. The in-plane wave vector $\mathbf{k}_{||}$ of measured electrons can be defined in terms of the experimental angles as

$$\mathbf{k}_{||} = \frac{\sqrt{2mE_{\mathrm{K}}}}{\hbar} \sin\theta[\cos\varphi \cdot \hat{\mathbf{x}} + \sin\varphi \cdot \hat{\mathbf{y}}], \qquad (3.3)$$

where m is the non-interacting electron mass, E_{K} is kinetic energy, and $\hbar$ is the reduced version of Planck's constant. Hence by collecting photoelectrons for a range of kinetic energies and emission angles, the occupied bandstructure within the sample system can be reconstructed from the ARPES measurements. Note that this typically involves changing the relative geometry of the sample plane and HA, which in turn will affect the photoionization matrix elements of the photoemission process (see Chpt. 2.2.1 and Ref. [39] for details). In the next section, an alternative experimental setup for measuring electronic bandstructures is discussed.

3.2 NanoESCA III Momentum Microscopy

An alternative to using HAs is to measure electronic bandstructures by *momentum microscopy*, using an energy-filtered photoemission electron micro-

---

[1]The in-plane wave vector $\mathbf{k}_{||}$ is conserved during the photoemission process. Note, however, that the $\mathbf{k}_\perp$ component is scrambled as an electron crosses the surface potential energy barrier into a vacuum. Since $\mathbf{k}_\perp$ is not a conserved property in photoemission experiments, it, therefore, has limited use when characterizing initial electronic states in a material [17]. An example of a case of $\mathbf{k}_\perp$ interpretation is discussed in Paper [5].

scope (PEEM). PEEM instruments offer precise control over the lateral size of the area from which photoemission is measured, typically down to a few micrometers in diameter. Hence, they can be ideal for measuring materials systems where the spatial coherency of properties is limited, e.g., on exfoliated flakes of van der Waals materials [40]. Furthermore, PEEM-based bandstructure measurements can usually overcome or circumvent some of the known challenges with 'conventional' ARPES. This makes momentum microscopy an exciting photoemission technique that allows more of the electronic properties of solids to be explored. In the following, the methodology of momentum microscopy measurements is outlined with particular emphasis on the NanoESCA III technology (Scienta Omicron/Focus GmbH).

A typical momentum-resolved PEEM experiment is shown in Fig. 3.2a. The sample in question is placed close to an optical column that contains electrostatic lenses, stigmators, and deflectors. The column is biased at 12-20 kV relative to the sample so that all photoelectrons emitted within the entire hemisphere of solid angles above the sample plane[2] get accelerated towards the objective lens [41, 42]. By introducing physical apertures, either in the back focal or reciprocal image plane, the sampling of electrons can be restricted to either (i) a small angular distribution, improving real-space resolution, or (ii) a small spatial 'excitation area' on the surface, improving reciprocal (i.e., $\mathbf{k}_{||}$) resolution [41, 43].

Upon exiting the PEEM column, the photoelectrons can pass through either one or several HAs that will filter them by energy (see the previous section). In the NanoESCA III, two hemispheres are exploited so that the propagating electrons form perfect 'Kepler ellipses' on their way through the energy filter (Fig. 3.2c). By placing two HAs back-to-back, a perfectly achromatic, two-dimensional image is formed at the final exit slit, as the second hemisphere compensates for any aberrations introduced by electrons entering the first hemisphere at a non-zero angle α [44].

After exiting the energy filter, electrons are projected towards the detector stage, where they form a two-dimensional, constant-energy real or reciprocal image, depending on the mode of operation. Hence by recording several reciprocal ($\mathbf{k}$-space) images at different kinetic energies, the occupied bandstructure can be reconstructed from the image stack (Fig. 3.2b).

The main strength of using momentum microscopy for ARPES measurements lies in the ability to record band structures from areas of µm-size diameters and simultaneously resolve a relatively large diameter in recipro-

---

[2]I.e., at polar angles $\theta = \pm 90°$ and all azimuthal/in-plane angles φ.
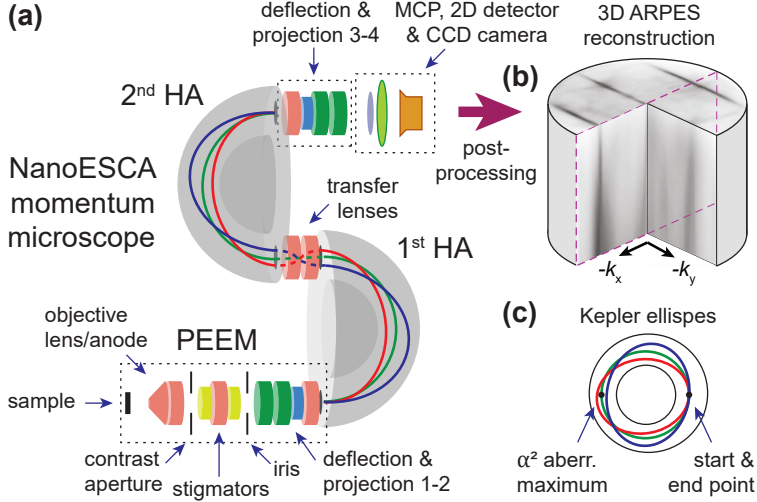
Figure 3.2: NanoESCA III Momentum Microscopy. **(a)**: Outline of NanoESCA-style momentum microscopy setup. Photoelectrons are excited from a grounded sample into a biased (12-20 kV) PEEM column that focuses and corrects the photoemission signal. Two hemispherical analyzers (HAs) filter the signal by energy and correct deflection-related aberrations. Finally, the energy-resolved signal is incident on a microchannel plate (MCP) amplifier and projected onto a 2D detector. A CCD camera is used to record constant-energy images of the detector signal. **(b)**: A volumetric reconstruction of an occupied bandstructure from a set of measured, constant-energy, reciprocal space images of Bi(112). **(c)**: 'Kepler ellipses' of photoelectrons with the same kinetic energy making one full ($\phi = 2\pi$) revolution in a radially directed electrostatic field.

cal space. Typically, such measurements can span beyond the first Brillouin zone for most materials, e.g., ± 2.75 Å^{-1} for the NanoESCA III. This eliminates the need to rotate the sample plane relative to the extraction lens so that features in **k**-space far away from the $\bar{\Gamma}$ point can be captured. Hence the measurement geometry and the associated photoionization matrix elements can be preserved throughout measurements [39].

When equipped with a He discharge lamp and liquid nitrogen cooling of the sample stage (≈ 77 K), the standard NanoESCA III setup can typically achieve working resolutions of 50 meV and 0.02 Å^{-1}. However, when cooled to liquid Helium temperature (≈ 40 K) and running the instrument with

smaller entrance slits and lower pass energies (see Eq. 3.2), resolutions of 12.0 meV and 0.005 Å^{-1} are readily achievable. With these settings, the NanoESCA can perform benchmark measurements such as resolving the Rasha splitting of the Au(111) surface state [44]. When used with synchrotron light, the NanoESCA also has a demonstrated track record of resolving energy renormalizations from many-body interactions [45]. Such measurements are typically only achieved using high-resolution ARPES setups equipped with high transmission hemispherical analyzers [46–49].

3.3   Manipulating the Photoemission Probing Depth

Within real materials, the practical depth beneath a surface that photoelectrons can escape from is limited by how far they can propagate without losing substantial energy and momentum. The *inelastic mean-free path* (IMFP) of photoelectrons is a measure of this propagation length. It is primarily defined by the material in which the electrons propagate. However, a kinetic energy-dependent behavior is still observed in most materials, allowing a 'universal' trend curve $\lambda(\varepsilon)$ to be established.

In crude terms, the IMFP is $\lambda \propto E_{\mathrm{K}}^{-2}$ for low kinetic energies ($E_{\mathrm{K}} \leq$ 30 eV), while a $\lambda \propto E_{\mathrm{K}}^{1/2}$ proportionality can be observed at at higher kinetic energies ($E_{\mathrm{K}} > 75$ eV) [26]. Since the E_{K} of a photoelectron ultimately is defined by the photoexcitation energy $h\nu$ (see Eq. 2.6), one can at this point already foresee that a higher $h\nu$ will allow electrons to be emitted from further beneath a sample surface. Hence the photoemission probing 'volume' ($\propto \lambda$) is expanded as $h\nu$ and E_{K} is increased, while the fractional intensity of signal received from the sample surface will *decrease*, resulting in more 'bulk'-sensitive photoemission measurements [50].

Starting with a simple attenuation model that is loosely based on Beer-Lamberts law [51], a straightforward relation between photoemission signal intensity, energy-dependent IMFP $\lambda(E_{\mathrm{K}})$ and photoemission angle θ to the surface normal can be established. Assume first that an electron is excited at angle θ and depth z beneath the surface and will leave the system with a probability [52]:

$$p(z) \propto e^{-z/[\lambda(E_{\mathrm{K}})\cos\theta]}. \tag{3.4}$$

Next, consider a layered system like the one sketched in Fig. 3.3a, where one elementary material of thickness t_{s} resides on top of another, bulk-like elementary material. At normal emission ($\theta = 0$), the added photoemission
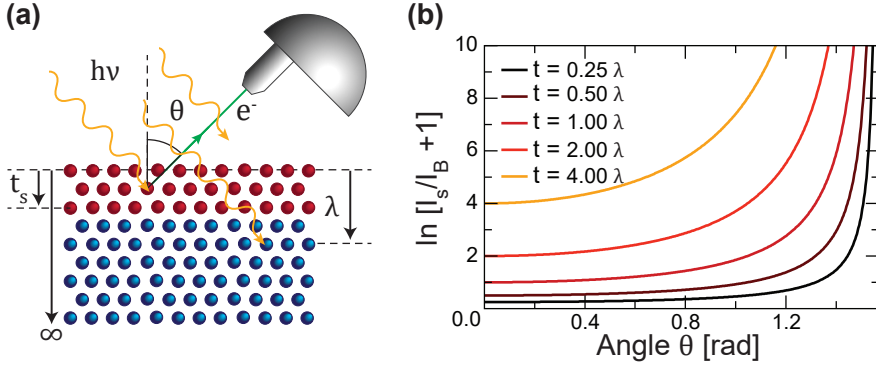
Figure 3.3: Measuring photoemission signals from a layered system. **(a)**: Sketch of a two-layer materials system probed using photoemission. The overlayer (red) has a thickness t_s, and the bulk underlayer is assumed infinitely thick. The measured intensity ratio of overlayer to bulk depends on the inelastic mean-free path λ and emission angle θ. **(b)**: The logarithmic behavior of the angle-dependent overlayer-to-bulk intensity ratio (Eq. 3.7), plotted as a function of emission angle θ for various overlayer thicknesses t_s. In the calculations, $\lambda = 1\,\text{nm}$ and $N_b\sigma_b = N_s\sigma_s$ are assumed.

per unit area from the top layer should be

$$I_s = \sigma_s N_s \int_0^{t_s} e^{-z/\lambda(E_K)}\mathrm{d}z = \sigma_s N_s \lambda(\varepsilon)\left[1 - e^{-t_s/\lambda(E_K)}\right], \qquad (3.5)$$

where σ_s and N_s are the elementary photoexcitation cross-section and atomic density in the layer, respectively. Similarly, the added photoemission intensity per unit area received from the bulk-like underlayer is approximated to

$$I_b = \sigma_b N_b \int_{t_s}^{\infty} e^{-z/\lambda(E_K)}\mathrm{d}z = \sigma_b N_b \lambda(E_K) e^{-t_s/\lambda(E_K)}, \qquad (3.6)$$

where the extent of the bulk has been assumed infinite[3], and σ_b and N_b are the elementary photoexcitation cross-section and atomic density in the bulk substrate, respectively.

From the ratio of bulk-to-surface intensity I_b/I_s, a useful expression for the surface overlayer thickness t_s can be found. Starting with the ratio of

---

[3]In most cases this is a reasonable approximation, as factor $\exp\{-z/\lambda(E_K)\}$ will diminish rapidly with increasing z. Commonly, $\lambda(E_K)$ is in the range of nanometers.

Eq. 3.5 to Eq. 3.6, the thickness t_s becomes, after some algebra:

$$\frac{t_s}{\lambda(E_K)} = \ln\left\{\frac{I_s\sigma_b N_b}{I_b\sigma_s N_s} + 1\right\}. \tag{3.7}$$

In cases where the angular dependence of I_b/I_s is useful, Eq. 3.7 is easily modified by the transformation $\lambda(E_K) \rightarrow \lambda(E_K)\cos\theta$. Also, in cases where the layer structure of materials with similar atomic density and photoionization cross-section are studied, i.e. $N_b \approx N_s$ and $\sigma_b \approx \sigma_s$, the expression can be simplified further. The logarithm from Eq. 3.7 is plotted in Fig. 3.3b for several different overlayer thicknesses t_s as a function of θ, assuming $\lambda(E_K) \approx 1\,\mathrm{nm}$ and equal atomic densities and cross-sections.

In Papers [1] and [4], the described energy- and angle-dependence of photoelectron intensity (Eq. 3.4) is exploited when the layer structure of the materials in question is probed, using Eq. 3.7. By carefully tuning $\lambda(E_K)$ and θ, the relative and absolute intensity changes of the measured XPS core levels can be used to distinguish surface-related stoichiometries from other components native to the bulk structures.

Chapter 4

Epitaxial Graphene

Arguably, what is most fascinating about graphene is its structural simplicity and the multitude of astounding properties that follow from it. Carbon allotropes come in a range of different shapes, abundancies, and with properties that are undoubtedly unique and extraordinary [53, 54]. Still, none of these have been met with the same craze or seen a similar breadth of topical appeal across the scientific disciplines as graphene has. For many years, carbon monolayers were but a theoretical construct: strictly two-dimensional materials had been deemed thermodynamically unstable and therefore not explored experimentally in great detail [55–57]. When graphene finally was experimentally realized in 2004[1], it came as a surprise to many that one could produce it routinely using conventional office supplies [59].

Graphene has since established itself in condensed matter research as the most prominent and commonly studied two-dimensional material. It is relatively simple to understand from a theoretical point of view, yet it sports several exotic properties. Examples include exceptional electrical and thermal conductivity [60, 61], extreme mechanical stability [62], massless Dirac fermions [63], and topological and mesoscopic phenomena such as an anomalous quantum Hall effect and unconventional superconductivity [64, 65]. By now, it is also relatively straightforward to produce in high quality and, therefore, an excellent platform for exploring and modifying physics in two dimensions.

In this Chapter, the electronic properties of graphene are first reviewed

---

[1]Its experimental realization pre-dates that of Novoselov and Geim, however, the product was never recognized as *graphene*. See, for instance, Ref. [58] for an updated review of the early graphene discoveries.

in Section 4.1. Next, different pathways to graphene formation are explored in Section 4.2, herein the so-called *transition-metal-mediated* approach. Finally, in Papers [1] and [2], it is argued how metal-mediated growth can provide an alternative pathway to graphene fabrication, circumventing the most common challenges with preparing high-quality graphene on semiconducting or insulating substrates.

4.1 The Structure of Graphene

Graphene consists of a single atomic layer of graphite, where carbon is arranged in a honeycomb lattice as shown in Fig. 4.1a. The atoms have a triangular Bravais lattice, with two atoms per unit cell that make up two submattices A and B. The lattice vectors can be written as

$$\mathbf{a}_1 = \frac{\delta}{2}\left(3, \sqrt{3}\right), \quad \mathbf{a}_2 = \frac{\delta}{2}\left(3, -\sqrt{3}\right), \tag{4.1}$$

where $\delta \approx 1.42\,\text{Å}$ is the interatomic distance between the nearest neigbors, A and B. In reciprocal space, the two vectors connecting adjacent graphene Brillouin zones are

$$\mathbf{b}_1 = \frac{2\pi}{3\delta}\left(1, \sqrt{3}\right), \quad \mathbf{b}_2 = \frac{2\pi}{3\delta}\left(1, -\sqrt{3}\right). \tag{4.2}$$

Carbon has atomic number 6. Therefore graphene, with its diatomic basis, has twelve electrons per unit cell. The first two electrons of each atom are placed in the innermost $1s$ orbital, accounting for both possible spin orientations $\uparrow$ and $\downarrow$. The remaining electrons are distributed into the atomic orbitals $2s$, $2p_x$, $2p_y$ and $2p_z$, all orthonormal and the latter three degenerate in energy. It turns out that the former three states will mix, or *hybridize*, into new orbitals to accommodate bonding between the carbon atoms, reducing the system's overall energy. A linear combination of the $2s$, $2p_x$, $2p_y$ gives the so-called sp^2 states:

$$\begin{aligned}
\left|sp_i^2\right\rangle &= \frac{1}{\sqrt{3}}\left|2s\right\rangle - \sqrt{\frac{2}{3}}\left|2p_y\right\rangle, \\
\left|sp_j^2\right\rangle &= \frac{1}{\sqrt{3}}\left|2s\right\rangle + \sqrt{\frac{2}{3}}\left(\frac{\sqrt{3}}{2}\left|2p_x\right\rangle + \frac{1}{2}\left|2p_y\right\rangle\right), \\
\left|sp_k^2\right\rangle &= -\frac{1}{\sqrt{3}}\left|2s\right\rangle + \sqrt{\frac{2}{3}}\left(-\frac{\sqrt{3}}{2}\left|2p_x\right\rangle + \frac{1}{2}\left|2p_y\right\rangle\right).
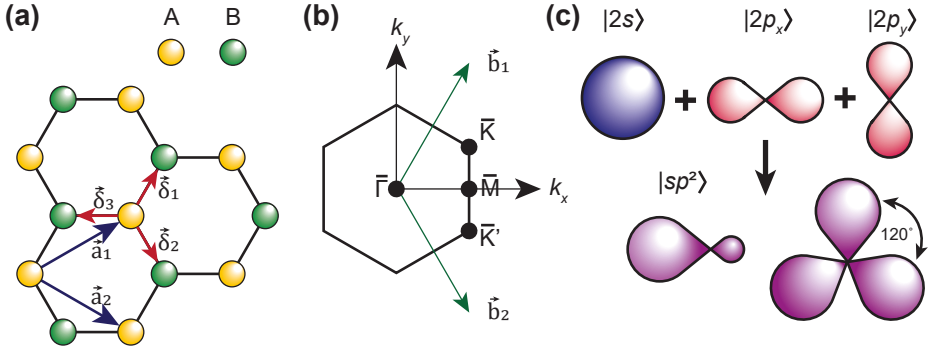\end{aligned} \tag{4.3}$$

Figure 4.1: The structure of graphene. **(a)**: The lattice structure of graphene, consisting of two triangular sub-lattices A and B. The vectors $\mathbf{a}_1$ and $\mathbf{a}_2$ are the lattice vectors, while $\boldsymbol{\delta}_l$, $l = 1, 2, 3$ are the vectors to the nearest neighbors on the opposite sub-lattice. **(b)**: The graphene Brillouin zone. The vectors $\mathbf{b}_1$ and $\mathbf{b}_2$ are the reciprocal lattice vectors, while $\bar{\Gamma}$, $\bar{K}$, $\bar{M}$ and $\bar{K}'$ are high symmetry points. **(c)**: sp^2 hybridization to form carbon σ-bonds. The resultant orbitals are oriented in-plane with mutual angles of $120°$.

All three are orthonormal and oriented in-plane with mutual $120°$ angles, as shown in Fig. 4.1c. Three electrons from each atom will occupy the sp^2 states to bond covalently with its neighbors. The final electron of each atom is therefore placed in the un-hybridized $2p_z$ orbital, which makes up the fourth and final state of the orthonormal basis set[2].

4.1.1 Electronic bands

The electronic band structure of graphene can be described using a tight-binding model approach as outlined in Refs. [66, 67]. Here, we summarize the methodology and the main findings. First, the atomic orbitals are used to construct new and periodic wavefunctions that satisfy Bloch's theorem. The wave function of an orbital μ (out of m possible ones) is then

$$\varphi_\mu(\mathbf{k}, \mathbf{r}) = \frac{1}{\sqrt{N}} \sum_{j}^{N} e^{i\mathbf{k}\cdot\mathbf{R}_j} \varphi_\mu(\mathbf{r} - \mathbf{R}_j), \quad (\mu = 1, \cdots, m), \qquad (4.4)$$

---

[2]The $2p_z$ orbital is antisymmetric with respect to the atomic plane, i.e., under the symmetry operation $z \to -z$, and therefore not involved in the hybridization or bonding.

where N are the number of atoms in the (sub)lattice, $\mathbf{R}_j$ is the position of the j'th atom, and $\mathbf{k}$ is the associated wave vector. For any given value of $\mathbf{k}$, the Bloch wave for orbital μ is thus the normalized sum of the atomic orbitals φ_j^μ at lattice positions $\mathbf{R}_j$, weighted by the phase factor $\exp\{i\mathbf{k} \cdot \mathbf{R}_j\}$. The generalized solutions to the Eigenvalue problem at $\mathbf{k}$, that is, the wave functions that solve Schrödinger's equations for the given system, are decribed as linear combinations of the Bloch orbitals:

$$\psi_\mathbf{k}^\alpha(\mathbf{r}) = \sum_{\mu'=1}^{m} c_{\mu'}^\alpha(\mathbf{k})\varphi_{\mathbf{k}\mu'}(\mathbf{r}), \tag{4.5}$$

where $c_{\mu'}^\alpha(\mathbf{k})$ are the coefficients to be determined and α is the index for the possible solutions – m in total due to the m constituent Bloch waves[3]. Within this approximation[4], we may now formulate a generalized matrix Eigenvalue problem for the system. Assuming the operation $\hat{H}\psi_\mathbf{k}^\alpha$ has a corresponding energy Eigenvalue $\mathcal{E}_\mathbf{k}^\alpha$, the time-independent Schrödinger's equation can be written as

$$\langle\psi_\mathbf{k}^\alpha|\,\hat{H}\,|\psi_\mathbf{k}^\alpha\rangle = \mathcal{E}_\mathbf{k}^\alpha\,\langle\psi_\mathbf{k}^\alpha|\psi_\mathbf{k}^\alpha\rangle$$

$$\sum_{\mu,\mu'=1}^{m} c_{\mathbf{k}\mu}^{\alpha\,\dagger}c_{\mathbf{k}\mu'}^\alpha\,\langle\varphi_{\mathbf{k}\mu}|\,\hat{H}\,|\varphi_{\mathbf{k}\mu'}\rangle = \mathcal{E}_\mathbf{k}^\alpha\sum_{\mu,\mu'=1}^{m} c_{\mathbf{k}\mu}^{\alpha\,\dagger}c_{\mathbf{k}\mu'}^\alpha\,\langle\varphi_{\mathbf{k}\mu}|\varphi_{\mathbf{k}\mu'}\rangle$$

$$\sum_{\mu,\mu'=1}^{m} c_{\mathbf{k}\mu}^{\alpha\,\dagger}c_{\mathbf{k}\mu'}^\alpha\,\mathcal{H}_{\mu\mu'}(\mathbf{k}) = \mathcal{E}_\mathbf{k}^\alpha\sum_{\mu,\mu'=1}^{m} c_{\mathbf{k}\mu}^{\alpha\,\dagger}c_{\mathbf{k}\mu'}^\alpha\,\mathcal{B}_{\mu\mu'}(\mathbf{k}), \tag{4.6}$$

where $\mathcal{H}_{\mu\mu'}(\mathbf{k})$ and $\mathcal{B}_{\mu\mu'}(\mathbf{k})$ are the overlap integrals between the orbital Bloch waves, with and without the Hamiltonian operator, respectively. By defining the row and column vectors

$$C_\mathbf{k}^{\alpha\,\dagger} = \begin{bmatrix} c_{\mathbf{k},1}^{\alpha\,\dagger} \cdots c_{\mathbf{k},m}^{\alpha\,\dagger} \end{bmatrix}, \qquad C_\mathbf{k}^\alpha = \begin{bmatrix} c_{\mathbf{k},1}^\alpha \\ \vdots \\ c_{\mathbf{k},m}^\alpha \end{bmatrix}, \tag{4.7}$$

Eq. 4.6 can be re-written as

$$C_\mathbf{k}^{\alpha\,\dagger}\boldsymbol{\mathcal{H}}_\mathbf{k}C_\mathbf{k}^\alpha = \mathcal{E}_\mathbf{k}^\alpha C_\mathbf{k}^{\alpha\,\dagger}\boldsymbol{\mathcal{B}}_\mathbf{k}C_\mathbf{k}^\alpha. \tag{4.8}$$

---

[3]We have already pre-empted some of these in our discussion of orbital hybridization, where the atomic wavefunctions combine linearly to accomodate bonding to other atoms.

[4]We have, for instance, neglected any contributions from the free states of the system.

Expressed in Eq. 4.8 is now an energy Eigenvalue problem where the α values of $\mathcal{E}$ for a given wave vector $\mathbf{k}$ are those defined by the non-trivial ($c_\mu^\alpha \neq 0$) solutions of

$$\det |\boldsymbol{\mathcal{H}} - \mathcal{E}\boldsymbol{\mathcal{B}}| = 0. \tag{4.9}$$

Eq. 4.9 is called the *secular equation*, and solving this gives the energy dispersion relations $\mathcal{E}(\mathbf{k})$ for each of the α different energy bands defined by the system. Next, solutions for the different graphene bands are presented.

Graphene π-bands

As the two atomic $2p_z$ orbitals remain untouched by the sp^2 hybridization these can be treated separately, simplifying Eq. 4.9 to a 2×2 matrix problem with orbital basis vectors $\big|2p_z^A\big\rangle$, $\big|2p_z^B\big\rangle$:

$$\det \left| \left[\begin{array}{cc} \mathcal{H}_{AA} & \mathcal{H}_{AB} \\ \mathcal{H}_{BA} & \mathcal{H}_{BB} \end{array} \right] - \mathcal{E} \left[\begin{array}{cc} \mathcal{B}_{AA} & \mathcal{B}_{AB} \\ \mathcal{B}_{BA} & \mathcal{B}_{BB} \end{array} \right] \right| = 0, \tag{4.10}$$

where the subscripts now refer to the $2p_z$ orbitals on sub-lattices A and B.

First, the overlap integrals for $\mathcal{H}$ and $\mathcal{B}$ are calculated using Eqs. 4.4–4.6. For nearest-neighbor interactions only, the diagonal terms of both matrices merely sum N overlaps of a single atom with itself, either on lattice site A or B. Then by definition, $\langle \psi_A | \psi_A \rangle = \langle \psi_B | \psi_B \rangle = 1$ for the normalized Bloch states and $\mathcal{B}_{AA} = \mathcal{B}_{BB} = 1$. Furthermore, $\mathcal{H}_{AA} = \mathcal{H}_{BB} = \varepsilon_{2p}$ are merely the on-site energies of the atomic $2p_z$ orbitals.

For the off-diagonal terms, the sums from Eq. 4.4 will run over each atom A(B) at $\mathbf{R}_j$ and its three nearest neighbors at $\mathbf{R}_j + \boldsymbol{\delta}_l$ ($l = 1, 2, 3$) from the other sub-lattice. This gives

$$\mathcal{H}_{AB} = \sum_{l=1}^{3} e^{i\mathbf{k}\cdot\boldsymbol{\delta}_l} \underbrace{\left\langle \varphi_{2p_z}^A (\mathbf{r} - \mathbf{R}_A) \right| \mathcal{H} \left| \varphi_{2p_z}^B (\mathbf{r} - \mathbf{R}_A - \boldsymbol{\delta}_l) \right\rangle}_{\equiv t} = \mathcal{H}_{BA}^\dagger, \tag{4.11}$$

$$\mathcal{B}_{AB} = \sum_{l=1}^{3} e^{i\mathbf{k}\cdot\boldsymbol{\delta}_l} \underbrace{\left\langle \varphi_{2p_z}^A (\mathbf{r} - \mathbf{R}_A) \big| \varphi_{2p_z}^B (\mathbf{r} - \mathbf{R}_A - \boldsymbol{\delta}_l) \right\rangle}_{\equiv b} = \mathcal{B}_{BA}^\dagger, \tag{4.12}$$

where $\mathbf{R}_B = \mathbf{R}_A + \boldsymbol{\delta}_l$ was inserted and the inner products t and b have been defined. The remaining sum is known as the *hopping term* and will from hereon be written as $S(\mathbf{k}) = \sum_{l=1}^{3} e^{i\mathbf{k}\cdot\boldsymbol{\delta}_l}$.

Inserting the matrix elements and solving the 2×2 determinant problem gives the two energy Eigenvalues

$$\mathcal{E}_{\pm}(\mathbf{k}) = \frac{\varepsilon_{2p} \pm t|S(\mathbf{k})|^{1/2}}{1 \pm b|S(\mathbf{k})|^{1/2}}, \qquad (4.13)$$

where the $+$'s and $-$'s in the numerator and denominator go together, giving the energy dispersions for the bonding π-band and the antibonding π^*-band, respectively[5]. Using the coordinates for three nearest neighbors $\boldsymbol{\delta}_1 = (\delta/2)(1, \sqrt{3})$, $\boldsymbol{\delta}_2 = (\delta/2)(1, -\sqrt{3})$ and $\boldsymbol{\delta}_3 = (-\delta, 0)$, $S(\mathbf{k})$ is finally written as

$$S(\mathbf{k}) = 1 + 4\cos\left(\frac{3k_x\delta}{2}\right)\cos\left(\frac{\sqrt{3}k_y\delta}{2}\right) + 4\cos^2\left(\frac{\sqrt{3}k_y\delta}{2}\right). \qquad (4.14)$$

The dispersion relations for the π- and π^*-bands are plotted in Fig. 4.2, using values for ε_{2p}, t and b as stated in Ref. [67]. Note how the two bands become degenerate at the high-symmetry points $\bar{\mathrm{K}}$ and $\bar{\mathrm{K}}'$, where the electron density of states is exactly zero. Graphene is thus a zero-gap semiconductor, or a *semi-metal*. In the undoped state, the $2p_z$ electrons from atoms A and B will occupy the two spin configurations $\uparrow$ and $\downarrow$ in the π-band, and E_{F} will intersect exactly at these degeneracy points.

Graphene σ-bands

There are three orbitals per atom participating in the covalent sp^2 bonding of graphene, namely the $2s$, $2p_x$ and $2p_y$. For a diatomic basis there are thus six unique Bloch waves that contribute six σ-bands to the electronic structure. To calculate these bands, the secular equation (4.9) is solved using the three orbital Bloch waves from each atom of both sub-lattices A and B. Choosing the ordering

$$\left[2s^{\mathrm{A}} \ 2p_x^{\mathrm{A}} \ 2p_y^{\mathrm{A}} \ 2s^{\mathrm{B}} \ 2p_x^{\mathrm{B}} \ 2p_y^{\mathrm{B}}\right], \qquad (4.15)$$

the overlap matrices $\boldsymbol{\mathcal{H}}$ and $\boldsymbol{\mathcal{B}}$ in Eq. 4.9 can be written as

$$\boldsymbol{\mathcal{H}} = \left[\begin{array}{cc} \mathcal{H}_{\mathrm{AA}(3\times3)} & \mathcal{H}_{\mathrm{AB}(3\times3)} \\ \mathcal{H}_{\mathrm{BA}(3\times3)} & \mathcal{H}_{\mathrm{BB}(3\times3)} \end{array}\right], \quad \boldsymbol{\mathcal{B}} = \left[\begin{array}{cc} \mathcal{B}_{\mathrm{AA}(3\times3)} & \mathcal{B}_{\mathrm{AB}(3\times3)} \\ \mathcal{B}_{\mathrm{BA}(3\times3)} & \mathcal{B}_{\mathrm{BB}(3\times3)}. \end{array}\right] \qquad (4.16)$$

[5]Note that t is conventionally defined to be a negative value within tight-binding formalism, hence the solutions with $\varepsilon_{2p} \pm t|S(k)|^{1/2}$ in the numerator give the values of lowest energy.
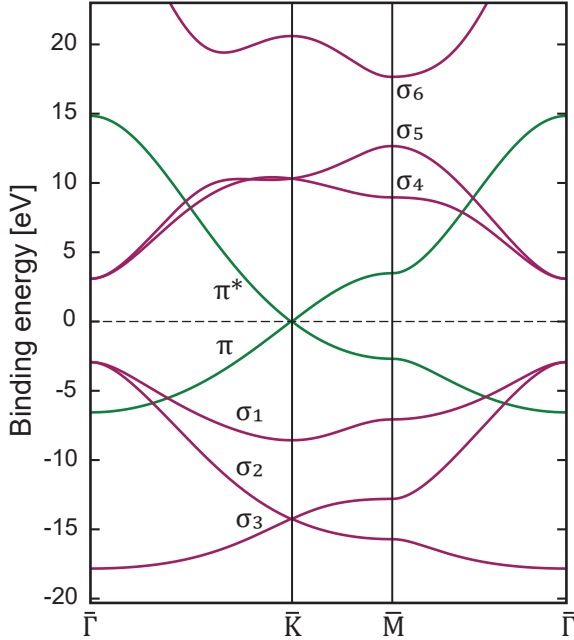
Figure 4.2: The band structure of graphene, calculated using a tight-binding approach with values for the overlap integrals and orbital energies taken from Ref. [67]. The two π-bands (green) and six σ-bands (purple) have been plotted along the high-symmetry directions of the graphene Brillouin zone.

Here, each matrix element is a 3×3 matrix with overlap integrals between the Bloch waves of sites A and/or B. When only nearest-neighbor interactions are considered, the matrices $\mathcal{H}_{\mathrm{AA}}$, $\mathcal{H}_{\mathrm{BB}}$, $\mathcal{B}_{\mathrm{AA}}$ and $\mathcal{B}_{\mathrm{BB}}$ only consider the overlap between Bloch waves of the same sub-lattice A or B. Since the atomic orbitals are orthonormal by definition, only Bloch waves constructed from the same orbital and overlapping with itself will yield non-zero terms. Hence the mentioned four matrices are *diagonal*: $\mathcal{B}_{\mathrm{AA}}$ and $\mathcal{B}_{\mathrm{BB}}$ are identity matrices and $\mathcal{H}_{\mathrm{AA}}$ and $\mathcal{H}_{\mathrm{BB}}$ have diagonal terms ε_{2s}, ε_{2p} and ε_{2p}.

To construct the off-diagonal matrices, one has to evaluate the overlap between the Bloch waves of $2s$, $2p_x$ and $2p_y$ in the directions parallel to the σ-bonds. First, the sums in Eq. 4.4 are again written so that every vector

$\mathbf{R}_{\text{B(A)}} = \mathbf{R}_{\text{A(B)}} \pm \boldsymbol{\delta}_l$. Then each matrix element is defined as

$$\mathcal{H}_{\mu\mu'} = \sum_{l=1}^{3} e^{\pm i\mathbf{k}\cdot\boldsymbol{\delta}_l} \left\langle \varphi_{\mu}^{\text{A(B)}}\big(\mathbf{r} - \mathbf{R}_{\text{A(B)}}\big)\Big| \mathcal{H} \left|\varphi_{\mu'}^{\text{B(A)}}\big(\mathbf{r} - \mathbf{R}_{\text{A(B)}} \mp \boldsymbol{\delta}_l\big)\right\rangle, \quad (4.17)$$

$$\mathcal{B}_{\mu\mu'} = \sum_{l=1}^{3} e^{\pm i\mathbf{k}\cdot\boldsymbol{\delta}_l} \left\langle \varphi_{\mu}^{\text{A(B)}}\big(\mathbf{r} - \mathbf{R}_{\text{A(B)}}\big)\Big| \varphi_{\mu}^{\text{B(A)}}\big(\mathbf{r} - \mathbf{R}_{\text{A(B)}} \mp \boldsymbol{\delta}_l\big)\right\rangle, \quad (4.18)$$

where μ and μ' denote either of the mentioned six atomic orbitals. Note that the sign in front of the nearest-neighbor vector $\boldsymbol{\delta}_l$ changes when the neighbors are switched between residing on sub-lattice B and sub-lattice A. The sums in Eqs. 4.17-4.18 are the hopping terms $S(\mathbf{k})$ and $S(\mathbf{k})^{\dagger}$ defined previously. To obtain the overlap terms $\langle \varphi_{\mu}| \mathcal{H} |\varphi_{\mu'}\rangle$ and $\langle \varphi_{\mu}|\varphi_{\mu'}\rangle$, each orbital is decomposed along the directions parallel and normal to the unit vectors along the σ-bonds. Based on the symmetries of the different orbitals, only four terms each of $\mathcal{H}_{\mu\mu'}$ and $\mathcal{B}_{\mu\mu'}$ will have non-vanishing matrix elements. The methodology to obtain these terms are explained in Sections II.3 and III.3 of Ref. [66] and summarized in Appendix A.

Finally, the Eigenvalue problem in Eq. 4.9 is solved using the correct overlap terms inserted in the 6×6 matrices $\mathcal{H}$ and $\mathcal{B}$ (Eq. 4.16). The resulting energy dispersions are shown in Fig. 4.2 together with the π-bands calculated in the previous section. For the calculations, tabulated values of the orbital energies and the overlap integrals were taken from Ref. [67]. The six orbital Bloch waves contribute six σ-bands, all of which are located several eV away from the Fermi level. The three σ-bands at deeper binding energies are filled with electrons. For most realistic doping levels, these do not participate in the thermal excitation of charged particles in the valence and conduction bands. In the study of graphene's electronic properties, they are often disregarded completely. However, a few recent studies have shown that the σ-bands can accommodate other, exotic phenomena for charge transfer: namely strong ($\lambda \approx 1$) electron-phonon interactions [68, 69] and inter-band electron scattering between $\sigma \rightleftarrows \pi$ [70]. In a more sophisticated, many-body picture, the role that the σ-bands play in transferring electronic charges can therefore not be neglected completely.

4.2   Fabricating Graphene

With its appeal for applications in semiconductor technology [71], spintronics [72], and superconductivity alike [73], the synthesis of high-quality

graphene on suitable substrates has been a central topic of condensed matter and materials science research for the last decades.

The first few realizations of few-layer graphene were obtained by micromechanical exfoliation from bulk graphite [59]. By this method, graphene flakes were achieved with unmatched crystalline quality, yielding soaringly high electron carrier mobilities ($\approx 2 \times 10^5$ cm^2 V^{-1} s^{-1}) for suspended flakes even at room temperature [74, 75]. While it may be ideal for characterization or prototyping, micromechanical exfoliation is undoubtedly less scalable than other techniques [76]. Graphene exfoliation, transfer, and subsequent inspection are all cumbersome activities, yielding less reproducible results in terms of graphene flake size, thickness, and quality than other methods.

The perhaps most common technique for graphene synthesis today is the high-temperature dissociation of gaseous hydrocarbons on crystalline metal catalyst surfaces [77–80]. With *chemical vapor deposition* (CVD), large areas of monolayer graphene can be grown on elementary metals relatively inexpensively [81], with exceptional structural coherency that can range up to several millimeters [82, 83]. The main drawback of CVD for producing quasi-free standing graphene layers is the required removal of the catalyst after growth. The graphene as-grown will typically bond strongly with the underlying metal substrate, and these bonds have to be broken for the graphene to re-obtain its desirable electronic properties [84]. It is, therefore, common that the metal catalyst is decomposed, either thermally or chemically, and the graphene is transferred onto a more suitable substrate. These steps tend to induce unwanted contaminants in the graphene layers, compromising their overall quality and, therefore, their full potential for subsequent device processing [76, 85]. The ultimate need for a transfer step thus limits the CVD technique's scalability.

To overcome the apparent setbacks of graphene transfer, one option is to synthesize graphene directly on a suitable substrate. The most commonly studied pathway to high-quality graphene on semiconducting layers is the thermal decomposition of silicon carbide (SiC) [86–89]. By heating either Si- or C-terminated SiC(0001) surfaces to temperatures beyond 1100 °C, Si atoms eventually sublimate, and the remaining carbon atoms will reconstruct. The surfaces then undergo a variety of different periodicities before an eventual $\left(6\sqrt{3} \times 6\sqrt{3}\right)$R30° 'buffer layer' reconstruction, or a quasi-free standing graphene layer is formed on the initially Si- or C-terminated face, respectively [90]. In the former case, this buffer layer consists of sp^3-hybridized carbon that is partially bonded to the underly-
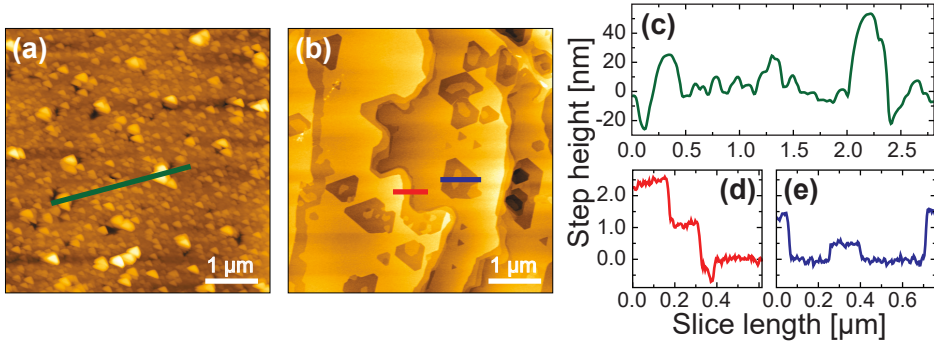
Figure 4.3: Comparison of surface roughness and domain sizes for different types of epitaxial graphene, measured using atomic force microscopy (AFM). **(a)**: The surface structure achieved from 'conventional' SiC sublimation. **(b)**: The resultant surface structure from 'sandwich'-style, graphene-on-SiC growth. Both micrographs have approximately the same field of view. **(c)**: A linear cut showing the topography at the position of the green line in (a). **(d, e)**: Topography cuts from the red and blue lines in (b), respectively.

ing substrate. However, it can be readily decoupled by, e.g., intercalation of foreign atoms, in which case it forms sp^2-bonded and quasi-free standing graphene [91]. In the case of both Si- and C-face graphene, subsequent heating to higher temperatures will lead to the formation of additional graphene layers [88].

Epitaxial graphene growth from the decomposition of SiC can be relatively easy to achieve, requiring little but heating of the bulk crystal in an inert atmosphere. The resultant graphene will form as nanometer-size grains of varying thickness on top of the decomposed SiC surface [92]. Over the years, several modifications to the growth recipe have been developed to maximize the lateral size of the graphene terraces. Some of these include heating SiC samples in a near atmospheric pressure of argon [89], in a vacuum with a surface-opposing Si flux [93], or in a 'sandwich'-like configuration, where each sample sublimates Si that co-deposits on the surface of the other [94]. In each case, the idea is to reduce the Si sublimation rate and minimize the associated surface roughness of the substrate so that larger graphene terraces can be formed. A comparison of the lateral graphene domain size achieved by 'conventional' thermal decomposition and 'sandwich' configuration growth is given in Fig. 4.3.

While epitaxial graphene growth from SiC sublimation can overcome the potential need to transfer the graphene layers, its suitability for integration into pre-existing frameworks for large-scale device processing is questionable. First of all, the high processing temperatures required to sublimate the surface Si is by far incommensurate with those of standard device workflows, such as the CMOS process [95, 96]. Secondly, SiC substrates in the context of semiconductor manufacturing can be challenging to work with, relatively expensive, and in many cases, not the underlayer of choice for graphene-based devices. To fully harness its two-dimensional properties, graphene should ideally be resting on dielectric layers or on top of layers of pure Si that can be further processed into dielectric layers by a standardized work-flow. Next, we discuss an alternative approach to graphene growth from SiC that has the potential to overcome some of the mentioned challenges.

4.2.1 Transition-Metal-Mediated Graphene from SiC

Instead of relying on high-temperature Si sublimation, epitaxial graphene can be grown at much lower temperatures by coating SiC surfaces with reactive transition metal layers before annealing [97–101]. Typically, the finite, temperature-dependent solubility of C and Si in transition metal is exploited [102–104]. At elevated temperatures, e.g., 600-900 °C, the transition metal will react with the underlying SiC at the interface to form one or several Si-rich metal silicide phases. As the transition metal eats into the SiC, carbon is simultaneously consumed, and transition-metal carbides are formed.

Eventually, a saturation level of carbon in the metal-carbide-silicide composite is reached. Thus, carbon will readily precipitate from the layers and migrate towards the surface where it re-hybridizes and bonds to form *graphene* or *graphite* [97, 105]:

$$\text{SiC} \quad + \quad \text{M} \quad \xrightarrow{\Delta\text{H}} \quad \text{M}_x\text{Si}_y \quad + \quad \text{C}_\text{gra}. \tag{4.19}$$
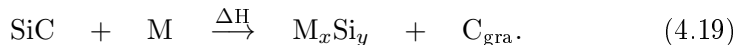
Here, M indicates the transition metal, ΔH represents heat, and x and y are stoichiometric coefficients. In the final configuration, graphene rests on top of a Si-rich transition-metal-silicide layer, which again is supported by the bulk SiC crystal. A sketch of transition-metal-mediated growth is shown in Fig. 4.4.

From Eq. 4.19, it can be seen that the amount of transition metal present will determine the achievable silicide stoichiometries and how much carbon is liberated from the reaction. Hence by carefully choosing the amount of
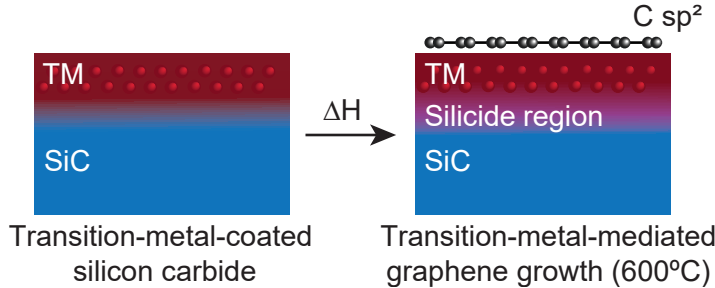
Figure 4.4: Transition-metal-mediated growth of epitaxial graphene from SiC. With annealing to 600-900 °C, the transition metal overlayer will react with the underlying SiC at the interface, forming transition metal silicide and liberating carbon. As a consequence of the heat present, the carbon atoms diffuse to the surface, re-hybridize, and form graphene.

transition metal present, one can effectively regulate the number of graphene layers formed at the surface.

In Paper [1], we compare the graphene growth achieved from transition metals Fe and Ru for a range of different temperatures and metal film thicknesses. Ru is shown to be more reactive at lower temperatures (450 °C), while similar amounts of graphene will form at intermediate temperatures (650-700 °C) using either Fe or Ru. In both cases, crystalline graphene domains larger than 10 μm will form, oriented at specific, preferred rotations relative to the underlying substrate. Additionally, it is shown that subsequent annealing to higher temperatures (750-800 °C) for longer durations leads to a diffusion of the transition metal into the bulk SiC crystal. Said diffusion eventually terminates the growth, resulting in quasi-freestanding graphene resting on top of Si-rich, transition-metal deficient surface layers.

In Paper [2], we show how the growth mechanisms from Paper [1] can be exploited to form precisely patterned graphene structures on transition-metal-treated SiC. We then extend the options of underlayers available by intercalating atomic Si through the graphene, lifting these up and away from the silicide/SiC. Finally, we demonstrate how these newfound Si underlayers can be subsequently oxidized *through* the graphene, forming insulating SiO_2. Thus from a set of relatively few and arguably straightforward growth steps, patterned graphene-on-Si or graphene-on-SiO_2 heterostructures can be manufactured on demand.

4.3 Paper 1

My contribution: This paper comprises measurements from several experiments at different facilities, most of which I have participated in and played a central role in. All analysis of all data presented has been performed by me, with input and suggestions from the other co-authors. I made all figures, wrote the first draft of the manuscript and the supplementary information, and implemented the improvements offered by the co-authors.

Low-Temperature Growth of Graphene on a Semiconductor

Authors

Håkon I. Røst
Rajesh Kumar Chellappan
Frode S. Strand
Antonija Grubišić-Čabo
Benjamen P. Reed
Mauricio J. Prieto
Liviu C. Tănase
Lucas de Souza Caldas
Thipusa Wongpinij
Chanan Euaruksakul
Thomas Schmidt
Anton Tadich
Bruce C. C. Cowie
Zheshen Li
Simon P. Cooil
Justin W. Wells

Low-Temperature Growth of Graphene on a Semiconductor

Håkon I. Røst,* Rajesh Kumar Chellappan,* Frode S. Strand, Antonija Grubišić-Čabo,
Benjamen P. Reed, Mauricio J. Prieto, Liviu C. Tănase, Lucas de Souza Caldas, Thipusa Wongpinij,
Chanan Euaruksakul, Thomas Schmidt, Anton Tadich, Bruce C. C. Cowie, Zheshen Li, Simon P. Cooil,
and Justin W. Wells*

ACCESS | Metrics & More | Article Recommendations | Supporting Information

ABSTRACT: The industrial realization of graphene has so far been limited by challenges related to the quality, reproducibility, and high process temperatures required to manufacture graphene on suitable substrates. We demonstrate that epitaxial graphene can be grown on transition-metal-treated 6H-SiC(0001) surfaces, with an onset of graphitization starting around 450−500 °C. From the chemical reaction between SiC and thin films of Fe or Ru, sp^3 carbon is liberated from the SiC crystal and converted to sp^2 carbon at the surface. The quality of the graphene is demonstrated by using angle-resolved photoemission spectroscopy and low-energy electron diffraction. Furthermore, the orientation and placement of the graphene layers relative to the SiC substrate are verified by using angle-resolved absorption spectroscopy and energy-dependent photoelectron spectroscopy, respectively. With subsequent thermal treatments to higher temperatures, a steerable diffusion of the metal layers into the bulk SiC is achieved. The result is graphene supported on magnetic silicide or optionally, directly on semiconductor, at temperatures ideal for further large-scale processing into graphene-based device structures.
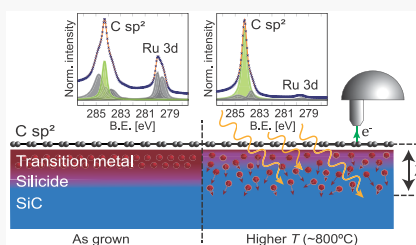
■ INTRODUCTION

Since its experimental discovery in 2004,[1] graphene—a two-dimensional carbon crystal in a honeycomb structure—has been deemed a promising candidate for device applications because of its exceptional electronic, thermal, optical, and mechanical properties.[2−6] However, the challenges associated with the production of large-scale high-quality graphene layers directly on semiconductor substrates have limited the integration of graphene with conventional device prototypes.

Until now, the most common techniques for preparing monolayer graphene include micromechanical exfoliation from bulk graphite, epitaxial growth on various transition metals[7−10] through chemical vapor deposition (CVD) of hydrocarbons, and thermal decomposition of bulk crystals such as silicon carbide.[11,12] Among these methods, epitaxial growth by CVD and thermal decomposition of SiC are normally favored as large-area single-crystalline graphene domains can be achieved routinely.[13−15] However, CVD grown graphene requires an additional transfer step onto a suitable substrate, limiting the scalability of the technique when it comes to producing graphene on a semiconductor or dielectric of uniform size and quality. The transfer may also introduce contaminants and affect the quality of the CVD graphene, compromising its suitability for device integration.[16] In comparison, graphene prepared on SiC can be directly converted into a device,[17] but the temperatures needed to trigger the thermal decomposition

of the SiC are by far incommensurate with those of device industry standards.[18]

In this study, we demonstrate how catalytic reactions between SiC surfaces and thin films of transition metals Fe and Ru can produce quasi-freestanding graphene layers at significantly lower temperatures than those of "conventional" epitaxial growth. Surface graphene layers are formed by allowing the thermally activated metal films to convert sp^3 carbon from the substrate into sp^2 carbon, which re-forms at the surface. A similar method has previously been successfully demonstrated at temperatures of 500−600 °C by using Fe on both SiC and diamond.[19,20] Here, we show that ordered graphene layers can be produced from SiC by using either Fe or Ru, with an onset of growth starting at around 450−500 °C. This metal-mediated approach leaves graphene resting on underlying layers of metal silicide, which can then be eliminated by subsequent thermal treatments to higher temperatures, driving diffusion of the metal ions into the bulk crystal.[21] The result is quasi-freestanding graphene resting
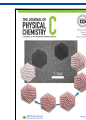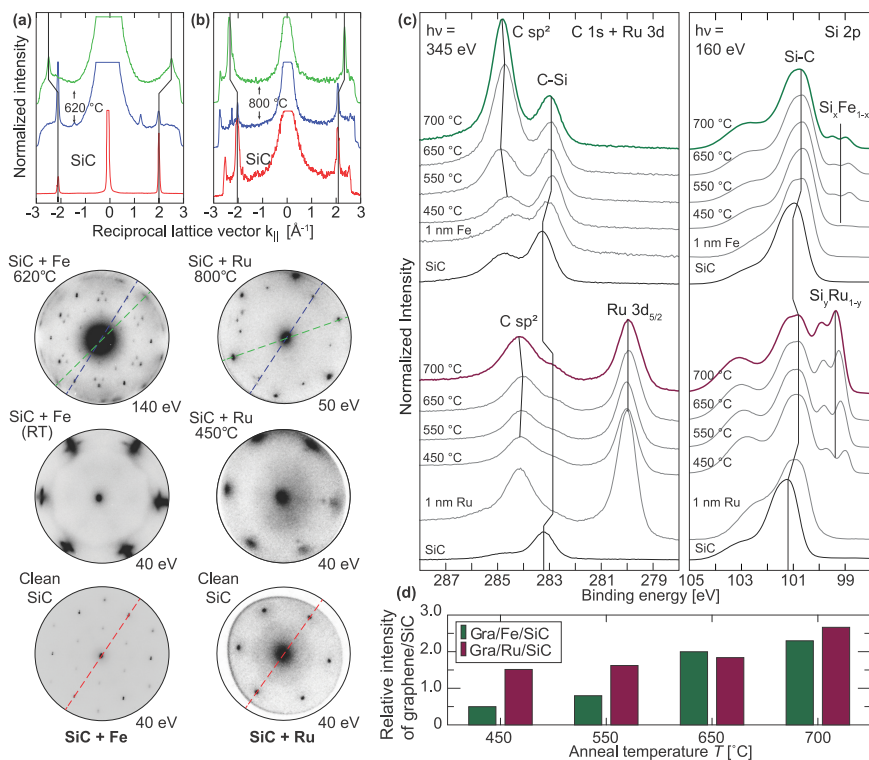
Figure 1. Gradual formation of graphene on SiC treated with Fe and Ru. (a, b) μ-LEED patterns of 6H-SiC coated with thin films of Fe and Ru, respectively, and then thermally treated to temperatures of 600−800 °C. The excitation energy/starting voltages were adjusted for the final images to increase the brightness of all relevant spots. Intensity cuts along high-symmetry directions of the reciprocal lattices of the two systems (topmost panels) reveal new diffraction maxima appearing with the formation of graphitic carbon at the surface. These appear at angles 30° (SiC + Ru) as well as 15° and 45° (SiC + Fe) relative to the (1×1) phase of the underlying SiC. All intensity cuts were normalized to the **k** values and intensities of the first-order SiC spots. (c) Core levels Si 2p, C 1s, and Ru 3d showing the formation of graphitic layers: silicon carbide, followed by deposition of Fe and Ru and successive thermal treatments in the range 450−700 °C. All core levels have been normalized to the intensity of the SiC signal ("C−Si" and "Si−C"). (d) Estimated ratio of graphitic carbon to silicon carbide signal measured within a few nanometers of the surface as a function of temperature.

on semiconducting substrates and grown at industrially compatible temperatures, ideal for further processing into large-scale, graphene-based device structures.

■ METHODS

Single crystal samples of n-type 6H-SiC(0001) (Tankeblue Semiconductor) were initially cleaned *ex situ* by using standard "RCA" chemical cleaning procedures to remove residual contaminants and native oxides.[22] The samples were then loaded into the relevant spectrometers and degassed *in situ* at 300 °C in ultrahigh vacuum (UHV) for durations of 6+ h. Finally, any residues of silicon oxide on the surfaces were removed by rapidly annealing each sample to roughly 900 °C for several cycles. Because of different heating setups for the different spectrometers, temperature differences of ±50 °C were achieved during the flashing. The preparation of clean 6H-SiC(0001) was confirmed by using X-ray photoelectron

spectroscopy (XPS) and low-energy electron diffraction (LEED). In each experimental setup, several different samples were loaded, cleaned, and compared. Slight variations in the XPS and reconstructions of the clean surface were observed; however, neither appeared to have any significant impact on the subsequent growth steps.

Fe and Ru films with different thicknesses in the range 0.5−2.0 nm were deposited on individual samples at constant rate by using calibrated e-beam evaporation cells. The transition-metal-covered samples were then annealed for short durations at increasing temperatures ranging from 450 to 700 °C to study the formation of transition metal (TM) silicides, the associated liberation of carbon atoms and the sp² reconstruction at the surface. The homogeneity of the metal films and the graphitic surface layers was verified across ranges of 500 μm by using low-energy electron diffraction (LEEM) and X-ray photoemission electron microscopy (XPEEM). Small-spot

low-energy electron diffraction (μ-LEED) was recorded from selected areas of 1.5 μm diameter within the same regions at every relevant preparation stage. Following graphene formation, small-spot angle-resolved photoemission spectroscopy (μ-ARPES) was extracted from diffractive plane measurements of the Fe/SiC system, also from areas of 1.5 μm diameter.

Subsequent annealing to 800 °C for a longer duration was performed on some samples to further study the thermally activated graphitization and to investigate any associated changes to the concentration level of metal in the surface layers. Measurements were performed both prior to and following the thermal treatments to monitor the change with every experimental step. The formation of additional silicides and sp^2 carbon was confirmed through photon-energy-dependent XPS measurements of the Si 2p and C 1s core levels and, where possible, NEXAFS measurements of the C 1s K-edge.

RESULTS AND DISCUSSION

The gradual formation of graphitic carbon at the surface of Fe/SiC and Ru/SiC as a function of temperature is illustrated in Figure 1. Chemically and thermally cleaned SiC crystals treated with thin films of Fe and Ru were studied after metallization and subsequent annealing to higher temperature by small-spot low-energy electron diffraction (μ-LEED) and high-energy-resolution X-ray photoelectron spectroscopy (XPS).

The developments of the surface diffraction patterns originating from the two systems are shown in Figures 1a and 1b. Following the initial high-temperature annealing, both samples display known surface reconstructions of the SiC(0001) face: namely, a (1 × 1) phase and a $(\sqrt{3} \times \sqrt{3})R30°$ silicate reconstruction.[23] Both indicate a clean surface devoid of excessive oxide, the latter being the result of a higher flash temperature toward 1000 °C.[24,25] From our investigations, both reconstructions of the initial surface have been observed to yield similar results in the successive growth steps.

With metallization, the additional Fe and Ru layers both seem to mimic the hexagonal arrangement of the Si atoms with a slight lattice mismatch: the newfound diffraction spots both appear at larger magnitudes of the momentum wave vector **k** than the first-order SiC spots. Note that while the Fe film crystallizes already at room temperature, the Ru needs an additional thermal treatment to 450 °C to order itself with similar quality on top of the SiC. The different crystallization energies required for the two metal films are believed to be related to their different structural mismatch with the SiC(0001) surface.

Upon thermal activation above 600 °C, the metallic spots disappear, and the original (1 × 1) phase of the SiC(0001) face again becomes visible, as seen from comparing the intensity profiles along the same high symmetry direction for the clean SiC (red dashed line) and after the thermal treatments (blue dashed line). The recurrence of the SiC pattern is also accompanied by several new diffractive features, some of which are similar to previous reports of the Fe/SiC system.[19] Notably, both systems show higher **k** features appearing at rotations 15° and 45° (Fe) or 30° (Ru) relative to the SiC spots. Investigating these more closely along their symmetry directions (green dashed line) and comparing them to the simultaneously visible SiC features reveal that the new spots occur at |**k**| ~ 2.36 Å^{-1} for Ru/SiC and |**k**| ~ 2.50 Å^{-1} for Fe/

SiC. Both values are within 10% of the |**k**| value associated with pristine graphene flakes of lattice constant a = 2.46 Å.[26]

At first glance, the newfound spots on Ru/SiC in Figure 1b could be interpreted to come from the SiC surface, as their |**k**| value is similar to the second-order spots of a $(\sqrt{3} \times \sqrt{3})R30°$ silicate reconstruction. However, no first-order spots from this reconstruction are observed, and hence the |**k**| ~ 2.36 Å^{-1} spots cannot be explained from the SiC surface alone. Also, the different |**k**| values and relative orientation of newfound surface layers on Fe/SiC and Ru/SiC are not surprising: both may well be explained from different interactions with Fe and Ru. Each new layer is expected to be ordered according to its underlying metal, which again should be oriented to minimize its lattice mismatch with the SiC(0001). Given the structural differences between Fe and Ru, variations in strain and rotation for the new surface layer are not unlikely.

The C 1s and Si 2p core levels for both material systems, from samples with similar preparation, are shown in Figures 1c and 1d. Both regions were acquired from photoelectrons with a shallow escape depth (λ ~ 0.5 nm) beneath the sample surface. Similar features indicative of clean SiC can be seen for both systems: dominant peak components from the Si—C bonding of the substrate can be found at binding energies 283.2 eV (C 1s) and 101.2 eV (Si 2p), with minor features at 284.8 and 103.5 eV, indicating some occurrence of C—C bonding[27,28] and silicon oxide formation.[29,30] Note that slight variations in the initial amount of C—C and silicon oxide can be seen from the XPS measurements of the two systems. However, our experiments show that this will have negligible impact on the successive growth steps.

With metallization, a shift of ~0.3 eV can be seen in the components C—Si and Si—C, indicating a charge transfer to the surface SiC from the overlaying metal. Annealing to 450 °C and then 550 °C gives rise to new components in the Si 2p regions at binding energies of 98.0—100.5 eV. Similar features have been reported previously and associated with the formation of transition metal silicide phases.[19,31−35] Second, an attenuation and broadening are observed in the transition metal core levels Ru 3d and Fe 3p (the latter is not shown). Both indicate a reaction between the metallic thin films and the underlying Si-rich layers. Third, an increasing signal from the higher binding energy component ("C sp^2" in Figure 1c) suggests that new species of carbon have been formed, consistent with the previously reported transition-metal-mediated liberation of C atoms from SiC that re-form into graphitic carbon.[19]

Additional thermal treatments to 650 and 700 °C reveal a continuation of the same trend in the C 1s core level, where the intensity of the sp^2 carbon and silicide components increase relative to the intensity of the substrate (SiC). To quantify the amount of graphitic carbon formed from the reaction, the C 1s region was deconvolved into peak components corresponding to C sp^2 and C—Si signal. For the Ru/SiC system, the Ru 3d$_{5/2}$ was initially fitted and used to estimate and deduct the intensity of Ru 3d$_{3/2}$ features at the appropriate binding energy in the region overlapping with the C 1s components (this will be discussed later). The development of the (C sp^2)/(C—Si) signal ratio with temperature is shown in Figure 1d: at 700 °C the C sp^2 signal is more than double that of the substrate C—Si.

Together with the newfound diffractive features from the Fe/SiC and Ru/SiC surfaces in Figures 1a and 1b, respectively,
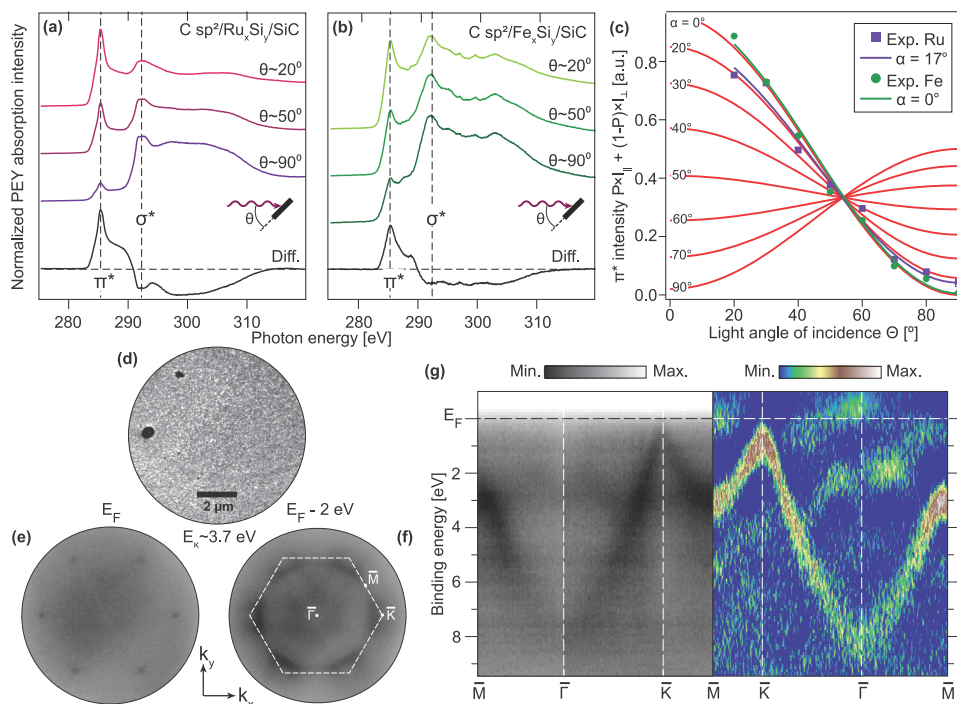
Figure 2. C 1s absorption spectra, layer orientation, and electronic structure of graphene. (a, b) Angle-dependent NEXAFS for graphene on Ru/SiC (a) and Fe/SiC (b) ranging from roughly grazing (~20°) to normal incidence. Prominent resonance features from the C 1s → π^* and C 1s → σ^* transitions can be seen at excitation energies 285.5 and 291.7 eV, respectively. A difference trace between the grazing and normal incidence spectra is also shown for each system to highlight the intensity changes with the light orientation. (c) Intensities of the LUMO (1s → π^*) absorption of graphene grown on Ru/SiC (purple) and Fe/SiC (green), plotted against the theoretical curves $I(\theta, \alpha)$ as described in eq 1. A best fit to each data set gives average angles $\alpha < 20°$ between the substrate surface normal and the vector perpendicular to the graphene layers. (d) LEEM micrograph (electron kinetic energy 3.7 eV) of the Fe/SiC surface following the formation of metal-mediated graphene at 600 °C. (e, f) Constant E vs $(\mathbf{k}_x, \mathbf{k}_y)$ surfaces from the graphene in (d), measured at E_F (e) and $E_F − 2$ eV (f) with an excitation energy of $h\nu = 115$ eV. The first Brillouin zone boundary (dashed line) and high symmetry points $\bar{\Gamma}$, $\bar{M}$, and $\bar{K}$ have been marked. (g) E vs $\mathbf{k}_\parallel$ intensity plots of occupied states in the gra/Fe/SiC system along principal directions $\bar{M} \to \bar{\Gamma}$, $\bar{\Gamma} \to \bar{K}$, and $\bar{K} \to \bar{M}$. The plot on the left shows the background-corrected band structure, while the plot on the right shows a second-derivative image (SDI), with a moderate boxcar averaging applied to amplify the graphene energy dispersion relative to the background.

and the mentioned attenuation of signals Ru 3d and Fe 3p, the results in Figure 1d indicate the formation of graphitic carbon on both metals at temperatures around 550 °C and higher. Similar results have been reported previously on the surfaces of bulk Ru[10] and Fe thin films,[19,20] where the precipitation of carbon is linked to the finite and temperature-dependent solubility of interstitial carbon in the two transition metals. Below 1000 °C, carbon is by far more soluble in Fe than in Ru.[36,37] The interstitial solubility in Ru is also expected to be highly temperature dependent. Addition of Si as a second alloying element has been shown to affect the carbon solubility in Fe.[38] Finally, the amount of carbon released from the chemical reaction between each metal and SiC will be dependent on the stoichiometry of the resultant silicide phase(s). It is therefore not surprising that similar thermal treatments for equally thick Fe and Ru films on SiC yield different amounts of graphitic surface carbon.

Near-edge X-ray absorption fine structure (NEXAFS) measurements of the C 1s K-edge from the Ru/SiC and Fe/SiC systems are presented in Figures 2a and 2b, respectively. The spectra were recorded from samples similar to those in Figure 1 before and after thermal treatments to 800 °C by using linearly polarized light at angles ranging from grazing (~20°) to normal incidence relative to the SiC(0001) plane. In both cases the annealing leads to new absorption resonances appearing at excitation energies 285.5 and 291.7 eV. While the latter indicates the existence of antibonding orbitals which overlap head-on (σ^*), the former is a fingerprint of antibonding p_z orbitals in sp^2-hybridized carbon, perpendicularly oriented to an aromatically configured macromolecular plane.[39,40] Hence, the strong 1s → π^* resonance supports the formation of new graphitic carbon on the samples.

The π^* resonances in Figure 2 also reveal a definite angle dependence, with stronger intensities observed when electrons

are exited by light near grazing incidence to the samples. This suggests a prominent geometric ordering in the layers.[41] To determine the orientation of the C−C bonds relative to the plane of the SiC substrate, we compared the intensity of the lowest unoccupied molecular orbital (LUMO) excitation to an analytical solution of the NEXAFS intensity outlined by Stöhr and Outka.[42,43] Essentially, for carbon systems of 3-fold or higher symmetries, the resonance intensity of the 1s → π^* transition, when excited by linearly polarized light, can be reduced to

$$I \propto P\left(\cos^2\theta\cos^2\alpha + \frac{1}{2}\sin^2\theta\sin^2\alpha\right) + \frac{1-P}{2}\sin^2\alpha \tag{1}$$

where P is the polarization factor of the light hitting the sample plane at angle θ. The angle α between the sample surface normal and the vector perpendicular to the molecular plane of the inherent C−C bonds can thus be used to determine the average orientation of the graphitic planes on the surface.

In Figure 2c, the recorded LUMO intensities for the carbon in both material systems are plotted against the theoretical curves given by eq 1 for light with nearly perfect linear polarization ($P > 0.9$). To establish the angular intensity from the newly formed C−C carbon alone, a Gaussian profile was fitted to the π^* absorption feature for incidence angles $\theta = 20°−90°$, and the background intensity of the clean SiC surface was subsequently deducted from the region. For the Ru/SiC system an additional, but presumably not angularly dependent, constant intensity offset was added to the Gaussians to account for any excitations from the Ru 3d state.

In the case of Fe/SiC, the measured average tilt angle α suggests that the graphene is precisely parallel to the substrate. For the Ru/SiC, the analysis reveals a larger tilt of roughly 17°, indicating that the graphene and its underlying layers are only more or less parallel. The reason for the larger α of Ru/SiC remains unclear but could be due to roughness at the interface, misalignment of the sample, or potentially other contributing factors.

To address the homogeneity of the sample surface, real-space analysis was also performed with LEEM. A surface micrograph from an Fe/SiC sample upon graphene formation at 600 °C is shown in Figure 2d. For low kinetic energies of the scattered electrons ($E_k \sim 3.7$ eV), the surface appears to be roughly uniform across ranges of 10+ μm. Only occasional submicrometer defects originating from the initial SiC surface can be seen. This suggests that on the given length scale coherent properties of the newfound graphene layers should be expected.

Next, the occupied electronic structure of the graphene was investigated with μ-ARPES. Measurements were performed on selected areas with 1.5 μm diameter, near the surface shown in Figure 2d and within the surrounding 50+ μm. The recorded band structures were compared with respect to doping induced by the substrate and variations in the number of graphene layers formed (if any).[26,44−46] In Figures 2e−g, a representative set of band structure measurements are shown. Two-dimensional plots of the electronic structure in reciprocal space ($\mathbf{k}_x$ vs $\mathbf{k}_y$) at constant energies relative to the Fermi level (E_F) are shown in Figures 2e and 2f. Near E_F, six distinguishable features from the π bands, i.e., Dirac "cones", appear at the $\overline{K}$ and $\overline{K}'$ points of the Brillouin zone. At 2 eV below E_F, another broad, hexagonal feature of smaller $\mathbf{k}$ values and with a 30° relative rotation can be seen.

In Figure 2g, the photoelectron intensity from the occupied states has been extracted for E vs $\mathbf{k}_\parallel$ along the principal symmetry directions of the surface Brillouin zone. Two similar plots are shown, where one (left) is the signal extracted from the constant energy surfaces and the other (right) is a second differential image (SDI) of the same signal with a moderate boxcar averaging applied. In both plots, the characteristic, near linearly dispersive bands of graphene are present around $\overline{K}$, indicating that at least one surface layer of graphene was formed from the reaction. The zero density of states crossing, i.e., the Dirac "point" E_D, is situated close to the Fermi level. This confirms the graphene not to be strongly doped from interactions with the underlying metal; however, weak doping cannot be ruled out within the resolution limits of the instrument (see the Supporting Information). Nonetheless, the measurements in Figures 2e−g agree with the literature,[10,19,20] in which a second layer of precipitated carbon from metals Fe and Ru will form quasi-freestanding graphene. The SDI in Figure 2g also reveals some additional, low $\mathbf{k}$ dispersive features around the $\overline{\Gamma}$ point at roughly 2 eV binding energy. The exact origin of these bands is uncertain but are assumed to arise from the metal's shallow d states and their interaction with the SiC surface.

With subsequent annealing to higher temperatures, both the gra/Fe/SiC and gra/Ru/SiC systems experience further changes to their structural composition (Figure 3). Not surprisingly, the relative intensity of graphene to SiC signal increases (Figure 1d), suggesting more metal has reacted with the SiC and liberated more carbon. Second, the signal intensity ratio between the two underlying layers, i.e., the metal (Fe or Ru) and the SiC substrate, shows a relatively higher proportion of SiC signal in the surface layers with increasing temperature (Figure 3a). After two short heat treatments to higher temperatures of 700 and 800 °C, the relative concentration of metal to SiC is <50% of the initial value. With any attenuation from the newfound graphene accounted for, these results suggest that the metal is in fact disappearing from the surface layers. Similar behavior was observed for intercalated adatoms of Fe[21,47] and Yb[48] at temperatures beyond 600 °C. The attenuation of Fe was explained by a temperature-driven diffusion into the underlying semiconductor substrate, and the same argument could easily be extended to Ru.

Assuming the metal is depleted from the surface layers by thermal diffusion, one could expect that probing deeper into the samples would reveal a relatively stronger XPS intensity from the diffused metallic species. In Figure 4, the C 1s regions of the gra/Fe/SiC and gra/Ru/SiC samples from Figure 3 are shown, but now probed with increasingly higher photo-excitation energies. Higher $h\nu$ gives longer inelastic mean-free paths λ for the excited photoelectrons, and so a signal from an increasingly thick slab of substrate material is being detected as $h\nu$ increases. In Figure 4a the C 1s of the gra/Fe/SiC, recorded with three selected photoexcitation energies corresponding to $\lambda \sim 0.5$ nm (surface sensitive), $\lambda \sim 0.9$ nm (moderately surface sensitive), and $\lambda \sim 1.6$ nm (substrate sensitive), is shown. The signal can be deconvolved into two main features at 282.9 and 284.3 eV. The former matches the binding energy of the previously observed SiC component, lowered by 0.3 eV due to interactions with the transition metal. The second feature is found at a binding energy roughly 0.1 eV lower than what is expected for neutral graphite and has a distinct asymmetric shape indicating a metallic surface nature.[14,15] At high surface sensitivity ($\lambda \sim 0.5$ nm), the sharp asymmetric feature
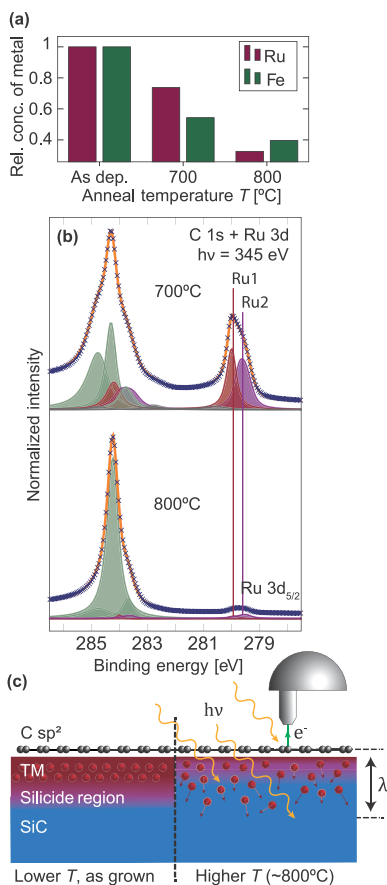
Figure 3. Diffusion of metal into the growth substrate. (a) Relative concentration of metal in the surface layers before and after high-temperature annealing. The measure of the metal content is given as the ratio of Ru and Fe core level signal to the substrate carbon signal, corrected for differences in cross sections and normalized to unity after deposition (room temperature). Diffusion into the SiC substrate is evident from the treatments to subsequently higher temperatures. (b) C 1s and Ru 3d core levels of the gra/Ru/SiC system, measured with photon energy $h\nu$ = 345 eV after subsequent heat treatments to 700 °C and then 800 °C. (c) Schematic of metal diffusion into the substrate of the SiC substrate during annealing to 800 °C.

dominates the intensity of the region, but at lower surface sensitivity ($\lambda \rightarrow 1.6$ nm) the weight is shifted toward the substrate peak. This matches well with the notion of a finite amount of graphene situated at the surface: at low λ most of the C 1s signal comes from the layers of sp^2 carbon, but at higher λ more substrate layers are added to the probing region and so the SiC signal dominates. The familiar 0.3 eV energy shift of the C−Si component (see Figure 1c) may indicate that the surface layers have been doped by the Fe and that the same doping level persists even after higher temperature annealing.

On the other hand, the small (0.1 eV) energy shift of the C sp^2 component indicates only weak doping of the graphene, consistent with what was observed from the band structure in Figure 2g and other systems.[10,19,20]

In Figure 4d, the same exercise is repeated for gra/Ru/SiC with the same photoexcitation energies. Note that the deconvolution is more complicated due to the overlapping C 1s and Ru 3d signals. However, from the known energy separation and intensity ratio of the $3d_{5/2}$ and $3d_{3/2}$ signals, one can accurately determine the components of Ru $3d_{3/2}$ based on those observed in the Ru $3d_{5/2}$ region. The overlapping C 1s and Ru $3d_{3/2}$ signal was thus deconvolved by placing features of the bare SiC and the predetermined Ru components together and adding the minimum number of additional features to optimize the fit.

Not surprisingly, the same distinct asymmetric feature seen in Figure 4a is also visible for gra/Ru/SiC in Figure 4d, now at 284.2 eV. Near the surface ($\lambda \sim 0.5$ nm) the SiC feature cannot be seen, but with increasing λ it again becomes visible at lower binding energy 282.8 eV. This indicates that within ±0.1 eV the doping from the Ru is similar to what was observed from the Fe in Figure 4a.

At moderate depth sensitivity, the Ru contributes with two distinct features: one at 280.0 eV (Ru1) corresponding to that of metallic Ru[49,50] and one at 0.4 eV lower binding energy (Ru2) matching with that observed for Ru silicides.[34,35,51] With increasing depth sensitivity, the relative weight of the two changes and new Ru features become visible at higher binding energies (Ru3). This indicates that different Ru species are present at different depths into the substrate, in line with the thermally activated diffusion of metal into the substrate that was shown in Figure 3.

Note that for the thermal treatments in Figure 4 the metal signal in the surface layers is reduced but not fully diminished. While the graphene (C sp^2) appear to be only weakly doped and thus ultimately not very affected, any metal impurities present in the SiC can work to reduce electron and hole mobility of the substrate. This may or may not be a potential concern for applications where the underlying semiconductor plays an active role, for example, in graphene-based field effect transistors (GFETs). A proper understanding of the impact of residual metal impurities in the SiC would require further investigations that are beyond the scope of this work.

To correctly determine the position of the graphene layers relative to the metal silicide and the SiC, the C 1s intensity was extracted for additional photoexcitation energies in the range 315−1200 eV. In Figure 4b, the variation of the graphene intensity relative to the total accumulated intensity within the scan regions of both material systems is shown. In the gra/Fe/SiC system the relative graphene intensity was estimated by first deconvolving the C 1s region and then comparing the sum of the asymmetric feature at 284.3 eV and the surface peaks (S1, S2) to the total signal. For the gra/Ru/SiC, the graphene signal was estimated by first determining the total Ru $3d_{5/2}$ intensity, calculating the Ru $3d_{3/2}$ intensity based on their known ratio, and deducting both of these intensities from the scan region. Note that for simplicity in the Ru case the total C 1s intensity was assumed to come from graphene, as the deconvolution in Figure 4d revealed the SiC signal from the substrate to be negligible except when using the very highest ($h\nu > 800$ eV) photoexcitation energies. Both systems show a negative exponential decay in graphene intensity with increasing $h\nu$, as expected from Beer−Lambert's law for a
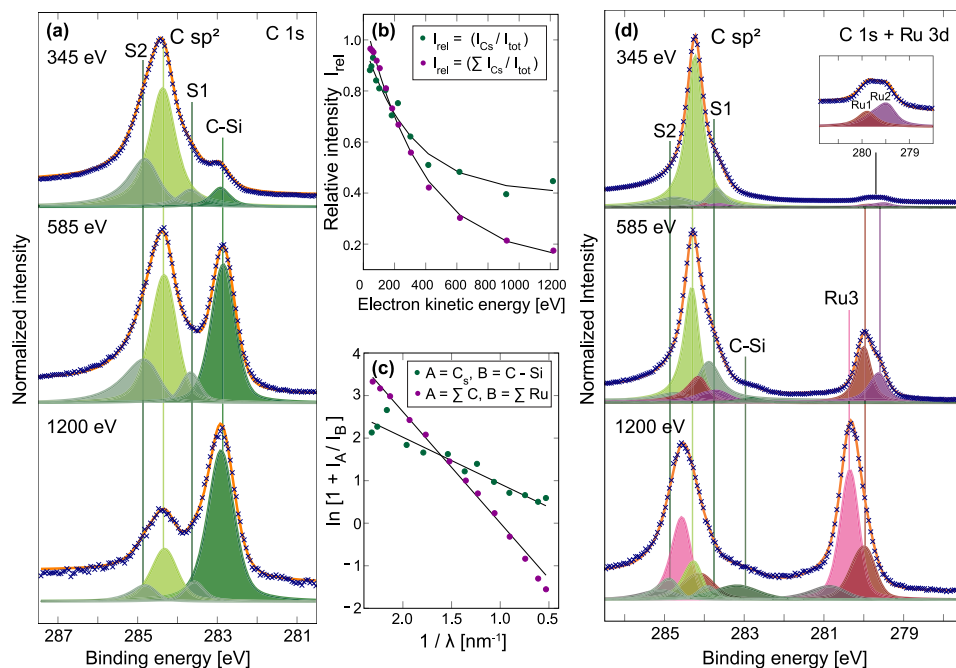
Figure 4. Depth profiling of graphene from mediated growth using Fe and Ru on SiC. (a, d) A selection of C 1s core level spectra from samples covered with Fe and Ru, respectively, after annealing to 800 °C. The three core levels in each set were measured with photon energies $h\nu$ = 345 eV (surface sensitive), $h\nu$ = 585 eV (moderately surface sensitive), and $h\nu$ = 1200 eV (substrate sensitive). (b) A full range of data points for the photoelectron intensity of graphene (I_{Cs}) relative to the total intensity (I_{tot}) from the energy regions in (a) and (d) as a function of kinetic energy for the exited photoelectrons. Note that the two data sets differ slightly in their normalizations, with green (gra/Fe/SiC) stating the fractional intensity of C sp² plus surface peaks (S1, S2), while for purple (gra/Ru/SiC) all carbon features were assumed to be surface carbon for simplicity. (c) The data from (b), replotted to show the relationship between the relative photoelectron intensity and the inverse inelastic mean-free path λ from a simple two-layer model: surface graphene (I_A) on top of an underlying and metal-rich substrate region (I_B). An evident linearity can be seen from the data, similar to that of the ideal two-layer model. As seen from (a) and (d) the Ru signal, but not Fe signal, can be seen in the relevant energy regions of the C 1s core level. Hence, for the gra/Fe/SiC system, the C sp² intensities (top layer) are compared to the carbon signal from the underlying SiC substrate (bottom layer), while for the gra/Ru/SiC system the metallic Ru signal is considered to be the bottom layer.

system with finite signal detected from the surface layers. On the basis of these observations, we used a simple two-layer model to determine the thickness of the graphene layers, assuming these to be residing on top of underlying transition metal and SiC. For each photoexcitation energy, the signal from surface carbon I_s was compared to the signal assigned to the underlying layers I within the same scan region, according to

$$\frac{d}{\lambda} = \ln\left[1 + \frac{I\sigma_s}{I_s\sigma}\right]$$

(2)

where σ_s and σ are the photoexcitation cross-sections for the topmost and lowermost layers, respectively, and d is the estimated thickness of the carbon overlayer. The total surface carbon signal of the gra/Fe/SiC system was thus compared to that of the underlying SiC substrate, while for the gra/Ru/SiC system, the total C 1s signal was compared to that of the underlying Ru. In Figure 4c, it is shown that a linear relationship between the logarithm in eq 2 and the inverse

inelastic mean-free path is obtained for both material systems. This is in accordance with the assumed layer structure from the simplified two-layer model. The gradient from the best fit of each data set gives an estimate of the thickness d of the graphene overlayers: 1.1 and 2.6 nm are obtained for the two systems gra/Fe/SiC and gra/Ru/SiC, respectively. If one assumes that the graphene layers are weakly bound together by van der Waals forces with an interlayer spacing equal to that of graphite (0.355 nm),[52] then roughly 3−8 layers have been formed, regulated by the applied temperature and the thickness of the mediating metal deposited.

◼ CONCLUSIONS

The metal-mediated growth of epitaxial few-layer graphene on the surface of 6H-SiC(0001) treated with Fe or Ru has been investigated, at a temperature far lower than that required for graphene growth directly from the SiC crystal. Using surface diffraction and surface sensitive photoemission measurements, we observed the onset of graphene formation after short thermal treatments to 450 °C, and the familiar electronic

structure of graphene was confirmed for the newly formed species at 600 °C by using ARPES. Further annealing to higher temperatures of 700−800 °C revealed the formation of additional graphene layers (3−8 layers). Both metals were seen to produce either neutral or weakly doped, quasi-freestanding multilayer graphene. The placement of the graphene near the sample surface and its parallel orientation relative to the underlying growth substrate were established from depth sensitive photoemission and angle-dependent absorption spectroscopy measurements, respectively. The tunable depth sensitivity of the photoemission measurements was also used to confirm that the mediating metal agents, Fe and Ru, can be made to diffuse into the SiC crystal with subsequent thermal treatments to higher temperatures.

From these investigations we have established a modified recipe for graphene production requiring a minimal number of processing steps. The controllable growth of high quality, few-layer graphene-on-semiconductor has been achieved at industrially compatible temperatures that so far have not been available by using other, more conventional growth techniques. The number of graphene layers formed is limited by the type and thickness of the transition metal film and the temperatures to which the material system is subjected. The option to use either Fe or Ru interchangeably over a range of different temperatures allows graphene with a tunable thickness to be formed. The possibility to diffuse the mediating metal agents into the substrate means graphene can be supported either on magnetic silicide layers or directly on SiC, as required. This makes metal-mediated graphene growth a realistic and promising candidate for realizing graphene-based devices within the pre-existing framework of large-scale device processing.

■ ASSOCIATED CONTENT

ⓈI   **Supporting Information**

The Supporting Information is available free of charge at https://pubs.acs.org/doi/10.1021/acs.jpcc.0c10870.

    Additional details regarding the experimental setup as well as relevant experimental parameters for the results presented in the text and in Figures 1−4 (PDF)

■ AUTHOR INFORMATION

Corresponding Authors

Håkon I. Røst − *Center for Quantum Spintronics, Department of Physics, Norwegian University of Science and Technology (NTNU), NO-7491 Trondheim, Norway;* ⓘ orcid.org/0000-0002-1853-8349; Email: hakon.i.rost@ntnu.no

Rajesh Kumar Chellappan − *Center for Quantum Spintronics, Department of Physics, Norwegian University of Science and Technology (NTNU), NO-7491 Trondheim, Norway;* Email: rajesh.k.chellappan@ntnu.no

Justin W. Wells − *Center for Quantum Spintronics, Department of Physics, Norwegian University of Science and Technology (NTNU), NO-7491 Trondheim, Norway;* ⓘ orcid.org/0000-0001-6366-366X; Email: justin.wells@ntnu.no

Authors

Frode S. Strand − *Center for Quantum Spintronics, Department of Physics, Norwegian University of Science and Technology (NTNU), NO-7491 Trondheim, Norway*

Antonija Grubišić-Čabo − *School of Physics & Astronomy, Monash University, Clayton, Victoria 3168, Australia;* ⓘ orcid.org/0000-0001-7683-0295

Benjamen P. Reed − *Department of Physics, Aberystwyth University, Aberystwyth SY23 3BZ, United Kingdom*

Mauricio J. Prieto − *Department of Interface Science, Fritz-Haber-Institute of the Max-Planck Society, 14195 Berlin, Germany;* ⓘ orcid.org/0000-0002-5087-4545

Liviu C. Tănase − *Department of Interface Science, Fritz-Haber-Institute of the Max-Planck Society, 14195 Berlin, Germany;* ⓘ orcid.org/0000-0002-4177-5676

Lucas de Souza Caldas − *Department of Interface Science, Fritz-Haber-Institute of the Max-Planck Society, 14195 Berlin, Germany*

Thipusa Wongpinij − *Synchrotron Light Research Institute, Nakhon Ratchasima 30000, Thailand*

Chanan Euaruksakul − *Synchrotron Light Research Institute, Nakhon Ratchasima 30000, Thailand*

Thomas Schmidt − *Department of Interface Science, Fritz-Haber-Institute of the Max-Planck Society, 14195 Berlin, Germany;* ⓘ orcid.org/0000-0003-4389-2080

Anton Tadich − *Australian Synchrotron, Clayton, Victoria 3168, Australia*

Bruce C. C. Cowie − *Australian Synchrotron, Clayton, Victoria 3168, Australia*

Zheshen Li − *Department of Physics and Astronomy, Aarhus University, 8000 Aarhus C, Denmark*

Simon P. Cooil − *Department of Physics, Aberystwyth University, Aberystwyth SY23 3BZ, United Kingdom; Semiconductor Physics, Department of Physics, University of Oslo (UiO), NO-0371 Oslo, Norway;* ⓘ orcid.org/0000-0002-0856-6020

Complete contact information is available at:
https://pubs.acs.org/10.1021/acs.jpcc.0c10870

Notes

The authors declare no competing financial interest.

■ ACKNOWLEDGMENTS

H.I.R., J.W.W. and S.P.C. would also like to thank Dr. Mark Edmonds, Dr. Federico Mazzola and Dr. Andrew Evans for fruitful discussions.

■ REFERENCES

(1) Novoselov, K. S.; Geim, A. K.; Morozov, S. V.; Jiang, D.; Zhang, Y.; Dubonos, S. V.; Grigorieva, I. V.; Firsov, A. A. Electric field effect in atomically thin carbon films. *Science* **2004**, *306*, 666−669.

(2) Bolotin, K. I.; Sikes, K. J.; Jiang, Z.; Klima, M.; Fudenberg, G.; Hone, J.; Kim, P.; Stormer, H. Ultrahigh electron mobility in suspended graphene. *Solid State Commun.* **2008**, *146*, 351−355.

(3) Neto, A. C.; Guinea, F.; Peres, N. M.; Novoselov, K. S.; Geim, A. K. The electronic properties of graphene. *Rev. Mod. Phys.* **2009**, *81*, 109.

(4) Balandin, A. A. Thermal properties of graphene and nano-structured carbon materials. *Nat. Mater.* **2011**, *10*, 569−581.

(5) Falkovsky, L. Optical properties of graphene. *J. Phys. Conf. Ser.* **2008**, *129*, 012004.

(6) Papageorgiou, D. G.; Kinloch, I. A.; Young, R. J. Mechanical properties of graphene and graphene-based nanocomposites. *Prog. Mater. Sci.* **2017**, *90*, 75−127.

(7) Varykhalov, A.; Sánchez-Barriga, J.; Shikin, A. M.; Biswas, C.; Vescovo, E.; Rybkin, A.; Marchenko, D.; Rader, O. Electronic and Magnetic Properties of Quasifreestanding Graphene on Ni. *Phys. Rev. Lett.* **2008**, *101*, 157601.

(8) N'Diaye, A. T.; Bleikamp, S.; Feibelman, P. J.; Michely, T. Two-dimensional Ir cluster lattice on a graphene Moiré on Ir(111). *Phys. Rev. Lett.* **2006**, *97*, 215501.

(9) Sutter, P.; Sadowski, J. T.; Sutter, E. Graphene on Pt (111): Growth and substrate interaction. *Phys. Rev. B: Condens. Matter Mater. Phys.* **2009**, *80*, 245411.

(10) Sutter, P. W.; Flege, J.-I.; Sutter, E. A. Epitaxial graphene on ruthenium. *Nat. Mater.* **2008**, *7*, 406−411.

(11) Berger, C.; Song, Z.; Li, T.; Li, X.; Ogbazghi, A. Y.; Feng, R.; Dai, Z.; Marchenkov, A. N.; Conrad, E. H.; First, P. N.; et al. Ultrathin epitaxial graphite: 2D electron gas properties and a route toward graphene-based nanoelectronics. *J. Phys. Chem. B* **2004**, *108*, 19912−19916.

(12) Hass, J.; Feng, R.; Li, T.; Li, X.; Zong, Z.; De Heer, W.; First, P.; Conrad, E.; Jeffrey, C.; Berger, C. Highly ordered graphene for two dimensional electronics. *Appl. Phys. Lett.* **2006**, *89*, 143106.

(13) Coraux, J.; N'Diaye, A. T.; Busse, C.; Michely, T. Structural coherency of graphene on Ir (111). *Nano Lett.* **2008**, *8*, 565−570.

(14) Emtsev, K.; Speck, F.; Seyller, T.; Ley, L.; Riley, J. D. Interaction, growth, and ordering of epitaxial graphene on SiC {0001} surfaces: A comparative photoelectron spectroscopy study. *Phys. Rev. B: Condens. Matter Mater. Phys.* **2008**, *77*, 155303.

(15) Emtsev, K. V.; Bostwick, A.; Horn, K.; Jobst, J.; Kellogg, G. L.; Ley, L.; McChesney, J. L.; Ohta, T.; Reshanov, S. A.; Röhrl, J.; et al. Towards wafer-size graphene layers by atmospheric pressure graphitization of silicon carbide. *Nat. Mater.* **2009**, *8*, 203−207.

(16) Zhang, Z.; Du, J.; Zhang, D.; Sun, H.; Yin, L.; Ma, L.; Chen, J.; Ma, D.; Cheng, H.-M.; Ren, W. Rosin-enabled ultraclean and damage-free transfer of graphene for large-area flexible organic light-emitting diodes. *Nat. Commun.* **2017**, *8*, 1−9.

(17) Lin, Y.-M.; Dimitrakopoulos, C.; Jenkins, K. A.; Farmer, D. B.; Chiu, H.-Y.; Grill, A.; Avouris, P. 100-GHz transistors from wafer-scale epitaxial graphene. *Science* **2010**, *327*, 662−662.

(18) Aliofkhazraei, M.; Ali, N.; Milne, W. I.; Ozkan, C. S.; Mitura, S.; Gervasoni, J. L. *Graphene Science Handbook: Electrical and Optical Properties*; CRC Press: 2016; Chapter 1, pp 5−6.

(19) Cooil, S.; Song, F.; Williams, G.; Roberts, O.; Langstaff, D.; Jørgensen, B.; Høydalsvik, K.; Breiby, D.; Wahlström, E.; Evans, D.; et al. Iron-mediated growth of epitaxial graphene on SiC and diamond. *Carbon* **2012**, *50*, 5099−5105.

(20) Cooil, S.; Wells, J.; Hu, D.; Niu, Y.; Zakharov, A.; Bianchi, M.; Evans, D. Controlling the growth of epitaxial graphene on metalized diamond (111) surface. *Appl. Phys. Lett.* **2015**, *107*, 181603.

(21) Shen, K.; Sun, H.; Hu, J.; Hu, J.; Liang, Z.; Li, H.; Zhu, Z.; Huang, Y.; Kong, L.; Wang, Y.; et al. Fabricating quasi-free-standing graphene on a SiC (0001) surface by steerable intercalation of iron. *J. Phys. Chem. C* **2018**, *122*, 21484−21492.

(22) Kern, W. The evolution of silicon wafer cleaning technology. *J. Electrochem. Soc.* **1990**, *137*, 1887−1892.

(23) Starke, U.; Bernhardt, J.; Schardt, J.; Heinz, K. SiC surface reconstruction: Relevancy of atomic structure for growth technology. *Surf. Rev. Lett.* **1999**, *6*, 1129−1141.

(24) Starke, U.; Schardt, J.; Bernhardt, J.; Franke, M.; Heinz, K. Stacking transformation from hexagonal to cubic SiC induced by surface reconstruction: A seed for heterostructure growth. *Phys. Rev. Lett.* **1999**, *82*, 2107−2110.

(25) Starke, U.; Riedl, C. Epitaxial graphene on SiC(0001) and SiC(): From surface reconstructions to carbon electronics. *J. Phys.: Condens. Matter* **2009**, *21*, 134016.

(26) Ohta, T.; Bostwick, A.; Seyller, T.; Horn, K.; Rotenberg, E. Controlling the electronic structure of bilayer graphene. *Science* **2006**, *313*, 951−954.

(27) Nakao, A.; Iwaki, M.; Sakairi, H.; Terasima, K. XPS characterization of nitrogen implanted silicon carbide. *Nucl. Instrum. Methods Phys. Res., Sect. B* **1992**, *65*, 352−356.

(28) Wang, Y.-Y.; Kusumoto, K.; Li, C.-J. XPS analysis of SiC films prepared by radio frequency plasma sputtering. *Phys. Procedia* **2012**, *32*, 95−102.

(29) Hollinger, G.; Himpsel, F. Probing the transition layer at the SiO2-Si interface using core level photoemission. *Appl. Phys. Lett.* **1984**, *44*, 93−95.

(30) Watanabe, H.; Hosoi, T.; Kirino, T.; Kagei, Y.; Uenishi, Y.; Chanthaphan, A.; Yoshigoe, A.; Teraoka, Y.; Shimura, T. Synchrotron X-ray photoelectron spectroscopy study on thermally grown SiO2/4H-SiC (0001) interface and its correlation with electrical properties. *Appl. Phys. Lett.* **2011**, *99*, 021907.

(31) Rührnschopf, K.; Borgmann, D.; Wedler, G. Growth of Fe on Si (100) at room temperature and formation of iron silicide. *Thin Solid Films* **1996**, *280*, 171−177.

(32) Gomoyunova, M.; Malygin, D.; Pronin, I.; Voronchikhin, A.; Vyalikh, D.; Molodtsov, S. Initial stages of iron silicide formation on the Si(100) 2 × 1 surface. *Surf. Sci.* **2007**, *601*, 5069−5076.

(33) Wang, Z.-J.; Dong, A.; Wei, M.; Fu, Q.; Bao, X. Graphene as a surfactant for metal growth on solid surfaces: Fe on graphene/SiC (0001). *Appl. Phys. Lett.* **2014**, *104*, 181604.

(34) Lu, Z.; Sham, T.; Norton, P.; Tan, K. Photoemission studies of silicon on the Ru (001) surface. *Appl. Phys. Lett.* **1991**, *58*, 161−163.

(35) Lizzit, S.; Larciprete, R.; Lacovig, P.; Dalmiglio, M.; Orlando, F.; Baraldi, A.; Gammelgaard, L.; Barreto, L.; Bianchi, M.; Perkins, E.; et al. Transfer-free electrical insulation of epitaxial graphene from its metal substrate. *Nano Lett.* **2012**, *12*, 4503−4507.

(36) Zhukov, A. Phase diagram of alloys of the system Fe-C. *Met. Sci. Heat Treat.* **1988**, *30*, 249−255.

(37) Arnoult, W. J.; McLellan, R. B. Solubility of carbon in rhodium, ruthenium, iridium, and rhenium. *Scr. Metall.* **1972**, *6*, 1013−1018.

(38) Sanbongi, K.; Ohtani, M.; Toita, K. On the effect of alloying elements on the solubility of carbon in molten iron. *Sci. rep. Res. Inst., Tohoku Univ., Ser. A* **1957**, 147−158.

(39) Pacilé, D.; Papagno, M.; Rodríguez, A. F.; Grioni, M.; Papagno, L.; Girit, Ç.; Meyer, J.; Begtrup, G.; Zettl, A. Near-edge X-ray absorption fine-structure investigation of graphene. *Phys. Rev. Lett.* **2008**, *101*, 066806.

(40) Shpilman, Z.; Gouzman, I.; Minton, T.; Shen, L.; Stacey, A.; Orwa, J.; Prawer, S.; Cowie, B.; Hoffman, A. A near edge X-ray absorption fine structure study of oxidized single crystal and polycrystalline diamond surfaces. *Diamond Relat. Mater.* **2014**, *45*, 20−27.

(41) Kim, K.-J.; Lee, H.; Choi, J.; Lee, H.; Kang, T.; Kim, B.; Kim, S. Temperature dependent structural changes of graphene layers on 6H-SiC (0001) surfaces. *J. Phys.: Condens. Matter* **2008**, *20*, 225017.

(42) Stöhr, J.; Outka, D. Determination of molecular orientations on surfaces from the angular dependence of near-edge X-ray-absorption

fine-structure spectra. *Phys. Rev. B: Condens. Matter Mater. Phys.* **1987**, *36*, 7891.

(43) Stöhr, J. *NEXAFS Spectroscopy*; Springer Science & Business Media: 2013; Vol. *25*; Chapter 9, pp 279−291.

(44) Bostwick, A.; Ohta, T.; Seyller, T.; Horn, K.; Rotenberg, E. Quasiparticle dynamics in graphene. *Nat. Phys.* **2007**, *3*, 36−40.

(45) Ohta, T.; Bostwick, A.; McChesney, J. L.; Seyller, T.; Horn, K.; Rotenberg, E. Interlayer interaction and electronic screening in multilayer graphene investigated with angle-resolved photoemission spectroscopy. *Phys. Rev. Lett.* **2007**, *98*, 206802.

(46) Siegel, D. A.; Hwang, C.; Fedorov, A. V.; Lanzara, A. Quasifreestanding multilayer graphene films on the carbon face of SiC. *Phys. Rev. B: Condens. Matter Mater. Phys.* **2010**, *81*, 241417.

(47) Sung, S.; Yang, J.; Lee, P.; Kim, J.; Ryu, M.; Park, H.; Lee, G.; Hwang, C.; Kim, K. S.; Kim, J.; et al. Spin-induced band modifications of graphene through intercalation of magnetic iron atoms. *Nanoscale* **2014**, *6*, 3824−3829.

(48) Watcharinyanon, S.; Johansson, L. I.; Xia, C.; Flege, J. I.; Meyer, A.; Falta, J.; Virojanadara, C. Ytterbium intercalation of epitaxial graphene grown on Si-face SiC. *Graphene* **2013**, *02*, 66−73.

(49) Fuggle, J.; Madey, T.; Steinkilberg, M.; Menzel, D. Photoelectron spectroscopic studies of adsorption of CO and oxygen on Ru (001). *Surf. Sci.* **1975**, *52*, 521−541.

(50) Kaga, Y.; Abe, Y.; Yanagisawa, H.; Kawamura, M.; Sasaki, K. Ru and RuO_2 thin films by XPS. *Surf. Sci. Spectra* **1999**, *6*, 68−74.

(51) Pasquali, L.; Mahne, N.; Montecchi, M.; Mattarello, V.; Nannarone, S. Formation and distribution of compounds at the Ru-Si (001) ultrathin film interface. *J. Appl. Phys.* **2009**, *105*, 044304.

(52) De Andres, P.; Ramírez, R.; Vergés, J. A. Strong covalent bonding between two graphene layers. *Phys. Rev. B: Condens. Matter Mater. Phys.* **2008**, *77*, 045403.

4.4   Paper 2

My contribution: Like Paper [1], this work comprises measurements using a range of different spectroscopic and microscopic techniques from several different facilities. I have participated and played a central role in most measurements and the analysis, except for the Raman spectroscopy performed by B. P. Reed and S. P. Cooil. I have made all figures and written the first draft of the manuscript and supplementary information. Finally, I have implemented the improvements suggested by the other co-authors.

A Simplified Method for Patterning Graphene on Dielectric Layers

Authors

Håkon I. Røst
Benjamen P. Reed
Frode S. Strand
Joseph A. Durk
D. Andrew Evans
Antonija Grubišić-Čabo
Gary Wan
Mattia Cattelan
Mauricio J. Prieto
Daniel M. Gottlob
Liviu C. Tănase
Lucas de Souza Caldas
Thomas Schmidt
Anton Tadich
Bruce C. C. Cowie
Rajesh Kumar Chellappan
Justin W. Wells
Simon P. Cooil

A Simplified Method for Patterning Graphene on Dielectric Layers

Håkon I. Røst,* Benjamen P. Reed, Frode S. Strand, Joseph A. Durk, D. Andrew Evans,
Antonija Grubišić-Čabo, Gary Wan, Mattia Cattelan, Mauricio J. Prieto, Daniel M. Gottlob,
Liviu C. Tănase, Lucas de Souza Caldas, Thomas Schmidt, Anton Tadich, Bruce C. C. Cowie,
Rajesh Kumar Chellappan, Justin W. Wells, and Simon P. Cooil*

ACCESS | Metrics & More | Article Recommendations | Supporting Information

ABSTRACT: The large-scale formation of patterned, quasi-freestanding graphene structures supported on a dielectric has so far been limited by the need to transfer the graphene onto a suitable substrate and contamination from the associated processing steps. We report μm scale, few-layer graphene structures formed at moderate temperatures (600−700 °C) and supported directly on an interfacial dielectric formed by oxidizing Si layers at the graphene/substrate interface. We show that the thickness of this underlying dielectric support can be tailored further by an additional Si intercalation of the graphene prior to oxidation. This produces quasi-freestanding, patterned graphene on dielectric SiO_2 with a tunable thickness on demand, thus facilitating a new pathway to integrated graphene microelectronics.

Graphene SiO_2 Silicide
Fe/Ru   SiC

150 μm

KEYWORDS: graphene, patterned growth, electrical decoupling, photoelectron spectroscopy, PEEM, LEEM, NEXAFS
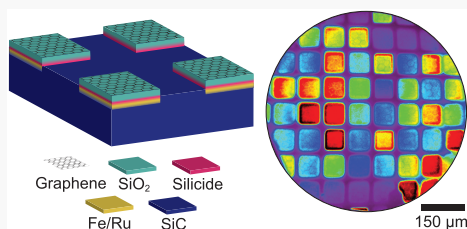
1. INTRODUCTION

The extraordinary properties and success of graphene in prototype electronic platforms have led to numerous synthesis routes and processing methods for patterning the material. While isolation of graphite layers by mechanical exfoliation led the field in characterizing the material properties,[1,2] using exfoliation for device fabrication suffers from a low yield and a lack of scalability.[3] Scalable methods that do not rely on exfoliation are therefore attractive.

Chemical vapor deposition (CVD) on metal[4,5] and semiconductor[6,7] substrates or high-temperature annealing of SiC[8−10] has gained the most traction for producing high-quality graphene films. A large number of routes for further processing are now available, such as photolithography,[11,12] electron beam lithography,[13,14] scanning probe lithography/etching,[15,16] and direct laser lithography.[17−19] However, these methods each have their own disadvantages, e.g., growth on a metal substrate requires the graphene to be transferred and patterning induces defects/contaminants that reduce device efficacy.[20,21]

A promising transfer-free method utilizes a transition-metal catalyst (Cu or Ni) deposited directly onto an oxide layer on a Si wafer.[22,23] Graphene is then formed by annealing in the presence of carbon, and the metal film is subsequently removed chemically, leaving the graphene in direct contact with the dielectric material. Although this method shows great potential, metal contamination remains a major issue.[24] An

alternative approach for removing metal from the graphene has been demonstrated,[25] as has a method for adding a dielectric layer under the graphene after growth.[26] Both modify the graphene−substrate interaction, which is known to impact the electronic properties of graphene.[27−30] Although there is no single method that suits all device applications, there is a desire for transfer-free methods that produce graphene free of contaminants and with control of the substrate interaction, directly on dielectric surfaces. In this work, we demonstrate transfer-free, patterned graphene structures on SiC, with optional decoupling by forming SiO_2 at the graphene−semiconductor interface.

2. METHODS

In our previous work, few-layer graphene on transition-metal silicide was prepared according to the metal-mediated approach as described elsewhere.[31,32] Thin films of Fe or Ru (1−2 nm) on 6H-SiC(0001) were thermally activated by annealing to temperatures of 600−700 °C for a short duration. This triggered transition-metal silicide formation at the interface and the associated liberation of carbon reconstructing
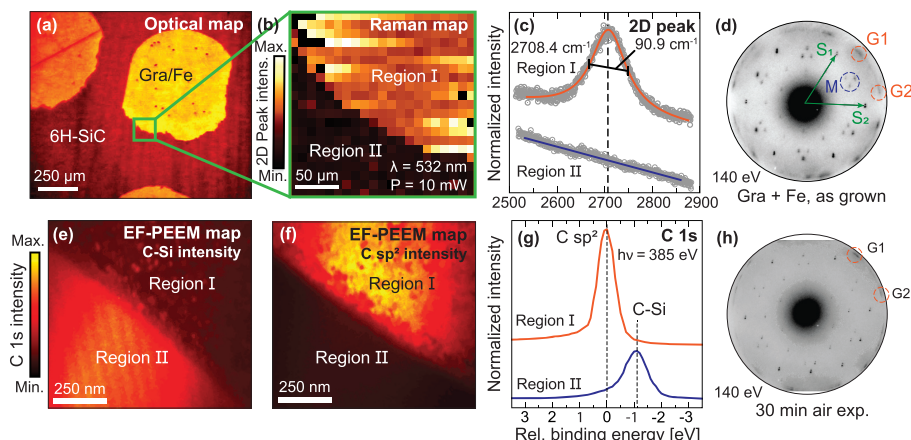
Figure 1. Localized graphene growth on top of patterned Fe. (a) Optical micrograph (artificially colored) showing circular regions of graphene on Fe patterned on 6H-SiC(0001). (b) Spatially resolved Raman showing the intensity of the 2D graphene peak near the edge of one of the patterned regions. (c) Intensity and full width at half-maximum (FWHM) of the 2D Raman peak recorded from the two different spatial Regions I and II in panel 1b. (d) Small-area low-energy electron diffraction (μ-LEED) pattern of Fe-mediated, patterned graphene on 6H-SiC(0001) grown at 600 °C. The threefold symmetric diffraction pattern of the substrate is described by vectors S_1 and S_2. Two distinct rotational domains of graphene (G1, G2) appear at higher $|\mathbf{k}|$, with ≈15 and 45° relative to the SiC. Additional spots (M) can be assigned to remnants of Fe beneath the graphene. (e, f) EF-PEEM measurements of a patterned region recorded at two different binding energies corresponding to C−Si and C sp^2 bonding, respectively. (g) C 1s core level extracted from Regions I and II in the EF-PEEM. The topmost trace (Region I) clearly demonstrates the confinement of graphene within the pattern, while the bottom trace (Region II) shows C−Si bonding characteristics for the SiC substrate. (h) μ-LEED pattern of the Fe-mediated graphene from panel 1d after 30 min. air exposure: G1 and G2 are still visible and thus indicate that the graphene is stable when exposed to air.

into graphitic (sp^2) layers on the surface. Following the growth, all samples were subsequently annealed to higher temperatures ($T > 700$ °C) to diffuse the metal into the bulk of the underlying SiC substrate.[25,32] This left the graphene layers supported directly on a thin film of Si.

To demonstrate the possibility of patterning graphene we followed the above approach, but now with predefined metallic regions (prior to graphene growth) in regular arrays of squares or circles by means of a simple shadow mask. The metals Fe and Ru were deposited under ultrahigh vacuum (UHV) onto chemically and thermally cleaned 6H-SiC substrates through solid masks made of a Mo foil with openings of 50 and 500 μm that were placed in proximity (<0.3 mm) to the sample surface.

3. RESULTS AND DISCUSSION

Selectively grown graphene exclusively on top of Fe islands is demonstrated in Figure 1, using Raman spectroscopy, energy-filtered photoemission electron microscopy (EF-PEEM), and low-energy electron diffraction (LEED). In the Raman spectrum, a distinctive "2D peak" from sp^2 hybridized carbon is observed at 2708.4 cm^{-1} (Figure 1c). The full width at half-maximum (FWHM) of the peak is 90.9 cm^{-1}, suggesting that either mono- or bilayer graphene has been created.[33] In Figure 1b, the spatial distribution and intensity of this peak are plotted, showing two distinctly different areas that indicate patterned graphene formation. Intensity from the graphene is predominantly found inside the Fe pattern (Region I), while negligible amounts can be seen from the nonmetalized SiC substrate (Region II).

The spatially resolved C 1s core level intensity from a similarly prepared sample is shown in Figure 1e, 1f. Distinct chemical components from two separate regions can be

distinguished (Figure 1g). Within the Fe pattern (Region I) an asymmetric peak shape appears at a binding energy of 284.5 eV, characteristic for sp^2 bonded carbon.[34,35] Outside the pattern (Region II) a symmetric peak from the C−Si bonds in SiC appears at 1.1 eV lower binding energy.[8] The spatially resolved Raman and EF-PEEM thus demonstrate that graphene forms only within the metalized regions.

The crystalline quality of the graphene formed is demonstrated from the small spot (1.5 μm) low-energy electron diffraction (μ-LEED) pattern in Figure 1d. Twelve spots appear at ≈15 and 45° rotation relative to the unreconstructed (1 × 1) SiC phase described by vectors S_1 and S_2. These twelve spots have a $|\mathbf{k}| = 2.50$ Å^{-1}, i.e., within ±2% of what is expected for pristine graphene layers[36] and are thus interpreted as two predominant graphene rotational domains, G1 and G2. Additional spots (M) are also observed that likely originate from an underlying bcc(110) lattice constrained by the hexagonal 6H-SiC(0001) surface. Similar features have been reported for Fe thin films on hexagonal surfaces[37,38] and are removed at a later stage.[32]

In our earlier work, thermalized thin films of Ru on 6H-SiC have been shown to produce graphene of a similar quality to those mediated by thin films of Fe.[32] The spatial distribution of C 1s core level signal from this system is resolved in Figure 2a. Again a distinct, asymmetric line shape appears only within the growth region at 284.3 eV binding energy, verifying that graphene forms exclusively within the patterned Ru.

The lateral resolution of the patterning can be ascertained from the sharpness of the boundary between the graphene region and the SiC substrate, as shown in the low-energy

electron microscopy (LEEM) image in Figure 2c. A fitted intensity profile along the edge gives a patterning resolution of 190 nm (Figure 2e). We suspect that this estimate is limited by the bright and dark fringes in the image, resulting from a sudden change in electrostatic potential and work function at the boundary,[39−41] rather than by the abruptness of the patterning.

When annealed for a longer duration, the patterned geometry and the photoemission signal from the graphene in each growth region are well preserved, as shown in Figure 2b, 2d. However, a higher photoemission intensity is seen around the edges of each structure. This may suggest locally enhanced nucleation and associated growth rate, as reported for epitaxial graphene on SiC[42−44] and other 2D materials.[45]

The chemical stability of the patterned graphene was tested by exposing both systems to air for 30 min. In Figure 1h, a LEED pattern from the same Fe-mediated graphene as in

Figure 2. EF-PEEM and LEEM of patterned graphene structures. (a) EF-PEEM micrograph from a sample of 6H-SiC patterned with Ru (Region II) and annealed to 800 °C. The sample is probed at the graphene binding energy, confirming that the graphene formed is confined within the metalized region. (c) LEEM micrograph of the same region probed for electron kinetic energy $E_k = 2.0$ eV. (e) Fitted intensity profile of the patterned graphene edge taken from within the dashed white area in panel 2b. The error function fit (in red) reveals a patterning resolution of $\Delta x = 190$ nm. (b,d,f) EF-PEEM micrographs showing patterned 2 nm Ru on SiC annealed to 750 °C for increasing the time duration to form graphene at the surface (b, d), and finally after 30 min of exposure to air (f). Each micrograph has been extracted for binding energies E_B close to the Fermi level E_F. The average work function (WF) within the squares is indicated in the lower right corner of each subpanel.

Figure 1d is shown after 30 min of exposure to air and a reintroduction to UHV. The two patterns are comparable, indicating that the surface graphene is stable to the exposure. However, the background intensity of the pattern is seen to increase.

Chemical stability is also demonstrated by the small variation in work function between the surfaces in Figure 2b, 2f, and 2. The graphene once formed (Figure 2b, 2d) has a work function of 4.30 eV, and after air exposure (Figure 2f), the work function increases slightly by 100 meV. Given the chemical inertness of graphene already established from our LEED measurements and in the literature,[46−48] this small energy increase hints at a change in the potential at the graphene interface. Furthermore, the intensity of secondary electrons (SEs) near the low-energy cutoff increases by roughly 1 order of magnitude. This can be explained by the longer inelastic mean-free path of photoelectrons associated with the wider band gap of SiO_2.[49] Together with the higher background intensity seen from the LEED (Figure 1h), these changes indicate silicon oxide formation at the graphene−substrate interface.

To further explore the possibility of electrically decoupling the graphene, insulating SiO_2 was grown directly at the semiconductor−graphene interface. To determine how the oxide growth would affect the patterned graphene, spatially resolved, high-resolution X-ray photoemission spectroscopy (XPS) and near-edge X-ray absorption fine structure (NEXAFS) measurements were performed both inside and outside of the graphene growth regions. Note that to perform spatially resolved, high-resolution spectroscopy like this, particularly the NEXAFS, samples of metal-mediated graphene were produced with a patterning scale of 5 mm to compensate for the larger spot size of the photoexcitation.

An oxide layer was grown by stepwise intercalation of Si and O_2 as previously demonstrated for CVD graphene grown on transition-metal substrates.[26] In the first step, patterned graphene was subjected to Si atoms at a flux of 0.15 Å/min for 40 min while being heated to 450 °C. Figure 3 shows the change induced to the carbon K-edge and the Si 2p and C 1s core levels for Fe- and Ru-mediated graphene samples. During deposition, the intensities and shapes of the $1s \rightarrow \pi^*$ excitations (Figure 3c) and the graphene core levels at 284.4 eV (Figure 3b, 3e) are well preserved. In contrast, signals from the substrate (C-Si) and Ru $3d_{5/2}$ (Ru, Ru1-Ru3) are attenuated strongly. New and prominent peaks (Si2) appear at lower binding energies relative to the surface Si−C and silicide (Si1) in the Si 2p region (Figure 3a, 3d). The preservation of the $1s \rightarrow \pi^*$ resonance, the stable graphene core level signal, and the mentioned attenuation of the Ru and SiC intensities, therefore, suggest that the added Si has intercalated the graphene layers without forming clusters on the surface.

Next, the samples were heated to 300 °C while being exposed to O_2 at 200 mbar to trigger the oxidation of the freshly intercalated Si. The shadow masks were then removed and the samples reintroduced to UHV. Spectroscopy measurements were repeated within the patterned graphene growth regions and on the bare and adjacent substrate for comparison (Figure 4). The photograph in Figure 4a shows the two regions under investigation, with a distinct boundary between them indicating the previous position of the now-removed shadow mask (Region II). The yellow spots indicate both the size and positions of the beam during photoexcitation(s).
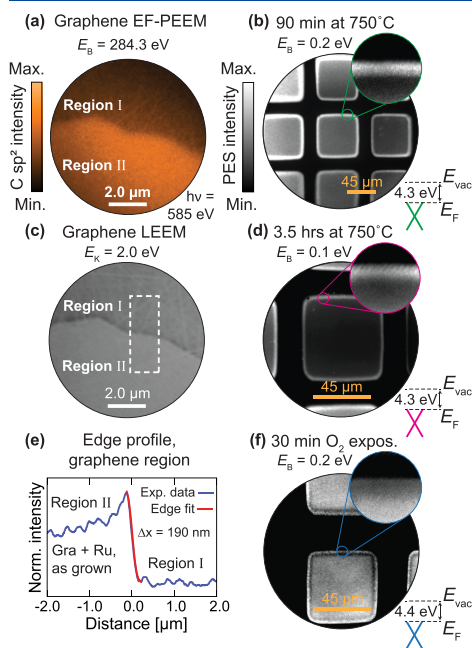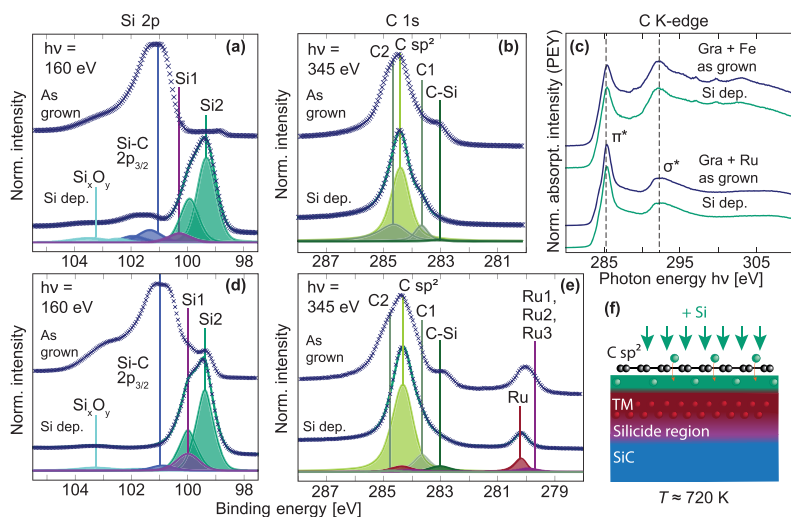
Figure 3. Spatially resolved XPS and NEXAFS demonstrating Si intercalation of metal-mediated graphene. (a, b) Surface-sensitive core levels Si 2p and C 1s from graphene growth using Fe, obtained before and after intercalation of 0.6 nm Si. The C 1s, consisting of graphene (C sp^2), substrate (C−Si), and two surface-related signals (C1, C2), is stable during the Si treatment. Newfound Si from the intercalation (Si2) can be distinguished from the silicide (Si1), substrate (Si−C), and oxide (Si$_x$O$_y$) components. (d, e) Surface-sensitive core levels C 1s and Si 2p from graphene growth, now using Ru, before and after intercalation of 0.6 nm Si. The deconvolved core levels from the treated surface reveal similar features as for the Fe-mediated system. (c) Near-edge X-ray absorption fine structure (NEXAFS) measurements of the carbon K-edge of graphene grown using either Fe or Ru, before and after Si intercalation. Both systems were excited with linearly polarized light at grazing ($\theta \approx 20°$) incidence relative to the sample plane. (f) Schematic demonstrating the intercalation of Si adsorbates between graphene and its underlying growth substrate.
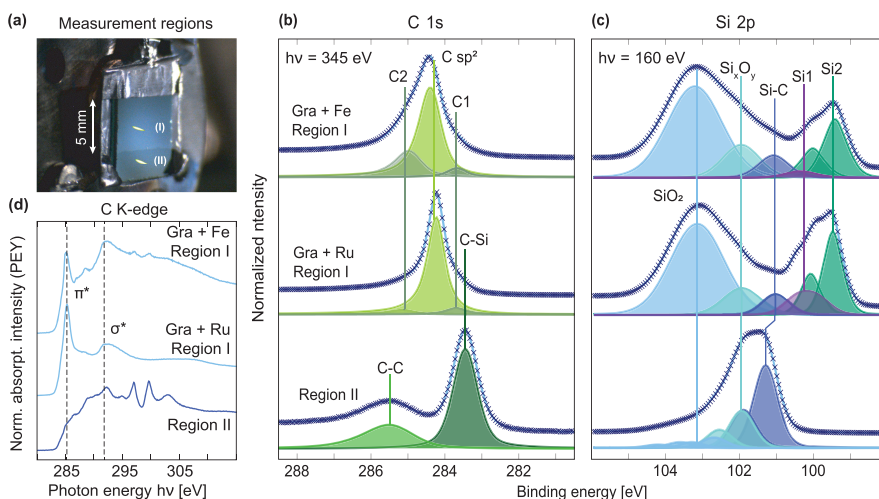
Figure 4. Spatially resolved NEXAFS and XPS of graphene after the growth of underlying SiO$_2$ layers. (a) Photograph showing two distinct regions, one exposed (I) and the other shadowed (II) during metallization, graphene growth, and Si intercalation. The two yellow areas indicate the positions and size of the photoexcitation light spot used during XPS and NEXAFS data acquisition. (b, c) Surface-sensitive C 1s and Si 2p core levels after exposure to 200 mbar oxygen while being heated to 300 °C. The same core levels but from the bare SiC substrate are shown for comparison. (d) Grazing incidence ($\theta \approx 20°$) NEXAFS of Si-intercalated epitaxial graphene grown using Fe or Ru after subsequent oxidation of the underlying Si. NEXAFS from the bare SiC substrate (Region II) is also shown.

With O_2 exposure, a broad, new feature appears in the Si 2p signal (Figure 4c) of Region I at around 103 eV. A similar peak at 103.6 eV has previously been assigned to the Si^{4+} of SiO_2.[50] The formation of SiO_2 in our data is furthermore supported by the loss of signal from the previously added Si, as seen by the strong attenuation of the Si2 signal. Comparing the Si 2p core levels from inside and outside the growth regions, the new SiO_2 feature does not appear in Region II but rather a small tail of intermediate oxide states (Si_xO_y).[51,52]

As expected, no signatures of graphene can be observed in the region previously shadowed by the mask (Region II). The NEXAFS shows no π^* resonance, and the only C 1s signals present are those corresponding to the C−C and C−Si bonds of the SiC surface.[53−56] Inside the pattern (Region I), the graphene does not show any signs of oxidation: the π^* resonances of the NEXAFS appear to be unchanged, and the energies, shapes, and intensities of the graphene core levels are well preserved. In Figure 4b, only a small redistribution of intensity can be seen between the surface C1 and C2 peaks. The characteristic Ru $3d_{5/2}$ signal from the Ru-mediated graphene system can no longer be distinguished at this stage. With the presence of SiO_2 verified from the Si 2p signal, the robustness of the graphene peaks suggests that the graphene is now supported directly on top of the SiO_2.

4. CONCLUSIONS

The demonstrated concepts of transfer-free and patterned graphene formation directly on dielectric thin films is an exciting development that allows structured graphene to be defined in a simple and straightforward manner with minimal extra processing required. Transition metals Fe and Ru can be used interchangeably to predefine the growth regions, and at moderate temperatures (600−700 °C), both will yield high-quality graphene that is robust against subsequent exposure to air. An underlying SiO_2 layer can easily be formed through stepwise intercalation of Si and O_2, in principle yielding oxides with precise thicknesses by controlling the dosage of each of the two constituents. Hence graphene−dielectric−semiconductor heterostructures with tailored and tunable oxide thicknesses can be produced. This simplistic approach is suitable for producing some of the building blocks for graphene-based device applications that rely on a semiconducting substrate/body, such as graphene-based field-effect transistors (GFETs)[57,58] and radiation sensors.[59] Our results thus demonstrate the principle and feasibility of transfer-free growth of graphene on dielectric, which may open up avenues for integrating the techniques presented into the established framework of semiconductor device processing.

■ ASSOCIATED CONTENT

ⓢ Supporting Information

The Supporting Information is available free of charge at https://pubs.acs.org/doi/10.1021/acsami.1c09987.

> Description of the TOC figure, a schematic outlining the growth procedure, and relevant experimental parameters for the results presented; and additional data outlining the Raman analysis, the metal diffusion into SiC, and comparative NEXAFS and XPS core levels from selected stages of the experiment (PDF)

■ AUTHOR INFORMATION

Corresponding Authors

Håkon I. Rost − *Center for Quantum Spintronics, Department of Physics, Norwegian University of Science and Technology (NTNU), NO-7491 Trondheim, Norway;* ● orcid.org/0000-0002-1853-8349; Email: hakon.i.rost@ntnu.no

Simon P. Cooil − *Department of Physics, Aberystwyth University, Aberystwyth SY23 3BZ, United Kingdom; Semiconductor Physics, Department of Physics, University of Oslo (UiO), NO-0371 Oslo, Norway;* ● orcid.org/0000-0002-0856-6020; Email: scooil@icloud.com

Authors

Benjamen P. Reed − *Department of Physics, Aberystwyth University, Aberystwyth SY23 3BZ, United Kingdom; Present Address: National Physical Laboratory (NPL), Hampton Road, Teddington TW11 0LW, U.K.*

Frode S. Strand − *Center for Quantum Spintronics, Department of Physics, Norwegian University of Science and Technology (NTNU), NO-7491 Trondheim, Norway*

Joseph A. Durk − *Department of Physics, Aberystwyth University, Aberystwyth SY23 3BZ, United Kingdom*

D. Andrew Evans − *Department of Physics, Aberystwyth University, Aberystwyth SY23 3BZ, United Kingdom;* ● orcid.org/0000-0002-4566-747X

Antonija Grubišić-Čabo − *School of Physics & Astronomy, Monash University, Clayton, Victoria 3800, Australia; Present Address: KTH Royal Institute of Technology, Applied Physics, Hannes Alfvéns väg 12, SE-114 19 Stockholm, Sweden.;* ● orcid.org/0000-0001-7683-0295

Gary Wan − *School of Physics, HH Wills Physics Laboratory, University of Bristol, Bristol BS8 1TL, United Kingdom;* ● orcid.org/0000-0003-3423-1440

Mattia Cattelan − *School of Chemistry, University of Bristol, Bristol BS8 1TS, United Kingdom; Present Address: Elettra Sincrotrone Trieste, s.s. 14 - km.163,5 in Area Science Park, Basovizza, Trieste 34149, Italy*

Mauricio J. Prieto − *Department of Interface Science, Fritz-Haber-Institute of the Max-Planck Society, 14195 Berlin, Germany;* ● orcid.org/0000-0002-5087-4545

Daniel M. Gottlob − *Department of Interface Science, Fritz-Haber-Institute of the Max-Planck Society, 14195 Berlin, Germany*

Liviu C. Tănase − *Department of Interface Science, Fritz-Haber-Institute of the Max-Planck Society, 14195 Berlin, Germany;* ● orcid.org/0000-0002-4177-5676

Lucas de Souza Caldas − *Department of Interface Science, Fritz-Haber-Institute of the Max-Planck Society, 14195 Berlin, Germany*

Thomas Schmidt − *Department of Interface Science, Fritz-Haber-Institute of the Max-Planck Society, 14195 Berlin, Germany;* ● orcid.org/0000-0003-4389-2080

Anton Tadich − *Australian Synchrotron, Clayton, Victoria 3168, Australia*

Bruce C. C. Cowie − *Australian Synchrotron, Clayton, Victoria 3168, Australia*

Rajesh Kumar Chellappan − *Center for Quantum Spintronics, Department of Physics, Norwegian University of Science and Technology (NTNU), NO-7491 Trondheim, Norway*

Justin W. Wells − *Center for Quantum Spintronics, Department of Physics, Norwegian University of Science and Technology (NTNU), NO-7491 Trondheim, Norway;*

Semiconductor Physics, Department of Physics, University of Oslo (UiO), NO-0371 Oslo, Norway; ● orcid.org/0000-0001-6366-366X

ACKNOWLEDGMENTS

REFERENCES

(1) Novoselov, K. S.; Geim, A. K.; Morozov, S. V.; Jiang, D.; Zhang, Y.; Dubonos, S. V.; Grigorieva, I. V.; Firsov, A. A. Electric Field Effect in Atomically Thin Carbon Films. *Science* **2004**, *306*, 666−669.

(2) Novoselov, K. S.; Jiang, Z.; Zhang, Y.; Morozov, S.; Stormer, H. L.; Zeitler, U.; Maan, J.; Boebinger, G.; Kim, P.; Geim, A. K. Room-Temperature Quantum Hall Effect in Graphene. *Science* **2007**, *315*, 1379.

(3) Yi, M.; Shen, Z. A Review on Mechanical Exfoliation for the Scalable Production of Graphene. *J. Mater. Chem. A* **2015**, *3*, 11700−11715.

(4) Li, X.; Cai, W.; An, J.; Kim, S.; Nah, J.; Yang, D.; Piner, R.; Velamakanni, A.; Jung, I.; Tutuc, E.; Banerjee, S. K.; Colombo, L.; Ruoff, R. S. Large-Area Synthesis of High-Quality and Uniform Graphene Films on Copper Foils. *Science* **2009**, *324*, 1312−1314.

(5) Zhou, H.; Yu, W. J.; Liu, L.; Cheng, R.; Chen, Y.; Huang, X.; Liu, Y.; Wang, Y.; Huang, Y.; Duan, X. Chemical Vapour Deposition Growth of Large Single Crystals of Monolayer and Bilayer Graphene. *Nat. Commun.* **2013**, *4*, No. 2096.

(6) Bekdüz, B.; Kaya, U.; Langer, M.; Mertin, W.; Bacher, G. Direct Growth of Graphene on Ge (100) and Ge (110) via Thermal and Plasma Enhanced CVD. *Sci. Rep.* **2020**, *10*, No. 12938.

(7) Wang, T.; Li, P.; Hu, X.; Gao, M.; Di, Z.; Xue, Z.; Zhang, M. Wafer-Scale Fabrication of Single-Crystal Graphene on Ge(110) Substrate by Optimized CH4/H2 Ratio. *Appl. Surf. Sci.* **2020**, *529*, No. 147066.

(8) Emtsev, K. V.; Bostwick, A.; Horn, K.; Jobst, J.; Kellogg, G. L.; Ley, L.; McChesney, J. L.; Ohta, T.; Reshanov, S. A.; Röhrl, J.; Rotenberg, E.; Schmid, A. K.; Waldmann, D.; Weber, H. B.; Seyller, T. Towards Wafer-Size Graphene Layers by Atmospheric Pressure Graphitization of Silicon Carbide. *Nat. Mater.* **2009**, *8*, 203−207.

(9) First, P. N.; de Heer, W. A.; Seyller, T.; Berger, C.; Stroscio, J. A.; Moon, J.-S. Epitaxial Graphenes on Silicon Carbide. *MRS Bull.* **2010**, *35*, 296−305.

(10) Forti, S.; Emtsev, K. V.; Coletti, C.; Zakharov, A. A.; Riedl, C.; Starke, U. Large-area Homogeneous Quasifree Standing Epitaxial Graphene on SiC(0001): Electronic and Structural Characterization. *Phys. Rev. B* **2011**, *84*, No. 125449.

(11) Wu, Z.-S.; Parvez, K.; Feng, X.; Müllen, K. Photolithographic Fabrication of High-Performance All-Solid-State Graphene-Based Planar Micro-Supercapacitors with Different Interdigital Fingers. *J. Mater. Chem. A* **2014**, *2*, 8288−8293.

(12) Ahlberg, P.; Hinnemo, M.; Song, M.; Gao, X.; Olsson, J.; Zhang, S. L.; Zhang, Z. B. A Two-in-One Process for Reliable Graphene Transistors Processed with Photo-Lithography. *Appl. Phys. Lett.* **2015**, *107*, No. 203104.

(13) Geim, A. K.; Novoselov, K. S. The Rise of Graphene. *Nat. Mater.* **2007**, *6*, 183−191.

(14) Fischbein, M. D.; Drndić, M. Electron Beam Nanosculpting of Suspended Graphene Sheets. *Appl. Phys. Lett.* **2008**, *93*, No. 113107.

(15) Tapasztó, L.; Dobrik, G.; Lambin, P.; Biró, L. P. Tailoring the Atomic Structure of Graphene Nanoribbons by Scanning Tunnelling Microscope Lithography. *Nat. Nanotechnol.* **2008**, *3*, 397−401.

(16) Kim, C.; Park, J.; Seo, Y.; Ahn, J.; Park, I.-S. Nanolithography on Graphene by using Scanning Tunneling Microscopy in a Methanol Environment. *Microsc. Microanal.* **2013**, *19*, 1569−1574.

(17) Singh, R. S.; Nalla, V.; Chen, W.; Wee, A. T. S.; Ji, W. Laser Patterning of Epitaxial Graphene for Schottky Junction Photo-detectors. *ACS Nano* **2011**, *5*, 5969−5975.

(18) Smits, E. C. P.; Walter, A.; de Leeuw, D. M.; Asadi, K. Laser Induced Forward Transfer of Graphene. *Appl. Phys. Lett.* **2017**, *111*, No. 173101.

(19) Binder, J.; Rogoza, J.; Tkachenko, L.; Pasternak, I; Sitek, J.; Strupinski, W.; Zdrojek, M.; Baranowski, J. M.; Stepniewski, R.; Wysmolek, A. Suspended Graphene on Germanium: Selective Local Etching via Laser-Induced Photocorrosion of Germanium. *2D Mater.* **2021**, *8*, No. 035043.

(20) Huang, P. Y.; Ruiz-Vargas, C. S.; Van Der Zande, A. M.; Whitney, W. S.; Levendorf, M. P.; Kevek, J. W.; Garg, S.; Alden, J. S.; Hustedt, C. J.; Zhu, Y.; Park, J.; McEuen, P. L.; Muller, D. A. Grains and Grain Boundaries in Single-Layer Graphene Atomic Patchwork Quilts. *Nature* **2011**, *469*, 389−392.

(21) Zhang, Z.; Du, J.; Zhang, D.; Sun, H.; Yin, L.; Ma, L.; Chen, J.; Ma, D.; Cheng, H.-M.; Ren, W. Rosin-Enabled Ultraclean and Damage-Free Transfer of Graphene for Large-Area Flexible Organic Light-Emitting Diodes. *Nat. Commun.* **2017**, *8*, No. 14560.

(22) Su, C.-Y.; Lu, A.-Y.; Wu, C.-Y.; Li, Y.-T.; Liu, K.-K.; Zhang, W.; Lin, S.-Y.; Juang, Z.-Y.; Zhong, Y.-L.; Chen, F.-R.; Li, L.-J. Direct Formation of Wafer Scale Graphene Thin Layers on Insulating Substrates by Chemical Vapor Deposition. *Nano Lett.* **2011**, *11*, 3612−3616.

(23) Kwak, J.; Chu, J. H.; Choi, J.-K.; Park, S.-D.; Go, H.; Kim, S. Y.; Park, K.; Kim, S.-D.; Kim, Y.-W.; Yoon, E.; Kodambaka, S.; Kwon, S.-Y. Near Room-Temperature Synthesis of Transfer-Free Graphene Films. *Nat. Commun.* **2012**, *3*, No. 645.

(24) Kaur, G.; Kavitha, K.; Lahiri, I. Transfer-Free Graphene Growth on Dielectric Substrates: A Review of the Growth Mechanism. *Crit. Rev. Solid State Mater. Sci.* **2019**, *44*, 157−209.

(25) Shen, K.; Sun, H.; Hu, J.; Hu, J.; Liang, Z.; Li, H.; Zhu, Z.; Huang, Y.; Kong, L.; Wang, Y.; Jiang, Z.; Huang, H.; Wells, J. W.; Song, F. Fabricating Quasi-Free-Standing Graphene on a SiC(0001) Surface by Steerable Intercalation of Iron. *J. Phys. Chem. C* **2018**, *122*, 21484−21492.

(26) Lizzit, S.; Larciprete, R.; Lacovig, P.; Dalmiglio, M.; Orlando, F.; Baraldi, A.; Gammelgaard, L.; Barreto, L.; Bianchi, M.; Perkins, E.; Hofmann, P. Transfer-Free Electrical Insulation of Epitaxial Graphene from its Metal Substrate. *Nano Lett.* **2012**, *12*, 4503−4507.

(27) Zhou, S. Y.; Gweon, G. H.; Fedorov, A. V.; First, P. N.; de Heer, W. A.; Lee, D. H.; Guinea, F.; Castro Neto, A. H.; Lanzara, A. Substrate-Induced Bandgap Opening in Epitaxial Graphene. *Nat. Mater.* 2007, 6, 770−775.

(28) Khomyakov, P. A.; Giovannetti, G.; Rusu, P. C.; Brocks, G.; van den Brink, J.; Kelly, P. J. First-Principles Study of the Interaction and Charge Transfer between Graphene and Metals. *Phys. Rev. B* 2009, 79, No. 195425.

(29) Giovannetti, G.; Khomyakov, P. A.; Brocks, G.; Karpan, V. M.; van den Brink, J.; Kelly, P. J. Doping Graphene with Metal Contacts. *Phys. Rev. Lett.* 2008, 101, No. 026803.

(30) Larciprete, R.; Ulstrup, S.; Lacovig, P.; Dalmiglio, M.; Bianchi, M.; Mazzola, F.; Hornekær, L.; Orlando, F.; Baraldi, A.; Hofmann, P.; Lizzit, S. Oxygen Switching of the Epitaxial Graphene-Metal Interaction. *ACS Nano* 2012, 6, 9551−9558.

(31) Cooil, S.; Song, F.; Williams, G.; Roberts, O.; Langstaff, D.; Jørgensen, B.; Høydalsvik, K.; Breiby, D.; Wahlström, E.; Evans, D.; Wells, J. Iron-Mediated Growth of Epitaxial Graphene on SiC and Diamond. *Carbon* 2012, 50, 5099−5105.

(32) Røst, H. I.; Chellappan, R. K.; Strand, F. S.; Grubišić-Čabo, A.; Reed, B. P.; Prieto, M. J.; Tănase, L. C.; Caldas, L. dS.; Wongpinij, T.; Euaruksakul, C.; Schmidt, T.; Tadich, A.; Cowie, B. C. C.; Li, Z.; Cooil, S. P.; Wells, J. W. Low-Temperature Growth of Graphene on a Semiconductor. *J. Phys. Chem. C* 2021, 125, 4243−4252.

(33) Malard, L.; Pimenta, M.; Dresselhaus, G.; Dresselhaus, M. Raman Spectroscopy in Graphene. *Phys. Rep.* 2009, 473, 51−87.

(34) Emtsev, K.; Speck, F.; Seyller, T.; Ley, L.; Riley, J. D. Interaction, Growth, and Ordering of Epitaxial Graphene on SiC {0001} Surfaces: A Comparative Photoelectron Spectroscopy Study. *Phys. Rev. B* 2008, 77, No. 155303.

(35) Cooil, S.; Wells, J.; Hu, D.; Niu, Y.; Zakharov, A.; Bianchi, M.; Evans, D. Controlling the Growth of Epitaxial Graphene on Metalized Diamond (111) Surface. *Appl. Phys. Lett.* 2015, 107, No. 181603.

(36) Ohta, T.; Bostwick, A.; Seyller, T.; Horn, K.; Rotenberg, E. Controlling the Electronic Structure of Bilayer Graphene. *Science* 2006, 313, 951−954.

(37) Allmers, T.; Donath, M. Growth and Morphology of Thin Fe Films on Flat and Vicinal Au (111): A Comparative Study. *New J. Phys.* 2009, 11, No. 103049.

(38) Cooil, S. Controlling the Growth of Graphene on Diamond Substrates, Ph.D. thesis. Aberystwyth University, 2014.

(39) Jesson, D.; Tang, W.-X. *Surface Electron Microscopy of Ga Droplet Dynamics on GaAs (001)*; Microscopy: Science, Technology, Applications and Education: Badajoz, Spain: Formatex, 2010; Vol. 4, p 11.

(40) Bailly, A.; Renault, O.; Barrett, N.; Desrues, T.; Mariolle, D.; Zagonel, L. F.; Escher, M. Aspects of Lateral Resolution in Energy-Filtered Core Level Photoelectron Emission Microscopy. *J. Phys.: Condens. Matter* 2009, 21, No. 314002.

(41) Cooil, S. P.; Mazzola, F.; Klemm, H. W.; Peschel, G.; Niu, Y. R.; Zakharov, A. A.; Simmons, M. Y.; Schmidt, T.; Evans, D. A.; Miwa, J. A.; Wells, J. W. In Situ Patterning of Ultrasharp Dopant Profiles in Silicon. *ACS Nano* 2017, 11, 1683−1688.

(42) Melios, C.; Panchal, V.; Giusca, C. E.; Strupiński, W.; Silva, S. R. P.; Kazakova, O. Carrier Type Inversion in Quasi-Free Standing Graphene: Studies of Local Electronic and Structural Properties. *Sci. Rep.* 2015, 5, No. 10505.

(43) Hassan, J.; Winters, M.; Ivanov, I.; Habibpour, O.; Zirath, H.; Rorsman, N.; Janzén, E. Quasi-Free-Standing Monolayer and Bilayer Graphene Growth on Homoepitaxial On-Axis 4H-SiC (0001) Layers. *Carbon* 2015, 82, 12−23.

(44) Melios, C.; Spencer, S.; Shard, A.; Strupiński, W.; Silva, S. R. P.; Kazakova, O. Surface and Interface Structure of Quasi-Free Standing Graphene on SiC. *2D Mater* 2016, 3, No. 025023.

(45) Lauritsen, J. V.; Nyberg, M.; Vang, R. T.; Bollinger, M. V.; Clausen, B. S.; Topsøe, H.; Jacobsen, K. W.; gsgaard, E. L.; Nørskov, J. K.; Besenbacher, F. Chemistry of One-Dimensional Metallic Edge States in MoS₂ Nanoclusters. *Nanotechnology* 2003, 14, 385−389.

(46) Dedkov, Y. S.; Fonin, M.; Laubschat, C. A Possible Source of Spin-Polarized Electrons: The Inert Graphene/Ni (111) System. *Appl. Phys. Lett.* 2008, 92, No. 052506.

(47) Podila, R.; Moore, T.; Alexis, F.; Rao, A. M. Graphene Coatings for Enhanced Hemo-Compatibility of Nitinol Stents. *RSC Adv.* 2013, 3, 1660−1665.

(48) Liao, L.; Peng, H.; Liu, Z. Chemistry Makes Graphene beyond Graphene. *J. Am. Chem. Soc.* 2014, 136, 12194−12200.

(49) Astašauskas, V.; Bellissimo, A.; Kuksa, P.; Tomastik, C.; Kalbe, H.; Werner, W. S. Optical and Electronic Properties of Amorphous Silicon Dioxide by Single and Double Electron Spectroscopy. *J. Electron Spectros. Relat. Phenomena* 2020, 241, No. 146829.

(50) Thøgersen, A.; Selj, J. H.; Marstein, E. S. Oxidation Effects on Graded Porous Silicon Anti-Reflection Coatings. *J. Electrochem. Soc.* 2012, 159, D276.

(51) Hollinger, G.; Himpsel, F. Probing the Transition Layer at the SiO₂-Si Interface using Core Level Photoemission. *Appl. Phys. Lett.* 1984, 44, 93−95.

(52) Watanabe, H.; Hosoi, T.; Kirino, T.; Kagei, Y.; Uenishi, Y.; Chanthaphan, A.; Yoshigoe, A.; Teraoka, Y.; Shimura, T. Synchrotron X-Ray Photoelectron Spectroscopy Study on Thermally Grown SiO₂/ 4H-SiC (0001) Interface and its Correlation with Electrical Properties. *Appl. Phys. Lett.* 2011, 99, No. 021907.

(53) Nakao, A.; Iwaki, M.; Sakairi, H.; Terasima, K. XPS Characterization of Nitrogen Implanted Silicon Carbide. *Nucl. Instrum. Methods Phys. Res., B* 1992, 65, 352−356.

(54) Wang, Y.-Y.; Kusumoto, K.; Li, C.-J. XPS Analysis of SiC Films Prepared by Radio Frequency Plasma Sputtering. *Phys. Procedia* 2012, 32, 95−102.

(55) Johansson, L.; Owman, F.; Mårtensson, P.; Persson, C.; Lindefelt, U. Electronic Structure of 6H-SiC(0001). *Phys. Rev. B* 1996, 53, 13803.

(56) Simon, L.; Kubler, L.; Ermolieff, A.; Billon, T. X-Ray Spectroscopy of the Oxidation of 6H-SiC (0001). *Phys. Rev. B* 1999, 60, 5673.

(57) Lin, Y.; Chiu, H.; Jenkins, K. A.; Farmer, D. B.; Avouris, P.; Valdes-Garcia, A. Dual-Gate Graphene FETs with f_T of 50 GHz. *IEEE Electron Device Lett.* 2010, 31, 68−70.

(58) Lin, Y.-M.; Dimitrakopoulos, C.; Jenkins, K. A.; Farmer, D. B.; Chiu, H.-Y.; Grill, A.; Avouris, P. 100-GHz Transistors from Wafer-Scale Epitaxial Graphene. *Science* 2010, 327, 662.

(59) Foxe, M.; Lopez, G.; Childres, I.; Jalilian, R.; Patil, A.; Roecker, C.; Boguski, J.; Jovanovic, I.; Chen, Y. P. Graphene Field-Effect Transistors on Undoped Semiconductor Substrates for Radiation Detection. *IEEE Trans. Nanotechnol.* 2012, 11, 581−587.

Chapter 5

Electron-Phonon Interactions

In an ordered solid-state system, one of the fundamental ways it can store and transfer energy is through the collective, elastic excitations of its constituent atoms away from their equilibrium positions. When such excitations form vibrational modes with well-defined frequencies and wavelengths, they can be treated as delocalized, wave-like energy excitations of the system. In a quantum mechanical description, only specific and discrete vibrational frequencies ω for the atoms will be permitted. The allowed vibrations act as delocalized quasiparticles, or *phonons*, with quantized energies defined by these elementary vibrational frequencies. Phonons transmit sound, heat, and light waves through matter. They are thus essential ingredients that determine material properties like heat capacity, and thermal and electrical conductivity [106, 107]. Since phonons readily interact with other degrees of freedom, they play a crucial role in several phenomena concerning many-body interactions. Notably, they can interact with electrons to form Cooper pairs, sustaining superconductivity in the weak coupling regime [108]. They are also suggested participants in high-temperature superconductivity [109].

In this Chapter, the interactions of electrons and phonons are discussed. Some of the relevant properties of phonons are summarized in Section 5.1, before coupling to electrons is discussed in Section 5.2. A familiar and well-studied candidate material for phonon-mediated superconductivity is the topic of Section 5.3.1. Finally, an alternative candidate is presented in Section 5.3.2 and further studied in Paper [3].

5.1   Phonon Excitations

Establishing the detailed properties of phonons in real, two- and three-dimensional systems can be an elaborate task. However, much of the physics can already be explored from relatively simple, classical models of one-dimensional atomic chains. The intention here is merely to outline some of the properties of phonons relevant for the subsequent discussions of electron-phonon interactions. For a more thorough treatment of phonons in general, the reader is referred to standard introductory textbooks on condensed matter, such as, e.g., Ashcroft & Mermin's 'Solid State Physics' [110], or Kittel's 'Quantum Theory of Solids' [111].

To illustrate the behavior of lattice vibrational excitations, consider a simple diatomic chain of N atoms separated by an equilibrium distance a. Atoms of unequal mass m and M occupy every second lattice site, i.e., they reside on two different sublattices A and B with $n/2$ atoms each. This situation is sketched in Fig. 5.1a.

Each atom on the chain is held in place by an elastic restoring force with spring constant K. The system is thus comprised of a chain of interconnected harmonic oscillators; consequentially, atomic displacements away from the equilibrium positions will lead to an increase in potential energy. Considering only nearest-neighbor interactions for the different atoms A and B, their equations of motion are [112]:

$$m\ddot{u}_{2n} = -K(2u_{2n} - u_{2n-1} - u_{2n+1}), \tag{5.1}$$

$$M\ddot{u}_{2n+1} = -K(2u_{2n+1} - u_{2n} - u_{2n+2}). \tag{5.2}$$

Here, the terms u_l denote the atomic positions along the chain, e.g., $u_l = u_{2n} = 2na$. The index $n \in \{0, \ldots, N/2\} \cap \mathbb{Z}$ and periodic boundary conditions are assumed so that $u_{N+1} = u_0$, as sketched in Fig. 5.1b. Solutions to these equations are waves of the form

$$u_{2n} = Ae^{-i(k2na+\omega t)}, \qquad u_{2n+1} = Be^{-i(k2na+\omega t)}, \tag{5.3}$$

where the A and B are displacement amplitudes for the two sub-lattices, and the wave number $k \in \left[-\pi/2a, \pi/2a\right)$ is restricted to half of the 1st Brillouin zone (BZ). Inserting the solutions from Eq. 5.3 into the equations of motion (Eqs. 5.1, 5.2) and solving to the angular frequency ω as a function of k yields the phonon *dispersion relations* [112]:

$$\omega^2 = \frac{K}{mM}\left[m + M \pm \sqrt{(m-M)^2 + 4mM\cos^2 ka}\right]. \tag{5.4}$$
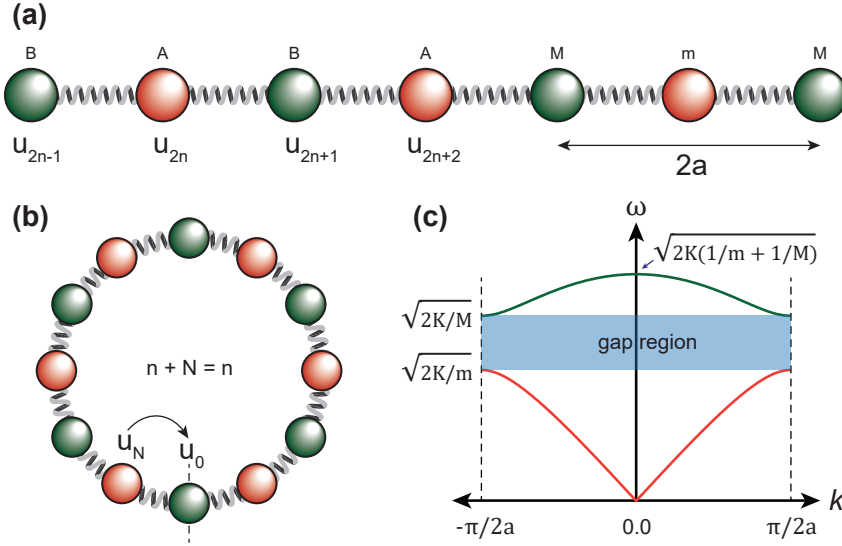
Figure 5.1: Phonon dispersions from a simple, diatomic 1D chain of atoms with periodic boundary conditions. **(a)**: Atoms of two sub-lattices A and B, interacting with their nearest neighbors via elastic restoring forces. All atoms have a separation a, and the constituent atoms of each sub-lattice are separated by $2a$. **(b)**: A visualization of periodic boundary conditions for the 1D atomic chain. **(c)**: Two distinct phonon dispersion relations $\omega(k)$ for a diatomic chain of atoms. The lower and higher energy branches are from the acoustic and optical phonon modes, respectively.

Eq. 5.4 describes two unequal dispersions, separated in energy throughout the full and reduced BZ. These are plotted together in Fig. 5.1c. At $k = \pm\pi/2a$, the energy gap between the two becomes

$$\hbar(\omega_+ - \omega_-) = \hbar\sqrt{2K}\left|\frac{\sqrt{M} - \sqrt{M}}{\sqrt{mM}}\right|, \tag{5.5}$$

i.e., the gap closes at the reduced zone boundary if $m \to M$ or vice versa. In Eq. 5.5, $\hbar$ is the reduced Planck's constant.

The two ω_+ and ω_- are commonly referred to as the *optical* and *acoustic* branches of the phonon dispersion, respectively. Their names can be related to their respective behavior in the long-wavelength limit. As $k \to 0$, the acoustic branch assumes the form $\omega_+ \propto k$, and the oscillating atoms of A and B move in phase with each other. This behavior is characteristic

67

of sound/acoustic waves. Conversely, for ω_+ the atoms of A and B will move out of phase with each other as $k \to 0$. If the two sub-lattices carry different charges, their out-of-phase movement will create an electric dipole with oscillation frequency ω_+. This behavior is commonly associated with the emission or absorption of electromagnetic waves, hence the name *optical* phonons [110].

In a quantum mechanical description, the oscillation of atoms in the 1D chain discussed so far can be described as a set of decoupled harmonic oscillators. The full energy of the N-atom system can be described by the Hamiltonian

$$\hat{H} = \sum_{l \neq 0} \left(\hat{a}_l^\dagger \hat{a}_l + \frac{1}{2} \right) \hbar \omega_l, \tag{5.6}$$

where $l \in (N/2, \ldots, N/2)$, and $\hat{a}_l^\dagger$ and $\hat{a}_l$ are bosonic creation and annihilation operators, respectively [112]. The number operator $\hat{n} \equiv \hat{a}_l^\dagger \hat{a}_l$ describes the total number of bosonic excitations in the system, each contributing an energy quantum $\hbar \omega_l$ to the total at a given oscillation frequency ω_l.

Furthermore, since phonons are bosons, their number occupancy $\hat{n} \approx \langle n \rangle$ can be described by Bose-Einstein statistics [113]. I.e., for a given oscillation frequency ω_l, the occupancy of excited phonons at a temperature T is

$$\langle n \rangle = \frac{1}{e^{\hbar \omega_l / k_B T} - 1}, \tag{5.7}$$

and the total phonon energy is consequently $E_l = (\langle n \rangle + 1/2)\hbar \omega_l$, as given by Eq. 5.6.

Finally, suppose the above discussion is extended to a three-dimensional crystal. In that case, the phonon excitation spectrum will consist of $3s$ different branches, where s is the number of atoms or ions in the primitive unit cell. Three of these branches will be *acoustic* phonons, while the remaining $3s - 3$ are optical phonon modes with finite frequencies where $k \to 0$ [111].

5.2 Electron-Phonon Interactions

While the properties of phonons can be interesting in their own right, arguably even more exotic phenomena can be achieved when they interact with other bosons and fermions to form *quasiparticles*. The interaction between electrons and phonons is particularly intriguing, being the driving mechanism behind the effective electron-electron attraction in conventional

superconductivity [108]. Next, the pairing mechanism between electrons and phonons is discussed, based on some of the concepts explained in Refs. [34, 107, 114].

5.2.1 Calculating the Electron-Phonon Interaction Strength

Consider the scattering of an electron in a crystal from an initial state $|\eta\rangle$ to an unoccupied final state $|\eta'\rangle$. Such excitations typically involve the transfer of energy and quasimomentum (i.e., $\mathbf{k}$). If the system in question forms a microcanonical ensemble, the crystal lattice and its constituent atoms and electrons can exchange energy, but the system's total energy is conserved. At finite temperatures, phonons will exist and propagate through the medium. These can interact with the electrons and scatter them from one state to another.

Given the total energy conservation, an increase in electron energy when scattered means the phonon it interacted with should be annihilated. In the opposite case, an electron energy reduction comes from generating a new phonon. Such inter-band scattering by phonon absorption and emission is sketched in Fig. 5.2.

The process of electron-phonon scattering is characterized by a Hamiltonian

$$\hat{H}_{\text{el-ph}} = \sum_{\mathbf{k}\sigma} \sum_{\mathbf{q},\nu} g^{\eta\eta',\nu}_{\mathbf{k},\mathbf{k}+\mathbf{q}} \left(\hat{a}_{\mathbf{q}\nu} + \hat{a}^{\dagger}_{-\mathbf{q},\nu} \right) \hat{c}^{\dagger}_{\mathbf{k}+\mathbf{q},\eta'\sigma} \hat{c}_{\mathbf{k},\eta\sigma}. \tag{5.8}$$

Here, $\left\{ \hat{c}^{\dagger}, \hat{c} \right\}$ and $\left\{ \hat{a}^{\dagger}, \hat{a} \right\}$ are creation and annihilation operators for electrons and phonons, respectively, while $\mathbf{k}$ and $\mathbf{q}$ are their associated quasi-momentum wave vectors. Furthermore, ν denote the phonon modes and σ represents electron spin ($\pm\hbar/2$). The terms $g^{\eta\eta',\nu}_{\mathbf{k},\mathbf{k}+\mathbf{q}}$ describe the scattering probabilities of an electron with wave vector $\mathbf{k}$ in state $|\eta\rangle$ to a final state $|\eta'\rangle$ at $\mathbf{k} + \mathbf{q}$, either by absorbing or emitting a phonon from mode ν. When these are known, they can be used to estimate the complex self-energy terms Σ_{ph} associated with their corresponding electron-phonon interactions. Chapter 7.3 shows how to estimate Σ from a similar electron-boson interaction using Green's functions and Matsubara formalism[1]. Here, we instead show how Σ_{ph} can be estimated using Eliashberg theory [115].

The so-called 'Eliashberg function' for an electron with wave vector $\mathbf{k}$ in

---

[1]This can, of course, be done for electron-phonon interactions as well. A decent summary is given by B. Hellsing *et al.* in Ref. [114].
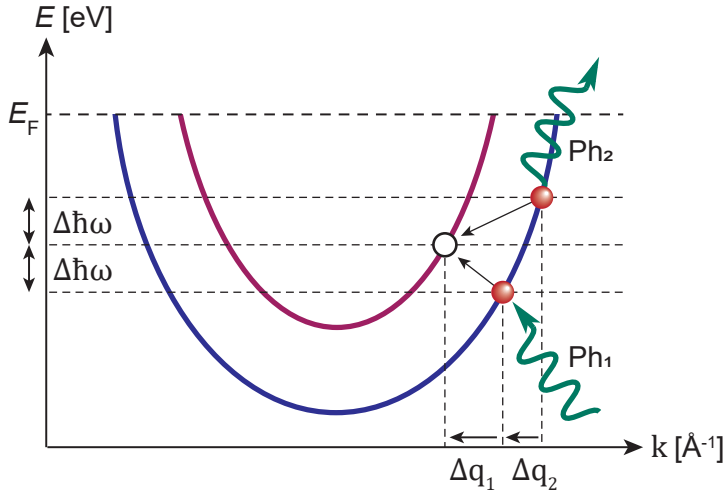
Figure 5.2: Inter-band phonon scattering of electrons into an empty final state. In the case of phonon absorption (Ph_1), the electron's energy is increased by $\Delta\hbar\omega$. With phonon emission (Ph_2), the electron energy is reduced by $\Delta\hbar\omega$.

an initial state $|\eta\rangle$ is [34]:

$$\alpha^2 F_{\mathbf{k}}^{\mathrm{E(A)}}(\omega) = \sum_{\mathbf{q},\nu,\eta'} \left| g_{\mathbf{k},\mathbf{k+q}}^{\eta\eta',\nu} \right|^2 \delta(\omega - \omega_{\mathbf{q}\nu}) \delta\big(\varepsilon_{\eta'} - \varepsilon_\eta \mp \hbar\omega_{\mathbf{q}\nu}\big), \qquad (5.9)$$

and describes the phonon density of states weighted by the electron-phonon interaction terms. The sum runs over all electronic final states $|\eta'\rangle$ and phonon modes $(\mathbf{q}, \nu)$. The signs '$-$' and '$+$' in the last Kronecker delta correspond to phonon emission and absorption, respectively.

From the Eliashberg emission (E) and absorption (A) terms in Eq. 5.9, the mass enhancement parameter λ_{ph} of the electron-phonon coupling can be calculated. Spectroscopically, λ_{ph} is often interpreted as the dimensionless electron-phonon coupling strength. Assuming the phonon energies to be much smaller than the electron energies[2], the $\mp\omega_{\mathbf{q}\nu}$ can be ignored and $\alpha^2 F_{\mathbf{k}}^{\mathrm{E}}(\omega) \approx \alpha^2 F_{\mathbf{k}}^{\mathrm{A}}(\omega)$. From this 'quasielastic' approximation, one can use the same Eliashberg function to describe both emission and absorption processes. The coupling strength is then the reciprocal moment of the sum of

---

[2]Electrons in a crystal typically have energies on the order of eV, while the energies of the maximum (i.e., Debye) frequency phonons are typically in the meV range [34].

Eliashberg terms:

$$\lambda_{\mathrm{ph}}(\mathbf{k}, \varepsilon_\eta) \approx 2 \int_0^{\omega_{\mathrm{max}}} \frac{\alpha^2 F_{\mathbf{k}}(\omega')}{\omega'} \mathrm{d}\omega'. \tag{5.10}$$

As will be further discussed in the next Section (5.2.2), electron-phonon interactions with finite λ_{ph} will induce renormalizations to 'ideal', one-particle band structures. The changes can be related to the real and imaginary parts of Σ_{ph}, both of which can be determined from the Eliashberg function. Using the quasielastic approximation described above, $\mathrm{Im}\,\Sigma_{\mathrm{ph}}$ can be written as an integral over all phonon scattering events that conserve energy and quasimomentum [107]:

$$\mathrm{Im}\,\Sigma_{\mathrm{ph}}(\mathbf{k}, \omega, T) = \pi \int_0^{\omega_{\mathrm{max}}} \alpha^2 F_{\mathbf{k}}(\omega') \big[1 + 2n(\omega', T)$$
$$+ f(\omega - \omega', T) + f(\omega + \omega', T) \big] \mathrm{d}\omega', \tag{5.11}$$

where $n(\omega, T)$ and $f(\omega, T)$ are Bose-Einstein and Fermi-Dirac distributions, respectively, and ω_{max} is the maximum phonon frequency in the system. Note how the temperature T dependence of $\mathrm{Im}\,\Sigma_{\mathrm{ph}}$ is purely in the distribution functions.

For the limit $T \to 0$, the expression in Eq. 5.11 will reduce to

$$\mathrm{Im}\,\Sigma_{\mathrm{ph}}(\mathbf{k}, \omega, T) = \pi \int_0^{\omega_{\mathrm{max}}} \alpha^2 F_{\mathbf{k}}(\omega') \mathrm{d}\omega'. \tag{5.12}$$

Similarly, in the high-temperature limit ($k_{\mathrm{B}}T \gg \hbar\omega_{\mathrm{max}}$), $\mathrm{Im}\,\Sigma_{\mathrm{ph}}$ can be reduced to [107]:

$$\mathrm{Im}\,\Sigma_{\mathrm{ph}}(\mathbf{k}, \omega, T) \approx \pi\lambda_{\mathrm{ph}}k_{\mathrm{B}}T. \tag{5.13}$$

Finally, the real part of the self-energy $\mathrm{Re}\,\Sigma_{\mathrm{ph}}$ can be obtained from Eqs. 5.11-5.13 via a Kramers-Kronig transformation since the two components are causally related[3] [106]. Next, the practical meaning of Σ and how it manifests in ARPES measurements will be explained.

---

[3]The Green's function $G(\mathbf{k}, \omega)$ of the interaction – whose imaginary part is proportional to the spectral function $\mathcal{A}(\mathbf{k}, \omega)$ (Eq. 2.14), is a linear response to an external perturbation and must therefore satisfy causality. Then by definition, its real and imaginary parts can be related by Kramers-Kronig relations. From $\mathcal{A}(\mathbf{k}, \omega)$ the real and imaginary terms of Σ can be estimated directly.

5.2.2 Measuring Electron-Phonon Coupling from ARPES

Experimentally, advances in instrumentation over the last 20 years (in particular) have allowed interactions between phonons and electrons to be studied with unprecedented detail. Particularly, the coupling strengths λ_{ph}, and also the energy and $\mathbf{k}$ dependencies of electron-phonon interactions can be readily determined from spectroscopic and diffractive measurements using ARPES (see Chpt. 2.3.1) and helium atom scattering (HAS), respectively [17, 28, 47]. Next, we will focus on how these parameters can be extracted from ARPES data. A decent review of how λ_{ph} can be extracted from HAS is found in Ref. [28].

In simple terms, electron-phonon interactions will modify the effective mass m^* and lifetime τ of the occupied electronic states in a system. In an ARPES measurement this manifests itself as an energy *renormalization* of the ideal, non-interacting bandstructure [47]. The situation is illustrated in Figure 5.3a. At binding energies close to the Fermi level ($E_B - E_F < 20\,\text{meV}$) the gradient of the band dispersion is altered, and consequentially the band appears 'flatter'. This corresponds to an increase in effective mass $m^* \propto (\mathrm{d}\varepsilon/\mathrm{d}k)^{-1}$, where the magnitude of the increase is given by

$$m^* = m_0(1 + \lambda_{ph}). \tag{5.14}$$

Here, m_0 is the electron mass without the phonon interaction and λ_{ph} is the mass enhancement parameter from Eq. 5.10. In the vicinity of the phonon coupling energy $\hbar\omega_D - E_F = 40\,\text{meV}$ the band also appears broadened in the energy direction. Both the energy deviation from the ideal band and the broadening can be accounted for by a change in quasiparticle self-energy Σ from the interactions with phonons.

The self-energy Σ consist of a real and an imaginary part:

$$\mathrm{Re}\,\Sigma = E(\mathbf{k}) - \varepsilon(\mathbf{k}), \tag{5.15}$$

$$\mathrm{Im}\,\Sigma = \frac{\hbar}{2\tau}, \tag{5.16}$$

where $E(\mathbf{k})$ and $\varepsilon(\mathbf{k})$ are the renormalized and ideal energy band dispersions, respectively [34]. Both components of Σ can be extracted from a measured ARPES signal $I(\mathbf{k}, \omega) \propto \mathcal{A}(\mathbf{k}, \omega)$ (see Chapter 2.3.1 for details). Furthermore, one can also be determined from the other using a Kramers-Kronig transformation [106]. The real and imaginary self-energy contributions for a phonon with $\hbar\omega_D = 40\,\text{meV}$ and $\lambda = 0.42$ are shown in Fig. 5.3b.
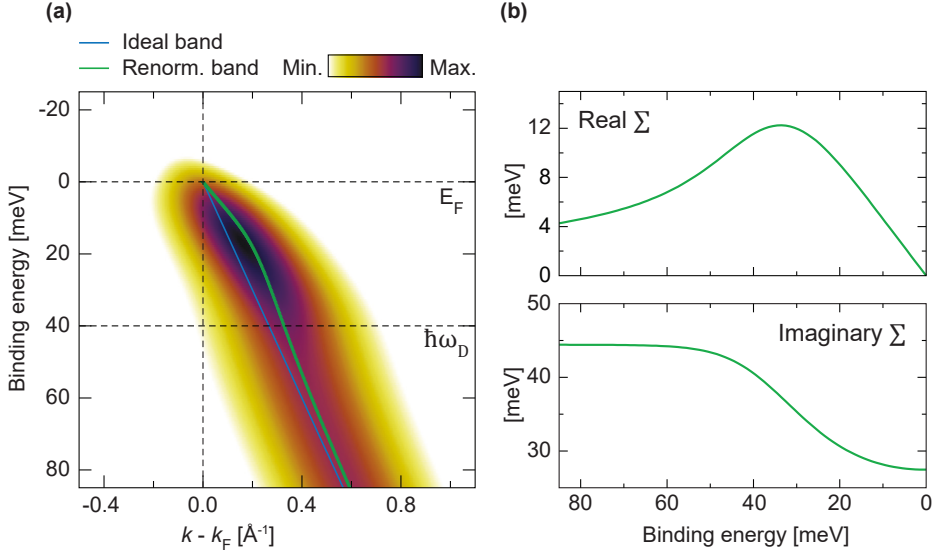
Figure 5.3: Energy renormalization near the Fermi level due to electron-phonon interactions. **(a)**: A simulated ARPES spectrum for a near-linear electron band at $T = 70$ K. The linear solid line (blue) represents the band-structure without phonon interactions, while the dotted line (green) represents the renormalized bandstructure with $\hbar\omega_D = 40$ meV and $\lambda = 0.42$. The two-dimensional simulation has been broadened by instrumental resolutions $\Delta E = 5$ meV and $\Delta k = 0.005$ Å^{-1}. **(b)**: The real and imaginary contributions to the self-energy Σ for the simulated coupling. All input values for the simulations have been based on those of the electron-phonon coupling in Mo(110) reported by T. Valla *et al.* [46].

Next, some practical aspects of extracting self-energies from ARPES measurements are discussed, and a few relevant relations are defined. From a two-dimensional ARPES plot like the one shown in Fig. 5.3a, one can extract linear cuts of the measured photoemission signal parallel to either the energy or quasimomentum axis. The former describes the photoemission intensity at a fixed emission angle θ as a function of kinetic energy and is known as an *energy distribution curve* (EDC)[4]. The latter gives photoemission intensity at constant kinetic energy as a function of θ (or $\mathbf{k}_{||}$, see Eq. 3.3) and is

---

[4]For a constant photon energy $h\nu$, each binding energy correspond to a different kinetic energy by $E_B = h\nu - E_K - \phi_S$ (Eq. 2.6).

known as a *momentum distribution curve* (MDC). By extracting a set of either EDCs or MDCs one can thus obtain the spectral function for the renormalized band as a function of either E_K, θ or $\mathbf{k}_{||}$, if the photoemission matrix elements are assumed to be constant over the range [34, 47, 116].

If also the momentum dependence of Σ is negligible, e.g., when a narrow range of $\mathbf{k}$ is measured, the spectral function as a function of energy takes on a relatively simple Lorentzian shape [117]. For a given temperature T, Eq. 2.14 (Chapter 2.3.1) simplifies to

$$\mathcal{A}(\omega) = \frac{\pi^{-1} \operatorname{Im} \Sigma(\omega)}{[\hbar\omega - \varepsilon(\mathbf{k}) - \operatorname{Re} \Sigma(\omega)]^2 + [\operatorname{Im} \Sigma(\omega)]^2}. \tag{5.17}$$

Eq. 5.17 states that the measured, renormalized energy dispersion will peak in intensity where $\hbar\omega - \varepsilon(\mathbf{k}) - \operatorname{Re} \Sigma(\omega) = 0$. If $\hbar\omega$ is the measured energy, then the $\hbar\omega$ vs. $\mathbf{k}$ position of maximum intensity is the same as the energy expressed in Eq. 5.15. Hence a way to obtain $\operatorname{Re} \Sigma$ from ARPES MDCs is provided if $\varepsilon(\mathbf{k})$ is known. Furthermore, each MDC line shape has a full width at half maximum (FWHM) of $2|\operatorname{Im} \Sigma|$. A perhaps even more practical re-write of $\operatorname{Im} \Sigma$ is

$$\operatorname{Im} \Sigma = |\mathrm{d}\varepsilon/\mathrm{d}k| \Delta k, \tag{5.18}$$

where $\mathrm{d}\varepsilon/\mathrm{d}k$ is the gradient of the energy dispersion and Δk is the measured half-width of the peak [118, 119]. Assuming that the ideal one-particle energy dispersion $\varepsilon(\mathbf{k})$ is known, both components of the self-energy can then be obtained directly from measurements of the ARPES peak position and linewidth. If $\varepsilon(\mathbf{k})$ is not known, it can be obtained by exploiting the self-consistency of $\operatorname{Re} \Sigma$ and $\operatorname{Im} \Sigma$ through the Kramers-Kronig transform. By postulating an initial guess for the one-particle band, one can evaluate the discrepancy between the measured terms from Eqs. 5.15, 5.18, and those obtained by transforming one into the other. The band suggestion can then be adjusted until convergence between the measured and transformed Σ values is reached [48, 120].

Finally, note that in some cases, Σ is better to be evaluated from the linewidth of EDCs. This is typically where $|\mathrm{d}\Sigma/\mathrm{d}k| \ll |\mathrm{d}\Sigma/\mathrm{d}\omega|$, e.g., near the maximum of a band that disperses nearly parallel to the Fermi surface [117]. In such cases, the ω dependencies in Eq. 5.17 is swapped with $\mathbf{k}$, so that each measured EDC linewidth should correspond to $2|\operatorname{Im} \Sigma|$ directly. Note, however, that since ARPES is measured at constant θ and $|\mathbf{k}| \propto \sqrt{E_K} \sin \theta$ (Eq. 3.3), $\mathbf{k}$ is usually not constant over the measured range of energies in an EDC [34]. Care must therefore be taken when extracting

self-energy values from EDCs, e.g., by evaluating only a narrow range where $\sqrt{E_K}\sin\theta$ can be assumed constant. For a more in-depth discussion, see for instance Refs. [116, 117, 121, 122].

5.3 Coupling in Hexagonal 2D Materials

While conventional, BCS superconductivity is typically a property of bulk-like elementary metals, a variety of similarly related, exotic physical phenomena that can also exist in two dimensions [123]. In the following, we present and discuss two different two-dimensional, hexagonal van der Waals (vdW) materials that have been deemed promising for superconductivity in 'reduced' dimensions.

5.3.1 Graphene: Strong Coupling at Large Binding Energies

Shortly after its experimental realization, predictions of potential super-conductivity in few-layer graphene sheets began to circulate. Around the same time, high-quality superconducting YbC_6 and CaC_6 had been grown by intercalating bulk graphite with rare-earth and alkali metal atoms, respectively. Therefore, the origin of the observed superconducting phase was a hot discussion topic [124–127]. Attention was soon then directed towards graphite's two-dimensional counterpart. In the years that followed, extensive experimental progress was made in realizing superconducting few-layer graphene intercalation compounds [128–131].

Much of the appeal behind graphene as a potential superconductor lies in its unique structural and electronic properties [63]. First, graphene has unusually small sheet resistivity, and its near-E_F electrons act like massless Dirac fermions moving at near light speed. Low intrinsic resistivity, i.e., negligible impurity scattering, and mobile electrons are some of the key ingredients needed to stabilize superconductivity. As outlined in Chapter 4.2, it is now reasonably straightforward to produce graphene sheets of extremely high crystalline quality, ensuring nearly perfect atomic ordering over several micrometers.

Secondly, the electron occupation of graphene can be modified relatively easily, e.g., by doping or proximity field effects [132, 133]. While applying strong external fields is typically not considered ideal for superconductivity, charge-transfer doping from the placement ad-atoms above or in between graphene layers can readily redistribute electrons at the Fermi surface [128,

134, 135]. Particularly at high doping levels, the electron state occupation of graphene can be pushed towards the van Hove (vH) singularity of the π- or π^*-band. In this regime, the $\mathbf{k}$ space scattering area of states available at the Fermi surface for electron pairing will increase dramatically. As a result, strong renormalization of the graphene band structure occurs, and concomitant superconductivity has been postulated [136–138].

Besides a plentiful distribution of nearly-free electrons and available scattering final states, the final and equally important ingredient for superconductivity is a reasonable distribution of 'propagators' that will allow the electrons to form attractive Cooper pairs. In the case of graphite superconductors, the primary mediators of such pairing are phonons [127, 129]. Quite surprisingly [68, 69] – and nonetheless, controversial [139], an unusually strong electron-phonon coupling has been observed beyond the graphene π-band vH singularity near its σ-band maxima. The observed coupling strength λ is approximately one order of magnitude higher than the one reported from the π-band [49]. If such strong enough doping could be achieved so that the σ-bands could cross E_{F}, phonon-mediated superconductivity with unusually high critical temperatures should, in principle, occur [69]. On the other hand, such extreme doping levels are somewhat questionable with respect to the chemical stability of the graphene sheets. From a simple argument of electron filling, this would require a complete emptying of the carbon p orbitals, leaving each atom with only three electrons to bond with its neighbors.

5.3.2   Hexagonal Boron Nitride: The Realistic Alternative

Another interesting yet less explored candidate for low-dimensional superconductivity is hexagonal Boron Nitride (hBN). It is strikingly similar to graphene, both in structure and Debye frequency [140, 141]. Like graphene, hBN is comprised of two substituent honeycomb lattices: one occupied by boron and the other by nitrogen, as shown in Fig. 5.4a. It has a diatomic basis and a triangular unit cell containing one atom from each sub-lattice. The lattice itself can be described using the same vectors $\mathbf{a}_1$, $\mathbf{a}_2$ as for graphene (Eq. 4.1), but swapping the graphene nearest-neighbor distance with $\delta_{\mathrm{B\text{-}N}} = 1.45\,\text{Å}$.

Since hBN has different atoms occupying its two sub-lattices, the structural inversion symmetry that can be seen in graphene is broken in the hBN case. Boron and nitrogen have atomic numbers 5 and 7, respectively: their atomic s and p orbitals, therefore, have different energies due to the dif-
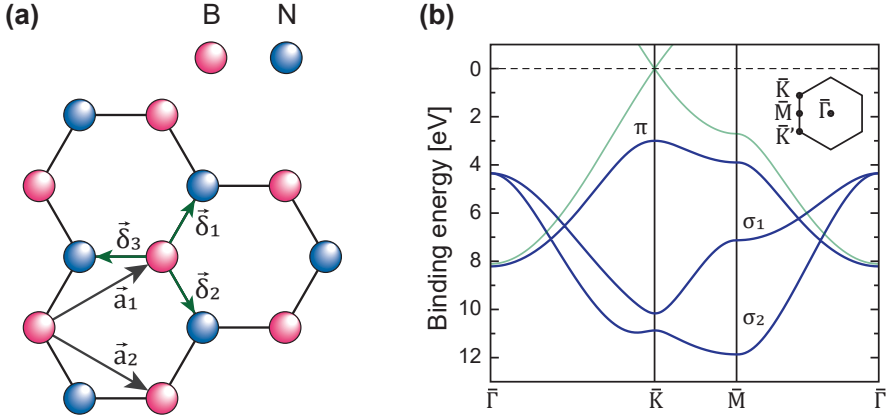
Figure 5.4: The atomic and electronic structure of hexagonal boron nitride (hBN). **(a)**: The lattice structure of hBN consists of two triangular sub-lattices, one occupied by boron and the other by nitrogen. The vectors $\mathbf{a}_1$ and $\mathbf{a}_2$ are vectors for hopping between equal atoms of the same sub-lattice, while $\boldsymbol{\delta}_l$ ($l = 1, 2, 3$) accommodate hopping to the nearest neighbours on the opposite sub-lattice. **(b)**: Electronic band structure of monolayer hBN. One π-band and two σ-bands are shown, having been obtained by first principles/density functional theory (DFT) calculations. Overlaid for comparison is the π-band of graphene in semi-transparent green. Calculations are courtesy of Thomas Frederiksen, 2022.

ferent numbers of charged particles in the atoms. Furthermore, the charge difference will affect the orbital localization lengths and the inter-atomic distance when bonding. As a result, an energy gap of approximately $5.95\,\mathrm{eV}$ is opened between the π- and π^*-bands at half-filling, making hBN a large-gap insulator instead of a Dirac material [142, 143]. The energy bands of hBN are shown in Fig. 5.4b.

From a doping point of view, the gapped band structure at the Fermi level makes hBN especially interesting. First, shifting the electron occupancy towards and beyond the hBN valence band maximum (VBM) should be feasible even for small amounts of added dopants, as no occupied states need to be emptied from the gap region. Furthermore, the abrupt change in eDOS and scattering phase-space at the VBM could be critical ingredients for strong electron-phonon coupling, i.e., similar to what was reported for the graphene σ-band maxima [68, 69]. To form Cooper pairs, hBN is therefore

particularly interesting as it provides much of the same physics as graphene. Yet it needs much lower doping concentrations to shift E_F into the relevant energy region [138].

In Paper 3, the renormalized valence band structure of exfoliated, few-layer hBN on top of graphene is studied by ARPES. The resultant bands reveal 'kinking' near the VBM, which can either be explained by an un-expected two-phonon scattering process or inter-band scattering with the underlying substrate material. This re-affirms the notion that hBN can be a viable candidate for achieving phonon-mediated superconductivity in low-dimensional, atomically flat van der Waals materials.

5.4   Paper 3

My contribution: ARPES measurements from exfoliated hBN can be particularly challenging, as they pose strict requirements of spot size and fo-cus due to the small size of the sample flakes. Furthermore, the flatness of the underlying substrate will significantly affect the quality of the measurements and what bands can be resolved. Epitaxial graphene substrates were used as these provide sufficient flatness and stack well with hBN from lattice match-ing. The graphene was grown by me, and the exfoliation of hBN flakes onto the substrates was performed by other co-authors. I acquired the ARPES and PEEM data presented in the paper, while the remaining measurements were conducted jointly with others. I also completed the self-energy analysis of the data and participated in their theoretical interpretation. Finally, I have written the first draft of the manuscript and made all the presented figures.

Phonon-Induced Mass Enhancements in a Wide Bandgap Material

In manuscript (July 2022).

Authors

Håkon I. Røst
Simon P. Cooil
Anna Cecilie Åsland
Ayaz Ali
Branson D. Belle
Jinbang Hu
Jerzy T. Sadowski
Federico Mazzola
Justin W. Wells

Chapter 6

Silicon δ-Layers

In pure semiconductors, introducing foreign atomic species can drastically increase the number of thermally generated charge carriers available in the system [144]. In the process known as 'doping', atoms with a different (i.e., higher or lower) number of valence electrons are incorporated into the structure of an intrinsic host material. This adds mobile charge carriers, either electrons or holes, altering the system's conductivity. In so-called 'δ-doping', the dopant atoms are distributed in near atomically thin, high-density sheets within bulk semiconductors [145]. The confined dopants in the plane induce a local and strong relative electrical potential to the adjacent semiconductor, similar to what can be observed in the 'depletion region' of a p-n junction[1]. A highly conductive, two-dimensional electron gas (2DEG) is thus formed within the semiconductor host. Such confined 2DEGs can be advantageous for many device applications, e.g., heterostructure field-effect transistors [146, 147], high current density and intraband tunneling diodes [148, 149], and scalable quantum computers [150].

In recent years, n-type phosphorus δ-doped silicon (Si:P) has attracted the most attention, mainly because of its potential as a silicon quantum device platform [151–153]. Si:P δ-layers are also attractive because they have well-established and relatively inexpensive fabrication recipes that lead to soaringly high charge carrier densities and near atomically thin dopant profiles [154–157].

This Chapter is dedicated to studying the Si:P δ-layer system. First, the

---

[1] For instance, the confined δ-layer can be thought of as an atomically thin n-type region with exceptionally high charge density, sandwiched between two p-type semiconductor regions.

electronic properties of Si:P δ-layers are presented in Section 6.1. Next, the typical fabrication of δ-layers is outlined in Section 6.2. In Section 6.3 the importance of knowing the arrangement of P atoms within the δ-layers is discussed, and also why the answer to this problem has remained elusive until recently. Finally, the relevance and benefit of studying sub-surface dopants using photoelectron diffraction are postulated, and a definite answer about the true dopant arrangement is given in Paper [4].

6.1   Electronic Properties

In Si:P δ-layer structures, the added electrons provided by the P atoms form a two-dimensional electron gas (2DEG) that is spatially confined within its semiconductor host. The active carrier densities provided by the high density of n-type dopants are typically well above the metal-to-insulator transition [158], and their free electron-like conduction happens primarily within the δ-layer and the nearest neighboring adjacent Si layers [159].

In a simple picture, donation of charge between the P dopants and the surrounding Si induces a local and strong change in the electric field normal to the δ-layer sheet. The resultant, 'delta'-like potential lead to significant electronic band bending in the narrow doping region around the ad-atoms. This shifts the Si conduction band minimum (CBM) beneath the Fermi level as shown in Fig. 6.1a [160]. The resultant electronic states are free electron-like and delocalized within the plane of the dopant region, but with exponentially decaying wave functions in the perpendicular direction [161].

The origin of the observed, near parabolic states of Si:P δ-layers can be explained from a surface projection of the bulk Si band structure. The situation is illustrated in Fig. 6.1b for a δ-layer located in the (001) plane. Si is an indirect band gap semiconductor, and its conduction band minima are situated at the X points of the bulk Brillouin zone (BZ) [162]. Since conduction is confined within the plane of the P dopant layer, the electronic states that participate should be effectively two-dimensional and independent of the wave vector $\mathbf{k}_\perp$ parallel or anti-parallel to the [001] direction. The conducting states are thus fully described within the surface-projected Brillouin zone (SBZ) of Si(001).

Projecting the bulk BZ onto the (001) plane places four of the CBM, i.e., the ones in-plane with the δ-layer, near the corners of the SBZ. These four contributions all appear at similar energy and in-plane wave vector $\mathbf{k}_{||}$. They are referred to as the 1Δ states, or collectively, the 'Δ manifold' [163].
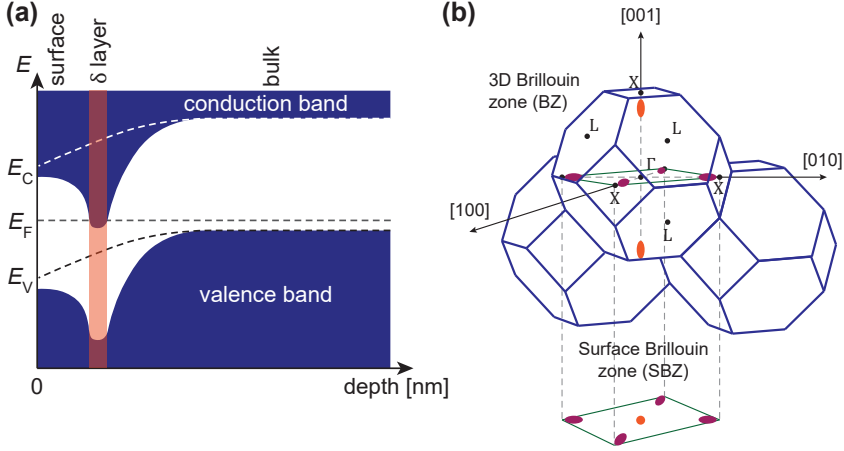
Figure 6.1: Electronic structure of Si:P δ-layers. **(a)**: A sketch of the valence and conduction bands of n-type Si (dashed lines), overlaid with the same bands for δ-doped Si (blue). The addition of a narrow P layer induces strong band bending near the dopant region, causing the conduction band to dip beneath the Fermi level (E_F). **(b)**: Projection of the bulk Si conduction band minima (CBM) of the bulk Brillouin zone (BZ) onto the (001) surface. The four in-plane CBM (purple) appear at the corners of the surface-projected Brillouin zone (SBZ), while the two out-of-plane CBM (orange) appear at the zone center.

The two remaining out-of-plane CBM appear at the center of the SBZ, where they form the bonding and anti-bonding 1Γ and 2Γ states, respectively. The energy difference between these two states is known as 'valley splitting', and its magnitude can have profound implications for the electronic behavior of the δ-layer system [164–166].

6.2 Fabrication of Si:P δ-layers

The growth of δ-layers has been extensively studied and refined over the years, not least to maximize the density of dopants and – consequently, the active carrier density n within the dopant plane [156, 157]. The basic preparation of a Si:P δ-layer system is illustrated in Fig. 6.2. Initially a clean, 2×1 reconstructed surface of Si(001) is exposed to gaseous PH$_3$, typically in doses of 1-2 Langmuirs (e.g., 5×10^{-9} mbar p.p. for 5 mins).
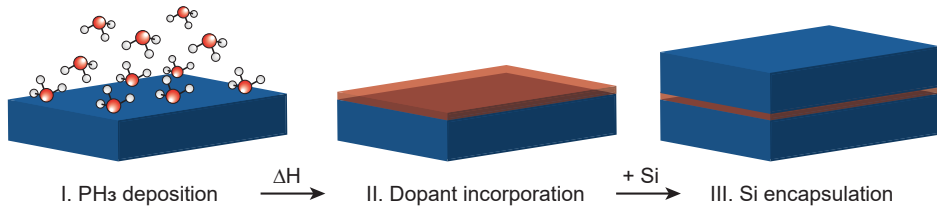
Figure 6.2: Epitaxial growth of Si:P δ-layers. Initially, PH$_3$ is chemisorbed on Si(001) at room temperature, dissociating as PH$_2$ + H $\rightarrow$ PH + 2H $\rightarrow$ P + 3H. Next, P dopants are incorporated into the surface at $T \approx 550\,^\circ$C by substituting and ejecting Si atoms. For a single dose of PH$_3$, the surface dopants will, in theory, occupy every 4th lattice site, yielding a $\leq 25\%$ ML coverage [169]. Finally, a Si overlayer ($> 0.5\,$nm) is deposited to encapsulate the P and form a two-dimensional free electron gas (2DEG) within the host material.

The incoming gas molecules bind to the Si $-$ Si surface dimers, dissociating in a matter of minutes as PH$_2$ + H, then PH + 2H, and finally P + 3H [167, 168]. The final P occupies the end-bridge site between Si dimers, and the three H atoms inhibit the neighboring Si atoms, thus preventing any further chemisorption of residual PH$_3$ gas [169]. Upon thermal exposure to $T > 400\,^\circ$C, the H atoms readily desorb as H$_2$, and the P atoms incorporate into the surface by ejecting Si [170, 171]. The doped surface layer is finally overgrown with atomic Si to encapsulate the dopants, and the full system is treated thermally to re-crystallize the overlayer.

Beyond the basic recipe, several other variations exist. Typically, these have been developed to maximize the active carrier density achievable from the δ-doping. For instance, after incorporating the P atoms, the surface can be exposed to a second dose of PH$_3$. Since the first incorporation anneal also desorbs H$_2$, remaining Si sites are free to accept subsequently added PH$_3$ molecules. The added gas can then dissociate as described, and P can again be incorporated into the surface from a second thermal treatment. From the resultant 'super-saturated' δ-layer structure, active carrier densities as high as 3.6×10^{14} cm^{-2} have been demonstrated [156].

A second pathway to maximizing active carrier densities is to minimize any segregation of P dopants within the δ-layer structure. Typically, a Si overlayer layer thickness of ≥ 9 ML is needed to 'lock' the dopants in and suppress any appreciable segregation. Furthermore, segregation is minimal

when the top Si is grown at room temperature, but at the expense of reduced crystalline quality [172]. The overlayer can, however, be re-crystallized from a rapid thermal anneal (RTA). This is typically an act of delicate balancing between time and temperature. Higher temperatures and longer durations give a more ordered Si overlayer but also an enhanced diffusion rate and segregation of the buried P atoms. Alternatively, the encapsulation layer can be grown at an elevated temperature, where $T = 250 - 270\,°C$ is ideal for optimal dopant activation while minimizing the P dopant segregation [173]. In the end, what growth parameters are optimal depends on the intended use of the δ-layer structure. E.g., the recipe of choice for device fabrication can be different from the ideal recipe for high-quality ARPES measurements, where a Si overlayer that is too thick or too rough will be detrimental to the achievable data quality [160, 161, 174].

6.3 The Importance of Dopant Arrangement

Despite the tremendous progress that has been made in realizing Si:P δ-layers over the last two decades, a few fundamental properties of the system are still unknown. One question that has remained unanswered until recently is what the atomic arrangement of the dopants is within the δ-layer. The answer is crucial for correctly understanding the electronic properties of the system and modeling its derived quantum devices. For instance, changing the in-plane distribution of P has a profound impact on the energy separation – i.e., the valley splitting, of the available quantum well states formed by the 2DEG [164–166]. Therefore, knowing the P dopant coordination and whether this can somehow be manipulated, e.g., by changing the concentration of dopants present in the layer, is essential for developing more mature δ-layer models and improving upon existing microelectronic fabrication practices.

Pre-existing studies of δ-layer systems have examined the Si-P surface chemistry as a function of PH_3 dosage, surface coverage, and of incorporation anneal temperature. Common to all is that they studied the distribution of P prior to the final Si encapsulation needed to produce Si:P quantum devices. Notably, a maximum P coverage was achieved for dosing at temperatures 500-550 °C, owing to the desorption of H_2 from the Si surface [170, 175]. Tsukidate and Suemitsu showed that one dose of PH_3 at 500 °C incorporates P atoms on 1/4 of the atomic sites, which then inhibit further adsorption. From repeated cycles of PH_3 dosing, H_2 desorption from Si sites and P

incorporation, an upper limit of ≈ 0.75 ML coverage was reached [176]. In this scenario, adjacent P atoms incorporated into the surface dimerize with each other, which should effectively reduce the overall free carrier density available in the final δ-layer. Whether the P$-$P dimers formed would survive Si encapsulation was then unknown and has proved surprisingly difficult to verify with certainty. McKibbin *et al.* since went on to develop different growth recipes to maximize the free carrier density while still retaining the sharpness of the δ-layers [156, 173, 177]. Different structural configurations have also been proposed, such as growing stacks of δ-layers separated by Si in a 'multi-layer' configuration, or co-deposition of PH$_3$ and Si [157, 163, 174]. These have been shown to retain many of the desirable properties of their atomically thin counterparts, and theoretical limits for the 3D active carrier density soar as high as 8.5×10^{20} cm^{-3} [157]. However, precise knowledge of the arrangement of dopants in the different finished δ-layer structures has remained elusive.

While there may be several reasons why proper knowledge of the dopant placements has not been obtained, the main conjecture is that there are few suitable techniques available for measuring this precisely. For instance, traditional X-ray diffraction (XRD) can, in principle, be performed with the radiation beam in-plane with the dopants. However, state-of-the-art in-plane XRD measurements of few-atomic-layer films have so far only been able to distinguish peaks originating from compounds with heavier elements in them, e.g., WS$_2$ and WSe$_2$ [178]. Annular dark-field (ADF) imaging using, for instance, a scanning transmission electron microscope (STEM) would also be exceptionally difficult due to the similar atomic masses of Si and P [179].

In Paper [4], we argue that X-ray photoelectron diffraction (XPD) is one particularly suitable and potentially overlooked technique for studying the in-plane distribution of P atoms in Si:P δ-layers. This is mainly owed to the chemical specificity that is available from photoemission measurements of atomic core levels (see Sections 2.2.1 and 2.2.2 for details). While the measured XPD intensity from buried layers will be substantially limited by the finite inelastic mean free path of the photoelectrons [26], we demonstrate that this problem can be circumvented through clever experimental design. I.e., by maximizing the P dopant concentration within the layer, minimizing the thickness of the needed Si encapsulation, extending the acquisition times, and tuning the photoexcitation energy to optimize the core level signals from the buried P, we can confidently determine the atomic arrangement

within the δ-layer. Furthermore, we prepare several samples with different dopant concentrations according to established recipes for single-to-multi-layer growth [156, 157, 163] and show how similar structural properties are present, despite their variations in doping concentration.

6.4 Paper 4

My contribution: All measurements were acquired in conjunction with the other co-authors, and the experimental work was split equally between the participants. I performed all the XPS analysis for the manuscript and participated in the XPD analysis and the discussions for the XPD simulations. I have also written the majority of the first draft of the manuscript and the supplementary note and made several of the figures presented.

Probing the Atomic Arrangement of Sub-Surface Dopants in a Silicon Quantum Device Platform

In manuscript (July 2022).

Authors

Håkon I. Røst
Ezequiel Tosi
Frode S. Strand
Anna Cecilie Åsland
Paolo Lacovig
Silvano Lizzit
Justin W. Wells

Chapter 7

Electron-Magnon Interactions

Analogous to the elementary vibrational excitations introduced in Chapter 5, condensed matter systems with long-range magnetic order can exhibit excitations in the form of propagating spin waves. Like phonons, spin waves are bosons and possess many of the same properties in the sense that they have well-defined excitation modes, heat capacity, and density of states, and can transmit energy through their host medium [111]. Furthermore, they can readily interact with other particles and quasiparticles, something which has been hypothesized to be one of the fundamental driving mechanisms behind unconventional, high T_c superconductivity [180–182].

This Chapter explores the interplay between conducting electrons and elementary magnetic excitations. First, the concept of magnetic ordering in correlated systems is summarized in Section 7.1, before the dispersion relations of magnetic spin waves are derived in Section 7.2. Next, methodologies for quantifying the self-energies from interactions between electrons and spin waves are outlined in Section 7.3, both theoretically and from ARPES measurements. An experimental study of the energy renormalizations from magnetic many-body effects in a well-known ferromagnet is then presented in Section 7.4 and Paper [5]. Finally, the concept of spin wave interactions between different materials across a magnetic interface is explored theoretically in Sections 7.5, 7.6 and Paper [6].

7.1 Magnetic ordering

To describe magnetic excitations in the form of spin waves, some basic properties of magnetically ordered systems are first defined and briefly discussed.

Consider a crystal with N atoms arranged in a regular Bravais lattice. Every lattice site is inhabited by electrons, at which each allowed energy state $|\varphi\rangle_n$ can be populated by a maximum of two electrons with opposite spins ($\uparrow, \downarrow$) according to Pauli's exclusion principle [183]. For simplicity, consider only one electron per atom, and thus a set of N spins $\{\mathbf{S}_i\}$ inhabiting the lattice sites, labeled as i. If kinetic energy contributions from hopping electrons are ignored, the (potential) energy of the half-filled system can be described using a Hamiltonian operator of the form

$$\hat{H} = -\sum_{i,j} J_{ij}\hat{S}_i \cdot \hat{S}_j - K\sum_i \left(\hat{S}_i^z\right)^2 - B\sum_i \hat{S}_i^z. \tag{7.1}$$

Here, the first summation is the so-called *Heisenberg model* for fermionic spinor interaction [184]. $\hat{S}_i$ are fermionic spin operators[1], while J_{ij} describes the exchange interaction strength between spins on lattice sites i and j and is related to the overlap of their charge distributions [106]. In the following Sections, only models with $J_{ij} \neq 0$ for nearest-neighbor interactions will be considered. The second sum accounts for the energy contribution from an easy axis anisotropy $K \geq 0$, where spins orienting themselves along the $\hat{\mathbf{z}}$ direction are energetically favored [6]. The final sum accounts for the interaction with a homogenous and external magnetic field of strength B along $\hat{\mathbf{z}}$.

In order to establish the concept of magnetic ordering, consider first the ground state energy from Eq. 7.1 without any easy-axis anisotropy ($K = 0$) or external magnetic fields ($B = 0$). The only (potential) energy contribution to the system is thus from the spinor-spinor interactions in the Heisenberg model. Depending on the sign of J_{ij}, the spins on different lattice sites i and j should align either parallel or antiparallel with each other to minimize the energy of the system. With only nearest-neighbor interactions, i.e., $J_{ij} = J$, all spins in the system should be aligned and parallel if $J > 0$. This simple picture yields a *ferromagnetic* ground state with a finite and net magnetic moment. Conversely, if $J < 0$, then antiparallel spin orientations are favored, and *antiferromagnetic* ordering with a net-zero magnetic moment is established. The two situations are sketched in Fig. 7.1a and 7.1b, respectively. In both cases, the ground state energy of the system is $U = lNJS^2$, where l is the number of nearest neighbors.

---

[1] I.e., satisfying $\left\langle \hat{\mathbf{S}}_i^2 \right\rangle = \hbar^2 S(S+1)$ with $S = 1/2$. A full summary is not given in this Chapter but can be found in, e.g., Ref. [19].
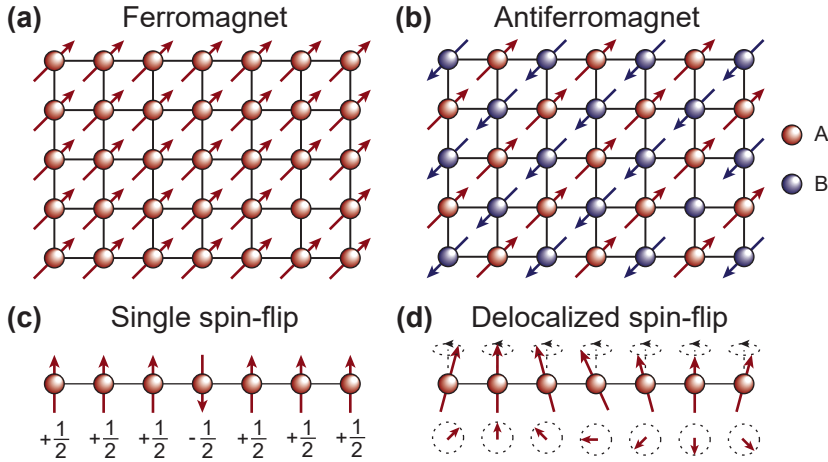
Figure 7.1: Magnetic ordering and spin excitations. **(a)**: Ferromagnetic order on a two-dimensional square lattice. **(b)**: Antiferromagnetic order on a two-dimensional square lattice. **(c)**: One complete spin-flip in a ferromagnet at a site i, costing a significant amount of energy due to the antiparallel alignment with its neighbors. **(d)**: A delocalized spin-flip, distributed over n lattice sites as a spin wave.

We note here that spontaneous magnetic ordering in real systems occurs only when the system's temperature is lower than some critical temperature T_c. Above T_c, the thermal fluctuations are strong enough to destroy the ordering. In contrast, at temperatures below T_c, thermal fluctuations will lead to spin-flip excitations, e.g., in the form of propagating spin waves. We also note that other phases of spontaneous magnetic ordering than ferromagnetism and antiferromagnetism can exist, e.g., *ferrimagnetic* ordering [106]. Nonetheless, the following discussion is restricted to ferro- and antiferromagnets as they exhibit the spin wave properties studied in Papers [5] and [6].

7.2 Spin Waves

The origin of magnetic spin waves can be understood and described from energy excitations of the ferro- and antiferromagnetic ground states using linear spin-wave theory. Consider again a Bravais lattice of N atoms, each of which is populated by one electron/spin as in Section 7.1. Without any

easy-axis anisotropy, the energy of the system (Eq. 7.1) is described by the Heisenberg model, and the interactions with the external magnetic field $\mathcal{B} = B\hat{\mathbf{z}}$. The presence of $\mathcal{B}$ ensures that every spin in a ferromagnetic ground state is aligned with $\hat{\mathbf{z}}$. Similarly, the antiferromagnetic ground state will have every second spin (i.e., on a sublattice A) aligned with $\hat{\mathbf{z}}$, and the remaining spins (sublattice B) antiparallel and along $-\hat{\mathbf{z}}$.

With the flip of one spin at a given site i in the lattice, the favorable interaction energy with each of its l nearest neighbors will be lost (Fig. 7.1c). Additionally, a perfect spin-flip changes the angle between the neighboring spins by $\pm\pi$, inducing a sign change for each of the l nearest-neighbor dot products in the sum. From the Heisenberg terms alone, the energy will increase by $2lJS^2$.

Alternatively, much lower excitation energy can be achieved if the spin-flip gets *delocalized*, i.e., shared by n spins at different lattice sites, each carrying $1/n$'th of a complete flip and being different from its neighbors by a corresponding phase difference. The resulting excitation is thus a wave-like oscillation of relative spin orientation across the n participants (Fig. 7.1d), and is known as a *magnon* [106]. Many of the properties of magnons are analogous to those of phonons, thus making them convenient to study using ARPES. This will be explored in Section 7.3.2 and Paper [5]. Next, the dispersion relations of ferro- and antiferromagnetic magnons are presented, following the derivations given in Chapter 4 of Ref. [111].

7.2.1   Ferromagnetic Spin Waves

The spin operators in Eq. 7.1 are inconvenient to work with since the components $\hat{S}_x$, $\hat{S}_y$, $\hat{S}_z$ are mutually non-commuting. More convenient are the independent spin raising and lowering operators $\hat{S}_i^{\pm} = \hat{S}_{ix} \pm i\hat{S}_{iy}$ paired with the $\hat{S}_i^z$ operator[2]. Since delocalized spin flips can be treated as quantized bosonic excitations with well-defined energies, their existence can be described using bosonic operators.

A convenient re-write of $\hat{S}_i^{\pm}$ and $\hat{S}_i^z$ is available using the Holstein-Primakoff transformation [111]:

---

[2]The 'i' that is multiplied with $\hat{S}_{iy}$ here is the imaginary unit, and should not be confused with the lattice position stated in the operator subscript.

$$\hat{S}_i^+ = \sqrt{2S - \hat{a}_i^\dagger \hat{a}_i} \hat{a}_i, \tag{7.2}$$

$$\hat{S}_i^- = \hat{a}_i^\dagger \sqrt{2S - \hat{a}_i^\dagger \hat{a}_i}, \tag{7.3}$$

$$\hat{S}_i^z = S - \hat{a}_i^\dagger \hat{a}_i, \tag{7.4}$$

where S is the total spin of all lattice sites and $\hat{a}_i^\dagger$ and $\hat{a}_i$ are bosonic creation and annihilation operators, respectively. The spin operators in Eqs. 7.2-7.4 satisfy spin commutation relations if the boson operators satisfy boson commutation relations and vice versa.

Next, $\hat{a}_i^\dagger$, $\hat{a}_i$ can be re-written using an inverse Fourier transform:

$$\hat{a}_i^\dagger = \frac{1}{\sqrt{N}} \sum_{\mathbf{q}} e^{i\mathbf{q} \cdot \mathbf{x}_i} \hat{a}_{\mathbf{q}}^\dagger, \tag{7.5}$$

$$\hat{a}_i = \frac{1}{\sqrt{N}} \sum_{\mathbf{k}} e^{-i\mathbf{q} \cdot \mathbf{x}_i} \hat{a}_{\mathbf{q}}, \tag{7.6}$$

where N is the number of atoms in the system, $\mathbf{q}$ is a wave vector within the 1st Brillouin zone, and $\mathbf{x}_i$ the vector position of the i'th atomic site. The operators $\hat{a}_{\mathbf{q}}^\dagger$ and $\hat{a}_{\mathbf{q}}$ create and annihilate magnons with wavevector $\mathbf{q}$, respectively. Note also that the transformations in Eqs. 7.5-7.6 are *canonical*, and hence $\hat{a}_{\mathbf{q}}^\dagger$, $\hat{a}_{\mathbf{q}}$ obey the same commutation relations as the original bosonic operators $\hat{a}_i^\dagger$, $\hat{a}_i$.

If the number of spin flips in the system is small compared to the total number of spins still aligned in the ferromagnet, i.e., the fractional spin flip $\langle \hat{a}_i^\dagger \hat{a}_i \rangle = \langle \hat{n}_i \rangle \ll S$, the roots in Eqs. 7.2 and 7.3 can be Taylor expanded. Keeping only the the terms up to quadratic order, one gets $\hat{S}_i^+ \approx \sqrt{2S}\hat{a}_i$, $\hat{S}_i^- \approx \sqrt{2S}\hat{a}_i^\dagger$ while $\hat{S}_i^z$ remains unchanged.

To find the Hamiltonian of the ferromagnetic system in terms of the magnon operators $\hat{a}_{\mathbf{q}}^\dagger$ and $\hat{a}_{\mathbf{q}}$, the quadratic expansions of $\hat{S}_i^+$ and $\hat{S}_i^-$, and $\hat{S}_i^z$ from Eq. 7.4 are inserted into 7.1. Operators $\hat{a}_i^\dagger$ and $\hat{a}_i$ are re-written using Eqs. 7.5-7.6. The Hamiltonian then becomes

$$\hat{H} = U + \sum_{\mathbf{q}} \hat{a}_{\mathbf{q}}^\dagger \hat{a}_{\mathbf{q}} \omega_{\mathbf{q}}, \tag{7.7}$$

where U is the ground state energy of the system and $\omega_{\mathbf{q}}$ describes the magnon excitation spectrum

$$\omega_{\mathbf{q}} = BS + 2JS \sum_{\boldsymbol{\delta}} [1 - \cos(\mathbf{q} \cdot \boldsymbol{\delta})]. \tag{7.8}$$

Here, $\boldsymbol{\delta}$ are the real space vectors from a lattice site i to its nearest neighbors. In the long wavelength limit, $|\mathbf{q} \cdot \boldsymbol{\delta}| \ll 1$, $\cos(\mathbf{q} \cdot \boldsymbol{\delta}) \approx 1 - \frac{1}{2}(\mathbf{q} \cdot \boldsymbol{\delta})^2$ and thus

$$\omega_\mathbf{q} \approx BS + JS \sum_{\boldsymbol{\delta}} (\mathbf{q} \cdot \boldsymbol{\delta})^2. \tag{7.9}$$

7.2.2 Antiferromagnetic Spin Waves

For the antiferromagnetic case, assume an exchange interaction that is $J < 0$ for nearest neighbors and otherwise zero. The adjacent spins inhabiting the two sublattices A and B are now *antiparallel* in the ground state. For zero easy-axis anisotropy and zero net external magnetic field, Eq. 7.1 becomes

$$\hat{H} = |J| \sum_{i,j} \hat{S}_i \cdot \hat{S}_j - B_\mathrm{A} \sum_i \hat{S}^z_{i \in \mathrm{A}} + B_\mathrm{A} \sum_j \hat{S}^z_{j \in \mathrm{B}}. \tag{7.10}$$

Here, i, j are the sites on each sublattice, both with maximum indices $N_\mathrm{A} = N_\mathrm{B} = N/2$. B_A is merely a fictitious field strength that is introduced here to ensure that the opposite spins on A and B align parallel and antiparallel to $\hat{\mathbf{z}}$, respectively [111].

As for the ferromagnetic case, only a small number of spin-flip excitations are considered. Hence the quadratically expanded Holstein-Primakoff transformations can again be used. Defining separate boson operators for the two sublattices, the Holstein-Primakoff spin operators for A and B become

$$\hat{S}^+_{i \in \mathrm{A}} = \sqrt{2S} \hat{a}_i, \qquad \hat{S}^-_{i \in \mathrm{A}} = \sqrt{2S} \hat{a}^\dagger_i, \qquad \hat{S}^z_{i \in \mathrm{A}} = S - \hat{a}^\dagger_i \hat{a}_i, \tag{7.11}$$

$$\hat{S}^+_{j \in \mathrm{B}} = \sqrt{2S} \hat{b}^\dagger_j, \qquad \hat{S}^-_{j \in \mathrm{B}} = \sqrt{2S} \hat{b}_j, \qquad \hat{S}^z_{j \in \mathrm{B}} = -S + \hat{b}^\dagger_j \hat{b}_j, \tag{7.12}$$

where the operators $\left\{ \hat{a}^\dagger_i, \hat{a}_i \right\}$ and $\left\{ \hat{b}^\dagger_j, \hat{b}_j \right\}$ create and annihilate spin flips on sublattices A and B, respectively.

Next, re-write the bosonic operators in terms of their inverse Fourier transform:

$$\hat{a}^\dagger_i = \frac{1}{\sqrt{N}} \sum_\mathbf{q} e^{i\mathbf{q} \cdot \mathbf{x}_i} \hat{a}^\dagger_\mathbf{q}, \qquad \hat{a}_i = \frac{1}{\sqrt{N}} \sum_\mathbf{k} e^{-i\mathbf{q} \cdot \mathbf{x}_i} \hat{a}_\mathbf{q}, \tag{7.13}$$

$$\hat{b}^\dagger_j = \frac{1}{\sqrt{N}} \sum_\mathbf{q} e^{i\mathbf{q} \cdot \mathbf{x}_i} \hat{b}^\dagger_\mathbf{q}, \qquad \hat{b}_j = \frac{1}{\sqrt{N}} \sum_\mathbf{k} e^{-i\mathbf{q} \cdot \mathbf{x}_i} \hat{b}_\mathbf{q}, \tag{7.14}$$

where $\left\{ \hat{a}^\dagger_\mathbf{q}, \hat{a}_\mathbf{q} \right\}$ and $\left\{ \hat{b}^\dagger_\mathbf{q}, \hat{b}_\mathbf{q} \right\}$ create and annihilate magnons with wave vector $\mathbf{q}$ on either sublattices. Note here that the wave vectors $\mathbf{q}$ are taken

to lie within the Brillouin zone associated with each sublattice, i.e., their *magnetic Brillouin zones*[3].

To reach the Hamiltonian for the antiferromagnetic phase in terms of the magnon operators, Eqs. 7.13-7.14 are fed into the operators in Eqs. 7.11-7.12 and inserted into Eq. 7.10. This gives

$$\hat{H} = U + 2JlS \sum_{\mathbf{q}} \left(\hat{a}_{\mathbf{q}}^{\dagger} \hat{a}_{\mathbf{q}} + \hat{b}_{-\mathbf{q}}^{\dagger} \hat{b}_{-\mathbf{q}} \right) + \gamma_{\mathbf{q}} \left(\hat{a}_{\mathbf{q}} \hat{b}_{-\mathbf{q}} + \hat{a}_{\mathbf{q}}^{\dagger} \hat{b}_{-\mathbf{q}}^{\dagger} \right), \qquad (7.15)$$

where U is the ground state energy[4], l is the number of nearest neighbors from sublattice B for a lattice site on A and vice versa, and $\gamma_{\mathbf{q}} \equiv (1/l) \sum_{\boldsymbol{\delta}} e^{i\mathbf{q} \cdot \boldsymbol{\delta}}$.

To diagonalize $\hat{H}$ in Eq. 7.15, a second canonical transformation known as the *Bogoliubov transformation* has to be performed. For conciseness, the steps are not re-created here, and the reader is referred to Ref. [111] for details. The final dispersion relation $\omega_{\mathbf{q}}$ given by the diagonalized Hamiltonian becomes:

$$\omega_{\mathbf{q}} = 2JlS \sqrt{1 - \gamma_{\mathbf{q}}^2}. \qquad (7.16)$$

If $|\mathbf{q} \cdot \boldsymbol{\delta}| \ll 1$, $\omega_{\mathbf{q}} \to 0$ as in the ferromagnetic case. Note, however, that in this limit the antiferromagnetic dispersion relation is linear $\omega_{\mathbf{q}} \propto |\mathbf{q}|$, whereas the ferromagnet had $\omega_{\mathbf{q}} \propto \mathbf{q}^2$.

7.3 Electron-Magnon Interactions

While magnons have many interesting properties in their own right, their interactions with conducting electrons can also induce an intriguing phase behavior. Magnons, like phonons, can scatter electrons between electronic states of well-defined energy and momentum. In some cases, e.g., on the Fermi surfaces of elementary metals, electron-phonon interactions can trigger an effective and attractive electron interaction and lead to superconductivity[5] [108]. While electron-phonon interactions in lower T_{c} superconductors

---

[3]For the identical sublattices, their magnetic Brillouin zones are equal and half the size of the full crystal Brillouin zone.

[4]At this point, the terms from the interaction with the fictitious field B_{A} have been removed for clarity. Remember that these do not represent an added, 'real' field interaction: they are merely needed to establish the ground state.

[5]I.e., if the coupling λ is sufficiently strong and the thermal energy in the system is within some critical range $\leq k_{\mathrm{B}} T_{\mathrm{c}}$.

have been extensively studied, much less understood is higher T_c superconductivity in correlated magnetic systems [185–188]. It has, however, been proposed that the attractive force between the superconducting electrons in these materials is from interactions with spin waves [180, 182].

Next, a few methodologies for estimating contributions to the self-energy Σ due to electron-magnon interactions are presented. First, calculations of Σ are outlined, using a Green's function approach and known magnon dispersion relations $\omega_{\mathbf{q}}$. Next, the estimation and distinction of electron-magnon interactions from ARPES measurements are explained in greater detail.

7.3.1 Calculating the Self-Energy of Electron-Magnon interactions

In systems where the magnon dispersion relations are well-known, energy renormalizations from electron-magnon interactions can be estimated using Green's functions and many-body perturbation theory [189]. Starting with a generalized Hamiltonian for an electron-boson interaction:

$$\hat{H}_{\text{el-bos}} = \sum_{\mathbf{k}\sigma\sigma'} \sum_{\mathbf{q},\nu} M^{\eta\eta',\nu}_{\mathbf{k},\mathbf{k}+\mathbf{q}} \left(\hat{a}_{\mathbf{q}\nu} + \hat{a}^{\dagger}_{-\mathbf{q},\nu} \right) \hat{c}^{\dagger}_{\mathbf{k}+\mathbf{q},\eta'\sigma'} \hat{c}_{\mathbf{k},\eta\sigma}(1 - \delta_{\sigma\sigma'}), \quad (7.17)$$

$\mathbf{k}$ and $\mathbf{q}$ are electron and boson quasimomentum wave vectors, ν is the boson mode, η and η' the initial and final electron states, respectively, σ and σ' denote electron spins of $\pm 1/2$, and $M^{\eta\eta',\nu}_{\mathbf{k},\mathbf{k}+\mathbf{q}}$ is the electron-boson interaction strength. The Hamiltonian operator thus describes the propagation of an electron from state η to η', either by absorbing or emitting a boson of mode ν with a wave vector $\mathbf{q}$ or $-\mathbf{q}$, respectively. Note that the Kronecker delta $\delta_{\sigma\sigma'}$ ensures that only spin-flip processes are considered, as expected from absorption or emission of magnons [45, 190]. Spin-flip scattering from electron-magnon interactions is sketched in Fig. 7.2.

The retarded, real-angular-frequency ω dependent Green's function for the interaction can be written as

$$G^{-1}_R(\mathbf{k},\omega) = G^{-1}_0(\mathbf{k},\omega) - \Sigma(\mathbf{k},\omega), \quad (7.18)$$

where Σ is the (complex) electron self-energy, and $G_0(\mathbf{k},\omega) = [\omega + i\delta - \varepsilon_{\mathbf{k}}]^{-1}$ is the non-interacting Green's function with energy states $\varepsilon_{\mathbf{k}}$ and a small physical broadening δ. Eq. 7.18 has been obtained using Dyson's equation
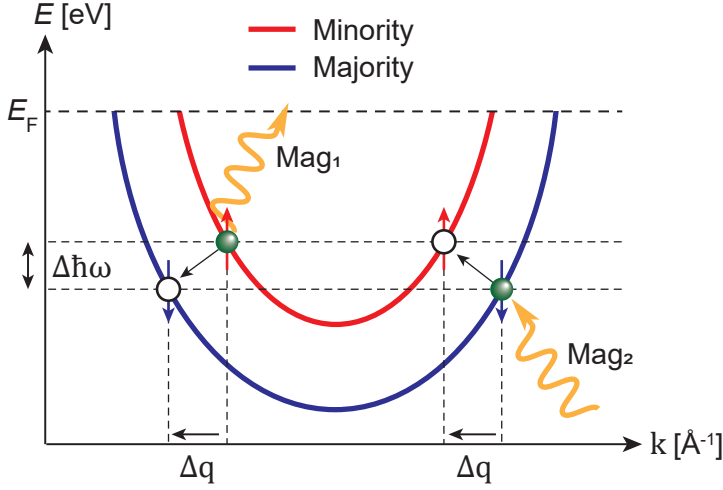
Figure 7.2: Inter-band magnon scattering of spin-polarized electrons. A magnon is either absorbed or emitted, propagating the electron to an empty final state and flipping the electron spin in the process. Magnon interactions hence enable scattering between bands of opposite spin characters.

on the imaginary axis, and analytic continuation to the real axis [191, 192]. Within the same formalism, $\Sigma(\mathbf{k}, \omega)$ at a temperature T is found to be

$$
\Sigma(\mathbf{k}, \omega) = - T \sum_{n=-\infty}^{\infty} \sum_{\mathbf{k}',\nu} M^{\nu} \bigg\{ D_{\nu}(\mathbf{q}, \omega - i\omega_n) G\big(\mathbf{k}', i\omega_n\big)
$$
$$
- \sum_{\pm} \pm \frac{G_R(\mathbf{k}', \omega \pm \omega_{\mathbf{q}\nu})}{2} \left(\tanh \frac{\omega \pm \omega_{\mathbf{q}\nu}}{2T} \mp \coth \frac{\omega_{\mathbf{q}\nu}}{2T} \right) \bigg\}, \quad (7.19)
$$

where $G(\mathbf{k}', i\omega_n)$ is the Matsubara Green's function, ω_n the fermionic Matsubara frequencies, $\omega_{\mathbf{q}\nu}$ the magnon dispersion relations (Eqs. 7.9, 7.16) and finally

$$
D_{\nu}\big(\mathbf{q}, i\omega_n - i\omega_n'\big) = \frac{-2\omega_{\mathbf{q}\nu}}{(\omega_n - \omega_{n'}) + \omega_{\mathbf{q}\nu}^2}, \quad (7.20)
$$

which is the branch-resolved magnon Matsubara propagator [193].

If the magnon dispersion relations $\omega_{\mathbf{q}\nu}$ are known exactly, the self-energy Σ can thus be estimated with precision. Using the approximation $G_R \approx G_0$ in Eq. 7.19, Eq. 7.18 reduces to

$$
G_R^{-1} \approx G_0^{-1} - \Sigma(G_0), \quad (7.21)
$$

which can furthermore be used to obtain the spectral function $A(\mathbf{k}, \omega) = \pi^{-1} \operatorname{Im} G_R(\mathbf{k}, \omega)$, and compared directly with bandstructure measurements. The true difficulty typically lies in knowing the analytical expression for the magnon dispersion relations. However, the expressions in Eqs. 7.19 and 7.20 can still be useful even if only approximations to $\omega_{\mathbf{q}\nu}$ exist. For instance, if the self-energy can be extracted from ARPES measurements (see Section 5.2.2 for details), the calculated Σ can be compared to the measured one. The fit between the two can then be optimized by adjusting some of the parameters of Σ (and herein $\omega_{\mathbf{q}\nu}$), e.g., the electron-magnon interaction strength M_ν and the spin exchange coupling strength J.

7.3.2 Measuring Electron-Magnon Interactions from ARPES

Similar to how electron-phonon interactions can be measured using ARPES, signatures of electron-magnon interactions can also be readily observed and quantified in systems with an appreciable magnetic ordering. Analogously, electron-magnon interactions will also manifest as renormalizations of the ideal, one-particle bandstructure. However, there are a few essential differences between the two that allow them to be distinguished in practice from ARPES measurements.

First, electron-magnon interactions can only occur between measured states with well-defined and opposite spin characters. Consider the emission of a photoelectron from a spin-polarized band. The photohole left behind can only be filled by an electron of equal spin character. The obvious – and in most cases more likely, relaxation mechanism is that an electron within the same spin band fills the state. To do so, the electron has to conserve its spin character but change its energy and momentum by finite amounts. The propagation can thus happen by the absorption and emission of a phonon if $\Delta E < \hbar\omega_{\mathrm{D}}^{\mathrm{ph}}$, where $\omega_{\mathrm{D}}^{\mathrm{ph}}$ is the Debye (cut-off) frequency of the system, and a corresponding $\Delta\mathbf{k}$ is defined by the phonon dispersion. Alternatively, the hole state can be filled with an electron from a different energy band, i.e., by inter-band scattering. This can again happen via phonon propagation from a band of equal spin character or a band of opposite spin if propagated by a magnon. With the absorption or emission of a magnon, a bosonic particle of integer spin is either created or annihilated, thus flipping the spin of the propagating electron (fermion) in the process. Propagation by magnons is often less pronounced in measured band structures, but it can occur with a finite probability if enough magnons and electron states with opposite spin are present.

In practice, phonons and magnon coupling in the same system tend to have very different characteristic energies [119, 194]. As a first approximation, one can distinguish their interactions with electrons based on their 'cut-off' energies. E.g., for the bulk ferromagnet Ni the Debye temperature is approximately $477\,\mathrm{K}$, and the maximum phonon energy is thus $k_B\Theta_D \approx 40\,\mathrm{meV}$ [195–197]. In comparison, the lowest measured cut-off energy for acoustic magnons in Ni is $\hbar\omega \approx 90\,\mathrm{meV}$ along the (111) direction [198], and couplings to the optical branch have been measured with energies as high as 340-350 meV [5, 119, 199].

A more subtle but important difference is that contributions to the self-energy from electron-phonon and electron-magnon interactions can have different functional forms. This is mainly due to their different dispersion relations and, consequently, the induced differences in their DOS. In the most simple picture, the $\mathrm{Im}\,\Sigma$ contribution from an electron-boson interaction can be assumed proportional to an integral of the boson DOS $\rho(\omega)$ over its available energy range

$$\mathrm{Im}\,\Sigma \propto \lambda \int_0^{\omega_{\max}} \rho(\omega')\mathrm{d}\omega', \qquad (7.22)$$

where λ is the dimensionless coupling strength (see Chapter 5.2.1) and $\omega_{\max}$ is the previously mentioned, characteristic cut-off energy for the boson distribution [194]. From Eq. 7.22 one can thus anticipate that for similar λ and $\omega_{\max}$, electron-phonon and electron-magnon couplings with unequal DOS distributions should have distinctive differences in their Σ terms.

For example, consider the differences between the two interactions in a bulk ferromagnetic system using a simple, isotropic Debye model at finite temperature T [117, 190]. Each energy dispersion is assumed proportional to a bosonic wave vector $\mathbf{q}$ up to their cut-off (maximum) frequencies $\omega_{\max}^{\mathrm{ph}}$, $\omega_{\max}^{\mathrm{mag}}$. For phonons in a three-dimensional Debye model, the dispersion relation is $\omega_{\mathrm{ph}} \propto |\mathbf{q}|$, and consequently $\rho_{\mathrm{ph}}(\omega) \propto \omega^2$. Similarly, ferromagnetic magnons will have $\omega_{\mathrm{mag}} \propto \mathbf{q}^2$ and $\rho_{\mathrm{mag}}(\omega) \propto \omega^{1/2}$ [106]. For simplicity, the electron-boson interaction matrix elements λ_{ph}, λ_{mag} are assumed equal and constant. Then the λ-weighted boson DOS functions – or *Eliashberg coupling* functions $\alpha^2(\omega)F(\omega)$, of the two interactions can then be written
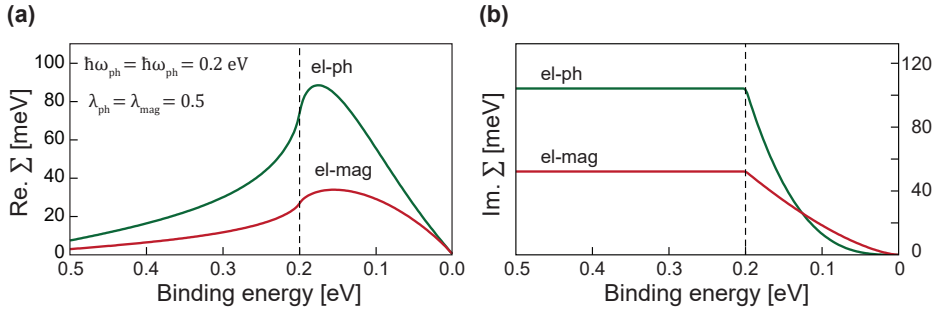
(a)

(b)

Figure 7.3: A comparison of the energy renormalizations from electron-phonon and electron magnon interactions at similar interaction energy $\hbar\omega$ and coupling strength λ.

as:

$$\alpha^2(\omega)F(\omega)_{\mathrm{ph}} = \begin{cases} \lambda\left(\omega/\omega_{\mathrm{max}}^{\mathrm{ph}}\right)^2, & \text{if } \omega \leq \omega_{\mathrm{max}}^{\mathrm{ph}}, \\ 0, & \text{otherwise,} \end{cases} \tag{7.23}$$

$$\alpha^2(\omega)F(\omega)_{\mathrm{mag}} = \begin{cases} \lambda(\omega/\omega_{\mathrm{max}}^{\mathrm{mag}})^{1/2}, & \text{if } \omega \leq \omega_{\mathrm{max}}^{\mathrm{mag}}, \\ 0, & \text{otherwise.} \end{cases} \tag{7.24}$$

Inserting either of the Eliashberg terms from Eqs. 7.24, 7.24 into Eq. 7.22 and accounting for fermion and boson distributions at finite T yields the imaginary self-energy expression (Eq. 5.11) already presented in Chapter 5.2.1:

$$\mathrm{Im}\,\Sigma_{\mathrm{el\text{-}bos}}(\omega, T) = \pi \int_0^{\omega_{\mathrm{max}}} \alpha^2 F(\omega') \cdot [1 + 2n(\omega', T) \\ + f(\omega + \omega', T) + f(\omega - \omega', T)]\mathrm{d}\omega'. \tag{7.25}$$

The corresponding $\mathrm{Re}\,\Sigma_{\mathrm{el\text{-}bos}}$ can be found using a Kramers-Kronig transformation [106].

In. Fig. 7.3, the resultant self-energy Σ contributions for electron-phonon and ferromagnetic electron-magnon coupling beneath the Fermi level are compared. Each Σ has been calculated from Eq. 7.25 with $\omega_{\mathrm{max}}^{\mathrm{ph}} = \omega_{\mathrm{max}}^{\mathrm{mag}} = 0.2\,\mathrm{eV}$ and $\lambda_{\mathrm{ph}} = \lambda_{\mathrm{mag}} = 0.5$. The different DOS terms lead to distinctive differences in the shapes of the real and imaginary terms. In Fig. 7.3a, the $\mathrm{Re}\,\Sigma$ of electron-phonon coupling appears steep and almost linear for most binding energies up to the inflection point at $\hbar\omega_{\mathrm{max}}$, whereas the $\mathrm{Re}\,\Sigma$ of

electron-magnon coupling resembles a broad 'hump' with magnitude $\approx 1/3$ even for similar coupling strength[6]. In Fig. 7.3b, the $\mathrm{Im}\,\Sigma$ terms of electron-phonon and electron-magnon coupling increase like ω^3 and $\omega^{3/2}$ towards the cut-off energy, respectively.

The above methodology is crude but very efficient for distinguishing the two coupling mechanisms. Combined with knowledge of the characteristic cut-off energies ω_{max} expected from the system, the occurrence of both can be verified, and their Σ contributions disentangled and quantified from ARPES measurements [118, 119, 190, 194]. In Paper [5], this framework is used to describe and quantify the different many-body interactions observed from the (111) face of a well-known bulk ferromagnet.

7.4   Paper 5

My contribution: The experimental work comprises lab-based momentum microscope (NanoESCA III) measurements performed in-house at NTNU, as well as higher resolution ARPES measurements performed at international synchrotron facilities. Together with the other co-authors, I performed all in-house measurements and the synchrotron measurements at Elettra. I also planned and coordinated the additional measurements performed remotely at MAX IV. Under the guidance of F. Mazzola, I performed and completed all the many-body analysis. Finally, I wrote the first complete drafts of the manuscript and the supplementary note and therein made all the figures presented in the text.

---

[6]Note that in the calculation, only magnon scattering from half of the electronic states is assumed, i.e., electrons scattering from bands of one spin character to final state bands of opposite character. A factor 1/2 is thus introduced both in the Eliashberg term (only 1/2 the final states are available for scattering) and in the Fermi-Dirac distributions of Eq. 7.25.

Disentangling Electron-Boson Interactions on the Surface of a Familiar Ferromagnet

In manuscript (July 2022).

Authors

Håkon I. Røst
Federico Mazzola
Johannes Bakkelund
Anna Cecilie Åsland
Jinbang Hu
Simon P. Cooil
Craig M. Polley
Justin W. Wells

7.5   Interfacial Electron-Magnon Interactions

So far, only interactions between electrons and spin waves inherent to the same material have been considered. A natural extension is to consider whether interactions can occur across magnetic interfaces, e.g., between magnons in one material and electrons in an adjacent, non-magnetic material. Several recent theoretical studies have proposed that the spin fluctuations at such interfaces, e.g., those of ferromagnetic or antiferromagnetic insulators, can generate an effective and attractive force between electrons in the non-magnet. If the strength of the magnetic interaction is sufficiently strong, it can, in principle, induce BCS and Amperean type pairing and sustain magnon-mediated superconductivity [200–203].

In Paper [6], such interactions between spins of magnetic insulators and conducting electrons in an adjacent topological insulator (TI) are explored. Electron-magnon couplings and their resultant self-energies are calculated according to the methodology outlined in Section 7.3.1, for both an underlying ferro- and antiferromagnetic insulator with finite and non-zero easy-axis anisotropies ($K > 0$). We show that, in theory, the strongest interfacial electron-magnon coupling can be achieved if the electrons of a TI interact with an uncompensated antiferromagnetic surface, i.e., coupling only to magnons from one sublattice of the antiferromagnet. We then proceed to study how the self-energies from the 'best-case' electron-magnon interaction would manifest themselves experimentally if measured using ARPES. The magnitude of the interfacial exchange coupling strength $\bar{J}$ is ramped up to experimentally determined values from similar systems [204, 205], and the spectral function $A(\mathbf{k}, \omega)$ (Eq. 2.14) is in each case simulated from the resultant self-energies Σ.

7.6   Paper 6

My contribution: While the electron-magnon interactions and resultant self-energies were calculated by K. Mæland, I performed the corresponding ARPES simulations and wrote a significant part of the last Section in the manuscript ('V. Towards Experimental Measurement'). I also contributed with co-author feedback on the first draft of the manuscript and helped implement improvements suggested by the referees.

Electron-magnon coupling and quasiparticle lifetimes on the surface of a topological insulator

Authors

Kristian Mæland
Håkon I. Røst
Justin W. Wells
Asle Sudbø

Electron-magnon coupling and quasiparticle lifetimes on the surface of a topological insulator

Kristian Mæland ⊙, Håkon I. Røst ⊙, Justin W. Wells, and Asle Sudbø ⊙*

Center for Quantum Spintronics, Department of Physics, Norwegian University of Science and Technology, NO-7491 Trondheim, Norway

The fermionic self-energy on the surface of a topological insulator proximity coupled to ferro- and antiferromagnetic insulators is studied. An enhanced electron-magnon coupling is achieved by allowing the electrons on the surface of the topological insulator to have a different exchange coupling to the two sublattices of the antiferromagnet. Such a system is therefore seen as superior to a ferromagnetic interface for the realization of magnon-mediated superconductivity. The increased electron-magnon-coupling simultaneously increases the self-energy effects. In this paper we show how the inverse quasiparticle lifetime and energy renormalization on the surface of the topological insulator can be kept low close to the Fermi level by using a magnetic insulator with a sufficient easy-axis anisotropy. We find that the antiferromagnetic case is most interesting from both a theoretical and an experimental standpoint due to the increased electron-magnon coupling, combined with a reduced need for easy-axis anisotropy compared to the ferromagnetic case. We also consider a set of material and instrumental parameters where these self-energies should be measurable in angle-resolved photoemission spectroscopy experiments, paving the way for a measurement of the interfacial exchange coupling strength.

I. INTRODUCTION

In conventional Bardeen-Cooper-Schrieffer (BCS) [1] superconductors (SC), electron-phonon coupling (EPC) generates an effective, attractive interaction between electrons. Other bosonic excitations also have the capacity to generate attractive electron interactions. For instance, spin fluctuations in magnetic insulators, i.e., magnons, can induce superconductivity in, e.g., normal metals and topological insulators (TI) [2–5] by combining materials into heterostructures [6–15]. Recently, both BCS- and Amperean-type pairings have been considered as mechanisms for superconductivity on the surface of a TI, exchange coupled to a ferromagnetic insulator (FM) or an antiferromagnetic insulator (AFM) [6,7]. Such systems have also been studied for other applications, including magnetization dynamics [16], confinement of Majorana fermions [17,18], magnetoelectric effects [19], and proximity-induced ferromagnetism [18].

In this paper, we consider the lifetime and energy renormalization of the fermionic quasiparticles on the TI surface in these systems, focusing on the fermion self-energy due to electron-magnon coupling (EMC). Its imaginary part is essentially a measure of the inverse quasiparticle lifetime [20] and is used to probe the stability of the fermionic states which underlie the superconducting theories that have been proposed. The real part of the self-energy is used to probe the renormalization of the fermionic states [20]. A similar study was done in Ref. [21] for EPC on the surface of an isolated TI.

In Ref. [10], the possibility of Amperean pairing was studied for a TI/FM heterostructure, using a self-consistent

strong-coupling approach. In the process, the fermion self-energy was studied, and a strong renormalization of the fermionic state was reported. Meanwhile, in Ref. [6], superconductivity in both TI/FM and TI/AFM heterostructures were studied within a weak-coupling approach, ignoring any energy renormalizations caused by the magnetic interface [6]. In this paper, we reveal for which material parameters the assumption of small renormalization of the fermionic states is permissible. To achieve this, we consider magnetic insulators with an easy-axis anisotropy.

In the AFM case, we also consider both compensated and uncompensated interfaces. Hence, the interfacial exchange coupling to the electrons on the TI surface may be different for the two sublattices of the AFM, where the two sublattices have magnetization ordered in opposite directions [6,22]. An uncompensated interface, where the electrons on the TI surface couple asymmetrically to the sublattices of the AFM, has been shown to increase EMC and hence increase the critical temperature for superconductivity [6,14,15].

On the other hand, a stronger EMC has the potential for more detrimental effects on the fermionic states. We find that the easy-axis anisotropy in the magnetic insulators and the degree of surface compensation in the AFM case can both be used to increase the lifetime of the fermionic states on the TI surface close to the Fermi level. For sufficient easy-axis anisotropy, we find that it is possible for the fermionic states on the TI surface to remain long-lived and weakly renormalized even when coupled to an uncompensated AFM surface. It is also found that the easy-axis anisotropy needed to stabilize the fermionic states in the AFM case is weaker than that needed in the FM case.

We first consider the case of a TI coupled to a FM in Sec. II, before moving on to the TI/AFM heterostructure in Sec. III. The results for the self-energy and the renormalized

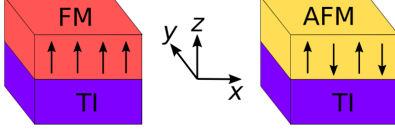*Corresponding author: asle.sudbo@ntnu.no

FIG. 1. Illustrations of the two heterostructures considered in this paper along with the coordinate system. We consider a topological insulator (TI) coupled to a ferromagnetic insulator (FM) or an antiferromagnetic insulator (AFM).

Green's function are considered for both systems in Sec. IV. In Sec. V, we examine a new set of material parameters giving self-energies that should be measurable using angle-resolved photoemission spectroscopy (ARPES). The conclusions are given in Sec. VI and the appendices give further details of the calculations.

II. FERROMAGNET

Our system is a three-dimensional (3D) TI with one surface in contact with a FM, as depicted in the left part of Fig. 1. This surface is the xy plane, and we assume an ordered state with magnetization in the z direction in the FM. We consider a TI with one Dirac cone such as Bi_2Se_3 or Bi_2Te_3 [23]. Examples of candidate FM materials include yttrium iron garnet (YIG) [24], EuO [11,25], and EuS [18]. We set $\bar{h} = k_B = a = 1$ in the equations throughout the paper. Here, $\bar{h}$ is the reduced Planck's constant, k_B is Boltzmann's constant, and a is the lattice constant.

A. Model

The Hamiltonian describing the interface between the TI and the FM contains a lattice formulation of the TI surface, H_{TI}, a Heisenberg model for the FM with an additional easy-axis anisotropy term, H_{FM}, and a model for the exchange coupling of lattice site spins in the FM to the electrons on the TI surface, H_{int}. We use the same model presented in Ref. [6], namely, $H = H_{TI} + H_{FM} + H_{int}$, with

$$H_{TI} = \frac{v_F}{2} \sum_i [(c_i^\dagger i\tau_y c_{i+\hat{x}} - c_i^\dagger i\tau_x c_{i+\hat{y}}) + \text{H.c.}]$$
$$+ \sum_i c_i^\dagger (2W\tau_z - \mu)c_i$$
$$- \frac{W}{2} \sum_i [(c_i^\dagger \tau_z c_{i+\hat{x}} + c_i^\dagger \tau_z c_{i+\hat{y}}) + \text{H.c.}], \quad (1)$$

$$H_{FM} = -J \sum_{\langle i,j \rangle} \mathbf{S}_i \cdot \mathbf{S}_j - K \sum_i S_{iz}^2, \quad (2)$$

$$H_{int} = -2\bar{J} \sum_i c_i^\dagger \boldsymbol{\tau} c_i \cdot \mathbf{S}_i. \quad (3)$$

Here, v_F is the Fermi velocity, $c_i^\dagger = (c_{i\uparrow}^\dagger, c_{i\downarrow}^\dagger)$, the fermionic operators $c_{i\sigma}^\dagger$ and $c_{i\sigma}$ create and destroy electrons with spin σ at lattice site i, respectively, $\boldsymbol{\tau} = (\tau_x, \tau_y, \tau_z)$ are the Pauli matrices, and H.c. denotes the Hermitian conjugate of the preceding term. Furthermore, $\hat{x}$ and $\hat{y}$ are unit vectors in the x direction and the y direction, respectively, μ is the chem-

ical potential, and $\langle i, j \rangle$ indicates that the lattice sites i and j located at $\mathbf{r}_i$ and $\mathbf{r}_j$ should be nearest neighbors. To ease computational requirements, we have assumed a 2D square lattice in the interfacial plane. The first line of H_{TI} represents the spin-momentum locking of electrons on the TI surface. The Wilson terms containing W are added to avoid additional Dirac cones at the Brillouin zone boundaries appearing from a direct discretization of the continuum model [26]. They are added so that the lattice model reproduces the correct physics [6,26]. The FM Hamiltonian contains an exchange interaction between nearest-neighbor lattice site spins, $\mathbf{S}_i$, with strength $J > 0$, and an easy-axis anisotropy term determined by $K > 0$ ensuring that ordering in the z direction is energetically favorable. The interfacial exchange coupling is parametrized by $\bar{J}$.

The next step is to obtain the fermions which diagonalize the TI Hamiltonian and the magnons which diagonalize the FM Hamiltonian. This was performed in Ref. [6] and we repeat the main points here. A Holstein-Primakoff (HP) transformation [27] is introduced for the spin operators $S_{i+} = \sqrt{2S}a_i$, $S_{i-} = \sqrt{2S}a_i^\dagger$, and $S_{iz} = S - a_i^\dagger a_i$, where the bosonic operators $a_i^\dagger$ and a_i create and destroy magnons at lattice site i, respectively. Furthermore, $S_{i\pm} = S_{ix} \pm iS_{iy}$, while S is the spin quantum number of the lattice site spins. Here, we have neglected any terms beyond quadratic in the magnon operators a_i, and we continue to do so throughout the analysis. This is permissible when assuming that the spins are nearly ordered, with only small quantum fluctuations, even when S is not large. Additionally, any constant terms in the Hamiltonian are neglected as these merely shift the zero point of the energy. Performing a Fourier transform (FT) on the magnon operators, $a_i = \frac{1}{\sqrt{N}} \sum_q a_q e^{-iq\cdot r_i}$, where N is the number of lattice sites on the interface, gives

$$H_{FM} = \sum_q \omega_q a_q^\dagger a_q, \quad (4)$$

with $\omega_q = 2KS + 4JS(2 - \cos q_x - \cos q_y)$. Notice the gap in the magnon spectrum due to the easy-axis anisotropy, $2KS$. The easy-axis anisotropy stabilizes the ground state with magnetization in the z direction, and a higher energy is needed to excite spin fluctuations. We refer to q as the momentum of the magnon, even though, since we have set $\bar{h} = a = 1$, it is technically a dimensionless version of the quasimomentum, restricted to the first Brillouin zone (1BZ) of the 2D square lattice.

Inserting the HP transformation, as well as a FT of both the magnon and the electron operators, $c_{i\sigma} = \frac{1}{\sqrt{N}} \sum_k c_{k\sigma} e^{-ik\cdot r_i}$, into H_{int} yields

$$H_{int} = \frac{V}{\sqrt{N}} \sum_{kq} (a_q c_{k+q,\downarrow}^\dagger c_{k\uparrow} + a_{-q}^\dagger c_{k+q,\uparrow}^\dagger c_{k\downarrow})$$
$$- 2\bar{J}S \sum_{k\sigma} \sigma c_{k\sigma}^\dagger c_{k\sigma}. \quad (5)$$

Here, $V = -2\bar{J}\sqrt{2S}$, $\sigma = 1$ for spin up, and $\sigma = -1$ for spin down. The first line describes EMC involving one magnon, while terms showing EMC with more than one magnon have been neglected. We have also neglected any Umklapp processes, since a small Fermi surface close to the 1BZ center means the Fermi momentum is much smaller than the
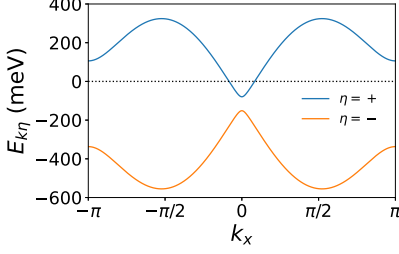
FIG. 2. The TI excitation spectrum $E_{k\eta}$ for the TI/FM heterostructure plotted along k_x with $k_y = 0$, $k_F = \pi/12$, $v_F = 429$ meV, $W = 0.3 v_F$, $\bar{J} = 18$ meV, and $S = 1$. The chemical potential is $\mu \approx 115$ meV.

reciprocal lattice vectors [6]. The terms in the second line do not contain magnon operators and are therefore moved to H_{TI}. These terms act like an external magnetic field on the TI and will open a gap in the fermionic spectrum. This is due to the magnetization along the z direction in the FM.

Next, the electron operators in H_{TI} are FT and a unitary transformation is used to diagonalize the Hamiltonian in terms of quasiparticles $\psi_{k\eta}$ with the helicity band index $\eta = \pm$,

$$H_{TI} = \sum_{k\eta} E_{k\eta} \psi_{k\eta}^\dagger \psi_{k\eta}. \qquad (6)$$

The excitation energies are $E_{k\eta} = -\mu + \eta F_k$, where we define $B_k = W(2 - \cos k_x - \cos k_y) - 2\bar{J}S$, $C_k = -v_F \sin k_y$, $D_k = -v_F \sin k_x$, and $F_k = \sqrt{B_k^2 + C_k^2 + D_k^2}$. Also defining $N_k = 2F_k(F_k + B_k)$, the electron operators are related to the quasiparticle operators as

$$c_{k\uparrow} = Q_{\uparrow+}(k)\psi_{k+} + Q_{\uparrow-}(k)\psi_{k-}, \qquad (7)$$

$$c_{k\downarrow} = Q_{\downarrow+}(k)\psi_{k+} + Q_{\downarrow-}(k)\psi_{k-}, \qquad (8)$$

with transformation coefficients

$$Q_{\uparrow+}(k) = -Q_{\downarrow-}(k) = (F_k + B_k)/\sqrt{N_k}, \qquad (9)$$

$$Q_{\uparrow-}(k) = \quad Q_{\downarrow+}^*(k) = (C_k + iD_k)/\sqrt{N_k}. \qquad (10)$$

The TI excitation spectrum is plotted in Fig. 2. The exchange coupling has introduced a gap of $4\bar{J}S$ in the original Dirac cone, similar to a mass gap for massive Dirac fermions [28]. The Wilson terms open gaps at the boundaries of the 1BZ, ensuring that there is only one Dirac cone present in the system [26].

Finally transforming H_{int} to the basis which diagonalizes H_{TI} gives

$$H_{int} = \frac{V}{\sqrt{N}} \sum_{kq} \sum_{\eta\eta'} [Q_{\downarrow\eta}^*(k+q)Q_{\uparrow\eta'}(k)a_q \psi_{k+q,\eta}^\dagger \psi_{k\eta'}$$
$$+ Q_{\uparrow\eta}^*(k+q)Q_{\downarrow\eta'}(k)a_{-q}^\dagger \psi_{k+q,\eta}^\dagger \psi_{k\eta'}]. \qquad (11)$$

B. Self-energy

At this point our calculations diverge from those of Ref. [6], as we now calculate the self-energy of the fermionic
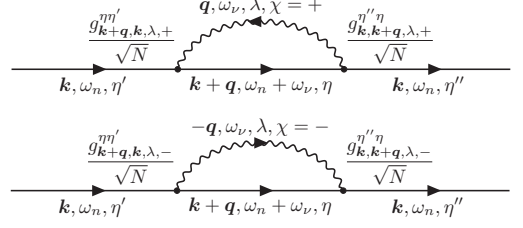
quasiparticles due to EMC. We include nonzero temperature by going to a sum over Matsubara frequencies and find [20,21,29–33]

$$\Sigma^{\eta''\eta'}(k, i\omega_n) = -\sum_q \sum_{\eta,\lambda,\chi=\pm} \frac{g_{k+q,k,\lambda,\chi}^{\eta\eta'} g_{k,k+q,\lambda,\chi}^{\eta''\eta}}{N}$$
$$\times T \sum_{\omega_\nu} D_0^\chi(q, i\omega_\nu) G_0^\eta(k+q, i\omega_n + i\omega_\nu), \qquad (12)$$

based on the sunset Feynman diagrams presented in Fig. 3. Hence, we have truncated our calculation of the self-energy at second order in the EMC, employing the Migdal approximation [32,34]. We have also used the fact that the tadpole diagram gives zero contribution in the systems considered in this paper, as shown in Appendix A. χ labels the direction of the magnon, i.e., the sign in front of q, while λ labels the magnon mode, which for the FM case is superfluous. Based on Eq. (11) we have, e.g., the coupling constant $g_{k+q,k,\chi=+}^{\eta\eta'} = V Q_{\downarrow\eta}^*(k+q)Q_{\uparrow\eta'}(k)$.

The bare fermion Green's function is [20,29] $G_0^\eta(k, i\omega_n) = 1/(i\omega_n - E_{k\eta})$, with $\omega_n = (2n+1)\pi T$. Upon introducing $\omega_\nu = 2\pi\nu T$, we use the bare magnon Green's function [20] $D_0^\chi(q, i\omega_\nu) = \chi/(i\omega_\nu - \chi\omega_q)$ for the magnon operator a_q when $\chi = +$ and $a_{-q}^\dagger$ when $\chi = -$, both with dispersion ω_q. Hence, we use separate propagators for a_q and $a_{-q}^\dagger$ as opposed to, e.g., EPC where one usually finds the propagator of the sum of these [33]. In other words, the magnons moving forward and backward in time are treated separately, before adding their respective contributions.

We first perform the sum over the Matsubara frequencies [20,30],

$$-T \sum_{\omega_\nu} \frac{\chi}{i\omega_\nu - \chi\omega_q} \frac{1}{i\omega_\nu + i\omega_n - E_{k+q,\eta}}$$
$$= \frac{\chi}{i\omega_n - E_{k+q,\eta} + \chi\omega_q} [B_E(\chi\omega_q) + F_D(E_{k+q,\eta})]. \quad (13)$$

Here, $B_E(\epsilon) = 1/(e^{\epsilon/T} - 1) = [\coth(\epsilon/2T) - 1]/2$ is the Bose-Einstein distribution and $F_D(\epsilon) = 1/(e^{\epsilon/T} + 1) = [1 - \tanh(\epsilon/2T)]/2$ is the Fermi-Dirac distribution.

Using $B_E(-\epsilon) = -1 - B_E(\epsilon)$ and an analytic continuation $i\omega_n \to \omega + i\delta$, where $\delta = 0^+$ [30,32,33], yields

$$-T \sum_{\omega_\nu} D_0^\chi(\boldsymbol{q}, i\omega_\nu) G_0^\eta(\boldsymbol{k}+\boldsymbol{q}, i\omega_n + i\omega_\nu)$$

$$= \frac{1}{2} \frac{\coth \frac{\omega_q}{2T} - \chi \tanh \frac{E_{\boldsymbol{k}+\boldsymbol{q},\eta}}{2T}}{\omega - E_{\boldsymbol{k}+\boldsymbol{q},\eta} + \chi \omega_q + i\delta}. \tag{14}$$

The following transformation is used in the sum over momentum:

$$\sum_{\boldsymbol{q}} \to \frac{N}{(2\pi)^2} \int_{-\pi}^{\pi} dq_x \int_{-\pi}^{\pi} dq_y. \tag{15}$$

Inserting Eqs. (14) and (15) into Eq. (12) gives

$$\Sigma^{\eta''\eta'}(\boldsymbol{k}, \omega) = \sum_{\eta, \chi = \pm} \frac{1}{8\pi^2} \int_{-\pi}^{\pi} dq_x \int_{-\pi}^{\pi} dq_y$$

$$\times g_{\boldsymbol{k}+\boldsymbol{q},\boldsymbol{k},\chi}^{\eta\eta'} g_{\boldsymbol{k},\boldsymbol{k}+\boldsymbol{q},\chi}^{\eta''\eta} \frac{\coth \frac{\omega_q}{2T} - \chi \tanh \frac{E_{\boldsymbol{k}+\boldsymbol{q},\eta}}{2T}}{\omega - E_{\boldsymbol{k}+\boldsymbol{q},\eta} + \chi \omega_q + i\delta}. \tag{16}$$

1. Imaginary part of the self-energy

In the following, we focus on the case where $\eta'' = \eta'$. Then, $g_{\boldsymbol{k},\boldsymbol{k}+\boldsymbol{q},\chi}^{\eta''\eta} = (g_{\boldsymbol{k}+\boldsymbol{q},\boldsymbol{k},\chi}^{\eta\eta'})^*$ and the coupling constant factor is real. Hence,

$$\text{Im}\,\Sigma^{\eta'\eta'}(\boldsymbol{k}, \omega) = \sum_{\eta, \chi = \pm} \frac{-1}{8\pi} \int_{-\pi}^{\pi} dq_x \int_{-\pi}^{\pi} dq_y |g_{\boldsymbol{k}+\boldsymbol{q},\boldsymbol{k},\chi}^{\eta\eta'}|^2$$

$$\times \delta(\omega - E_{\boldsymbol{k}+\boldsymbol{q},\eta} + \chi \omega_q)$$

$$\times \left(\coth \frac{\omega_q}{2T} - \chi \tanh \frac{E_{\boldsymbol{k}+\boldsymbol{q},\eta}}{2T} \right). \tag{17}$$

Transforming to polar coordinates yields

$$\text{Im}\,\Sigma^{\eta'\eta'}(\boldsymbol{k}, \omega) = \sum_{\eta, \chi = \pm} \frac{-1}{8\pi} \int_{-\pi}^{\pi} d\theta \int_0^{c(\theta)} dq\, q |g_{\boldsymbol{k},q,\theta,\chi}^{\eta\eta'}|^2$$

$$\times \delta(\omega - E_{\boldsymbol{k},q,\theta,\eta} + \chi \omega_{q,\theta})$$

$$\times \left(\coth \frac{\omega_{q,\theta}}{2T} - \chi \tanh \frac{E_{\boldsymbol{k},q,\theta,\eta}}{2T} \right). \tag{18}$$

Here, $q_x = q \cos\theta$ and $q_y = q \sin\theta$. The upper cutoff $c(\theta) = \pi / \max(|\sin\theta|, |\cos\theta|)$ ensures that the integral is limited to the 1BZ. We calculate this integral using [35]

$$\delta(f(r)) = \sum_i \frac{\delta(r - r_i)}{|f'(r_i)|}, \tag{19}$$

for a continuously differentiable function $f(r)$ with roots r_i and where $f'(r_i) \neq 0$. Here, the expression inside the δ function is $f_{\eta\chi}(q) = \omega - E_{\boldsymbol{k},q,\theta,\eta} + \chi \omega_{q,\theta}$. Its roots are found numerically, labeled q_i if they satisfy $0 \leqslant q_i \leqslant c(\theta)$, and ignored otherwise. Integrating over q gives

$$\text{Im}\,\Sigma^{\eta'\eta'}(\boldsymbol{k}, \omega) = \sum_{\eta, \chi = \pm} \frac{-1}{8\pi} \int_{-\pi}^{\pi} d\theta \sum_i \frac{|g_{\boldsymbol{k},q_i,\theta,\chi}^{\eta\eta'}|^2}{|f'_{\eta\chi}(q_i)|}$$

$$\times q_i \left(\coth \frac{\omega_{q_i,\theta}}{2T} - \chi \tanh \frac{E_{\boldsymbol{k},q_i,\theta,\eta}}{2T} \right). \tag{20}$$

Some details of this treatment of the δ function are commented on in Appendix B.

2. Real part of the self-energy

The real part of the self-energy can be found using the Kramers-Kronig relation [36],

$$\text{Re}\,\Sigma^{\eta'\eta'}(\boldsymbol{k}, \omega) = \frac{1}{\pi} P \int_{-\infty}^{\infty} \frac{\text{Im}\,\Sigma^{\eta'\eta'}(\boldsymbol{k}, \omega')}{\omega' - \omega} d\omega', \tag{21}$$

with P indicating the Cauchy principal value. Here, this integral is calculated using the trapezoidal rule. An important consideration is that the points that are chosen for ω' are evenly distributed around the singularity at ω.

III. ANTIFERROMAGNET

We now replace the FM with an AFM and assume a staggered state with magnetization along the z direction on the bipartite lattice of the AFM. The system is illustrated in the right part of Fig. 1. Examples of candidate AFM materials include Cr_2O_3 [37], Fe_2O_3 [38], and MnF_2 [12,39].

A. Model

We use the same model presented in Ref. [6], namely, $H = H_{TI} + H_{AFM} + H_{int}$, with

$$H_{AFM} = J_1 \sum_{\langle i,j \rangle} \boldsymbol{S}_i \cdot \boldsymbol{S}_j + J_2 \sum_{\langle\langle i,j \rangle\rangle} \boldsymbol{S}_i \cdot \boldsymbol{S}_j - K \sum_i S_{iz}^2, \tag{22}$$

$$H_{int} = -2\bar{J}_A \sum_{i \in A} \boldsymbol{c}_i^\dagger \boldsymbol{\tau} \boldsymbol{c}_i \cdot \boldsymbol{S}_i - 2\bar{J}_B \sum_{i \in B} \boldsymbol{c}_i^\dagger \boldsymbol{\tau} \boldsymbol{c}_i \cdot \boldsymbol{S}_i, \tag{23}$$

and H_{TI} as in Eq. (1). Here, $\langle\langle i, j \rangle\rangle$ indicates that the lattice sites i and j should be next-nearest neighbors. Once again, we have assumed a 2D square lattice in the interfacial plane for computational convenience. The AFM Hamiltonian contains an exchange interaction between nearest-neighbor lattice site spins with strength $J_1 > 0$ and between next-nearest neighbors with strength J_2. If $J_2 < 0$ this term stabilizes the AFM state, while if $J_2 > 0$ it acts as a frustration. We assume $|J_2| \ll J_1$ such that the system remains in the staggered state also for $J_2 > 0$. The easy-axis anisotropy term is the same as in the FM case. The sublattices of the bipartite lattice in the AFM are labeled A and B. The exchange coupling to the electrons on the TI surface is parametrized by $\bar{J}_A$ and $\bar{J}_B$ for lattice site spins on the A and B sublattices, respectively. We allow $\bar{J}_A$ and $\bar{J}_B$ to be different, which can describe an uncompensated antiferromagnetic interface where one sublattice is more exposed than the other [6]. This is illustrated in Fig. 4. We introduce $\bar{J} \equiv \bar{J}_B$ and $\Omega \equiv \bar{J}_A/\bar{J}_B$, and we let $0 \leqslant \Omega \leqslant 1$ parametrize the sublattice asymmetry of the exchange coupling.

Obtaining the eigenexcitations of the TI and the AFM follows a similar methodology as the FM case [6], and we focus on the main differences. We assume the lattice site spins on the A sublattice point in the positive z direction and opposite alignment on the B sublattice. A HP transformation is introduced for the spin operators $S_{i+}^A = \sqrt{2S} a_i$, $S_{i-}^A = \sqrt{2S} a_i^\dagger$, $S_{iz}^A = S - a_i^\dagger a_i$, $S_{i+}^B = \sqrt{2S} b_i^\dagger$, $S_{i-}^B = \sqrt{2S} b_i$, and $S_{iz}^B = -S + b_i^\dagger b_i$. Next, we introduce FT of the magnon operators, $a_i = \frac{1}{\sqrt{N_A}} \sum_{\boldsymbol{q} \in \diamond} a_{\boldsymbol{q}} e^{-i\boldsymbol{q}\cdot\boldsymbol{r}_i}$ and $b_i = \frac{1}{\sqrt{N_B}} \sum_{\boldsymbol{q} \in \diamond} b_{\boldsymbol{q}} e^{-i\boldsymbol{q}\cdot\boldsymbol{r}_i}$. Here, N_A
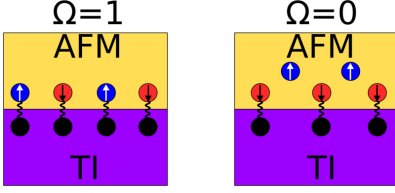
FIG. 4. An illustration of the interfacial exchange coupling between electrons in the TI and lattice site spins in the AFM. For a compensated interface, with $\Omega \equiv \bar{J}_A/\bar{J}_B = 1$, we have an equal coupling to both sublattices. For a completely uncompensated interface, with $\Omega = 0$, the electrons in the TI couple to only one of the sublattices in the AFM. The figure is inspired by Ref. [6].

and N_B are the number of lattice sites in the sublattices, and we assume $N_A = N_B = N/2$, where N is the total number of lattice sites on the interface. The sums over $\boldsymbol{q}$ are restricted to the reduced Brillouin zone (RBZ) of the sublattices, which is indicated by $\boldsymbol{q} \in \Diamond$. H_{AFM} is not diagonal in the original sublattice magnons a_q and b_q. Hence, a Bogoliubov transformation is introduced, expressing new magnon operators as $\alpha_{q+} = u_q a_q - v_q b_{-q}^\dagger$ and $\alpha_{q-} = u_q b_q - v_q a_{-q}^\dagger$. Requiring that the new operators are bosonic fixes $|u_q|^2 - |v_q|^2 = 1$. We assume u_q and v_q are real, as well as inversion symmetric in $\boldsymbol{q}$. Requiring that the AFM Hamiltonian is diagonal in terms of these new magnon operators yields

$$H_{\mathrm{AFM}} = \sum_{\boldsymbol{q} \in \Diamond} \sum_{\lambda = \pm} \omega_q \alpha_{q\lambda}^\dagger \alpha_{q\lambda}, \qquad (24)$$

with $\omega_q = \sqrt{\lambda_q^2 - \gamma_q^2}$, $\lambda_q = 2KS + 8J_1S + 8J_2S(\cos q_x \cos q_y - 1)$, and $\gamma_q = 4J_1S(\cos q_x + \cos q_y)$. The gap in the AFM magnon spectrum, $\omega_{q=0} = \sqrt{32J_1KS^2 + 4K^2S^2}$, is significantly greater than the gap in the FM case, $2KS$, provided $K \ll J \approx J_1$. On the other hand, even with comparable gaps, there are far more low-energy magnons in the FM than in the AFM. The reason is that the ungapped FM spectrum is quadratic for small $|\boldsymbol{q}|$, while the ungapped AFM spectrum is linear for small $|\boldsymbol{q}|$.

The FT of the electron operators is now written $c_{i\sigma} = \frac{1}{\sqrt{N}} \sum_{\boldsymbol{k} \in \Box} c_{k\sigma} e^{-i\boldsymbol{k}\cdot\boldsymbol{r}_i}$, where $\boldsymbol{k} \in \Box$ indicates that the sum runs over the entire 1BZ. Inserting the HP transformation, as well as a FT of both the magnon and the electron operators, into H_{int} yields some terms describing EMC and some terms that do not contain magnon operators. The latter terms are included in H_{TI}, similar to the FM case.

Next, the electron operators in H_{TI} are FT and a unitary transformation is used to diagonalize the Hamiltonian in terms of quasiparticles $\psi_{k\eta}$ with helicity index $\eta = \pm$,

$$H_{\mathrm{TI}} = \sum_{\boldsymbol{k} \in \Box, \eta} E_{k\eta} \psi_{k\eta}^\dagger \psi_{k\eta}. \qquad (25)$$

The definition of $B_{\boldsymbol{k}}$ is changed to $B_{\boldsymbol{k}} = W(2 - \cos k_x - \cos k_y) - JS(\Omega - 1)$, while the other definitions remain the same as in the FM case. As opposed to the FM case, this means that the fermion spectrum can be ungapped if $\Omega = 1$, since, with equal coupling to the two sublattices, no net

magnetization affects the TI. Additionally, the fermion gap is smaller for the same J with $\Omega = 0$, since a smaller net magnetization affects the TI surface.

Finally transforming H_{int} to the bases which diagonalize H_{TI} and H_{AFM} gives

$$\begin{aligned}
H_{\mathrm{int}} = \frac{U}{\sqrt{N}} \sum_{\substack{\boldsymbol{k} \in \Box \\ \boldsymbol{q} \in \Diamond \\ \eta\eta'}} & \{[(\Omega u_q + v_q)\alpha_{q+} + (\Omega v_q + u_q)\alpha_{-q,-}^\dagger] \\
& \times Q_{\downarrow\eta}^*(\boldsymbol{k}+\boldsymbol{q}) Q_{\uparrow\eta'}(\boldsymbol{k}) \psi_{\boldsymbol{k}+\boldsymbol{q},\eta}^\dagger \psi_{k\eta'} \\
& + [(\Omega u_q + v_q)\alpha_{-q,+}^\dagger + (\Omega v_q + u_q)\alpha_{q-}] \\
& \times Q_{\uparrow\eta}^*(\boldsymbol{k}+\boldsymbol{q}) Q_{\downarrow\eta'}(\boldsymbol{k}) \psi_{\boldsymbol{k}+\boldsymbol{q},\eta}^\dagger \psi_{k\eta'} \},
\end{aligned} \qquad (26)$$

where $U = -2\bar{J}\sqrt{S}$.

The factors in the Bogoliubov transformation are

$$u_q = \sqrt{\lambda_q/2\omega_q + 1/2}, \qquad (27)$$

$$v_q = \mathrm{sgn}(-\gamma_q/\lambda_q)\sqrt{u_q^2 - 1}. \qquad (28)$$

As it turns out, $v_q \approx -u_q$ when $\boldsymbol{q} \to 0$, an approximation which becomes better as $K \to 0$. Hence, the combinations like $\Omega u_q + v_q$ appearing in the EMC Hamiltonian in Eq. (26) are small for $\Omega = 1$, i.e., a compensated AFM interface with equal coupling to both sublattices, while they can be very large for $\Omega = 0$, i.e., a totally uncompensated AFM interface where the electrons on the TI surface couple to only one sublattice. This was also explained in Ref. [6], where Fig. 7, in addition to plotting u_q and v_q, shows how a positive J_2, i.e., a frustration of the AFM, can also increase the coupling. We therefore consider $J_2 = 0.05J_1$ in this paper.

Another point is that if the easy-axis anisotropy parameter K is removed, $\lim_{q\to 0} u_q = \infty$ and $\lim_{q\to 0} v_q = -\infty$. Hence, the coupling constants of the EMC would be infinite at $\boldsymbol{q} = 0$ if $\Omega \neq 1$. This in turn would lead to a divergent self-energy within the presented framework. This divergent behavior might be removed by using a self-consistent approach where renormalized propagators are used in calculating the self-energy. It may also be necessary to include higher-order diagrams in the calculations. We will continue to use the bare propagators and truncate at second order in EMC. Therefore, we will keep $K > 0$, introducing a gap in the magnon spectrum as well as making $u_{q=0}$ and $v_{q=0}$ finite. A similar divergence would also occur for the TI/FM heterostructure at $K = 0$ within the presented framework. There, the reason is that $\lim_{q\to 0} q \coth(\omega_{q,\theta}/2T) = \infty$ since $\omega_{q,\theta}$ is quadratic for small q and ungapped when $K = 0$.

B. Self-energy

With two magnon modes due to the presence of two sublattices, we now keep the sum over $\lambda = \pm$ in Eq. (12). Based on Eq. (26) we have, e.g., $g_{\boldsymbol{k}+\boldsymbol{q},\boldsymbol{k},\lambda=+,\chi=+}^{\eta\eta'} = U(\Omega u_q + v_q)Q_{\downarrow\eta}^*(\boldsymbol{k}+\boldsymbol{q})Q_{\uparrow\eta'}(\boldsymbol{k})$. The expressions for the magnon propagators are unchanged, apart from a redefinition of the magnon spectrum, and are now applied to the magnon operators $\alpha_{q\lambda}$ when $\chi = +$ and $\alpha_{-q,\lambda}^\dagger$ when $\chi = -$, all with

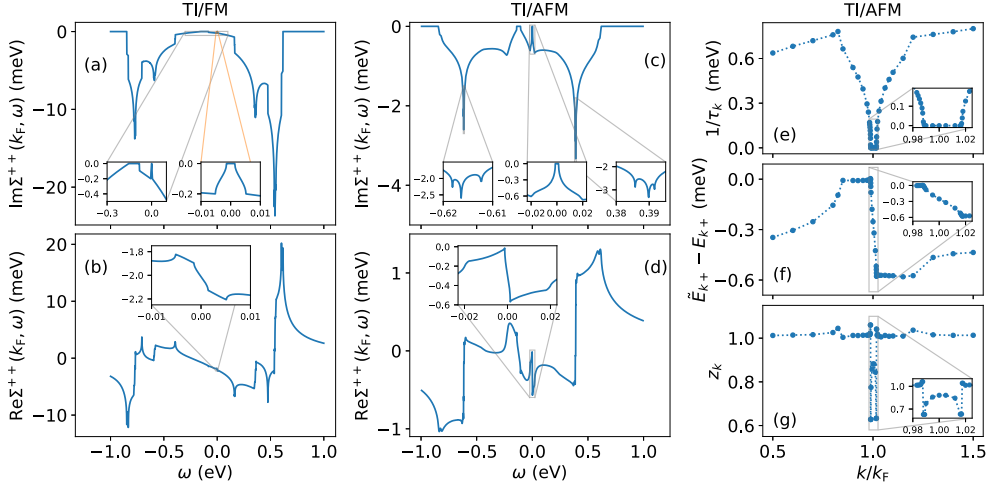FIG. 5. (a) $\mathrm{Im}\Sigma^{++}(\boldsymbol{k}_\mathrm{F}, \omega)$ and (b) $\mathrm{Re}\Sigma^{++}(\boldsymbol{k}_\mathrm{F}, \omega)$ for the TI/FM heterostructure, with $k_\mathrm{F} = \pi/12$, $v_\mathrm{F} = 429\,\mathrm{meV}$, $W = 0.3v_\mathrm{F}$, $J = 7\,\mathrm{meV}$, $\bar{J} = 18\,\mathrm{meV}$, $K = J/10$, $S = 1$, and $T = 10^{-7}\,\mathrm{eV}$. (c) $\mathrm{Im}\Sigma^{++}(\boldsymbol{k}_\mathrm{F}, \omega)$ and (d) $\mathrm{Re}\Sigma^{++}(\boldsymbol{k}_\mathrm{F}, \omega)$ for the TI/AFM heterostructure, with $J_1 = 7\,\mathrm{meV}$, $J_2 = 0.05J_1$, $K = J_1/10^3$, $\Omega = 0$, and otherwise the same parameters. The insets show behaviors that are not easily visible in the main plots. (e) The inverse lifetime, $1/\tau_k$, (f) the shift of the excitation spectrum, $\tilde{E}_{k+} - E_{k+}$, and (g) the quasiparticle residue, z_k, for the TI/AFM heterostructure with the same parameters. The insets show the behaviors close to the Fermi level. The circles show the calculated points, while the dotted lines are included for visualization. As is mentioned in the text, the results are plotted in the positive k_x direction, with $k_y = 0$. The same applies to the remaining figures plotting results as functions of momentum.

dispersion $\omega_{\boldsymbol{q}}$. The sum over momentum is transformed as

$$
\sum_{\boldsymbol{q} \in \Diamond} \rightarrow \frac{N}{(2\pi)^2} \int_{-\pi}^{\pi} dq_x \int_{-\pi+|q_x|}^{\pi-|q_x|} dq_y
$$
$$
\rightarrow \frac{N}{(2\pi)^2} \int_{-\pi}^{\pi} d\theta \int_0^{c(\theta)} dq q. \qquad (29)
$$

Here, $q_x = q\cos\theta$ and $q_y = q\sin\theta$. The upper cutoff $c(\theta) = \pi/(|\sin\theta| + |\cos\theta|)$ ensures that the integral is limited to the RBZ.

Otherwise proceeding just as in the FM case gives

$$
\mathrm{Im}\Sigma^{\eta'\eta'}(\boldsymbol{k}, \omega) = \sum_{\eta, \lambda, \chi=\pm} \frac{-1}{8\pi} \int_{-\pi}^{\pi} d\theta \sum_i \frac{|g_{\boldsymbol{k}, q_i, \theta, \lambda, \chi}^{\eta\eta'}|^2}{|f'_{\eta\chi}(q_i)|}
$$
$$
\times q_i \left(\coth\frac{\omega_{q_i, \theta}}{2T} - \chi\tanh\frac{E_{\boldsymbol{k}, q_i, \theta, \eta}}{2T} \right), \qquad (30)
$$

while the real part of the self-energy is obtained using Eq. (21).

IV. SELF-ENERGY AND RENORMALIZED GREEN'S FUNCTION

In both the FM case and the AFM case, we assume an electron-doped system with $\mu > 0$. It is then the positive helicity band which crosses the Fermi level, and so we focus on Σ^{++} from now on. Due to the lattice nature of our treatment, the system is not isotropic, though both $E_{\boldsymbol{k}\eta}$ and $\omega_{\boldsymbol{q}}$ are nearly isotropic close to the center of the 1BZ. Therefore, our results will be similar in all directions for $\boldsymbol{k}$. The representative

direction $k_x \geqslant 0$, $k_y = 0$, is chosen in all figures, using $k = |\boldsymbol{k}| = k_x$ and $\boldsymbol{k}_\mathrm{F} = (k_\mathrm{F}, 0) = (\pi/12, 0)$. With the Fermi momentum fixed, the chemical potential is determined by setting the Fermi energy to zero, $E_\mathrm{F} \equiv E_{k_\mathrm{F},+} = 0$, yielding $\mu = F_{k_\mathrm{F}}$. The chemical potential should not be too high since the bulk bands will then influence the physics on the TI surface [40]. With the parameters used in this paper, μ is kept in the region of 100 to 160 meV, ensuring that it is reasonable to ignore the bulk bands in the treatment of the TI surface [40].

The imaginary part of the self-energy is shown as a function of ω at $\boldsymbol{k} = \boldsymbol{k}_\mathrm{F}$ in Figs. 5(a) and 5(c) for the FM case and the AFM case, respectively. The insets show that $|\mathrm{Im}\Sigma^{++}(\boldsymbol{k}_\mathrm{F}, \omega)|$ is small for small $|\omega|$, i.e., close to the Fermi level. This indicates that the fermionic quasiparticles close to the Fermi level are long-lived. The use of $|\mathrm{Im}\Sigma^{++}(\boldsymbol{k}_\mathrm{F}, \omega)|$ as an indication of the inverse lifetime is made more clear in Sec. IV A.

We note that for both the FM case and the AFM case there is a drop of $|\mathrm{Im}\Sigma^{++}(\boldsymbol{k}_\mathrm{F}, \omega)|$ to zero for negative values of ω comparable to the chemical potential. We find that this extended zero is located around $\omega = -\mu - \omega_{\boldsymbol{q}=\boldsymbol{k}_\mathrm{F}}$ and that the extent of the zero corresponds to the gap in the excitation spectrum of the TI. For the AFM case, setting $\Omega = 1$ would close the gap, and there would be a single zero at $\omega = -\mu - \omega_{\boldsymbol{q}=\boldsymbol{k}_\mathrm{F}}$. A similar behavior was found for a Dirac-type fermionic spectrum in Ref. [32] where the self-energy due to EPC is explored in graphene. The suppression of the imaginary part of the self-energy is attributed to the vanishing fermionic density of states (DOS) at the Dirac points. The same explanation holds here, with the adjustment that for a gapped fermionic excitation spectrum there is a range of
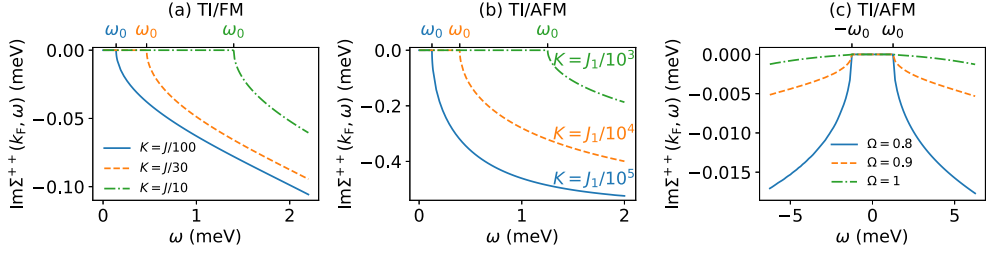
FIG. 6. $\text{Im}\Sigma^{++}(\boldsymbol{k}_F, \omega)$ for the (a) TI/FM and (b) TI/AFM heterostructure, with the same parameters as those in Fig. 5 except that we vary K. One can clearly see that the quick increase in $|\text{Im}\Sigma^{++}(\boldsymbol{k}_F, \omega)|$ sets in at $|\omega| = \omega_{q=0} = \omega_0$, i.e., at the gap in the magnon spectrum. This is shown by the upper ticks, where the color indicates the corresponding curve. (c) $\text{Im}\Sigma^{++}(\boldsymbol{k}_F, \omega)$ for the TI/AFM heterostructure with $K = J_1/10^3$, varying Ω, and otherwise the same parameters as those in Fig. 5. We see that any $\Omega < 1$ shows the same behavior as $\Omega = 0$, except that the effect is weaker, in the sense that $|\text{Im}\Sigma^{++}(\boldsymbol{k}_F, \omega)|$ is smaller at the same value of ω.

energies where the fermionic DOS is zero. Another adjustment is that while Ref. [32] studies optical phonons with a fixed frequency, we here study magnons with momentum-dependent frequencies. Naively, this should remove the suppression of $|\text{Im}\Sigma^{++}|$, but, as it turns out, the δ function involved in calculating the self-energy, $\delta(f_{\eta\chi}(q))$, fixes q to certain values in such a way that the suppression remains. To be specific, when $\omega \approx -\mu - \omega_{q=k_F}$, satisfying the δ function requires $q \approx -k_F$, fixing the magnon frequencies to $\omega_q \approx \omega_{q=k_F}$. Hence, scatterings with fermions close to the Dirac point are the relevant processes, just as in Ref. [32].

Another similarity of the FM and AFM cases is the large peaks in $|\text{Im}\Sigma^{++}(\boldsymbol{k}_F, \omega)|$ located at intermediate $|\omega|$. This is attributed to energy ranges around the extrema of the fermionic excitation energies, where $E_{k\eta}$ values are relatively flat, giving a large DOS. Combined with the fact that all magnons are energetically available, this gives a significant increase in the available electron-magnon scattering channels. Also note that these peaks in $|\text{Im}\Sigma^{++}(\boldsymbol{k}_F, \omega)|$ are stronger for the FM case than for the AFM case at the same parameters. In the FM case, ω_q values, and to some extent $E_{k\eta}$ values, are more slowly varying, further increasing the available scattering channels.

The real part of the self-energy at $k = k_F$ is shown in Figs. 5(b) and 5(d) for the FM case and the AFM case, respectively. All the exotic behavior found in $\text{Re}\Sigma^{++}(\boldsymbol{k}_F, \omega)$ can be traced back to rapid changes of $\text{Im}\Sigma^{++}(\boldsymbol{k}_F, \omega)$ at the same values of ω. The real part of the self-energy can be used as an indication of the shift in the fermion spectrum. This is made more clear in Sec. IV A.

Figure 6 explores the behavior close to the Fermi level, i.e., for small $|\omega|$, in greater detail. In Fig. 6(a), we focus on the TI/FM heterostructure and show how the easy-axis anisotropy of the FM, K, and in turn the gap in the magnon spectrum, $\omega_{q=0} = 2KS$, determines the extent of ω values where $|\text{Im}\Sigma^{++}(\boldsymbol{k}_F, \omega)|$ is exponentially suppressed. The extent of this thermal suppression turns out to be exactly $|\omega| < \omega_{q=0}$, due to the fact that the temperature is kept significantly lower than the gap in the magnon spectrum. The low temperature, $T \ll \omega_{q=0}$, means that very few fermion states with energy between E_F and $E_F + \omega_{q=0}$ are occupied, while almost all

states below E_F are occupied. Hence, for fermionic quasiparticles with energy $|\omega| < \omega_{q=0}$ the Pauli principle ensures that there are very few available electron-magnon scattering channels [32,33]. Once $|\text{Im}\Sigma^{++}(\boldsymbol{k}_F, \omega)|$ becomes nonzero for $\omega > \omega_{q=0}$, it increases as $(\omega - \omega_{q=0})^\nu$, where $\nu < 1$. This is non-Fermi liquid behavior, although the extended suppression of $\text{Im}\Sigma^{++}(\boldsymbol{k}_F, \omega)$ closer to $\omega = 0$ ensures that the system behaves as a Fermi liquid close to the Fermi level. A similar non-Fermi liquid behavior was found in Ref. [10], considering an ungapped magnon spectrum. We have shown that introducing an easy-axis anisotropy, and so a gap in the magnon spectrum, can move the non-Fermi liquid behavior away from the Fermi level.

In Fig. 6(b) the same effect is shown for the TI/AFM heterostructure. Since, with $J_1 = J$ and the same K, the gap in the AFM magnon spectrum is significantly larger than that in the FM case, a lower degree of easy-axis anisotropy is needed in the AFM case to stabilize the fermionic state close to the Fermi level. Also notice that, with comparable gaps, the self-energy increases more rapidly in the AFM case with $\Omega = 0$ than in the FM case. This is due to the increase in EMC for small $\boldsymbol{q}$ with $\Omega \ll 1$ not found in the FM case. Otherwise, the behavior is similar to that of the FM case.

We have thus far considered the strongest possible coupling with $\Omega = 0$ for the AFM case. In Fig. 6(c) the behavior is now shown for $\Omega > 0$. The general behavior is similar for all $\Omega < 1$, even though $|\text{Im}\Sigma^{++}(\boldsymbol{k}_F, \omega)|$ decreases as Ω is increased. This makes sense, since the EMC decreases when Ω is increased. Even for $\Omega = 1$ we find an initial fast increase of $|\text{Im}\Sigma^{++}(\boldsymbol{k}_F, \omega > \omega_{q=0})|$ in the sense that is goes like $(\omega - \omega_{q=0})^\nu$ with $\nu < 1$, but the behavior quickly transitions to a $\nu > 1$ type of increase.

A. Renormalized excitation spectrum, lifetime of quasiparticles, and quasiparticle residue

For the upper helicity band, the renormalized Green's function is given as [20,34]

$$G^+(\boldsymbol{k}, \omega) = \frac{1}{\omega - E_{k+} - \Sigma^{++}(\boldsymbol{k}, \omega)}. \tag{31}$$

Using Fermi liquid theory [20], this can be rewritten as

$$G^+(\boldsymbol{k}, \omega) = \frac{z_{\boldsymbol{k}}}{\omega - \tilde{E}_{\boldsymbol{k}+} + i/\tau_{\boldsymbol{k}}}, \qquad (32)$$

where the renormalized excitation spectrum $\tilde{E}_{\boldsymbol{k}+}$ is the solution of

$$\tilde{E}_{\boldsymbol{k}+} = E_{\boldsymbol{k}+} + \mathrm{Re}\Sigma^{++}(\boldsymbol{k}, \tilde{E}_{\boldsymbol{k}+}), \qquad (33)$$

the quasiparticle lifetime $\tau_{\boldsymbol{k}}$ is given by

$$\frac{1}{\tau_{\boldsymbol{k}}} = -\frac{\mathrm{Im}\Sigma^{++}(\boldsymbol{k}, \tilde{E}_{\boldsymbol{k}+})}{1 - \frac{\partial \mathrm{Re}\Sigma^{++}}{\partial \omega}\big|_{\tilde{E}_{\boldsymbol{k}+}}}, \qquad (34)$$

and the quasiparticle residue $z_{\boldsymbol{k}}$ is

$$z_{\boldsymbol{k}} = \frac{1}{1 - \frac{\partial \mathrm{Re}\Sigma^{++}}{\partial \omega}\big|_{\tilde{E}_{\boldsymbol{k}+}}}. \qquad (35)$$

We choose to calculate these quantities for the TI/AFM heterostructure with an uncompensated interface. The increased EMC, combined with the fact that the easy-axis anisotropy is more effective in producing a gap in the magnon spectrum, is the reason we find the AFM case to be more interesting than the FM case and hence worth exploring in greater detail.

The inverse quasiparticle lifetime is shown in Fig. 5(e). As indicated by the imaginary part of the self-energy in Fig. 5(c), the inverse quasiparticle lifetime is exponentially suppressed around the Fermi level, ensuring that the fermionic states are long-lived excitations of the system. Meanwhile, once we move far enough away from the Fermi level, i.e., an energy amount determined by the gap in the magnon spectrum, the inverse quasiparticle lifetime increases rapidly. In other words, the quasiparticle lifetime decreases substantially, and the stability of the fermionic states becomes questionable.

Note that the extent of the exponential suppression of the inverse lifetime is not symmetric about $k = k_{\mathrm{F}}$. This can be understood from the rapid change in the shift of the excitation spectrum, $\tilde{E}_{\boldsymbol{k}+} - E_{\boldsymbol{k}+}$, for k close to k_{F} shown in Fig. 5(f). Our calculations predict some sharp "kinks" in the renormalized excitation spectrum, which should in principle be observable when measuring the occupied electronic states using ARPES. However, the effects are too small at the chosen parameters to be measurable in current experimental setups [41–47]. Additionally, we note that the bare band $E_{\boldsymbol{k}+}$ varies over an energy range of the order of 100 meV for the same momenta, and so the obtained renormalization of the energy can be classified as very weak.

Figure 5(g) shows the quasiparticle residue. Around the Fermi level we have $z_{\boldsymbol{k}} > 0$, ensuring that the system behaves like a Fermi liquid. The physical interpretation is that a large part of the original fermionic quasiparticle behavior exhibited by the $\psi_{\boldsymbol{k}}$ operators remains after taking the EMC interaction terms in Eq. (26) into account. Meanwhile, further away from the Fermi level $z_{\boldsymbol{k}} > 1$, which is somewhat unusual. It does not seem to make sense that the quasiparticle residue is greater than 1. The mathematical explanation is that $\mathrm{Re}\Sigma^{++}(\boldsymbol{k}, \omega)$ is an increasing function of ω around $\omega = \tilde{E}_{\boldsymbol{k}+}$ at the same values of $\boldsymbol{k}$ where $z_{\boldsymbol{k}} > 1$. Physically, this connects to the non-Fermi liquid behavior exhibited by $|\mathrm{Im}\Sigma^{++}(\boldsymbol{k}, \omega)|$ once

it starts increasing rapidly. The interpretation of $z_{\boldsymbol{k}}$ as a quasiparticle residue is a result of Fermi liquid theory, which may not be valid at the parameters where $z_{\boldsymbol{k}} > 1$.

In Figs. 5(e)–5(g), $0.5 \leqslant k/k_{\mathrm{F}} \leqslant 1.5$, meaning that $-\mu/2 \lesssim E_{\boldsymbol{k}+} \lesssim \mu/2 \approx 57$ meV. We now compare $1/\tau_{\boldsymbol{k}}$ in Fig. 5(e) to $-\mathrm{Im}\Sigma^{++}(\boldsymbol{k}_{\mathrm{F}}, \omega)$ in Fig. 5(c) and $\tilde{E}_{\boldsymbol{k}+} - E_{\boldsymbol{k}+}$ in Fig. 5(f) to $\mathrm{Re}\Sigma^{++}(\boldsymbol{k}_{\mathrm{F}}, \omega)$ in Fig. 5(d) for $-\mu/2 \lesssim \omega \lesssim \mu/2$. Though not exactly the same, it is clear that the plots of the self-energy as functions of ω at the Fermi momentum provide a good indication of the results for $1/\tau_{\boldsymbol{k}}$ and $\tilde{E}_{\boldsymbol{k}+} - E_{\boldsymbol{k}+}$ as functions of k. Hence, the results for $\Sigma^{++}(\boldsymbol{k}_{\mathrm{F}}, \omega)$ in Figs. 5(a) and 5(b) for the FM case give a good indication of how the quasiparticle lifetime and the renormalized excitation spectrum behave for that system as well. For the same values of k/k_{F}, the inverse lifetime is smaller and the shift in the excitation spectrum is larger in the FM case. However, the renormalization of the energy is still small compared to the energy range of the bare band.

V. TOWARDS EXPERIMENTAL MEASUREMENT

We have thus far considered material parameters relevant for the theoretical calculations in Ref. [6] and shown that the assumption of low renormalization of the fermionic state makes sense, at least at a low temperature of $T = 10^{-7}$ eV, corresponding to $T \approx 10^{-3}$ K. ARPES experiments are, however, typically performed at significantly higher temperatures [41–47]. We choose $T = 2.2$ meV, corresponding to $T \approx 25$ K, as a temperature which is readily achievable experimentally. This temperature is much greater or comparable to the magnon gaps we have considered thus far. Hence, more electron-magnon scattering channels become available close to the Fermi level, and the suppression of $|\mathrm{Im}\Sigma^{++}(\boldsymbol{k}_{\mathrm{F}}, \omega)|$ close to $\omega = 0$ is lost. In order to increase the magnon gaps, we increase the nearest-neighbor coupling slightly and consider higher degrees of easy-axis anisotropy.

An interfacial exchange coupling of $\bar{J} = 18$ meV is similar to the values used in several theoretical papers previously [6,11–13]. These values are, among other measurements, based on an experiment involving a FM deposited on a SC, where the effect of the FM on the superconducting transition is used to estimate the interfacial exchange coupling [48]. Alternatively, comparable values have been estimated from measurements of the effective Zeeman field at FM/SC and FM/normal metal (NM) interfaces [11,49,50]. To get values of the self-energy that are measurable in ARPES, we consider a system where the interfacial exchange coupling is significantly larger, namely, $\bar{J} = 100$ meV. Similar values of $\bar{J}$ are used in Refs. [16,51], based on an experiment with magnetic impurities in the bulk of a TI. There, the exchange interaction between magnetic impurities and charge carriers is estimated from the behavior of the magnetoresistance [52]. Also, a larger value of $\bar{J}$ is estimated for the FM/NM interface of YIG and gold in Ref. [11] based on measurements of the spin-mixing conductance [24,53,54]. It is emphasized that $\bar{J} = 100$ meV is not chosen with some specific set of materials in mind, but as a general value that should in principle be achievable for TI/(A)FM interfaces based on the examples listed here. Increasing $\bar{J}$ simultaneously increases the gap in
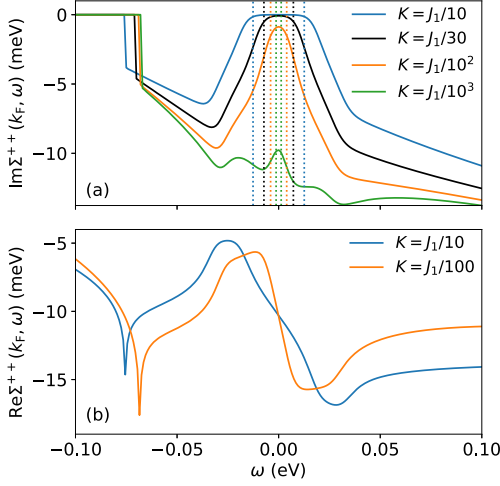
FIG. 7. (a) $\mathrm{Im}\Sigma^{++}(\boldsymbol{k}_\mathrm{F}, \omega)$ for the TI/AFM heterostructure, with $k_\mathrm{F} = \pi/12$, $v_\mathrm{F} = 429\,\mathrm{meV}$, $W = 0.3v_\mathrm{F}$, $J_1 = 10\,\mathrm{meV}$, $J_2 = 0.05J_1$, $J = 100\,\mathrm{meV}$, $S = 1$, $\Omega = 0$, $T = 2.2\,\mathrm{meV}$, and various K. The vertical dotted lines show the positions of $\omega = \pm\omega_{q=0}$ for the parameters corresponding to the solid lines of the same color. (b) $\mathrm{Re}\Sigma^{++}(\boldsymbol{k}_\mathrm{F}, \omega)$ with the same parameters, focusing on two choices for the easy-axis anisotropy.

the fermion spectrum, and so the chemical potential corresponding to $k_\mathrm{F} = \pi/12$ is now $\mu \approx 152\,\mathrm{meV}$.

Furthermore, we focus on the TI/AFM structure with $\Omega = 0$ since this revealed the strongest EMC. It should be noted that there is a discrepancy between our model and the most realistic experimental realization of a completely uncompensated interface [13]. With $\Omega = 0$, the lattice on the surface of the TI should match one of the sublattices of the AFM, not the original square lattice. This sublattice is still a square lattice; however, its lattice constant is a factor of $\sqrt{2}$ larger. As elaborated in Ref. [13], this has consequences for the size of the Brillouin zone for the fermions on the TI surface as well. Our model was chosen so that it could describe any value of Ω satisfying $0 \leqslant \Omega \leqslant 1$, at the cost of this discrepancy in the specific case of $\Omega = 0$. We expect that the results regarding increased EMC at $\Omega = 0$, the effect of the magnon gap on the self-energy close to the Fermi level, and the order of magnitude of the self-energy would be similar also if this detail were to be treated more accurately, or if other lattice configurations were studied.

Figure 7(a) shows the imaginary part of the self-energy for the new parameters. Values of K such that the magnon gap is just below and much greater than the temperature have been chosen, showing how the magnon gap affects the self-energy close to the Fermi level. Notice that increasing K decreases $|\mathrm{Im}\Sigma^{++}(\boldsymbol{k}_\mathrm{F}, \omega)|$ outside the gap region as well. This is because increasing K, and so increasing the gap in the magnon spectrum, decreases the maximum magnitude of the Bogoliubov factors u_q and v_q in Eqs. (27) and (28). Hence, the EMC is not as strong for larger easy-axis anisotropy.

The corresponding real part of the self-energy is shown in Fig. 7(b), from now on focusing on two choices for K. The values of the self-energy shown in these figures should be measurable in ARPES for common energy resolutions at the given temperature [41–47]. We also note that the effects of EMC in the TI should dominate over EPC at these parameters, based on the EPC calculations presented in Ref. [21].

From the one-particle Green's function in Eq. (31) one defines the *spectral function* [55]:

$$\mathcal{A}(\boldsymbol{k}, \omega) = -\pi^{-1}\mathrm{Im}G^+(\boldsymbol{k}, \omega)$$

$$= \frac{-\pi^{-1}\mathrm{Im}\Sigma^{++}(\boldsymbol{k}, \omega)}{[\omega - E_{\boldsymbol{k}+} - \mathrm{Re}\Sigma^{++}(\boldsymbol{k}, \omega)]^2 + [\mathrm{Im}\Sigma^{++}(\boldsymbol{k}, \omega)]^2}.$$

$$(36)$$

In the context of photoexcitation from an interacting N-electron system, $\mathcal{A}(\boldsymbol{k}, \omega)$ describes the probability of removing an electron with momentum $\boldsymbol{k}$ and energy ω relative to E_F [56]. The measured intensity of the photoexcitation will be proportional to

$$I(\boldsymbol{k}, \omega) \propto [\mathcal{M}(\boldsymbol{k}, \omega) \cdot \mathcal{A}(\boldsymbol{k}, \omega) \cdot g(\boldsymbol{k}, \omega) \cdot F_\mathrm{D}(\omega)] * R_\omega * R_k,$$

$$(37)$$

where $\mathcal{M}(\boldsymbol{k}, \omega)$ describes the photoexcitation matrix elements and $g(\boldsymbol{k}, \omega)$ is the electronic DOS. The Fermi-Dirac distribution $F_\mathrm{D}(\omega)$ scales the photoemission intensity around the Fermi level. R_ω and R_k represent the energy and the momentum resolution, respectively.

For nonzero and finite values of Σ^{++}, $\mathcal{A}(\boldsymbol{k}, \omega)$ has a Lorentzian line profile when measured at constant $\boldsymbol{k}$ or ω. $\mathrm{Im}\Sigma^{++}$ is then directly related to the linewidth in an ARPES measurement [57]. Similarly, because the intensity is maximum at $\omega = \tilde{E}_{\boldsymbol{k}+}$ [see Eq. (33)], $\mathrm{Re}\Sigma^{++}$ is seen in an ARPES measurement as a renormalization of the occupied band. Thus, using the calculated Green's function, which includes the bare band and the complex Σ^{++}, it is possible to simulate an ARPES measurement. In other words carrying out the reverse of the procedure which is typically used to extract an unknown self-energy from measured ARPES data [58,59].

To perform this simulation, we use the self-energy as a function of the renormalized energy band $\tilde{E}_{\boldsymbol{k}+}$, namely, $\Sigma^{++}(\boldsymbol{k}, \omega = \tilde{E}_{\boldsymbol{k}+}) = \Sigma^{++}(\tilde{E}_{\boldsymbol{k}+})$. This is then used as an energy-dependent self-energy whose momentum dependence is neglected, which should be a reasonable approximation [58]. Additionally, a minimal, constant contribution of 5 meV representing electron-impurity scattering has been added to $|\mathrm{Im}\Sigma^{++}|$ to induce a nonzero and more realistic linewidth of the bands [60,61].

$|\mathrm{Re}\Sigma^{++}(\tilde{E}_{\boldsymbol{k}+})|$ and the shifted $|\mathrm{Im}\Sigma^{++}(\tilde{E}_{\boldsymbol{k}+})|$ are shown in Figs. 8(a) and 8(b), respectively, selecting $K = J_1/10$ and $K = J_1/100$ for the easy-axis anisotropy. Compared to Fermi liquid theory, $|\mathrm{Im}\Sigma^{++}(\tilde{E}_{\boldsymbol{k}+})|$ should have a functional form similar to $1/\tau_k$ as can be seen from Eq. (34). Meanwhile, $\mathrm{Re}\Sigma^{++}(\tilde{E}_{\boldsymbol{k}+})$ corresponds to the shift in the excitation spectrum as can be seen in Eq. (33). Notice the significant renormalization of the energy band even for a magnon gap far above the considered temperature. This indicates that a weak-coupling approach to superconductivity in these systems, requiring low renormalization, is best suited at temperatures
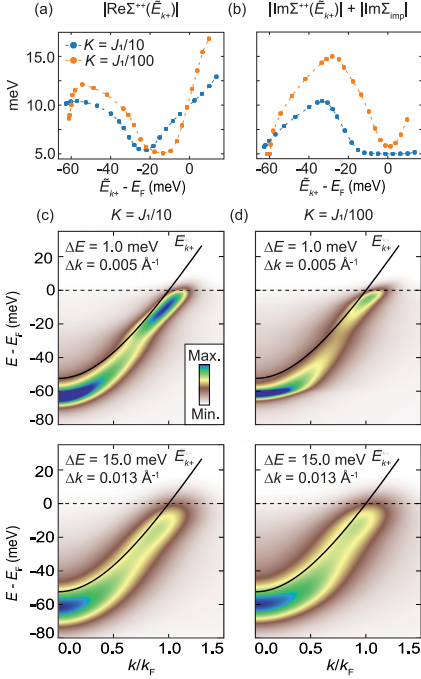
FIG. 8. (a,b) Magnitude of the self-energies $\mathrm{Re}\Sigma^{++}(\tilde{E}_{k+})$ and $\mathrm{Im}\Sigma^{++}(\tilde{E}_{k+})$ for the TI/AFM heterostructure, with the same parameters as those in Fig. 7. A constant energy offset of 5 meV has been added to the imaginary part to account for a small, but finite broadening due to electron-impurity scattering Σ_{imp}. The points show the calculated values, while the dashed lines have been added for visualization. (c,d) Simulations of instrumentally broadened ARPES data showing the positive helicity state E_{k+} renormalized by the self-energies Σ^{++} obtained with $K = J_1/10$ and $K = J_1/100$, respectively. Setting $a = 7$ Å, state-of-the-art resolutions for energy, E, and momentum, k, have been used for the topmost two panels, while the lowermost two panels show the same data with good laboratory-based resolution.

that are several orders of magnitude smaller than the gap in the magnon spectrum. Otherwise, strong-coupling approaches should be preferred, where the renormalization is taken into account.

Artificially constructed ARPES images showing the positive helicity band E_{k+} of the TI/AFM system with the included self-energy contributions are presented in Figs. 8(c) and 8(d) for $K = J_1/10$ and $K = J_1/100$, respectively. We emphasize that the plots presented are not measured ARPES data of the system as described, but rather simulated intensity plots based on the theoretically calculated self-energies in Figs. 8(a) and 8(b). The simulated plots are produced using Eqs. (36) and (37), suppressing any variations in the DOS, g, and photoexcitation matrix elements $\mathcal{M}$ for simplicity. The lattice constant is set to $a = 7$ Å, such that our choice of Fermi velocity corresponds to $v_F \approx 4.56 \times 10^5$ m/s, which is

within the range of reported values [6,8,21,40,62,63]. Each set of figures is then convolved with two different sets of assumed energy, E, and momentum, k, resolutions. The upper panels include state-of-the-art, synchrotron ARPES resolutions ($\Delta E = 1$ meV, $\Delta k = 0.005$ Å^{-1}) [43–45]. The lower panels include good laboratory-based resolutions, (i.e., Specs Phoibos 150 analyzer and non-monochromated He I source; $\Delta E = 15$ meV, $\Delta k = 0.013$ Å^{-1}) [46,47].

In the case of excellent instrumental resolutions, both the renormalization and the variation in linewidth because of the magnon interaction are readily observable. For the majority of the energy values the band appears at higher k relative to the undressed dispersion E_{k+}, signaling an increased effective mass, m^*, for electrons in the occupied states. A "kink" in the band structure appears around 40–60 meV below E_F, coinciding with the increased $|\mathrm{Re}\Sigma^{++}|$ in this energy range seen from Fig. 8(a). Furthermore, broadening of the bands is evident from the decreased photoemission intensity between 20 and 50 meV below E_F, being minimal around 30 meV below E_F where $|\mathrm{Im}\Sigma^{++}|$ is at its maximum [Fig. 8(b)].

The same characteristics as described can also be seen from the plots simulated using "home laboratory" resolutions. Although being harder to resolve by eye, measures of $\mathrm{Re}\Sigma^{++}$ and $\mathrm{Im}\Sigma^{++}$ would still be straightforward to extract using the analytic approach described in Refs. [58,59]. Thus, we conclude that the predicted self-energy effects due to EMC should be readily observable in a real ARPES experiment using an instrumental setup of reasonable performance.

The results presented here are naturally dependent on the choice of material parameters. For instance, the interfacial exchange coupling $\bar{J}$, for which a wide range of values has been proposed [6,11–13,16,51], is directly correlated to the magnitude of the self-energy. Hence, given a TI/FM or TI/AFM heterostructure, we expect that one could compare measured ARPES spectra to the calculations presented here in order to verify the presence and magnitude of the interfacial exchange coupling. To our knowledge, $\bar{J}$ has not been measured for either of the heterostructures presented in this paper. If ARPES is performed using the "home laboratory" energy and momentum resolutions presented here, $\bar{J}$ cannot be much lower than 100 meV for this method to succeed. However, a state-of-the-art (synchrotron) ARPES setup should in principle have sufficient resolutions to measure lower values of $\bar{J}$. Note also that the spin quantum number will affect the magnitude of the self-energy, and the value of S in an experimental realization could be different from $S = 1$, as chosen in the figures.

VI. CONCLUSION

We have explored self-energy effects on the surface of a topological insulator due to magnetic fluctuations in an adjacent ferromagnet or antiferromagnet. Useful applications of such systems include superconductivity and magnetoelectric effects. In such cases it is often important that the fermionic quasiparticles on the surface of the topological insulator are long-lived excitations. In weak-coupling approaches to superconductivity it is also required that the renormalization of the excitation energies is weak. We have shown how an easy-axis anisotropy in the magnetic insulators can be used to increase the lifetime of the quasiparticles close to the Fermi
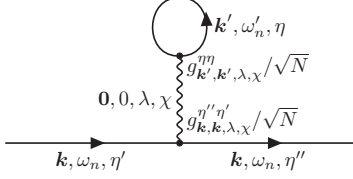
FIG. 9. The tadpole diagram is also relevant for second-order EMC. Momentum and energy conservation fixes $\boldsymbol{q} = \boldsymbol{0}$ and $\omega_\nu = 0$ for the magnon. Unlike EPC [21], the coupling constants remain nonzero. However, it turns out that $g^{\eta\eta}_{\boldsymbol{k}',\boldsymbol{k}',\lambda,\chi}$ is antisymmetric under inversion of $\boldsymbol{k}'$, explaining why this Feynman diagram gives zero contribution to the self-energy.

level. Additionally, we reported a set of parameters where the assumption of weak renormalization of the energy is valid. Finally, we studied a system at higher temperature and with a stronger interfacial exchange coupling, giving self-energies measurable in ARPES. We suggest that these calculations could be used, upon comparison to experimental results, e.g., to measure the magnitude of the interfacial exchange coupling. Additionally, we find that a greater easy-axis anisotropy is needed at higher temperatures to increase the lifetime of the quasiparticles on the surface of the topological insulator. However, the energy renormalization remains significant. Therefore, strong-coupling approaches to superconductivity will in general be needed in these systems, unless one is interested solely in low-temperature results.

ACKNOWLEDGMENTS

APPENDIX A: TADPOLE DIAGRAM

In this Appendix, we show that the tadpole diagram shown in Fig. 9 gives zero contribution to the self-energy. Denoting

this contribution $\Sigma^{\eta''\eta'}_{\mathrm{T}}$, we have

$$
\begin{aligned}
\Sigma^{\eta''\eta'}_{\mathrm{T}}(\boldsymbol{k}) &= \frac{2}{N} \sum_{\boldsymbol{k}'} T \sum_{\omega'_n} \sum_{\lambda,\chi,\eta=\pm} D^\chi_0(\boldsymbol{0},0) G^\eta_0(\boldsymbol{k}',\omega'_n) \\
&\quad \times g^{\eta''\eta'}_{\boldsymbol{k},\boldsymbol{k},\lambda,\chi} g^{\eta\eta}_{\boldsymbol{k}',\boldsymbol{k}',\lambda,\chi} \\
&= \frac{-2}{N} \sum_{\boldsymbol{k}'} \sum_{\lambda,\chi,\eta=\pm} \frac{F_{\mathrm{D}}(E_{\boldsymbol{k}'\eta})}{\omega_{\boldsymbol{q}=0}} g^{\eta''\eta'}_{\boldsymbol{k},\boldsymbol{k},\lambda,\chi} g^{\eta\eta}_{\boldsymbol{k}',\boldsymbol{k}',\lambda,\chi}. \quad \text{(A1)}
\end{aligned}
$$

Notice that $E_{\boldsymbol{k}'\eta}$ is inversion symmetric in $\boldsymbol{k}'$. Moreover, by inspecting Eqs. (9), (10), (11), and (26), it becomes clear that $g^{\eta\eta}_{\boldsymbol{k}',\boldsymbol{k}',\lambda,\chi}$ will, for both the TI/FM heterostructure and the TI/AFM heterostructure, always contain a combination $(F_{\boldsymbol{k}'} + B_{\boldsymbol{k}'})(C_{\boldsymbol{k}'} \pm iD_{\boldsymbol{k}'})/N_{\boldsymbol{k}'}$ which is antisymmetric under inversion of $\boldsymbol{k}'$. Therefore, the summand in $\Sigma^{\eta''\eta'}_{\mathrm{T}}$ is inversion antisymmetric, yielding $\Sigma^{\eta''\eta'}_{\mathrm{T}} = 0$.

APPENDIX B: DETAILS OF δ-FUNCTION TREATMENT

There are three cases that require some care when treating the δ function in the imaginary part of the self-energy, namely, if $q = 0$ is a root of $f_{\eta\chi}(q)$, if $q = c(\theta)$ is a root, or if double roots appear. With $K > 0$, we find that any roots at $q = 0$ give zero contribution. Only half the borders of the 1BZ/RBZ are included in the sum over $\boldsymbol{q}$. If there is a zero there, the procedure is exactly the same as for a zero at $0 < q < c(\theta)$ except for a factor $1/2$, since the zero is at the edge of the integration interval. For notational convenience, this detail is left out of Eqs. (20) and (30).

Double roots appear if $f'_{\eta\chi}(q) = 0$, and the method we have presented fails. The occurrence of double roots generally happens at a finite set of distinct values of θ. As we approach a double root by varying θ, two distinct roots move closer to each other. Hence, the derivatives $f'_{\eta\chi}(q)$ at these roots approach zero and the integrand in the θ integral diverges. Numerically, we split up the integration interval for θ to handle such improper integrals.

[1] J. Bardeen, L. N. Cooper, and J. R. Schrieffer, Phys. Rev. **108**, 1175 (1957).

[2] C. L. Kane and E. J. Mele, Phys. Rev. Lett. **95**, 146802 (2005).

[3] M. Z. Hasan and C. L. Kane, Rev. Mod. Phys. **82**, 3045 (2010).

[4] X.-L. Qi and S.-C. Zhang, Rev. Mod. Phys. **83**, 1057 (2011).

[5] M. He, H. Sun, and Q. L. He, Front. Phys. **14**, 43401 (2019).

[6] E. Erlandsen, A. Brataas, and A. Sudbø, Phys. Rev. B **101**, 094503 (2020).

[7] H. G. Hugdal, S. Rex, F. S. Nogueira, and A. Sudbø, Phys. Rev. B **97**, 195438 (2018).

[8] H. G. Hugdal and A. Sudbø, Phys. Rev. B **102**, 125429 (2020).

[9] J. Linder, Y. Tanaka, T. Yokoyama, A. Sudbø, and N. Nagaosa, Phys. Rev. Lett. **104**, 067001 (2010).

[10] M. Kargarian, D. K. Efimkin, and V. Galitski, Phys. Rev. Lett. **117**, 076806 (2016).

[11] N. Rohling, E. L. Fjærbu, and A. Brataas, Phys. Rev. B **97**, 115401 (2018).

[12] E. L. Fjærbu, N. Rohling, and A. Brataas, Phys. Rev. B **100**, 125432 (2019).

[13] E. Thingstad, E. Erlandsen, and A. Sudbø, Phys. Rev. B **104**, 014508 (2021).

[14] E. Erlandsen, A. Kamra, A. Brataas, and A. Sudbø, Phys. Rev. B **100**, 100503(R) (2019).

[15] E. Erlandsen and A. Sudbø, Phys. Rev. B **102**, 214502 (2020).

[16] I. Garate and M. Franz, Phys. Rev. Lett. **104**, 146802 (2010).

[17] L. Fu and C. L. Kane, Phys. Rev. Lett. **100**, 096407 (2008).

[18] P. Wei, F. Katmis, B. A. Assaf, H. Steinberg, P. Jarillo-Herrero, D. Heiman, and J. S. Moodera, Phys. Rev. Lett. **110**, 186807 (2013).

[19] D. Baasanjav, O. A. Tretiakov, and K. Nomura, Phys. Rev. B **90**, 045149 (2014).

[20] H. Bruus and K. Flensberg, *Many-Body Quantum Theory in Condensed Matter Physics: An Introduction* (Oxford University, Oxford, 2004).

[21] S. Giraud and R. Egger, Phys. Rev. B **83**, 245322 (2011).

[22] A. Kamra, A. Rezaei, and W. Belzig, Phys. Rev. Lett. **121**, 247702 (2018).

[23] H. Zhang, C.-X. Liu, X.-L. Qi, X. Dai, Z. Fang, and S.-C. Zhang, Nat. Phys. **5**, 438 (2009).

[24] M. Haertinger, C. H. Back, J. Lotze, M. Weiler, S. Geprägs, H. Huebl, S. T. B. Goennenwein, and G. Woltersdorf, Phys. Rev. B **92**, 054437 (2015).

[25] A. Mauger and C. Godart, Phys. Rep. **141**, 51 (1986).

[26] Y.-F. Zhou, H. Jiang, X. C. Xie, and Q.-F. Sun, Phys. Rev. B **95**, 245137 (2017).

[27] T. Holstein and H. Primakoff, Phys. Rev. **58**, 1098 (1940).

[28] T. Wehling, A. Black-Schaffer, and A. Balatsky, Adv. Phys. **63**, 1 (2014).

[29] A. A. Abrikosov, L. P. Gorkov, and I. E. Dzyaloshinski, *Methods of Quantum Field Theory in Statistical Physics* (Dover, New York, 1963).

[30] G. D. Mahan, *Many-Particle Physics* (Springer, New York, 2000).

[31] M. Calandra and F. Mauri, Phys. Rev. B **76**, 205411 (2007).

[32] C.-H. Park, F. Giustino, M. L. Cohen, and S. G. Louie, Phys. Rev. Lett. **99**, 086804 (2007).

[33] W.-K. Tse and S. Das Sarma, Phys. Rev. Lett. **99**, 236802 (2007).

[34] A. B. Migdal, J. Exptl. Theor. Phys. (U.S.S.R.) **34**, 1438 (1958) [Sov. Phys. JETP **7**, 996 (1958)].

[35] X. Wen, J. Comput. Phys. **226**, 1952 (2007).

[36] J. S. Toll, Phys. Rev. **104**, 1760 (1956).

[37] B. N. Brockhouse, J. Chem. Phys. **21**, 961 (1953).

[38] P. R. Elliston and G. J. Troup, J. Phys. C **1**, 169 (1968).

[39] G. G. Low, A. Okazaki, R. W. H. Stevenson, and K. C. Turberfield, J. Appl. Phys. **35**, 998 (1964).

[40] H. G. Hugdal, M. Amundsen, J. Linder, and A. Sudbø, Phys. Rev. B **99**, 094505 (2019).

[41] J. Schäfer, D. Schrupp, E. Rotenberg, K. Rossnagel, H. Koh, P. Blaha, and R. Claessen, Phys. Rev. Lett. **92**, 097205 (2004).

[42] A. Hofmann, X. Y. Cui, J. Schäfer, S. Meyer, P. Höpfner, C. Blumenstein, M. Paul, L. Patthey, E. Rotenberg, J. Bünemann, F. Gebhard, T. Ohm, W. Weber, and R. Claessen, Phys. Rev. Lett. **102**, 187204 (2009).

[43] S. V. Borisenko, Synchrotron Radiat. News **25**, 6 (2012).

[44] P. Rosenzweig, H. Karakachian, D. Marchenko, K. Küster, and U. Starke, Phys. Rev. Lett. **125**, 176403 (2020).

[45] H. Iwasawa, Electron. Struct. **2**, 043001 (2020).

[46] A. Tamai, W. Meevasana, P. D. C. King, C. W. Nicholson, A. de la Torre, E. Rozbicki, and F. Baumberger, Phys. Rev. B **87**, 075113 (2013).

[47] P. Rosenzweig, H. Karakachian, S. Link, K. Küster, and U. Starke, Phys. Rev. B **100**, 035445 (2019).

[48] G. M. Roesler, Jr., M. E. Filipkowski, P. R. Broussard, Y. U. Idzerda, M. S. Osofsky, and R. J. Soulen, Jr., Proc. SPIE **2157**, 285 (1994).

[49] G.-X. Miao, J. Chang, B. A. Assaf, D. Heiman, and J. S. Moodera, Nat. Commun. **5**, 3682 (2014).

[50] X. Hao, J. S. Moodera, and R. Meservey, Phys. Rev. Lett. **67**, 1342 (1991).

[51] Q. Liu, C.-X. Liu, C. Xu, X.-L. Qi, and S.-C. Zhang, Phys. Rev. Lett. **102**, 156603 (2009).

[52] J. S. Dyck, P. Hájek, P. Lošt'ák, and C. Uher, Phys. Rev. B **65**, 115212 (2002).

[53] B. Heinrich, C. Burrowes, E. Montoya, B. Kardasz, E. Girt, Y.-Y. Song, Y. Sun, and M. Wu, Phys. Rev. Lett. **107**, 066604 (2011).

[54] C. Burrowes, B. Heinrich, B. Kardasz, E. A. Montoya, E. Girt, Y. Sun, Y.-Y. Song, and M. Wu, Appl. Phys. Lett. **100**, 092403 (2012).

[55] A. Damascelli, Phys. Scr. **T109**, 61 (2004).

[56] S. Hüfner, *Photoelectron Spectroscopy: Principles and Applications* (Springer Science & Business Media, Berlin, 2013), Chap. 1.

[57] J. E. Gayone, C. Kirkegaard, J. W. Wells, S. V. Hoffmann, Z. Li, and P. Hofmann, Appl. Phys. A **80**, 943 (2005).

[58] I. Pletikosić, M. Kralj, M. Milun, and P. Pervan, Phys. Rev. B **85**, 155447 (2012).

[59] F. Mazzola, T. Frederiksen, T. Balasubramanian, P. Hofmann, B. Hellsing, and J. W. Wells, Phys. Rev. B **95**, 075430 (2017).

[60] A. Bostwick, T. Ohta, T. Seyller, K. Horn, and E. Rotenberg, Nat. Phys. **3**, 36 (2007).

[61] M. Bianchi, E. D. L. Rienks, S. Lizzit, A. Baraldi, R. Balog, L. Hornekær, and P. Hofmann, Phys. Rev. B **81**, 041403(R) (2010).

[62] C. Brüne, C. X. Liu, E. G. Novik, E. M. Hankiewicz, H. Buhmann, Y. L. Chen, X. L. Qi, Z. X. Shen, S. C. Zhang, and L. W. Molenkamp, Phys. Rev. Lett. **106**, 126803 (2011).

[63] I. Sochnikov, L. Maier, C. A. Watson, J. R. Kirtley, C. Gould, G. Tkachov, E. M. Hankiewicz, C. Brüne, H. Buhmann, L. W. Molenkamp, and K. A. Moler, Phys. Rev. Lett. **114**, 066801 (2015).

Chapter 8

Conclusion and Outlook

In this thesis, the properties of several exciting quantum materials have been studied. Particularly the structure of and the interactions that occur in systems with 'reduced' (i.e., spatially confined and/or near atomically thin) dimensions have been emphasized. At the very core is the experimental and theoretical work presented in Papers [1–6]. In the following, a summary is given for each one, together with a few concluding remarks and an outlook on potential further work within each topic.

Low-Temperature, Epitaxial Graphene Growth

In Paper [1], we showed how the clever use of transition metal thin films could facilitate epitaxial graphene growth from SiC crystals at significantly reduced temperatures. Using either Fe or Ru interchangeably, graphene growth was shown to initiate already at 450 °C, with monolayers forming at approximately 600 °C and multilayer (3-8 atomic layers) growth at 700-800 °C. As opposed to other, more established growth recipes, our transition-metal-mediated approach can, therefore, readily form graphene with µm size domains at temperatures within the practical limitations of conventional semiconductor workflows, e.g., the CMOS process. Furthermore, we showed how the added transition metal could be removed by thermal diffusion, thus leaving the graphene resting directly on semiconducting layers.

In Paper [2] we extended the work of Paper [1], showing how patterned graphene structures could be achieved by defining geometries of the transition metal thin films on top of the SiC prior to annealing. We also demonstrated how atomic intercalation through the graphene layers could be ex-

ploited to grow additional layers of pure Si under the graphene, thus lifting it off from the SiC substrate. Finally, the added Si layers were oxidized, forming an insulating SiO_2 layer underneath the graphene that can be tuned in thickness, depending on the thickness of the Si and the extent of the oxidation.

While SiC single crystals may not be the material of choice in a business largely revolving around Si, our discoveries nonetheless show great promise for integration in existing device fabrication routines. For instance, it has been shown that thin films of SiC can readily be grown on top of Si [206], which would significantly reduce production costs and make transition-metal-mediated graphene a viable addition to Si-based devices. Secondly, our relatively straightforward and inexpensive approach to graphene patterning can potentially eliminate the need for cumbersome lithographic post-processing. We note here that the size limits of the described patterning method have not yet been investigated, and therefore, this part of our study in Paper [2] merely serves as proof of principle.

An extension of the work in Papers [1] and [2] would be to investigate if other transition metals, e.g., Ni or Co, would yield better graphene quality with the same growth. Also, the grown graphene should be further processed into graphene test device structures to monitor their performance under typical device operating conditions.

Electron-Phonon Interactions in Hexagonal Materials

In Paper [3], we investigated some of the many-body interactions that occur in the valence band of hexagonal boron nitride (hBN), far away from the Fermi level. Indications of electron-phonon couplings were observed from the valence band maximum at high binding energies, reminiscent of those observed in the σ-band of graphene [68, 69]. As these σ-band electron-phonon couplings have been controversial in the past [139], our discovery of similar interactions in a different two-dimensional, hexagonal van der Waals material adds rigor to the previous findings and conclusion.

Furthermore, we observe an unusual second boson coupling, at approximately two times the maximum energy expected for optical phonons. While the origin of this second coupling is unclear, it matches well in energy with a potential two-phonon intra-band scattering process. Another possible origin could be phonon-mediated scattering between the hBN valence band and the van Hove (vH) singularity of the underlying graphene substrate. A more detailed theoretical study of electron-phonon scattering mechanisms in

hBN/graphene heterostructures is therefore needed to assess the true origin of the observed couplings.

Given the promise that highly doped graphene structures have shown for sustaining superconductivity, a second extension would be to investigate how the observed interactions in hBN change with either n-type or p-type doping. Given that hBN is an insulator with a large energy bandgap, shifting the Fermi level in hBN towards either the conduction or valence band should require much lower doping concentrations than what is needed to reach energy singularity points in graphene. It would be interesting to study the mentioned electron-phonon couplings in hBN with light, moderate, and strong doping concentrations and see if strong band renormalizations will occur. E.g., similar to the renormalizations observed in graphene when the Fermi level is shifted towards the vH singularity.

Atomic Arrangement in δ-Layer Structures

In Paper [4], we studied the in-plane arrangement of an ultrathin, 'δ-like' layer of phosphorous dopants in a silicon quantum device platform. Through clever experimental design and use of the chemical specificity available from XPD, we were able to unambiguously determine the atomic placement of the added phosphorous dopants in several systems with different doping concentrations. In all the observed cases, the phosphorous atoms would predominantly occupy the same lattice sites as Si atoms in bulk. I.e., they would dope the Si host material substitutionally. Furthermore, no signs of detrimental P$-$P dimerization were present.

Our work thus settles a decades-long dispute about δ-dopant placement once and for all. The answer to this problem is of great importance for understanding how such silicon quantum devices should perform. This is because their free carrier properties, specifically the 'valley splitting' of the free electron-like states induced in the δ-layer, will vary substantially with minor changes in dopant arrangement within the plane.

With the structure of the most common Si-based quantum device platform now established, it would be interesting to investigate the properties of other δ-layer systems and if their dopant atoms behave similarly or differently within the Si bulk. For instance, much less attention has been given to p-type δ-layer structures in later years, yet these can have several interesting properties. E.g., they have been predicted to be superconducting and can therefore be potential candidates for propagating and sustaining superconducting hole spin qubits [207].

Electron-Magnon Interactions

In Paper [5], a detailed study of the many-body interactions on Ni(111) was presented. From our investigations, both electron-phonon and electron-magnon interactions could be observed. These were disentangled and quantified by their coupling strength λ, based on their characteristic interaction energies and the functional form of their resultant, complex self-energies. In the spin minority bands, the electron-magnon interactions showed an interesting dependence on momentum and position in the Brillouin zone. In contrast, the electron-phonon couplings were practically position and momentum independent. Electron-phonon interactions of intermediate ($\lambda > 0.5$) coupling strength were also observed in near-parabolic spin majority bands that did not cross the Fermi level.

In Paper [6], the discussion of electron-magnon interactions was extended to the coupling between ferro- and antiferromagnets and electrons in an adjacent and intrinsically non-magnetic material across the magnetic interface. This theoretical study demonstrated the energetic nature of such interface coupling and the shape and magnitudes of their resultant, complex self-energies. Our studies showed that for conducting electrons in an adjacent topological insulator (TI), the strongest electron-magnon coupling could be achieved with uncompensated antiferromagnetic surfaces, where only one sub-lattice of the antiferromagnet participated in the interaction. We then simulated how the resultant self-energies would manifest themselves in model ARPES measurements of the TI/antiferromagnet heterostructure.

Electron-magnon couplings are potent pairing mechanisms in magnetic systems and critical ingredients in unconventional superconductivity. Understanding what parameters would affect their likelihood and coupling strength could offer insight into how unconventional superconductivity can be modified, and potentially also triggered and sustained in new materials. Particularly for the pairing mechanisms described in Paper [6], it would be interesting to find suitable candidate systems that could enable concomitant ARPES studies of interfacial electron-magnon coupling.

Appendix A

Interactions of s and p Orbitals

To calculate the bandstructure of graphene within the tight-binding model, the elements of the two matrices $\mathcal{H}$ and $\mathcal{B}$ in the *secular equation* (4.9) need to be estimated. These describe the overlap between the orbitals $2s$, $2p_x$, $2p_y$ and $2p_z$ from the atoms at sub-lattices A and B (see Fig. 4.1a), along the directions of the inter-atomic σ- and π-bonds. Each matrix element depends on the inter-atomic distance, but the other important factor is how the different orbitals pair when the overlap integrals are performed. Here, it will be shown which matrix elements of $\mathcal{H}$ and $\mathcal{B}$ contribute with non-vanishing terms, and how this can be determined, based on simple symmetry arguments for the s and p orbitals.

First, let us consider the overlap between an s and a p orbital as shown in Fig. A.1a. The p orbital is oriented along a direction $\mathbf{a}$ that represents one of the Cartesian directions $\{\hat{\mathbf{x}}, \hat{\mathbf{y}}, \hat{\mathbf{z}}\}$, with an arbitrary rotation relative to the direction $\mathbf{d}$ of the bond. Let $\mathbf{n}$ be the direction normal to $\mathbf{d}$. The p orbital can then be decomposed as

$$\mathbf{a}\left|p_a\right\rangle = \mathbf{a} \cdot \mathbf{d}\left|p_d\right\rangle + \mathbf{a} \cdot \mathbf{n}\left|p_n\right\rangle = \left|p_d\right\rangle \cos\theta + \left|p_d\right\rangle \sin\theta, \qquad (A.1)$$

where θ is the angle between $\mathbf{a}$ and $\mathbf{d}$ defined by $\mathbf{a} \cdot \mathbf{d}/|\mathbf{a}||\mathbf{d}| = \cos\theta$. The Hamiltonian matrix element between an s and a p orbital is then written as

$$\left\langle s\right| \hat{H} \left|p_a\right\rangle = \left\langle s\right| \hat{H} \left|p_d\right\rangle \cos\theta + \left\langle s\right| \hat{H} \left|p_n\right\rangle \sin\theta = H_{sp\sigma} \cos\theta, \qquad (A.2)$$

where $H_{sp\sigma} \equiv \left\langle s\right| \hat{H} \left|p_d\right\rangle$, and $\left\langle s\right| \hat{H} \left|p_n\right\rangle$ vanishes (s is even and p is odd along direction $\hat{\mathbf{n}}$). The subscripts of $H_{sp\sigma}$ indicate that it is made from orbitals s and p, forming a σ-bond with their non-vanishing components along $\mathbf{d}$. The Hermitian conjugate $\left\langle p_d\right| \hat{H} \left|s\right\rangle = H_{sp\sigma}^{\dagger} = H_{ps\sigma}$ is found by interchanging
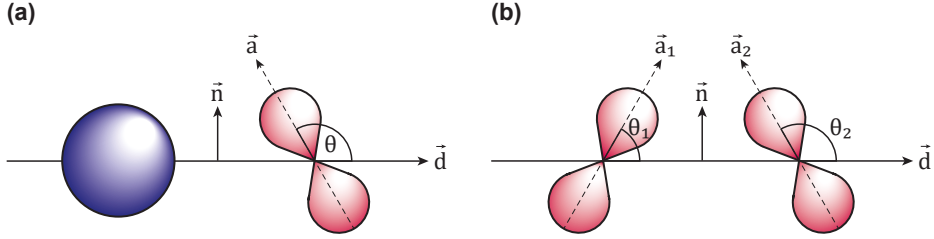
Figure A.1: Decomposition of overlapping s and/or p orbitals. **(a)**: A randomly oriented p orbital with direction **a**, overlapping with a spherically symmetric s orbital. The p orbital can be decomposed as contributions in the directions **d** and **n**. **(b)**: Two overlapping p orbitals with directions $\mathbf{a}_1$ and $\mathbf{a}_2$, at angles θ_1 and θ_2 relative to **d**, respectively.

the two orbitals in the inner product. This corresponds to the same bond, but along $-\mathbf{d}$ where $\theta \to \pi - \theta$ and $cos\theta \to -cos\theta$. Hence $H_{sp\sigma}^{\dagger} = -H_{sp\sigma}$ according to Eq. A.2.

Next, the overlap between two p orbitals is considered (Fig. A.1b). The bonding is again in direction **d**, with the two orbitals oriented along vectors $\mathbf{a}_1$ and $\mathbf{a}_2$, at angles θ_1 and θ_2 relative to the bond. The matrix element between orbitals p_{a1} and p_{a2} is

$$\langle p_{a1}| \hat{H} |p_{a2}\rangle = \langle p_{d1}| \hat{H} |p_{d2}\rangle \cos\theta_1 \cos\theta_2 + \langle p_{n1}| \hat{H} |p_{n2}\rangle \sin\theta_1 \sin\theta_2$$
$$= H_{pp\sigma} \cos\theta_1 \cos\theta_2 + H_{pp\pi} \sin\theta_1 \sin\theta_2. \tag{A.3}$$

Like before, the subscripts indicate the orbitals involved and the bond formed: $H_{pp\sigma}$ is a σ-bond formed from the components of two p orbitals and along **d**, and $H_{pp\pi}$ a π-bond from the normal components along **n**. Note that the cross-terms vanish because of the orthogonality between $|p_d\rangle$ and $|p_n\rangle$. The Hermitian conjugate $\langle p_{a1}| \hat{H} |p_{a2}\rangle^{\dagger} = \langle p_{a2}| \hat{H} |p_{a1}\rangle$ is again found by taking $\mathbf{d} \to -\mathbf{d}$ and $\theta \to \pi - \theta$. Then $\sin\theta_1 \sin\theta_2 \to \sin\theta_1 \sin\theta_2$ and $\cos\theta_1 \cos\theta_2 \to (-\cos\theta_1)(-\cos\theta_2)$. Thus, the Hermitian conjugates are equal to each other.

In Fig. A.2, eight different cases for overlaps between s and p orbitals on nearest-neighbor atomic sites have been sketched. For cases (5)-(8), the oddness of the atomic p orbital(s) and even-odd pairing of the two bonding orbitals lead to vanishing overlap integrals. For cases (1)-(4), the pairing is *even* and hence these four will have non-zero matrix elements.

To estimate the elements for matrix $\mathcal{B}$ instead of $\mathcal{H}$ the same method-
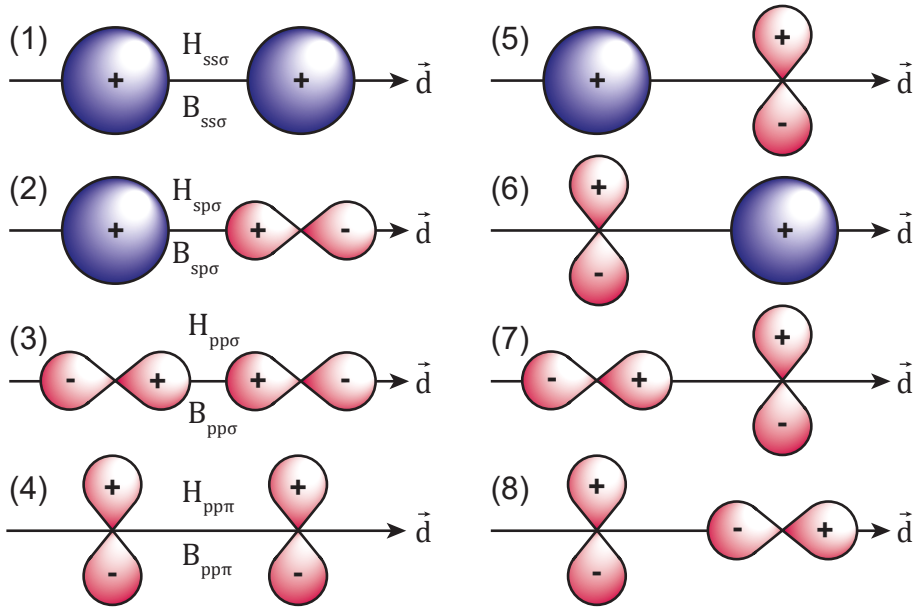
Figure A.2: Overlaps between s and p orbitals in the nearest-neighbor approximation. Cases (1)-(4) have non-vanishing overlap integrals, while the oddness of the p orbitals gives vanishing integrals for the remaining cases (5)-(8).

ology can be applied, but omitting the $\hat{H}$ operator from the inner products. In Table A.1, values for the orbital energies ε_{2s}, ε_{2p} and the terms H_{ijk}, B_{ijk} ($i, j = \{s, p\}$; $k = \{\sigma, \pi\}$) have been listed, as taken from Ref. [67].

Table A.1: Fundamental overlap integral values of the matrix elements from $\mathcal{H}$ and $\mathcal{B}$ in Eq. 4.9, used for the calculating the graphene bandstructure in the tight-binding approximation with nearest-neighbor interactions. Data taken from Ref. [67].

Indices $[ijk]$	$\mathcal{H}_{ijk}$ [eV]	$\mathcal{S}_{ijk}$ [no units]
$ss\sigma$	-6.769	0.212
$sp\sigma$	-5.580	0.102
$pp\sigma$	-5.037	0.146
$pp\pi$	-3.033	0.129
ε_{2s}	-8.868	
ε_{2p}	0	

Appendix B

Additional Papers

This appendix contains the 'additional' Papers [7–9], where the author has had a less significant (read: not first or second position) contribution to the work. Nonetheless, these have been included here for completeness. Their corresponding Supplementary documents can be found in Appendix C.

Electronic and structural properties of the natural dyes curcumin, bixin and indigo

Authors

Leander Michels
Annika Richter
Rajesh K. Chellappan
Håkon I. Røst
Alenka Behsen
Kristin H. Wells
Luciano Leal
Vilany Santana
Rosana Blawid
Geraldo J. da Silva
Simon P. Cooil
Justin W. Wells
Stefan Blawid

Check for updates

Electronic and structural properties of the natural dyes curcumin, bixin and indigo

Leander Michels, [ID] [a] Annika Richter,[a] Rajesh K. Chellappan,[b] Håkon I. Røst, [ID] [b] Alenka Behsen,[c] Kristin H. Wells, [ID] [d] Luciano Leal,[e] Vilany Santana,[e] Rosana Blawid,[f] Geraldo J. da Silva,[g] Simon P. Cooil,[h] Justin W. Wells [ID] *[bh] and Stefan Blawid[i]

An optical, electronic and structural characterisation of three natural dyes potentially interesting for application in organic solar cells, curcumin ($C_{21}H_{20}O_6$), bixin ($C_{25}H_{30}O_4$) and indigo ($C_{16}H_{10}N_2O_2$), was performed. X-Ray Diffraction (XRD) measurements, showed that curcumin has a higher degree of crystallinity compared to bixin and indigo. The results from the Pawley unit cell refinements for all dyes are reported. Optical absorption spectra measured by UV-Visible Spectroscopy (UV-Vis) on thermally evaporated films revealed that bixin undergoes chemical degradation upon evaporation, while curcumin and indigo appear to remain unaffected by this process. Combined Ultraviolet Photoemission Spectroscopy (UPS) and Inverse Photoemission Spectroscopy (IPES) spectra measured on the dyes revealed that all of them are hole-conducting materials and allowed for the determination of their electronic bandgaps, and Fermi level position within the gap. UV Photo-Emission Electron Microscopy (PEEM) revealed the workfunction of the dye materials and indicated that indigo has a negative electron affinity. PEEM was also used to study degradation by UV irradiation and showed that they are quite robust to UV exposure.

Introduction

Molecular dyes have become an essential part of dye sensitized solar cells (DSCs), and during the last two decades, significant improvements in efficiency and lifetime have been demonstrated. A significant proportion of these dyes are based on natural organic materials – for example derived from the coloured pigments found in fruit, flowers, and other plant material.[1–13]

Whilst solar cells based on synthesised polymers are currently marking the standard in higher performance organic photovoltaics (OPV),[14–16] there is a lot of potential in uncovering the suitability of natural materials. Using natural materials in organic photovoltaics, as opposed to synthetic polymers, is appealing considering that the processing of the latter often requires hazardous halogenated solvents.[17] On top of that, the sustainable harvesting of useful materials from nature could prove to be cost-effective, accessible in developing regions and free from environmental concerns. Some industries have already established this type of sustainable supply chain processes in the Amazon region.[18]

In this work, natural dyes, which due to their strong absorption in the visible spectrum have high potential for application in OPV, were investigated using optical, chemical, electronic and structural characterization methods. Specifically, we investigated three naturally occurring dyes; curcumin ($C_{21}H_{20}O_6$), bixin ($C_{25}H_{30}O_4$) and indigo ($C_{16}H_{10}N_2O_2$). The structure of the three dye molecules are depicted in Fig. 1. Curcumin is a pigment of turmeric and has been used as a spice and home-remedy against different ailments, most prominently in India, for centuries.[19,20] Bixin is the main carotenoid found in the seeds of the annatto tree native to South America and is extensively used as a food colourant,[21,22] while indigo is the common dye used in the production of denim cloth for blue jeans.[23] These materials have low toxicity (both tumeric and bixin are approved for consumption and labelled as E100 and E160b, respectively, in the European Union), and low price (tumeric and indigo currently have bulk prices around 3–5 US$ per kg, and bixin is approximately an order of magnitude more expensive).

[a]Department of Physics, Norwegian University of Science and Technology (NTNU), 7491 Trondheim, Norway

[b]Center for Quantum Spintronics, Department of Physics, Norwegian University of Science and Technology (NTNU), 7491 Trondheim, Norway. E-mail: quantum. wells@gmail.com

[c]Department of Clinical and Molecular Medicine, Norwegian University of Science and Technology (NTNU), 7491 Trondheim, Norway

[d]Department of Materials Science and Engineering, Norwegian University of Science and Technology (NTNU), 7491 Trondheim, Norway

[e]Department of Electrical Engineering, University of Brasília, 70910-900 Brasília, Brazil

[f]Department of Agronomy, Federal Rural University of Pernambuco, 52171-900 Recife, Brazil

[g]Institute of Physics, University of Brasília, 70910-900 Brasília, Brazil

[h]Department of Physics, University of Oslo, Sem Slands Vei 24, 7491, Oslo, Norway

[i]Center for Informatics, Federal University of Pernambuco, 50740-560 Recife, Brazil
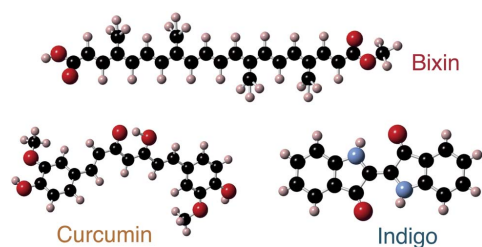
Fig. 1 Schematic depiction of three dye molecules: bixin, curcumin and indigo. The bixin molecule is drawn entirely as a schematic, but the curcumin and indigo molecules are the calculated (relaxed) structures; see 'calculations' section for details. Other tautomeric forms may also be possible. The molecules contain carbon (black spheres), hydrogen (peach), oxygen (red) and indigo additionally contains nitrogen (blue).

Experimental

All dyes used in this work were purchased from Sigma-Aldrich in powder form: Indigo (product number 229296), bixin (05989) and curcumin (both 78246 with ≥99.5% purity and curcuma longa powder C1386 with ≥60% purity were used).

Throughout this work, two different sample preparation methods have been used: (1) samples were prepared by thermal evaporation in vacuum using a custom built thermal evaporator, calibrated with an integrated thermocouple to monitor the temperature and (2) samples where prepared by drop-casting dye material dissolved in a solvent (ethanol or chloroform) onto a substrate and allowing the solvent to evaporate. All experimental methods were used on all samples, to allow any dependence on the preparation methods to be observed.

X-ray diffraction was performed at the XRD2 beamline at the Brazilian Synchrotron Light Laboratory (LNLS). The diffraction patterns were collected at a beam energy of 8 keV ($\lambda = 1.54978$ Å). The dyes were loaded as-supplied into a cavity in a Cu sample holder sealed on one side by 1.5 μm thin Al foil, which was demonstrated to have a high transparency at this photon energy. The scattered X-ray intensities were collected as a function of scattering angle 2θ.

UV-visible spectroscopy was performed in order to measure the spectral absorbance. For this experiment dye samples were prepared on 1 mm thick quartz glass holders, because quartz has very low absorbance in the wavelength range of interest (≈300–800 nm).

For studying the chemistry and electronic structure of the dyes, Photoemission Spectroscopy (PES) measurements were carried out in an ultra-high vacuum chamber. The samples were prepared by thermal evaporation on a non-reactive and clean (carbon-free) MoS_2 substrate, which was cleaved immediately before introducing it into the vacuum chamber. For studying the valence band states, Ultraviolet Photoemission Spectroscopy (UPS) was performed with a UV discharge lamp using the He-Iα emission line at 21.22 eV. For X-ray Photoelectron Spectroscopy (XPS) core-level acquisitions, an unmonochromated Mg-Kα X-ray source ($h\nu = 1254$ eV) was used. Imaging and UV degradation testing was performed using a NanoESCA PEEM with illumination from a high intensity unmonochromated Hg discharge lamp.

Conduction band states were studied by Inverse Photoemission Spectroscopy (IPES) in isochromat mode with an instrument built by PSP Vacuum Technology. This instrument uses a variable energy electron gun based on a low temperature BaO secondary electron emitter, and a modified channeltron detector which detects photons of fixed energy (≈9.6 eV).
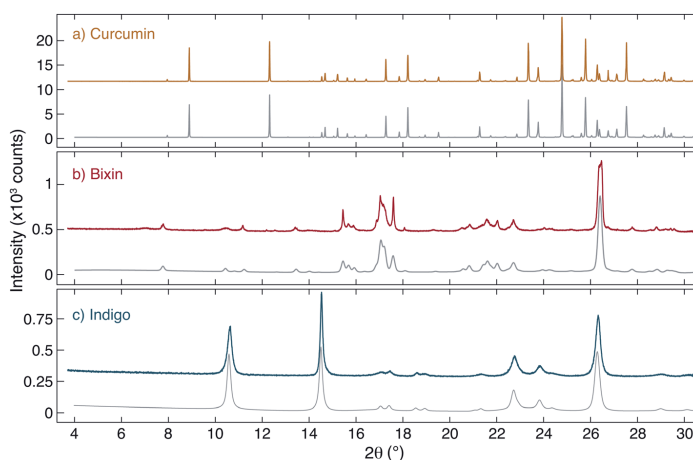

Fig. 2 Measured and simulated XRD signals. (a) Curcumin, (b) bixin and (c) indigo: in each case the upper (coloured) trace shows the data collected at the XRD2 beamline of the LNLS, and the lower trace (grey) shows simulated patterns obtained based on Pawley unit cell refinement. The structural parameters used are described in Table 1.

During XRD, XPS, PEEM, UPS and IPES acquisitions, care was taken to look for (and avoid) conditions under which beam damage of the materials could be occurring.

Results and discussion

The structure of the dyes was studied using X-ray diffraction. The measured diffraction patterns of curcumin, bixin and indigo together with simulated patterns obtained from a Pawley unit cell refinement[24,25] are shown in Fig. 2. Curcumin is found to show a significantly higher crystallinity (*i.e.* larger crystallites) than the other two dyes, as evidenced by the Bragg peak intensities and widths.

As a starting point for the Pawley refinement, the crystal structures found by Reid *et al.*[26] (curcumin), Kelly *et al.*[27] (bixin) and Süsse, Wolf *et al.*[28,29] (indigo) were used. In the case of indigo, both polymorphs indigo A and B (whose unit cells differ only slightly except for the parameter β) are expected to be present in the sample with the vast majority being indigo B. The refined unit cell parameters for all crystals are listed in Table 1. In all cases, the structure was found to be in reasonably good agreement with literature values and only a small refinement of the structural parameters from ref. 26–31 was needed. The geometric parameters used to refine the curcumin crystal structure were fixed in the refinement of indigo and bixin samples.

The solid-state structure of curcumin in the monoclinic space group $P2/n$ was first reported in 1982 by Tønnesen,[32] and later by several others.[26,33–35] Additional polymorphs of curcumin have also been reported, *i.e.* keto–enol tautomers, low temperature phases and possibly other polymorphs.[34–36] On the other hand, our finding of the common $P2/n$ phase is uncontroversial as the main form in simple dye extractions such as ours.

The available literature regarding the structure of bixin and indigo is less plentiful and generally uncontroversial. Our refined structural parameters for indigo differ by only a few percent from that of Süsse, Wolf *et al.*,[28,29] and our XRD results are visually similar to ref. 37. In the case of bixin, Pinzón-García

et al. studied bixin compounds for biomedical applications found that their material to be a semi-crystalline solid.[38] This is significantly different from the results reported here, which show a higher degree of crystallinity. A direct comparison between our XRD data and the data in ref. 38 reveals that the same peaks are present in both studies, however in ref. 38 the peaks are much weaker, broader and fit on top of a 'humped' background. This background intensity is large compared to the peak intensities and is maximal at $2\theta \approx 20°$. In our measurements, the background intensity is low and unstructured, and the peaks are significantly sharper. We interpret this to mean that we essentially see a similar crystal structure but that our crystallite size is significantly larger; *i.e.* the data is ref. 38 are indicative of very small crystallites and hence their sample is described as a 'semi-crystalline solid'. We suggest that this is probably a consequence of differences in the sample preparation which can cause the crystallisation of organic materials to be quite distinct.

Optical absorption spectra measured by UV-Visible Spectroscopy are shown in Fig. 3 for the three dyes used in this study. For each dye, measurements were performed both on
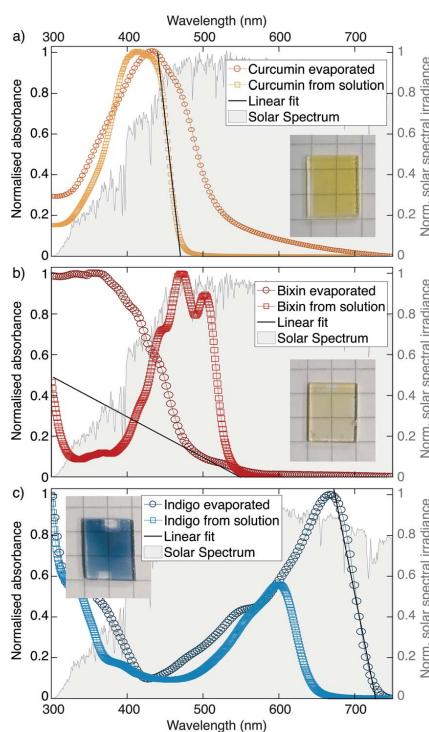

Fig. 3 UV-visible Absorption spectra. (a) Curcumin, (b) bixin and (c) indigo measured on evaporated films and in films prepared from solutions of the dyes in chloroform. Photographs of the evaporated samples are also shown.

Table 1 Refined lattice parameters of curcumin, bixin and indigo A and B obtained from Pawley unit cell refinement of measured XRD patterns and crystallite size analysis from Pawley fits. Indigo A phase occurs only in small amounts, and this makes the analysis have a higher uncertainty. Bixin has a very weak signal so the uncertainty is also relatively large. Note: uncertainties may be underestimated. Asterisk (*) indicates that the value is fixed to the literature value[29]

	Curcumin	Bixin	Indigo A	Indigo B
Space group	$P2/n$	$P\bar{1}$	$P2_1/c$	$P2_1/c$
a [Å]	12.7434(1)	11.479(2)	9.387(5)	10.939(2)
b [Å]	7.2207(2)	12.000(2)	5.682(3)	5.853(1)
c [Å]	20.056(1)	8.916(1)	11.898(7)	12.300(1)
α [°]	90	104.15(2)	90	90
β [°]	94.991(2)	93.37(1)	117*	130.20(2)
γ [°]	90	91.27(1)	90	90
Size [nm]	710 ± 20	84 ± 5	3.2 ± 0.2	37 ± 3

Table 2 Overview of the workfunction (obtained from the secondary cutoff observed with UPS/PEEM), optical bandgaps (obtained from UV-Vis absorption spectra) and electronic bandgaps (measured by photoemission spectroscopies UPS and IPES), together with the DFT calculated optical and HOMO–LUMO gaps. Note: the curcumin calculations are performed on 'trans' molecules (*i.e.* differing from the model if Fig. 5 by the placement of the central H atom), however this does not play an important role in the E_g calculation. Note also that the UPS-IPES bandgap uncertainty is an optimistic estimate

| | Empirical | | | | Calculated | |
| | Workfunction [eV] | E_g optical [eV] | | E_g electronic [eV] | E_g optical [eV] (single molecule) | E_g [eV] (HOMO–LUMO) |
		Evaporated	In solution	UPS/IPES		
Curcumin	3.2 ± 0.1	2.33 ± 0.02	2.64 ± 0.01	2.3 ± 0.1	3.08	3.60
Bixin	3.3 ± 0.1	2.5 ± 0.1	2.33 ± 0.02	2.8 ± 0.1	2.62	2.22
Indigo	1.7 ± 0.1	1.71 ± 0.01	1.92 ± 0.01	1.9 ± 0.1	1.81	2.05

a film which had been thermally evaporated on a quartz glass substrate as well as from a drop-cast solution of the dye in chloroform. The measured spectral absorbance was normalised in order to better compare the samples independent of film thickness. The graphs are underlaid with the AM 1.5 spectrum of solar irradiance (data from ref. 39). For visualisation purposes photographs of the evaporated films are also shown as insets.

In the case of curcumin and indigo, the spectra measured on the evaporated films are shifted to higher wavelengths compared to the measurements of the solutions, which can be explained by supramolecular polymerisation, as first described by Scheibe *et al.*[40] In the case of bixin, however, the spectrum of the evaporated film is shifted to shorter wavelengths, which is in line with the visibly yellow colour of the sample (as opposed to the red powder from which it is made). This suggests that bixin undergoes chemical degradation under the influence of the high temperatures involved during evaporation. We therefore infer that bixin is damaged by evaporation, but curcumin and indigo appear not to be.

From the absorption spectra presented in Fig. 3 estimations for the optical bandgap of the dyes were derived (see Table 2). The maximum wavelength at which the molecules absorb was determined by placing a linear fit on the absorption edge and finding the intersection with the x-axis. The prediction of the absorption edge could be slightly improved by applying the so-called Tauc relation.[41] The strong shift of the absorption edge of the evaporated bixin film towards shorter wavelengths corresponds to an increased bandgap as compared to the drop cast sample. Since a larger bandgap can generally be associated with a shorter conjugation length this could be an indicator that the evaporation causes the long conjugated chain of the molecule to break apart.

The electronic bandgap has also been measured using UPS and IPES. The UPS and IPES spectra for each dye are displayed together in Fig. 4. The graphs include linear fits applied to determine the valence and conduction band edges. The tail of the IPES data is a result of the gradual onset of photoionisation in the sodium chloride coated photocathode in the detector, and is also seen when measuring a polycrystalline Ag reference
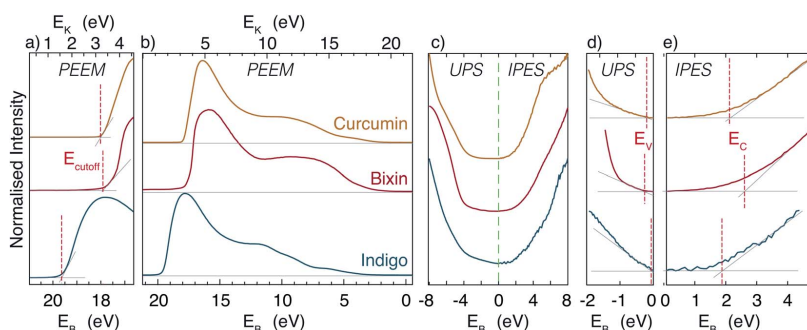

Fig. 4 Combined PEEM, UPS and IPES spectra of curcumin, bixin and indigo. (a) Detail of the low energy secondary cutoff, collected using PEEM (with the extracted value of E_{cutoff} indicated) and (b) the full bandwidth from E_{cutoff} to the Fermi level. (c) An overview of the states near to the bandgap for the three dyes. A zoom-in on the detail of (d) the valence band maxima and (e) the conduction band minima from the three dyes (coloured traces), together with the linear fits/extrapolations (fine grey lines) applied to extract the valence and conduction band edges. The vertical dashed red lines indicate the extracted values. All data is from samples prepared by in vacuum evaporation, except the UPS measurement of bixin: sample degradation by the UV source precluded this possibility and so this measurement is performed on a sample prepared from solution. Despite this precaution, the unusually large value of the conduction band minimum is thought to be indicative of sample degradation.

sample. It is therefore not considered to be primary signal, and is ignored. As can be seen from the figure, there is a moderate uncertainty involved in the extraction of the band extrema, due to the fact that the signal reduces in a nonlinear manner. This is an indication that the composition of the sample is not uniform; *i.e.* that it may have non uniform doping (from impurities such as water), *etc.*

In all three dyes the valence band edge is found to be much closer to the Fermi level than the conduction band edge. This means that the materials are p-type in character, *i.e.* that they are hole-conducting materials, as is the case for most organic semiconductors.[42]

The electronic bandgaps calculated as the difference between the valence and conduction band edges are listed in Table 2. The large bandgap observed in bixin stems mostly from the high conduction band edge, which is in line with the likely damaging of the molecule in the evaporated film on which the IPES measurement was performed. Additional uncertainty in the spectra of bixin is added by the fact that the films were very thin. As a result of this, contributions from organic contaminants cannot be ruled out, and that the UPS-IPES bandgap extraction for bixin is not completely reliable. However, for curcumin and indigo, the UPS-IPES bandgap analysis is reliable, and agrees well with the UV-vis measurement, indicating that the electronic and optical bandgaps are similar. Furthermore, the UPS-IPES also reveals the Fermi level position, and hence shows the relatively strong natural p-type nature of these dyes. Finally, the difference between the electronic bandgap and the optical gap is in general caused by the exciton binding energy. From the UV-Vis of evaporated films and the UPS/IPES measurements we would estimate exciton binding energies of ≈ 0 eV and 0.2 eV for curcumin and indigo, respectively.

The energy of the low energy secondary cutoff E_{cutoff} has also been extracted from UPS measurements (carried out using a biased sample in a PEEM instrument), and is shown in Fig. 4(a), together with the full bandwidth of the UPS signal in Fig. 4(b). From these measurements, it is straightforward to estimate the sample workfunction (*i.e.* E_{cutoff} relative to the Fermi energy). These values are shown in Table 2. For all dyes, the workfunction is surprising low, and in the case of indigo, the value we find is exceptionally low. In fact, for indigo, the workfunction of ≈ 1.7 eV is less than both the bandgap and the energy of the CBM, thus indicating that the electron affinity is negative. A negative electron affinity could potentially be useful for discouraging the process of electron–hole recombination, which is detrimental to PV efficiency.

XPS core level measurements have also been performed, and are plotted in Fig. 5. Widescans were performed to check for contamination, but only the expected components (*i.e.* C, N and O) were seen. The C 1s peak is of particular interest, and hence these sample were prepared on a freshly cleaved MoS_2 substrate; on which it is straightforward to prepare a new surface which is free of carbon.[43] Furthermore, being a van der Waals layered material, the surface contains no dangling bonds, and has been seen to be unreactive towards organic material.[43] The C 1s components have a rich structure due to the large number of inequivalent carbon atoms contained by each
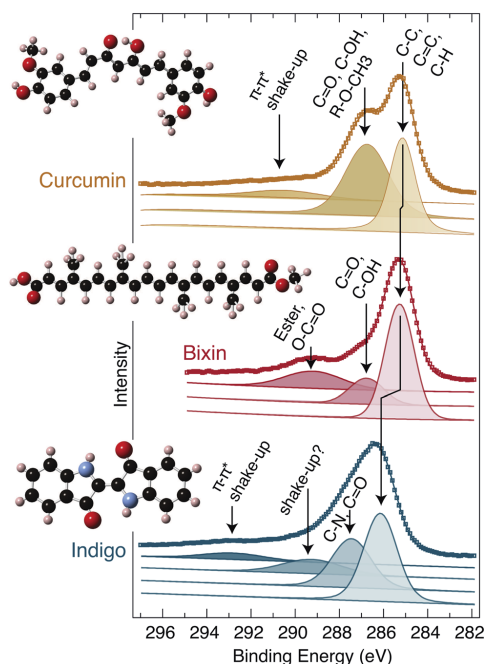

Fig. 5 XPS measurements. The C 1s spectra of curcumin, bixin and indigo. The curcumin and indigo samples were prepared by in-vacuum thermal evaporation, but the bixin sample was necessary prepared from solution. The raw data in presented using coloured squares together with fitted envelopes (solid lines) and the separated individual components from which the fits are comprised. Each component is labelled to indicate its chemical origin. The structure of the molecules are shown as insets to the figure. Note: for curcumin[26] and indigo[50] the calculated structure is used, but for bixin the inset is a schematic. All data are collected with a Mg-Kα X-ray source.

molecule. It is not feasible to deconvolute all of the individual carbon environments due to their small separation and broadness, but it is possible to identify groups of similar atomic environments. In Fig. 5, both the raw data (square markers) and fitted curves (continuous lines) are plotted, and the individual components which contribute to the overall fit are shown below. The tallest peak in each case is the lowest binding energy component; due to the C–C, C=C and C–H bonding which are prevalent in all three molecules. The neighbouring peak at higher binding energy (≈ 287–288 eV) is caused by carbon with an alcohol, aldehyde or ketone group attached, as well as the ether group (in the case of curcumin) or nitrogen neighbour (in the case of indigo). Additionally, curcumin and indigo exhibit a π–π* 'shake-up' at high binding energy (EB ≈ 291 and 293 eV, respectively), which is due to excitations between the filled and empty conjugated π states of the aromatic rings. Bixin also has a small higher binding energy peak (EB ≈ 290 eV) which is due to the ester and carboxylic carbon atoms. Finally, indigo exhibits a small and broad peak (EB ≈ 289 eV) which we

are unable to definitively explain, but suggest that it may also be due to a shake-up process.

The bixin C 1s components presented here are consistent with those published by Felicissimo *et al.*,[44] however there is a systematic shift in the binding energies. This could be due to differences in doping, instrument calibration, contamination or sample preparation.

Our assignment of the shake-up features[45] and carbon components has been based on published literature of a range of carbon containing materials, *i.e.* ref. 43 and [46–49]. Our analysis shows that, except for a small component in the indigo C 1s (which may be due to an additional shake-up process), all of the constituent components can be identified and matched with the expected chemical environments. *i.e.* this offers additional confirmation that the dyes have not been degraded during the preparation and XPS measurements.

Calculations

In addition to measuring the optical and electronic gap, we also computed the optical gap of the three dyes for a single molecule in vacuum. To achieve this, first the molecular geometry was optimised *via* density functional theory (DFT) employing a B3LYP functional with a 6-311+G(d,p) basis set. Although DFT is a ground state theory, we report also as reference the energy differences found between the highest occupied molecular orbital (HOMO) and the lowest unoccupied molecular orbital (LUMO). However, the HOMO–LUMO gap does not serve as an estimate of the fundamental gap, which is substantially underestimated by DFT.[51] Freezing the optimised geometry, the charge density response to a weak time-periodic external potential is computed *via* time dependent (TD) DFT. Fifty entries were considered in the coupling matrix between occupied and unoccupied states and the optical gap determined as the lowest dipole-allowed eigenvalue. For the TD-DFT computations the hybrid exchange–correlation functional CAM-B3LYP is used. The results are summarised in Table 2.

In case of curcumin, the computed single-molecule optical gap overestimates the values extracted from UV-vis both for evaporated samples (by $\approx 30\%$) as well as for the dyes in solution (by $\approx 17\%$). There are several potential reasons for this; for example, curcumin exists in different tautomeric forms and previous studies[52] have reported that the calculated gap is significantly different for the enol and keto forms (*i.e.* with and without a central hydrogen in the bridge site between the two O groups). It is also important to point out that the calculated values depend on the basis set used: we use B3LYP/6-31+G(d,p) whereas in the study by Abduljalil *et al.* a number of different basis sets are used.[52] On the other hand, Abduljalil *et al.* show results using 6-31+G(d,p) (which should be closely comparable with our calculations) and report HOMO–LUMO gap values of 3.60 eV (keto) and 3.25 eV (enol). In other words, whilst it is questionable whether the enol or keto form is the most appropriate to use, DFT nonetheless yields a value of E_{g} which is significantly higher than our experimental findings. We believe that this discrepancy may be an indication that single-molecule calculations do not adequately describe the experimental case.

This is fully consistent with the XRD analysis which shows that curcumin forms large (*i.e.* 300 nm) crystallites. In other words, the long range order present in the experimental films cause a significant deviation from the single-molecule case.

In the case of indigo the computed single-molecule optical gap agrees surprisingly well with the empirical value extracted from UV-vis for the evaporated sample (only 6% over-estimation). This points to only weakly interacting indigo molecules in the film. In addition to our own findings, we point out that in the work of Irimia-Vladu *et al.* a variety of methods are used and the optical and electronic gaps are reported.[37] Their reported values (all of which are around 1.7 eV) are at the lower end of our range, but in general the agreement between our work and theirs is very satisfactory. From the comparison of the optical gap extracted from UV-vis for evaporated samples and the bandgap extracted from UPS/IPES, an estimation of the exciton binding energy is possible. The difference gives ≈ 0 eV and 0.2 eV for curcumin and indigo, respectively. The very weakly coupled electron–hole pair in curcumin is interesting since it should facilitate charge separation in photovoltaic devices. If the finding is related to the good crystallinity of curcumin evidenced throughout the present work remains to be investigated.

For both indigo and curcumin, reliable measurements could be performed on evaporated samples. In the case of bixin, this does not seem to be possible because the thermal evaporation appears to significantly degrade the molecule, evidenced for example by a change in colour. Furthermore, whilst it appeared that XPS and UPS measurements could be performed without causing damage, degradation during the IPES measurement is likely. Thus, the most reliable empirical value for bixin is the optical gap of 2.33 eV measured in solution. If we assume a similar redshift as observed for the other two dyes, an optical gap in the order of 2.1 eV may be inferred for a hypothetical non-degraded bixin film. Thus, in comparison with the computed single-molecule optical gap of 2.62 eV, intermolecular interactions appear to be significant in bixin as in the case of curcumin.

Ageing due to UV exposure and heat

In order to evaluate the robustness of natural dyes in PV applications, we have also tested their response to UV exposure and heat. In addition to the He discharge lamp used in our PEEM instrument for the valence band and workfunction measurements, the instrument is also equipped with a high intensity Hg discharge lamp (photon energy ≈ 5 eV). We estimate the photon flux in the visible and UV range to be $\approx \times 10^4$ higher than solar flux: in other words, 1 h of exposure corresponds to ≈ 2 years of 12 h per day exposure to sunlight.

We conducted an experiment in which we first collected the full valence band and secondary cutoff using He illumination (*i.e.* Fig. 3(a) and (b)). We then left the sample exposed to high intensity illumination from the Hg lamp for up to 3 h (*i.e.* equivalent to ≈ 6 years of operation in sunlight), whilst occasionally remeasuring the valence band and secondary cutoff measurements to look for signs of damage. We have reported

a similar approach for accelerating UV induced changes previously.[43,53]

Following 2–3 h of Hg illumination, no dramatic changes are observed in the valence band structure. The VB intensity of bixin is seen to reduce by $\approx 20\%$, relative to the pristine sample. For indigo, the intensity reduction is less notable at $\approx 10\%$, and for curcumin no reduction is seen at all. All three dyes keep the same VB shape indicating that no dramatic change in bonding has occurred. All 3 dyes show a change of workfunction: curcumin and bixin show an increase of ≈ 0.5 eV whereas indigo shows a decrease of about the same magnitude. In short, after 2–3 h of exposure to an intense Hg source (simulating ≈ 6 years of operation in sunlight), some signs of degradation are seen in all three dyes. In all three cases, the degradation is not severe, and it is least noticeable in curcumin.

In addition to UV exposure, we have also tested the robustness to heating: Bixin appears to be damaged at quite low temperatures, but survives temperatures of at least ≈ 40 °C. Both curcumin and indigo can be heated to their evaporation temperature (≈ 170 °C without damage, as evidenced by the fact that the evaporated samples are extremely similar to samples prepared from solution. In other words, the dyes can generally survive temperatures sufficient for most PV applications, but bixin is least robust in this regard.

Conclusion

We have performed a comprehensive study of three natural dyes: curcumin, bixin and indigo. The material used here has been purified to a high standard, and the purpose of this work is to reveal the intrinsic structural, chemical and electronic properties of the selected dyes, and to consider their potential as components in an organic photovoltaic structure. In larger quantities, these materials are cheap (currently the market price for tumeric is 3 USD per kg, and indigo 5 USD per kg), they are also non-toxic (curcumin E100 and bixin E160b are both safe to consume), abundant and present no significant environmental concerns. In many respects, they are ideal candidates for 'socially responsible' photovoltaics.

Our work has utilised a wide range of experimental methods (X-ray diffraction, UV-visible absorption spectroscopy, X-ray photoelectron spectroscopy, UV photoemission spectroscopy, photoemission electron microscopy and inverse photoemission spectroscopy) combined with TD-DFT calculations. We have studied both thermally evaporated thin films, and samples prepared from solution. In line with the theme of low-budget and accessible materials, these preparation methods are also low budget and readably scalable. All three dyes were found to have bandgaps in a suitable range for PV applications (*i.e.* ≈ 1.7 to 2.8 eV) and low workfictions. Indigo was found to have an unusually low workfunction, indicating a negative electron affinity.

We report that all three materials can be satisfactorily prepared using low budget methods. However, whilst curcumin and indigo can easily be thermally evaporated without any sign of degradation, bixin needs to be handled more carefully. The thermally evaporated films of curcumin and indigo appear to be uniform, flat, continuous, and generally high quality and 'well behaved'. Not only is bixin degraded by thermal evaporation, but our measurement methods (especially IPES) may also cause degradation. Whilst this can be circumvented for the case of this study, it raises the question of its stability (and therefore suitability) in a real photovoltaic. Presumably some form of encapsulation would be used,[54] which may act to protect the dye molecules, but the fact that bixin is relatively easy to damage serves as a warning sign. Additional studies of its ageing under UV exposure would be straightforward to carry out[53] and could assist in concluding whether it is robust enough for applications involving extended UV exposure. In this regard, curcumin and indigo are of least concern since no sign of degradation was seen, even after significant exposure to high intensity UV.

The efficiency (and feasibility) of using natural dyes in photovoltaics has attracted significant attention. Whilst the reported efficiency for cells utilising these particular dyes is low (bixin on a TiO_2 substrate has shown 0.53% (ref. 10) and curcumin, mixed with red cabbage, has been reported to return a 0.6% efficiency[55]), the easy accessibility of the materials and preparation methods, coupled with the low toxicity, low cost and low environmental impact, makes such photovoltaics especially appealing in developing and 'off-grid' markets, and for low power applications.

Finally, our conclusion is that the robustness of curcumin and indigo, together with their 'close to optimal' bandgaps and doping make them the best candidates that we have studied so far in the search for natural materials for photovoltaic applications. Moreover, curcumin revealed an exceptionally low exciton binding energy. Whilst it may be possible to find even better candidates, our findings reassure us that low cost, socially and environmentally responsible photovoltaic for low power applications are certainly feasible.

Conflicts of interest

There are no conflicts to declare.

Acknowledgements

References

1 A. Kay and M. Graetzel, *J. Phys. Chem.*, 1993, **97**, 6272.

2 G. P. Smestad and M. Gratzel, *J. Chem. Educ.*, 1998, **75**, 752.

3 A. Polo and N. Y. Murakami Iha, *Sol. Energy Mater. Sol. Cells*, 2006, **90**, 1936.

4 S. Hao, J. Wu, Y. Huang and J. Lin, Solar Cells and Solar Energy Materials 2004, *Sol. Energy*, 2006, **80**, 209.

5 E. Yamazaki, M. Murayama, N. Nishikawa, N. Hashimoto, M. Shoyama and O. Kurita, *Sol. Energy*, 2007, **81**, 512.

6 M. S. Roy, P. Balraju, M. Kumar and G. D. Sharma, *Sol. Energy Mater. Sol. Cells*, 2008, **92**, 909.

7 K. Wongcharee, V. Meeyoo and S. Chavadej, *Sol. Energy Mater. Sol. Cells*, 2007, **91**, 566.

8 D. Zhang, S. M. Lanier, J. A. Downing, J. L. Avent, J. Lum and J. L. McHale, *J. Photochem. Photobiol., A*, 2008, **195**, 72.

9 G. Calogero and G. D. Marco, *Sol. Energy Mater. Sol. Cells*, 2008, **92**, 1341.

10 N. M. Gómez-Ortíz, I. A. Vázquez-Maldonado, A. R. Pérez-Espadas, G. J. Mena-Rejón, J. A. Azamar-Barrios and G. Oskam, 17th International Materials Research Congress 2008, *Sol. Energy Mater. Sol. Cells*, 2010, **94**, 40.

11 M. Peymannia, K. Gharanjig and A. M. Arabi, *Int. J. Energy Res.*, 2020, **44**, 309.

12 S. K. Das, S. Ganguli, H. Kabir, J. I. Khandaker and F. Ahmed, *Transactions on Electrical and Electronic Materials*, 2020, **21**, 105.

13 H. A. Maddah, V. Berry and S. K. Behura, *Renewable Sustainable Energy Rev.*, 2020, **121**, 109678.

14 X. Liu, H. Chen and S. Tan, *Renewable Sustainable Energy Rev.*, 2015, **52**, 1527.

15 L. Meng, Y. Zhang, X. Wan, C. Li, X. Zhang, Y. Wang, X. Ke, Z. Xiao, L. Ding, R. Xia, H.-L. Yip, Y. Cao and Y. Chen, *Science*, 2018, **361**, 1094.

16 Y. Cui, H. Yao, J. Zhang, T. Zhang, Y. Wang, L. Hong, K. Xian, B. Xu, S. Zhang, J. Peng, Z. Wei, F. Gao and J. Hou, *Nat. Commun.*, 2019, **10**, 2515.

17 S. Zhang, L. Ye, H. Zhang and J. Hou, *Mater. Today*, 2016, **19**, 533.

18 D. M. Boehe, L. S. Pongeluppe and S. G. Lazzarini, Nature and the development of a sustainable supply chain in the amazon region, in *Multinationals in Latin America: Case Studies*, ed. L. Liberman, S. Garcilazo and E. Stal, Palgrave Macmillan, London, UK, 2014, pp. 49–71.

19 H. P. T. Ammon and M. A. Wahl, *Planta Med.*, 1991, **57**, 1.

20 H. Hatcher, R. Planalp, J. Cho, F. M. Torti and S. V. Torti, *Cell. Mol. Life Sci.*, 2008, **65**, 1631.

21 M. J. Scotter, L. A. Wilson, G. P. Appleton and L. Castle, *J. Agric. Food Chem.*, 2000, **48**, 484.

22 D. Das and S. Chandra Bhattacharya, *Indian J. Fibre Text. Res.*, 2007, **32**, 366.

23 E. D. Głowacki, G. Voss, L. Leonat, M. Irimia-Vladu, S. Bauer and N. S. Sariciftci, *Isr. J. Chem.*, 2012, **52**, 540.

24 A. A. Coelho, *J. Appl. Crystallogr.*, 2018, **51**, 210–218.

25 G. S. Pawley, *J. Appl. Crystallogr.*, 1981, **14**, 357.

26 J. W. Reid, J. A. Kaduk, S. V. Garimella and J. S. Tse, *Powder Diffr.*, 2015, **30**, 67.

27 D. R. Kelly, A. A. Edwards, J. A. Parkinson, G. Olovsson, J. Trotter, S. Jones, K. M. A. Malik, M. B. Hursthouse and D. E. Hibbe, *J. Chem. Res.*, 1996, **445**, 2640.

28 P. Süsse and A. Wolf, *Naturwissenschaften*, 1980, **67**, 453.

29 P. Süsse, M. Steins and V. Kupcik, *Z. Kristallogr.*, 1988, **184**, 269.

30 Q.-L. Suo, Y.-C. Huang, L.-H. Weng, W.-Z. He, C.-P. Li, Y.-X. Li and H.-L. Hong, *Food Sci.*, 2006, **27**, 27.

31 G. Britton, S. Liaaen-Jensen and H. Pfander, *Carotenoids: Natural Functions*, ed. G. Britton, S. Liaaen-Jensen and H. Pfander, Birkhäuser, Basel, 2008, vol. 4.

32 H. H. Tønnesen, J. Karlsen and A. Mostad, *Acta Chem. Scand., Ser. B*, 1982, **36**, 475.

33 S. P. Parimita, Y. V. Ramshankar, S. Suresh and T. N. Guru Row, *Acta Crystallogr., Sect. E: Struct. Rep. Online*, 2007, **63**, o860.

34 P. Sanphui, N. R. Goud, U. B. R. Khandavilli, S. Bhanoth and A. Nangia, *Chem. Commun.*, 2011, **47**, 5013.

35 M. A. Matlinska, R. E. Wasylishen, G. M. Bernard, V. V. Terskikh, A. Brinkmann and V. K. Michaelis, *Cryst. Growth Des.*, 2018, **18**, 5556.

36 A. Renuga Parameswari, B. Devipriya, S. J. Jenniefer, P. Thomas Muthiah and P. Kumaradhas, *J. Chem. Crystallogr.*, 2012, **42**, 227.

37 M. Irimia-Vladu, E. D. Głowacki, P. A. Troshin, G. Schwabegger, L. Leonat, D. K. Susarova, O. Krystal, M. Ullah, Y. Kanbur, M. A. Bodea, V. F. Razumov, H. Sitter, S. Bauer and N. S. Sariciftci, *Adv. Mater.*, 2012, **24**, 375.

38 A. D. Pinzón-García, P. Cassini-Vieira, C. C. Ribeiro, C. E. de Matos Jensen, L. S. Barcelos, M. E. Cortes and R. D. Sinisterra, *J. Biomed. Mater. Res., Part B*, 2017, **105**, 1938.

39 National Renewable Energy Laboratory (NREL), *Reference solar spectral irradiance: Air mass 1.5*, 2020, http://rredc.nrel.gov/solar/spectra/am1.5/.

40 G. Scheibe, *Angew. Chem.*, 1937, **50**, 212.

41 E. C. Prima, N. N. Hidayat, B. Yuliarto, Suyatman and H. K. Dipojono, *Spectrochim. Acta, Part A*, 2017, **171**, 112.

42 H. Hoppe and N. S. Sariciftci, *J. Mater. Res.*, 2004, **19**, 1924.

43 J. Vinje, M. Falck, F. Mazzola, S. P. Cooil, H. Koch, I.-M. Høyvik and J. Wells, *Langmuir*, 2017, **33**, 9666.

44 M. P. Felicissimo, C. Bittencourt, L. Houssiau and J.-J. Pireaux, *J. Agric. Food Chem.*, 2004, **52**, 1810.

45 M. P. Keane, A. N. de Brito, N. Correia, S. Svensson and S. Lunell, *Chem. Phys.*, 1991, **155**, 379.

46 C. Wagner, W. Riggs, L. Davis and J. Moulder, *Handbook of X-ray photoelectron spectroscopy*, ed. G. Mullenberg, Perkin-Elmer Corporation, 1979.

47 N. E. Zander, J. A. Orlicki, A. M. Rawlett and T. P. Beebe, *ACS Appl. Mater. Interfaces*, 2012, **4**, 2074.

48 F. Mazzola, T. Trinh, S. Cooil, E. R. Østli, K. Høydalsvik, E. T. B. Skjønsfjell, S. Kjelstrup, A. Preobrajenski, A. A. Cafolla, D. A. Evans, D. W. Breiby and J. W. Wells, *2D Materials*, 2015, **2**, 025004.

49 Y. Gao, X. Liang, W. Bao, C. Wu and S. Li, *IEEE Trans. Dielectr. Electr. Insul.*, 2019, **26**, 107.

50 F. Kettner, L. Hüter, J. Schäfer, K. Röder, U. Purgahn and H. Krautscheid, *Acta Crystallogr., Sect. E: Struct. Rep. Online*, 2011, **67**, o2867.

51 L. Kronik, T. Stein, S. Refaely-Abramson and R. Baer, *J. Chem. Theory Comput.*, 2012, **8**, 1515.

52 H. M. Abduljalil, M. K. Muhsen and H. A. Hussein Madlool, *Journal of University of Babylon for Pure and Applied Sciences*, 2018, **26**, 48.

53 M. Jorge, S. Cooil, M. T. Edmonds, L. Thomsen, M. Nematollahi, F. Mazzola and J. W. Wells, *Mater. Res. Express*, 2017, **4**, 115502.

54 V. Tannira, A Study on the Photo-Stability of Spray Dried Bixin That is Encapsulated with Carbohydrates, PhD thesis, Lund University, 2017, student paper.

55 S. Furukawa, H. Iino, T. Iwamoto, K. Kukita and S. Yamauchi, 8th International Conference on Nano-Molecular Electronics, *Thin Solid Films*, 2009, **518**, 526.

One-Dimensional Spin-Polarised Surface States – A Comparison of Bi(112) with Other Vicinal Bismuth Surfaces

Authors

Anna Cecilie Åsland
Johannes Bakkelund
Even Thingstad
Håkon I. Røst
Simon P. Cooil
Jinbang Hu
Ivana Vobornik
Jun Fujii
Asle Sudbø
Justin W. Wells
Federico Mazzola

Enhanced Hydrophobicity of CeO$_2$ Thin Films by Surface Engineering

Authors

Damir Mamedov
Anna Cecilie Åsland
Simon P. Cooil
Håkon I. Røst
Johannes Bakkelund
Justin W. Wells
Smagul Karazhanov

Appendix C

Supplementary Documents

This appendix contains the Supplementary documents for Papers [1–9], in the same order as the papers have been listed in the thesis.

Supporting Information: Low Temperature Growth of Graphene on a Semiconductor

Håkon I. Røst,[*,†] Rajesh Kumar Chellappan,[*,†] Frode S. Strand,[†] Antonija Grubišić-Čabo,[‡] Benjamen P. Reed,[¶,△] Mauricio J. Prieto,[§] Liviu C. Tănase,[§] Lucas de Souza Caldas,[§] Thipusa Wongpinij,[∥] Chanan Euaruksakul,[∥] Thomas Schmidt,[§] Anton Tadich,[⊥] Bruce C.C. Cowie,[⊥] Zheshen Li,[#] Simon P. Cooil,[¶,@] and Justin W. Wells[*,†]

†*Center for Quantum Spintronics, Department of Physics, Norwegian University of Science and Technology (NTNU), NO-7491 Trondheim, Norway.*

‡*School of Physics & Astronomy, Monash University, Clayton, Victoria 3168, Australia.*

¶*Department of Physics, Aberystwyth University, Aberystwyth SY23 3BZ, United Kingdom*

§*Department of Interface Science, Fritz-Haber-Institute of the Max-Planck Society, Faradayweg 4-6, 14195, Berlin, Germany*

∥*Synchrotron Light Research Institute, 111 University Avenue, Muang District, Nakhon Ratchasima 30000, Thailand.*

⊥*Australian Synchrotron, 800 Blackburn Rd., Clayton, Victoria 3168, Australia.*

#*Department of Physics and Astronomy, Aarhus University, Ny Munkegade 120, 8000 Aarhus C, Denmark.*

@*Semiconductor Physics, Department of Physics, University of Oslo (UiO), NO-0371 Oslo, Norway*

△*Present address: National Physical Laboratory (NPL), Hampton Road, Teddington, TW11 0LW, UK.*

E-mail: hakon.i.rost@ntnu.no; rajesh.k.chellappan@ntnu.no; justin.wells@ntnu.no

Photoelectron Spectroscopy Measurements

High-energy-resolution X-ray Photoelectron Spectroscopy (XPS) measurements of the gra/Fe/SiC and gra/Ru/SiC were performed at the MatLine and "Soft X-ray" (SXR) endstations of the synchrotron radiation sources ASTRID (Aarhus) and the Australian Synchrotron (Melbourne, Victoria), respectively. At MatLine, core levels Fe 3p, Si 2p, C 1s, Ru 3d and O 1s were measured with photon energies ranging from 120-600 eV using a SCIENTA SES-200 analyzer, with energy resolutions 100-850 meV. The exact photon energy used, and therefore the binding energy of each core level spectrum, was calibrated using the core level signal generated by second order harmonic light from the same excitation energy as the principal peak. At SXR, the same core levels were recorded using excitation energies ranging from 100-1200 eV using a Specs Phoibos 150 analyzer, with an overall energy resolution in this range of 150-175 meV. The binding energy of each peak was calibrated to the Fermi level position of the metalized SiC substrate recorded over the corresponding photon energy range. All core level spectra were fitted using the Levenberg-Marquardt nonlinear least square method, using asymmetric pseudo-Voigt approximations to the Mahan functions of each chemical component as described by Schmid *et al.*[1] For the core level backgrounds, an "active" approximation to the Shirley-Vegh-Salvi-Castle background[2] was used: individual contributions to the background from each chemical component peak were modeled by error functions and fitted dynamically together with all peaks and background components to simulate the full photoemission signal of the region.

NEXAFS Measurements

Near-Edge X-Ray Absorption Fine Structure (NEXAFS) measurements were performed at the SXR endstation, in partial electron yield (PEY) mode and using linearly polarized light at incidence angles roughly 20-100° relative to the sample plane. For each measurement of the C 1s K-edge, a reference sample of highly oriented pyrolytic graphite (HOPG), as well

as a grounded gold mesh were placed upstream from the analysis chamber. During each scan, NEXAFS spectra for the reference sample and the drain current on the Au mesh were recorded simultaneously using a small portion of the beam. Additionally, the absolute photon intensities coming into the analysis chamber were subsequently measured over the same scan regions using a calibrated photodiode. The recorded NEXAFS signal was normalized to the drain current on the Au mesh (for details, see Ref. 3), and the spectral response of the photodiode was used as a secondary normalization to correct for any carbon contamination on the Au mesh. Using the well-known exciton resonance in HOPG occurring at 291.65 eV, the spectra of the HOPG reference that was measured in parallel with each scan was used to absolutely calibrate the energy scale of the data via a rigid shift. All energy and intensity flux corrections were performed using the Quick As NEXAFS Tool (QANT).[4]

Small Area LEEM, XPEEM, LEED and ARPES Measurements

Spatially resolved characterization of the surface graphene growth was performed using low-energy electron microscopy (LEEM), X-ray photoemission electron microscopy (XPEEM) and surface diffraction (μ-LEED). Measurements were carried out at the BL3.2Ub (aka "PEEM") endstation at the Synchrotron Light Research Institute (SLRI), Muang Distrinct, Thailand, and at the UE49-PGM-SMART endstation at BESSYII, Helmholtz-Zentrum Berlin, Germany. Additionally, bandstructure measurements were performed at UE49-PGM-SMART using small area angle-resolved photoemission spectroscopy (μ-ARPES).

Samples of gra/Fe/SiC and gra/Ru/SiC were prepared in a similar manner at the two facilities, using similar settings for the LEEM/PEEM instruments wherever possible. Clean 6H-SiC(0001) was confirmed by the lack of O 1s signal seen from plane XPS measurements, as well as a (1×1) or a $(\sqrt{3} \times \sqrt{3})$R30° reconstruction, indicating an atomically clean surface. Small differences in C-C signal from the C 1s were also observed. Neither the difference in

initial surface reconstruction nor the mentioned differences in XPS signal had any significant impact on the subsequent growth steps.

Metals were deposited using calibrated Fe and Ru sources, and the thickness of each film was confirmed from XPEEM and LEEM measurements. All μ-LEED measurements were recorded from selective areas of 1.5 µm diameter. Furthermore, similar measurements were performed in several different regions within a roughly 500 µm range of each sample to verify the homogeneity of the surface layers. A 40 eV excitation energy was used for all μ-LEED measurements, except the diffraction patterns after graphene formation at 620 °C (gra/Fe/SiC) and 800 °C (gra/Ru/SiC). Here, 140 eV and 50 eV were used, respectively, to reveal both the features native to graphene and the underlying SiC substrate. The μ-ARPES measurements of the graphene formed was recorded from 1.5 µm areas at room temperature. The measurements were performed with excitation energy $h\nu = 115$ eV, in energy steps of 100 meV and with an overall energy resolution of 500 meV.

References

(1) Schmid, M.; Steinrück, H.-P.; Gottfried, J. M. A new asymmetric Pseudo-Voigt function for more efficient fitting of XPS lines. *Surf. Interface Anal.* **2014**, *46*, 505–511.

(2) Herrera-Gomez, A.; Bravo-Sanchez, M.; Ceballos-Sanchez, O.; Vazquez-Lepe, M. Practical methods for background subtraction in photoemission spectra. *Surf. Interface Anal.* **2014**, *46*, 897–905.

(3) Watts, B.; Thomsen, L.; Dastoor, P. Methods in carbon K-edge NEXAFS: Experiment and analysis. *J. Electron. Spectros. Relat. Phenomena* **2006**, *151*, 105–120.

(4) Gann, E.; McNeill, C. R.; Tadich, A.; Cowie, B. C. C.; Thomsen, L. *Quick AS NEXAFS Tool (QANT)*: a program for NEXAFS loading and analysis developed at the Australian Synchrotron. *J. Synchrotron Rad.* **2016**, *23*, 374–380.

Supporting Information: A Simplified Method for Patterning Graphene on Dielectric Layers

Håkon I. Røst,*,† Benjamen P. Reed,‡,△ Frode S. Strand,† Joseph A. Durk,‡ D. Andrew Evans,‡ Antonija Grubišić-Čabo,¶,▽ Gary Wan,§ Mattia Cattelan,‖,†† Mauricio J. Prieto,⊥ Daniel M. Gottlob,⊥ Liviu C. Tănase,⊥ Lucas de Souza Caldas,⊥ Thomas Schmidt,⊥ Anton Tadich,# Bruce C.C. Cowie,# Rajesh Kumar Chellappan,† Justin W. Wells,†,@ and Simon P. Cooil*,‡,@

†*Center for Quantum Spintronics, Department of Physics, Norwegian University of Science and Technology (NTNU), NO-7491 Trondheim, Norway.*
‡*Department of Physics, Aberystwyth University, Aberystwyth SY23 3BZ, United Kingdom*
¶*School of Physics & Astronomy, Monash University, 1 Wellington Rd., Clayton, Victoria 3800, Australia.*
§*School of Physics, HH Wills Physics Laboratory, University of Bristol, Tyndall Avenue, Bristol, BS8 1TL, United Kingdom*
‖*School of Chemistry, University of Bristol, Cantocks Close, Bristol, BS8 1TS, United Kingdom*
⊥*Department of Interface Science, Fritz-Haber-Institute of the Max-Planck Society, Faradayweg 4-6, 14195, Berlin, Germany*
#*Australian Synchrotron, 800 Blackburn Rd., Clayton, Victoria 3168, Australia.*
@*Semiconductor Physics, Department of Physics, University of Oslo (UiO), NO-0371 Oslo, Norway*
△*Present address: National Physical Laboratory (NPL), Hampton Road, Teddington, TW11 0LW, UK.*
▽*Present address: KTH Royal Institute of Technology, Applied Physics, Hannes Alfvéns väg 12, SE-114 19 Stockholm, Sweden.*
††*Present address: Elettra Sincrotrone Trieste, s.s. 14 - km.163,5 in Area Science Park, Basovizza, Trieste, 34149, Italy*

E-mail: hakon.i.rost@ntnu.no; scooil@icloud.com

Table of Contents (TOC) Graphic

The TOC graphic contains: (left) a schematic showing the final stage of the growth as described in more detailed in the following section, and (right) an artificially colored PEEM micrograph of patterned graphene on Ru, based on the photoemission yield near the low-energy secondary electron cutoff (SEC). The color scale of the micrograph as been chosen to amplify small variations in photoemission intensity between the structures.
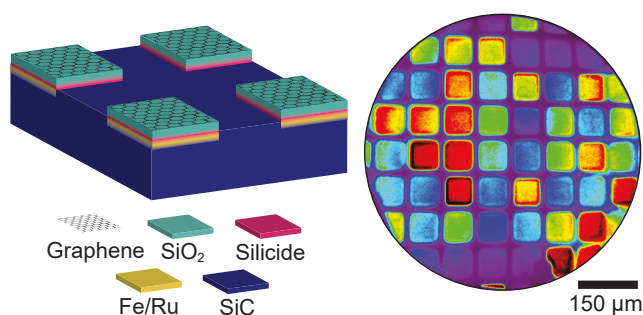
Figure S1: TOC graphic

Sample Preparation

The preparation of patterned graphene structures on SiO_2 is outlined in Figure S2. Graphene on SiC was grown according to the metal-mediated approach, utilizing thermally activated thin films of transition metals (TMs) Fe or Ru on top of HF etched and thermally cleaned 6H-SiC(0001) surfaces (see Refs. 1–3). The metal thin films were deposited through finely meshed, (50 and 500 µm) shadow masks, forming patterned metal islands with thicknesses 1-2 nm on the clean SiC surfaces (step I). These metal treated regions served as growth sites for graphene upon thermal activation to temperatures 600-700 °C, confining the lateral spread of graphene to within the boundary of each island (step II). X-ray photoelectron spectroscopy (XPS) measurements of graphene formation on Ru/SiC are shown in FIGs. S3e and S3f.

Upon formation the samples were heated to higher temperatures ($T > 700\,°C$) for longer durations to diffuse the transition metal into the SiC substrate (step III). Finally, the samples were either i) exposed to atomic Si for 40 minutes at a rate of $0.15\,Å/\,min$ while being heated to $450\,°C$ and then exposed to air, or ii) exposed to air directly (step IV). All samples were finally reintroduced to vacuum and gently annealed to $300\,°C$ to desorb any contaminants from the air exposure.
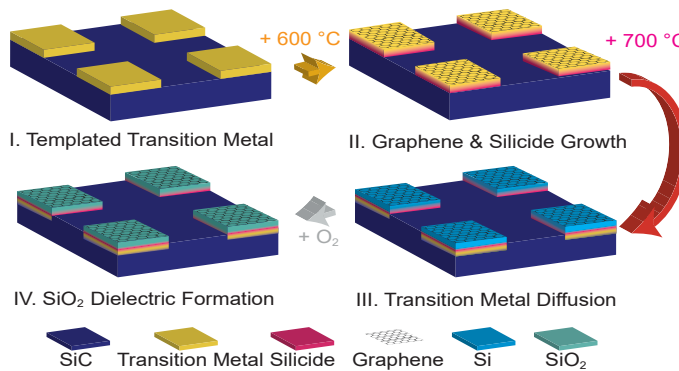
Figure S2: A Schematic overview of the four growth steps used to form patterned graphene structures on SiO_2.

Small-Spot EF-PEEM, LEEM and LEED Measurements

In order to assess the selectivity of graphene growth on top of the transition metal, samples patterned with Fe or Ru were studied before and after the thermal treatments using spatially resolved electron microscopy, electron diffraction and energy-resolved photoemission microscopy. At the UE49-PGM-SMART endstation of BESSY II, Helmholtz-Zentrum Berlin, Germany, graphene was prepared on SiC covered with $500\,µm$ diameter islands of Fe or Ru thin films as described. Inside the graphene growth regions, energy-filtered PEEM (EF-PEEM) measurements of the C 1s, Fe 2p and Ru 3d core levels were performed at $300\,K$.

For the double aberration-corrected measurements of the C 1s shown in the main text, the overall energy resolution was 540-620 meV.

The lateral resolution of the patterned graphene was determined from the edge profile between the growth region and the SiC substrate. The region close to the edge was measured using low-energy electron microscopy (LEEM) with an electron kinetic energy $E_{\mathrm{K}} = 2.0\,\mathrm{eV}$ and fitted using an error function. From the optimized fit the standard deviation of the corresponding Gaussian was extracted and used to determine the full width at half maximum (FWHM) of the profile. The sharpest feature observed in the experiments had a FWHM of 190 nm. Given that the lateral resolution achievable with this instrument setup has been shown to be better than 20 nm (see Ref. **?**), the FWHM obtained was assumed to represent the resolution of the pattern under the limitations of the lensing effects already discussed in the main text.

Small spot low-energy electron diffraction (μ-LEED) measurements were collected from selected areas of 1.5 μm diameter using excitation energy 140 eV. Similar measurements were performed in several different regions across the diameter of each patterned feature, as well as in selected areas outside to verify that graphene had formed exclusively within the patterned regions. These measurements also confirmed the homogeneity of the newfound graphene layers.

Small-Area XPS and Work Function Measurements

Small area XPS and spatially resolved work function measurements were performed at the Bristol NanoESCA Facility, United Kingdom, to study the development of the patterned graphene on Ru with successive heat treatments and exposure to oxygen. XPS measurements of the C 1s, Ru 3d, Si 2p and O 1s core levels were performed using monochromatic Al Kα radiation ($h\nu = 1486.7\,\mathrm{eV}$) and an ARGUS CU analyzer, with an overall energy resolution of less than 300 meV. The development of the C 1s and Si 2p core levels at each relevant

stage of the experiment is showcased in Figures S3e and S3f, respectively.

The spatially resolved work functions (WFs) and associated SECs were recorded within the patterned graphene regions at 300 K using a NanoESCA II aberration corrected EF-PEEM equipped with a non-monochromatic Hg photoexcitation source ($h\nu \approx 5.2\,\text{eV}$) and a 150 μm contrast aperture, using pass energy $E_\text{P} = 50\,\text{eV}$ and a 0.5 mm entrance slit. With the given settings, the instrument had a lateral resolution better than 150 nm and an overall energy resolution better than 150 meV. The NanoESCA allows accurate determination of the material work function ϕ_S using a fixed pass energy E_P, and tunable photoelectron retardation R and biasing of the sample under investigation. The energy of emitted electrons relative to the Fermi level $E - E_\text{F}$ can be recorded according to the relation:

$$E - E_\text{F} = h\nu - E_\text{B} = R + E_\text{P} + \phi_\text{A} = E_\text{K} + \phi_\text{S}, \tag{1}$$

where $h\nu$ is the photoexcitation energy, E_B is the binding energy in the electron(s) photoexcited form the sample, E_K is their kinetic energy after being ejected to vacuum and ϕ_A is the analyzer work function. At zero E_K the electrons are unable to escape the sample, and ϕ_S is directly related to the measured energy position of the SEC relative to the Fermi level.[4]

Raman spectroscopy measurements

Following the iron-mediated graphitization of SiC at the UE-49-PGM-SMART endstation, the sample was removed from UHV and Raman mapping measurements were acquired using a HORIBA Jobin Yvon LabRAM HR Raman spectrometer at the Department of Physics, Aberystwyth University. A 10 mW 532 nm laser source was coupled to a x100 objective to form a 10 μm diameter circular spot on the G/Fe/SiC sample surface. A diffraction grating with 1800 lines/mm was selected, with confocal hole and slit widths of 1000 μm and 500 μm respectively.

To demonstrate the occurrence of graphene within the growth regions, Raman spectra
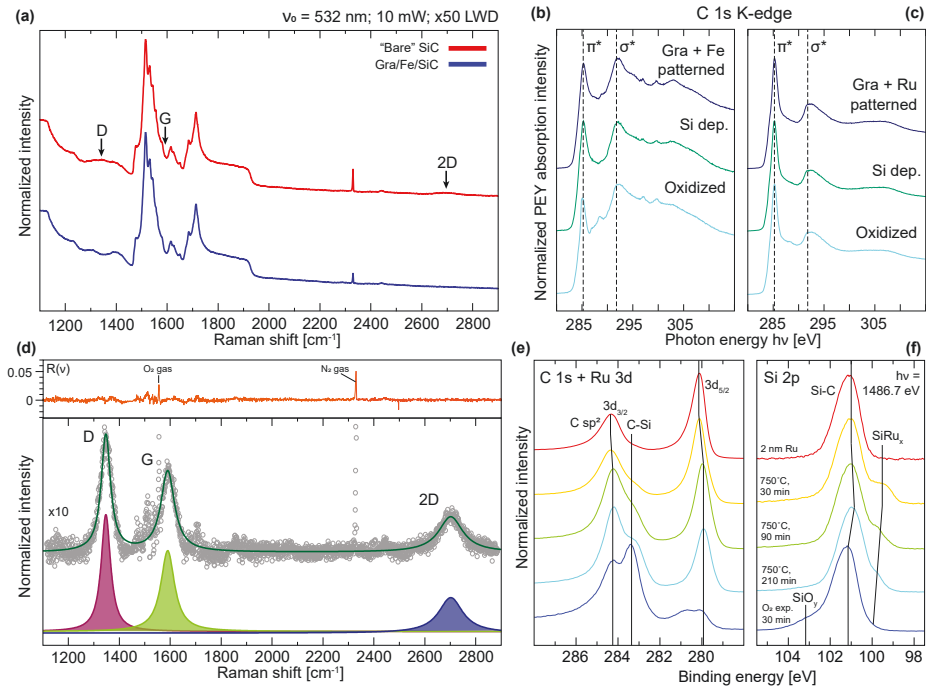
Figure S3: **Small-area Raman, NEXAFS and XPS measurements of patterned graphene.** **(a)** Raman spectroscopy measurements of SiC (red) and patterned graphene (500 µm circular regions) grown on a thin film of Fe on SiC (blue). Both excitation spectra were recorded using a 10 mW green (532 nm) laser with 10 µm spot size in separate regions of the sample; namely inside and outside of the graphene growth region. The approximate Raman shifts for the relevant vibrational modes excited, namely the D, G and 2D peaks, have been marked. **(b)** The near-edge X-ray absorption fine structure (NEXAFS) for graphene grown on patterned islands of Fe on SiC, before (dark blue) and after subsequent Si intercalation (green) and oxidation of the Si intercalants (light blue). **(c)** Similar NEXAFS measurements, but for graphene grown on patterned Ru on SiC. The measurements in both (b) and (c) were recorded using linearly polarized light at near grazing incidence ($\theta \approx 20°$) to the sample plane. **(d)** The difference spectrum of the two curves in (a), fitted using three Lorentzian peaks representing the three characteristic vibrational modes commonly seen in graphene Raman spectroscopy. The residual wave $R(v)$ bewtween the fit and the difference curve is also shown (top), together with annotations for additional excitations commonly observed in ambient systems. **(e,f)** X-ray photoelectron spectroscopy (XPS) measurements of the C 1s and Si 2p core levels, respectively, before (red) and after (yellow) deposition of 2 nm Ru, and with annealing to 750 °C for increasing duration (green) until substantial graphene formation is observed (light blue). The final two curves (dark blue) showcase the core levels after exposing the sample to oxygen at 200 mbar for 30 minutes.

S6

with an energy window 1100-2900 cm^{-1} were recorded both inside the growth regions and outside, i.e. from the bare SiC substrate. Both spectra were normalized to the SiC feature at 1510 cm^{-1} (Figure S3a), and a difference spectrum was calculated between the two. The residual background was then fitted with a spline and that intensity was subtracted from each data set to remove any differences in the backgrounds from the SiC. The background corrected difference spectrum was finally fitted using Lorentzian peaks to obtain measures of the characteristic G, D and 2D peaks of the graphene as grown (Figure S3d).

To verify the spatial distribution of graphene exclusively inside the growth region, a Raman map with dimensions of 200 µm × 200 µm (10 µm step size, 400 spectra) was acquired, specifically centred on the edge of a graphene/Fe spot. The energy of the spectrometer was set around 2700 cm^{-1} (2500 to 2900 cm^{-1}) to record the characteristic 2D Raman mode indicative of ordered graphene/graphite at each point of the Raman map. Due to a lack of surface-enhancement effect for the Raman signal (i.e. usually observed for graphene on SiO$_2$/Si, see Refs. 5,6), extended acquisition times and multiple accumulations were required: a gate time of 120 seconds with 10 accumulations was used to improve the signal-to-noise ratio for peak fitting and remove noise from cosmic rays. Once recorded, similar background corrections and fittings as for the wide energy window were performed to obtain the overall intensity and FWHM of the graphene 2D peak as a function of its spatial location.

Synchrotron XPS and NEXAFS measurements

High-energy-resolution XPS and near edge X-ray absorption fine structure (NEXAFS) measurements were performed at the "Soft X-Ray" (SXR) endstation of the Australian Synchrotron (Melbourne, Victoria). The core levels C 1s, Si 2p, Fe 3p and Ru 3d were recorded at each relevant stage of the sample preparation, with excitation energies in the range 100-1200 eV using a Specs Phoibos 150 analyser with an overall energy resolution of 150-175 meV. The binding energy of each core level was calibrated to the metallic Fermi level position of

SiC with Fe or Ru added, over the corresponding energy range.

Upon graphene formation, NEXAFS measurements of the C 1s K-edge were performed at each successive stage of the experiment to assess the quality and stability of the graphene layers (see Figs. S3b and S3c). All measurements were performed in partial electron yield (PEY) mode and using linearly polarized light at grazing incidence angle ($\theta \approx 20°$) relative to the sample plane. During each measurement, a reference sample of HOPG was measured simultaenously with the sample for energy calibration of the spectra, whilst the photocurrent from a 50% transmissive gold mesh located just before the sample was used to measure the variation in photon flux during the scan. Additionally, the absolute photon intensities coming in to the analysis chamber were subsequently measured over the same energy range using a calibrated photodiode. The recorded NEXAFS spectra were normalized to the corresponding drain current on the Au mesh (for details, see Ref. 7), and the spectral response of the photodiode was used as a secondary normalization to correct for any carbon contamination on the Au mesh. Using the well known exciton resonance in HOPG occuring at 291.65 eV, the HOPG reference spectra measured in parallel with each scan were used to absolutely calibrate the energy scale of the data via a rigid shift. All energy and intensity flux corrections were performed using the Quick As NEXAFS Tool (QANT).[8]

Metal Diffusion into SiC

Diffusion of the metals Fe and Ru into the SiC substrate upon higher temperature annealing ($T > 700\,°C$) was ascertained by evaluating the relative intensity of Fe 3p and Ru 3d against the Si 2p signal of the substrate. By comparing the intensity of the metal to the underlying Si, any common attenuation of the two due to formation of carbon at the surface would, to a first approximation, be accounted for. As discussed in Ref. 3, consecutive heat treatments to 700 °C and then 800 °C of the gra/Fe/SiC and gra/Ru/SiC systems reduced the relative concentration of metal to SiC near the surface to < 50% of what was observed upon metallization.

An example of how the intensity of the Fe 3p core level of metallized SiC develops with temperature is shown in Figure S4. The Fe 3p signal at each stage has been scaled by the intensity of corresponding Si 2p signal, both recorded with $h\nu = 1254\,\text{eV}$ and with any differences in photoelectron inelastic mean-free paths (IMFPs) and photo-ionization cross-sections corrected for.
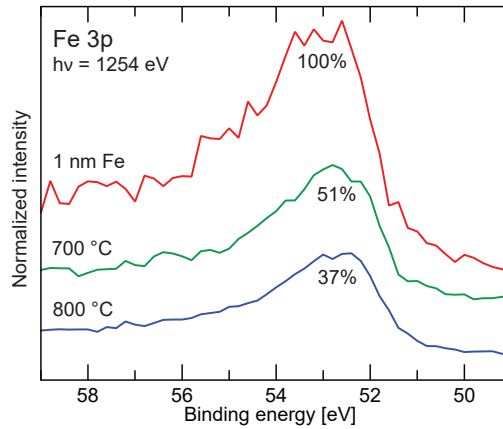
Figure S4: Development of the Fe 3p core level for metallized 6H-SiC with increasing temperature. The intensity of each Fe 3p peak has been normalized to the Si 2p intensity at the same experimental stage, corrected for differences in IMFPs and photo-ionization cross-sections. Annealing above $700\,^\circ\text{C}$ reduces the concentration of Fe near the surface by $> 60\%$.

References

(1) Cooil, S.; Song, F.; Williams, G.; Roberts, O.; Langstaff, D.; Jørgensen, B.; Høydalsvik, K.; Breiby, D.; Wahlström, E.; Evans, D.; Wells, J. Iron-Mediated Growth of Epitaxial Graphene on SiC and Diamond. *Carbon* **2012**, *50*, 5099–5105.

(2) Cooil, S.; Wells, J.; Hu, D.; Niu, Y.; Zakharov, A.; Bianchi, M.; Evans, D. Controlling the Growth of Epitaxial Graphene on Metalized Diamond (111) Surface. *Appl. Phys. Lett.* **2015**, *107*, 181603.

(3) Røst, H. I.; Chellappan, R. K.; Strand, F. S.; Grubišić-Čabo, A.; Reed, B. P.; Prieto, M. J.; Tǎnase, L. C.; Caldas, L. d. S.; Wongpinij, T.; Euaruksakul, C.; Schmidt, T.; Tadich, A.; Cowie, B. C. C.; Li, Z.; Cooil, S. P.; Wells, J. W. Low-Temperature Growth of Graphene on a Semiconductor. *J. Phys. Chem. C* **2021**, *125*, 4243–4252.

(4) Escher, M.; Weber, N.; Merkel, M.; Krömker, B.; Funnemann, D.; Schmidt, S.; Reinert, F.; Forster, F.; Hüfner, S.; Bernhard, P.; Ziethen, C.; Elmers, H.; Schönhense, G. NanoESCA: Imaging UPS and XPS with High Energy Resolution. *J. Electron Spectros. Relat. Phenomena* **2005**, *144-147*, 1179–1182, Proceeding of the Fourteenth International Conference on Vacuum Ultraviolet Radiation Physics.

(5) Wang, Y.; Ni, Z.; Shen, Z.; Wang, H.; Wu, Y. Interference Enhancement of Raman Signal of Graphene. *Applied Physics Letters* **2008**, *92*, 043121.

(6) Yoon, D.; Moon, H.; Son, Y.-W.; Choi, J. S.; Park, B. H.; Cha, Y. H.; Kim, Y. D.; Cheong, H. Interference Effect on Raman Spectrum of Graphene on SiO_2/Si. *Phys. Rev. B* **2009**, *80*, 125422.

(7) Watts, B.; Thomsen, L.; Dastoor, P. Methods in Carbon K-Edge NEXAFS: Experiment and Analysis. *Journal of Electron Spectroscopy and Related Phenomena* **2006**, *151*, 105–120.

(8) Gann, E.; McNeill, C. R.; Tadich, A.; Cowie, B. C. C.; Thomsen, L. *Quick AS NEXAFS Tool (QANT)*: A Program for NEXAFS Loading and Analysis Developed at the Australian Synchrotron. *J. Synchrotron Rad.* **2016**, *23*, 374–380.

Bibliography

[1] H. I. Røst et al. "Low-Temperature Growth of Graphene on a Semi-conductor". In: *The Journal of Physical Chemistry C* 125.7 (2021), pp. 4243–4252. DOI: `10.1021/acs.jpcc.0c10870`.

[2] H. I. Røst et al. "A Simplified Method for Patterning Graphene on Dielectric Layers". In: *ACS Applied Materials & Interfaces* 13.31 (2021), pp. 37510–37516. DOI: `10.1021/acsami.1c09987`.

[3] H. I. Røst et al. "Phonon-Induced Mass Enhancements in a Wide Bandgap Material". In: *Manuscript* (July 2022).

[4] H. I. Røst et al. "Probing the Atomic Arrangement of Sub-Surface Dopants in a Silicon Quantum Device Platform". In: *Manuscript* (July 2022).

[5] H. I. Røst et al. "Disentangling Electron-Boson Interactions on the Surface of a Familiar Ferromagnet". In: *Manuscript* (July 2022).

[6] K. Mæland et al. "Electron-magnon coupling and quasiparticle lifetimes on the surface of a topological insulator". In: *Physical Review B* 104 (2021), p. 125125. DOI: `10.1103/PhysRevB.104.125125`.

[7] L. Michels et al. "Electronic and structural properties of the natural dyes curcumin, bixin and indigo". In: *RSC Advances* 11.23 (2021), pp. 14169–14177. DOI: `10.1039/d0ra08474c`.

[8] A. C. Åsland et al. "One-Dimensional Spin-Polarised Surface States – A Comparison of Bi(112) with Other Vicinal Bismuth Surfaces". In: *Manuscript* (July 2022).

[9] D. Mamedov et al. "Enhanced Hydrophobicity of CeO_2 Thin Films by Surface Engineering". In: *ChemRxiv preprint* (2022). DOI: `10.26434/chemrxiv-2022-8v3hz`.

[10] A. Einstein. "Über einen die Erzeugung und Verwandlung des Lichtes betreffenden heuristischen Gesichtspunkt". In: *Annalen der Physik* 322.6 (1905), pp. 132–148. DOI: 10.1002/andp.19053220607.

[11] K. Siegbahn. "Electron Spectroscopy for Atoms, Molecules, and Condensed Matter". In: *Reviews of Modern Physics* 54 (1982), pp. 709–728. DOI: 10.1103/RevModPhys.54.709.

[12] S. Hüfner. *Photoelectron Spectroscopy: Principles and Applications.* 3rd ed. Berlin: Springer Science & Business Media, 2003. Chap. 1, 6, 11. ISBN: 3-540-41802-4.

[13] S. D. Kevan and W. Eberhardt. *Angle-Resolved Photoemission: Theory and Current Applications.* Ed. by Stephen Douglas Kevan. Elsevier Amsterdam, 1992. Chap. 4. ISBN: 0-444-88183-2.

[14] J. Stöhr. *NEXAFS Spectroscopy.* Vol. 25. Springer Science & Business Media, 1996. ISBN: 3-540-54422-4.

[15] D. P. Woodruff. "Adsorbate structure determination using photoelectron diffraction: Methods and applications". In: *Surface Science Reports* 62.1 (2007), pp. 1–38. DOI: 10.1016/j.surfrep.2006.10.001.

[16] J. Linder. *Intermediate Quantum Mechanics.* 1st ed. Bookboon, 2017. Chap. 4. ISBN: 978-87-403-1783-1.

[17] A. Damascelli. "Probing the electronic structure of complex systems by ARPES". In: *Physica Scripta* 2004.T109 (2004), p. 61. DOI: 10.1238/physica.topical.109a00061.

[18] D. Attwood and A. Sakdinawat. *X-Rays and Extreme Ultraviolet Radiation: Principles and Applications.* 2nd ed. Cambridge University Press, 2021. Chap. 1. ISBN: 978-1-107-06289-4.

[19] D. J. Griffiths. *Introduction to Quantum Mechanics.* 2nd ed. Cambridge University Press, 2017. Chap. 3, 4. ISBN: 978-1-107-17986-8.

[20] Ph. Hofmann. *Surface Physics: An Introduction.* 2016. Chap. 5. ISBN: 978-87-996090-0-0.

[21] J. W. Kim and A. Kim. "Absolute work function measurement by using photoelectron spectroscopy". In: *Current Applied Physics* 31 (2021), pp. 52–59. DOI: 10.1016/j.cap.2021.07.018.

[22]   F. J. García de Abajo, M. A. Van Hove, and C. S. Fadley. "Multiple scattering of electrons in solids and molecules: A cluster-model approach". In: *Physical Review B* 63 (2001), p. 075404. DOI: `10.1103/PhysRevB.63.075404`.

[23]   L. Bignardi et al. "Growth and structure of singly oriented single-layer tungsten disulfide on Au(111)". In: *Physical Review Materials* 3 (2019), p. 014003. DOI: `10.1103/PhysRevMaterials.3.014003`.

[24]   H. Bana et al. "Epitaxial growth of single-orientation high-quality MoS_2 monolayers". In: *2D Materials* 5.3 (2018), p. 035012. DOI: `10.1088/2053-1583/aabb74`.

[25]   A. J. U. Holt et al. "Electronic properties of single-layer CoO_2/Au(111)". In: *2D Materials* 8.3 (2021), p. 035050. DOI: `10.1088/2053-1583/ac040f`.

[26]   M. P. Seah and W. A. Dench. "Quantitative electron spectroscopy of surfaces: A standard data base for electron inelastic mean free paths in solids". In: *Surface and Interface Analysis* 1.1 (1979), pp. 2–11. DOI: `10.1002/sia.740010103`.

[27]   M. A. Van Hove, W. H. Weinberg, and C.-M. Chan. *Low-Energy Electron Diffraction: Experiment, Theory and Surface Structure Determination*. Vol. 6. Springer Science & Business Media, 2012. ISBN: 978-3-642-82721-1.

[28]   B. Holst et al. "Material properties particularly suited to be measured with helium scattering: selected examples from 2D materials, van der Waals heterostructures, glassy materials, catalytic substrates, topological insulators and superconducting radio frequency materials". In: *Physical Chemistry Chemical Physics* 23.13 (2021), pp. 7653–7672. DOI: `10.1039/D0CP05833E`.

[29]   J. Liu, R. E. Saw, and Y.-H. Kiang. "Calculation of Effective Penetration Depth in X-Ray Diffraction for Pharmaceutical Solids". In: *Journal of Pharmaceutical Sciences* 99.9 (2010), pp. 3807–3814. DOI: `10.1002/jps.22202`.

[30]   G. Hähner. "Near edge X-ray absorption fine structure spectroscopy as a tool to probe electronic and structural properties of thin organic films and liquids". In: *Chemical Society Reviews* 35 (2006), pp. 1244–1255. DOI: `10.1039/B509853J`.

[31]   F. Song et al. "Direct measurement of electrical conductance through a self-assembled molecular layer". In: *Nature Nanotechnology* 4.6 (2009), pp. 373–376. DOI: 10.1038/nnano.2009.82.

[32]   J. Stöhr and D. A. Outka. "Determination of molecular orientations on surfaces from the angular dependence of near-edge x-ray-absorption fine-structure spectra". In: *Physical Review B* 36 (1987), pp. 7891–7905. DOI: 10.1103/PhysRevB.36.7891.

[33]   R. D. Mattuck. *A Guide to Feynman Diagrams in the Many-Body Problem*. 2nd ed. Courier Corp., 1992. Chap. 0. ISBN: 0070409544.

[34]   Ph. Hofmann et al. "Electron–phonon coupling at surfaces and interfaces". In: *New Journal of Physics* 11.12 (2009), p. 125005. DOI: 10.1088/1367-2630/11/12/125005.

[35]   R. Leckey, J. D. Riley, and A. Stampfl. "Angle resolved photoemission using a toroidal energy analyser". In: *Journal of Electron Spectroscopy and Related Phenomena* 52 (1990), pp. 855–866. DOI: 10.1016/0368-2048(90)85069-L.

[36]   A. Damm et al. "Application of a time-of-flight spectrometer with delay-line detector for time- and angle-resolved two-photon photoemission". In: *Journal of Electron Spectroscopy and Related Phenomena* 202 (2015), pp. 74–80. DOI: 10.1016/j.elspec.2015.03.009.

[37]   F. Hadjarab and J. L. Erskine. "Image properties of the hemispherical analyzer applied to multichannel energy detection". In: *Journal of Electron Spectroscopy and Related Phenomena* 36.3 (1985), pp. 227–243. DOI: 10.1016/0368-2048(85)80021-9.

[38]   C. Tusche et al. "Imaging properties of hemispherical electrostatic energy analyzers for high resolution momentum microscopy". In: *Ultramicroscopy* 206 (2019), p. 112815. DOI: 10.1016/j.ultramic.2019.112815.

[39]   R. P. Day et al. "Computational framework chinook for angle-resolved photoemission spectroscopy". In: *npj Quantum Materials* 4.1 (2019), pp. 1–10. DOI: 10.1038/s41535-019-0194-8.

[40]   M. Cattelan and N. A. Fox. "A Perspective on the Application of Spatially Resolved ARPES for 2D Materials". In: *Nanomaterials* 8.5 (2018). DOI: 10.3390/nano8050284.

[41]   B. Krömker et al. "Development of a momentum microscope for time resolved band structure imaging". In: *Review of Scientific Instruments* 79.5 (2008), p. 053702. DOI: 10.1063/1.2918133.

[42]   M. J. Prieto and T. Schmidt. "LEEM and PEEM as probing tools to address questions in catalysis". In: *Catalysis Letters* 147.10 (2017), pp. 2487–2497. DOI: 10.1007/s10562-017-2162-x.

[43]   A. Bailly et al. "Aspects of lateral resolution in energy-filtered core level photoelectron emission microscopy". In: *Journal of Physics: Condensed Matter* 21.31 (2009), p. 314002. DOI: 10.1088/0953-8984/21/31/314002.

[44]   C. Tusche, A. Krasyuk, and J. Kirschner. "Spin resolved bandstructure imaging with a high resolution momentum microscope". In: *Ultramicroscopy* 159 (2015). Special Issue: LEEM-PEEM 9, pp. 520–529. DOI: 10.1016/j.ultramic.2015.03.020.

[45]   E. Młyńczak et al. "Kink far below the Fermi level reveals new electron-magnon scattering channel in Fe". In: *Nature Communications* 10.1 (2019), pp. 1–5. DOI: 10.1038/s41467-019-08445-1.

[46]   T. Valla et al. "Many-Body Effects in Angle-Resolved Photoemission: Quasiparticle Energy and Lifetime of a Mo(110) Surface State". In: *Physical Review Letters* 83 (1999), pp. 2085–2088. DOI: 10.1103/PhysRevLett.83.2085.

[47]   J. E. Gayone et al. "Determining the electron-phonon mass enhancement parameter λ on metal surfaces". In: *Applied Physics A* 80.5 (2005), pp. 943–949. DOI: 10.1007/s00339-004-3120-1.

[48]   I. Pletikosić et al. "Finding the bare band: Electron coupling to two phonon modes in potassium-doped graphene on Ir(111)". In: *Physical Review B* 85 (2012), p. 155447. DOI: 10.1103/PhysRevB.85.155447.

[49]   J. C. Johannsen et al. "Electron–phonon coupling in quasi-free-standing graphene". In: *Journal of Physics: Condensed Matter* 25.9 (2013), p. 094001. DOI: 10.1088/0953-8984/25/9/094001.

[50]   F. Song et al. "Extracting the near surface stoichiometry of $BiFe_{0.5}Mn_{0.5}O_3$ thin films; a finite element maximum entropy approach". In: *Surface Science* 606.23 (2012), pp. 1771–1776. DOI: 10.1016/j.susc.2012.06.016.

[51] A. Sassaroli and S. Fantini. "Comment on the modified Beer–Lambert law for scattering media". In: *Physics in Medicine & Biology* 49.14 (2004), N255. DOI: 10.1088/0031-9155/49/14/N07.

[52] J. M. Hill et al. "Properties of oxidized silicon as determined by angular-dependent X-ray photoelectron spectroscopy". In: *Chemical Physics Letters* 44.2 (1976), pp. 225–231. DOI: 10.1016/0009-2614(76)80496-4.

[53] J. E. Graebner. "Thermal Conductivity of Diamond". In: *Diamond: Electronic Properties and Applications*. Ed. by L. S. Pan and D. R. Kania. Boston, MA: Springer US, 1995, pp. 285–318. ISBN: 978-1-4615-2257-7.

[54] A. P. Ramirez. "Superconductivity in alkali-doped C_{60}". In: *Physica C: Superconductivity and its Applications* 514 (2015). Superconducting Materials: Conventional, Unconventional and Undetermined, pp. 166–172. DOI: 10.1016/j.physc.2015.02.014.

[55] R. E. Peierls. "Bemerkungen über umwandlungstemperaturen". In: *Helvetica Physica Acta* 7.2 (1934), p. 81.

[56] R. E. Peierls. "Quelques propriétés typiques des corps solides". In: *Annales de l'institut Henri Poincaré*. Vol. 5. 3. 1935, pp. 177–222.

[57] L. D. Landau. "Phys. Z Sowjetunion, 11". In: *TSS* 26 (1937), p. 545.

[58] A. K. Geim. "Graphene prehistory". In: *Physica Scripta* T146 (2012), p. 014003. DOI: 10.1088/0031-8949/2012/t146/014003.

[59] K. S. Novoselov et al. "Electric Field Effect in Atomically Thin Carbon Films". In: *Science* 306.5696 (2004), pp. 666–669. DOI: 10.1126/science.1102896.

[60] K. S. Novoselov et al. "Two-dimensional gas of massless Dirac fermions in graphene". In: *Nature* 438.7065 (2005), pp. 197–200. DOI: 10.1038/nature04233.

[61] A. A. Balandin et al. "Superior Thermal Conductivity of Single-Layer Graphene". In: *Nano Letters* 8.3 (2008), pp. 902–907. DOI: 10.1021/nl0731872.

[62] C. Lee et al. "Measurement of the elastic properties and intrinsic strength of monolayer graphene". In: *Science* 321.5887 (2008), pp. 385–388. DOI: 10.1126/science.1157996.

[63]   A. H. Castro Neto et al. "The electronic properties of graphene". In: *Reviews of Modern Physics* 81 (2009), pp. 109–162. DOI: 10.1103/RevModPhys.81.109.

[64]   V. P. Gusynin and S. G. Sharapov. "Unconventional Integer Quantum Hall Effect in Graphene". In: *Physical Review Letters* 95 (2005), p. 146801. DOI: 10.1103/PhysRevLett.95.146801.

[65]   Y. Cao et al. "Unconventional superconductivity in magic-angle graphene superlattices". In: *Nature* 556.7699 (2018), pp. 43–50. DOI: 10.1038/nature26160.

[66]   B. Gharekhanlou and S. Khorasani. "An overview of tight-binding method for two-dimensional carbon structures". In: *Graphene: Properties, Synthesis and Applications*. Ed. by Zhiping Xu. Nova Science Publishers, Inc, 2011. Chap. 1, pp. 1–36. ISBN: 978-1-61470-949-7.

[67]   R. Saito, G. Dresselhaus, and M. S. Dresselhaus. *Physical Properties of Carbon nanotubes*. 1st. World Scientific Publishing Company, 1998. Chap. 2, pp. 17–21, 25–33. ISBN: 1-86094-093-5.

[68]   F. Mazzola et al. "Kinks in the σ Band of Graphene Induced by Electron-Phonon Coupling". In: *Physical Review Letters* 111 (2013), p. 216806. DOI: 10.1103/PhysRevLett.111.216806.

[69]   F. Mazzola et al. "Strong electron-phonon coupling in the σ band of graphene". In: *Physical Review B* 95 (2017), p. 075430. DOI: 10.1103/PhysRevB.95.075430.

[70]   B. Hellsing et al. "Phonon-induced linewidths of graphene electronic states". In: *Physical Review B* 98 (2018), p. 205428. DOI: 10.1103/PhysRevB.98.205428.

[71]   K. S. Novoselov et al. "A roadmap for graphene". In: *Nature* 490.7419 (2012), pp. 192–200. DOI: 10.1038/nature11458.

[72]   W. Han et al. "Graphene spintronics". In: *Nature Nanotechnology* 9.10 (2014), pp. 794–807. DOI: 10.1038/nnano.2014.214.

[73]   A. Nimbalkar and H. Kim. "Opportunities and challenges in twisted bilayer graphene: a review". In: *Nano-Micro Letters* 12.1 (2020), pp. 1–20. DOI: 10.1007/s40820-020-00464-8.

[74]   X. Du et al. "Approaching ballistic transport in suspended graphene". In: *Nature Nanotechnology* 3.8 (2008), pp. 491–495. DOI: 10.1038/nnano.2008.199.

[75] K.I. Bolotin et al. "Ultrahigh electron mobility in suspended graphene".
      In: *Solid State Communications* 146.9 (2008), pp. 351–355. DOI: 10.
      1016/j.ssc.2008.02.024.

[76] N. Mishra et al. "Graphene growth on silicon carbide: A review". In:
      physica status solidi (a) 213.9 (2016), pp. 2277–2289. DOI: 10.1002/
      pssa.201600091.

[77] A. T. N'Diaye et al. "Two-Dimensional Ir Cluster Lattice on a Graphene
      Moiré on Ir(111)". In: *Physical Review Letters* 97 (2006), p. 215501.
      DOI: 10.1103/PhysRevLett.97.215501.

[78] A. Varykhalov et al. "Electronic and Magnetic Properties of Quasifree-
      standing Graphene on Ni". In: *Physical Review Letters* 101 (2008),
      p. 157601. DOI: 10.1103/PhysRevLett.101.157601.

[79] P. W. Sutter, J.-I. Flege, and E. A. Sutter. "Epitaxial graphene on
      ruthenium". In: *Nature Materials* 7.5 (2008), pp. 406–411. DOI: 10.
      1038/nmat2166.

[80] P. Sutter, J. T. Sadowski, and E. Sutter. "Graphene on Pt(111):
      Growth and substrate interaction". In: *Physical Review B* 80 (2009),
      p. 245411. DOI: 10.1103/PhysRevB.80.245411.

[81] S. Bae et al. "Roll-to-roll production of 30-inch graphene films for
      transparent electrodes". In: *Nature Nanotechnology* 5.8 (2010), pp. 574–
      578. DOI: 10.1038/nnano.2010.132.

[82] J. Coraux et al. "Structural Coherency of Graphene on Ir(111)". In:
      Nano Letters 8.2 (2008), pp. 565–570. DOI: 10.1021/nl0728874.

[83] H. Zhou et al. "Chemical vapour deposition growth of large single
      crystals of monolayer and bilayer graphene". In: *Nature Communica-
      tions* 4.1 (2013), pp. 1–8. DOI: 10.1038/ncomms3096.

[84] R. Larciprete et al. "Oxygen Switching of the Epitaxial Graphene–Metal
      Interaction". In: *ACS Nano* 6.11 (2012), pp. 9551–9558. DOI: 10.
      1021/nn302729j.

[85] Z. Zhang et al. "Rosin-enabled ultraclean and damage-free trans-
      fer of graphene for large-area flexible organic light-emitting diodes".
      In: *Nature Communications* 8.1 (2017), pp. 1–9. DOI: 10.1038/
      ncomms14560.

[86]   C. Berger et al. "Ultrathin Epitaxial Graphite: 2D Electron Gas Prop-
       erties and a Route toward Graphene-based Nanoelectronics". In: *The
       Journal of Physical Chemistry B* 108.52 (2004), pp. 19912–19916.
       DOI: 10.1021/jp040650f.

[87]   J. Hass et al. "Highly ordered graphene for two dimensional elec-
       tronics". In: *Applied Physics Letters* 89.14 (2006), p. 143106. DOI:
       10.1063/1.2358299.

[88]   K. V. Emtsev et al. "Interaction, growth, and ordering of epitaxial
       graphene on SiC {0001} surfaces: A comparative photoelectron spec-
       troscopy study". In: *Physical Review B* 77.15 (2008), p. 155303. DOI:
       10.1103/PhysRevB.77.155303.

[89]   K. V. Emtsev et al. "Towards wafer-size graphene layers by atmo-
       spheric pressure graphitization of silicon carbide". In: *Nature Mate-
       rials* 8.3 (2009), pp. 203–207. DOI: 10.1038/nmat2382.

[90]   U. Starke and C. Riedl. "Epitaxial graphene on SiC(0001) and SiC(000$\bar{1}$):
       from surface reconstructions to carbon electronics". In: *Journal of
       Physics: Condensed Matter* 21.13 (2009), p. 134016. DOI: 10.1088/
       0953-8984/21/13/134016.

[91]   I. Gierz et al. "Electronic decoupling of an epitaxial graphene mono-
       layer by gold intercalation". In: *Physical Review B* 81 (2010), p. 235408.
       DOI: 10.1103/PhysRevB.81.235408.

[92]   J. Hass, W. A. de Heer, and E. H. Conrad. "The growth and mor-
       phology of epitaxial multilayer graphene". In: *Journal of Physics:
       Condensed Matter* 20.32 (2008), p. 323202. DOI: 10.1088/0953-
       8984/20/32/323202.

[93]   R. M. Tromp and J. B. Hannon. "Thermodynamics and Kinetics of
       Graphene Growth on SiC(0001)". In: *Physical Review Letters* 102
       (2009), p. 106104. DOI: 10.1103/PhysRevLett.102.106104.

[94]   X. Z. Yu et al. "New synthesis method for the growth of epitaxial
       graphene". In: *Journal of Electron Spectroscopy and Related Phenom-
       ena* 184.3-6 (2011), pp. 100–106. DOI: 10.1016/j.elspec.2010.12.
       034.

[95]   M. Aliofkhazraei et al. *Graphene Science Handbook: Electrical and
       Optical Properties*. CRC Press, Taylor & Francis Group, 2016. Chap. 1,
       pp. 5–6. ISBN: 9781466591318.

[96]   R. C. Jaeger, G. W. Neudeck, and R. F. Pierret. *Introduction to Microelectronic Fabrication*. 2nd ed. Vol. 5. Prentice Hall, 2002. Chap. 9. ISBN: 0-201-44494-1.

[97]   S. P. Cooil et al. "Iron-mediated growth of epitaxial graphene on SiC and diamond". In: *Carbon* 50.14 (2012), pp. 5099–5105. DOI: 10.1016/j.carbon.2012.06.050.

[98]   Z.-Y. Juang et al. "Synthesis of graphene on silicon carbide substrates at low temperature". In: *Carbon* 47.8 (2009), pp. 2026–2031. DOI: 10.1016/j.carbon.2009.03.051.

[99]   P. Macháč et al. "Graphene preparation by annealing of Co/SiC structure". In: *Applied Surface Science* 320 (2014), pp. 544–551. DOI: 10.1016/j.apsusc.2014.09.104.

[100]   C. Li et al. "Preparation of single-and few-layer graphene sheets using Co deposition on SiC substrate". In: *Journal of Nanomaterials* 2011 (2011), p. 44. DOI: 10.1155/2011/319624.

[101]   K. V. Munthali et al. "Solid state reaction of ruthenium with 6H-SiC under vacuum annealing and the impact on the electrical performance of its Schottky contact for high temperature operating SiC-based diodes". In: *Brazilian Journal of Physics* 44.6 (2014), pp. 739–745. DOI: 10.1007/s13538-014-0257-z.

[102]   K. Sanbongi, M. Ohtani, and K. Toita. "On the effect of alloying elements on the solubility of carbon in molten iron". In: *Science Reports of the Research Institutes, Tohoku University, Ser. A* 9 (1957), pp. 147–158. URL: https://cir.nii.ac.jp/crid/1572261551872046592.

[103]   W. J. Arnoult and R. B. McLellan. "Solubility of carbon in rhodium, ruthenium, iridium, and rhenium." In: *Scripta Metallurgica* 6 (1972), pp. 1013–1018. DOI: 10.1016/0036-9748(72)90163-9.

[104]   A. A. Zhukov. "Phase diagram of alloys of the system Fe-C". In: *Metal Science and Heat Treatment* 30.4 (1988), pp. 249–255. DOI: 10.1007/BF00774573.

[105]   S. P. Cooil et al. "Controlling the growth of epitaxial graphene on metalized diamond (111) surface". In: *Applied Physics Letters* 107.18 (2015), p. 181603. DOI: 10.1063/1.4935073.

[106]   C. Kittel. *Introduction to Solid State Physics*. 8th ed. John Wiley & Sons, Inc., 2021. Chap. 4, 12, 15. ISBN: 978-0-471-41526-8.

[107]   G. Grimvall. *The Electron-phonon Interaction in Metals*. North-Holland Publishing Company, 1981. ISBN: 9780444861054.

[108]   J. Bardeen, L. N. Cooper, and J. R. Schrieffer. "Theory of Superconductivity". In: *Physical Review* 108 (1957), pp. 1175–1204. DOI: `10.1103/PhysRev.108.1175`.

[109]   A. Lanzara et al. "Evidence for ubiquitous strong electron–phonon coupling in high-temperature superconductors". In: *Nature* 412.6846 (2001), pp. 510–514. DOI: `10.1038/35087518`.

[110]   N. W. Ashcroft and N. D. Mermin. *Solid State Physics*. HRW international editions. Holt, Rinehart and Winston, 1976. Chap. 22–26. ISBN: 0-03-083993-9.

[111]   C. Kittel. *Quantum Theory of Solids*. 2nd ed. Wiley, 1987. Chap. 2, 4. ISBN: 978-0-471-62412-7.

[112]   D. Tong. *Lectures on Applications in Quantum Mechanics – Phonons*. Available at `http://www.damtp.cam.ac.uk/user/tong/aqm.html` (2022/06/17).

[113]   Ph. Hofmann. *Solid State Physics: An Introduction*. John Wiley & Sons, 2015. Chap. 4. ISBN: 978-3-527-41282-2.

[114]   B. Hellsing, A. Eiguren, and E. V. Chulkov. "Electron-phonon coupling at metal surfaces". In: *Journal of Physics: Condensed Matter* 14.24 (2002), pp. 5959–5977. DOI: `10.1088/0953-8984/14/24/306`.

[115]   W. L. McMillan. "Transition Temperature of Strong-Coupled Superconductors". In: *Physical Review* 167 (1968), pp. 331–344. DOI: `10.1103/PhysRev.167.331`.

[116]   C. Kirkegaard, T. K. Kim, and Ph. Hofmann. "Self-energy determination and electron–phonon coupling on Bi(110)". In: *New Journal of Physics* 7 (2005), pp. 99–99. DOI: `10.1088/1367-2630/7/1/099`.

[117]   S. LaShell, E. Jensen, and T. Balasubramanian. "Nonquasiparticle structure in the photoemission spectra from the Be(0001) surface and determination of the electron self energy". In: *Physical Review B* 61 (2000), pp. 2371–2374. DOI: `10.1103/PhysRevB.61.2371`.

[118]   X. Y. Cui et al. "High-resolution angle-resolved photoemission spectroscopy of iron: A study of the self-energy". In: *Journal of Magnetism and Magnetic Materials* 310.2, Part 2 (2007). Proceedings of the 17th International Conference on Magnetism, pp. 1617–1619. DOI: `10.1016/j.jmmm.2006.10.639`.

[119]   A. Hofmann et al. "Renormalization of Bulk Magnetic Electron States at High Binding Energies". In: *Physical Review Letters* 102 (2009), p. 187204. DOI: `10.1103/PhysRevLett.102.187204`.

[120]   A. A. Kordyuk et al. "Bare electron dispersion from experiment: Self-consistent self-energy analysis of photoemission data". In: *Physical Review B* 71 (2005), p. 214513. DOI: `10.1103/PhysRevB.71.214513`.

[121]   N. V. Smith, P. Thiry, and Y. Petroff. "Photoemission linewidths and quasiparticle lifetimes". In: *Physical Review B* 47 (1993), pp. 15476–15481. DOI: `10.1103/PhysRevB.47.15476`.

[122]   E. D. Hansen, T. Miller, and T.-C. Chiang. "Observation of Photoemission Line Widths Narrower than the Inverse Lifetime". In: *Physical Review Letters* 80 (1998), pp. 1766–1769. DOI: `10.1103/PhysRevLett.80.1766`.

[123]   Y. Saito, T. Nojima, and Y. Iwasa. "Highly crystalline 2D superconductors". In: *Nature Reviews Materials* 2.1 (2016), pp. 1–18. DOI: `10.1038/natrevmats.2016.94`.

[124]   T. E. Weller et al. "Superconductivity in the intercalated graphite compounds C_6Yb and C_6Ca". In: *Nature Physics* 1.1 (2005), pp. 39–41. DOI: `10.1038/nphys0010`.

[125]   N. Emery et al. "Superconductivity of Bulk CaC_6". In: *Physical Review Letters* 95 (2005), p. 087003. DOI: `10.1103/PhysRevLett.95.087003`.

[126]   K. Sugawara, T. Sato, and T. Takahashi. "Fermi-surface-dependent superconducting gap in C_6Ca". In: *Nature Physics* 5.1 (2009), pp. 40–43. DOI: `10.1038/nphys1128`.

[127]   T. Valla et al. "Anisotropic Electron-Phonon Coupling and Dynamical Nesting on the Graphene Sheets in Superconducting CaC_6 using Angle-Resolved Photoemission Spectroscopy". In: *Physical Review Letters* 102 (2009), p. 107007. DOI: `10.1103/PhysRevLett.102.107007`.

[128]   J. L. McChesney et al. "Extended van Hove Singularity and Superconducting Instability in Doped Graphene". In: *Physical Review Letters* 104 (2010), p. 136803. DOI: `10.1103/PhysRevLett.104.136803`.

[129]   S.-L. Yang et al. "Superconducting graphene sheets in CaC_6 enabled by phonon-mediated interband interactions". In: *Nature Communications* 5.1 (2014), pp. 1–5. DOI: `10.1038/ncomms4493`.

[130] W. Kyung et al. "Interlayer-state-driven superconductivity in CaC_6 studied by angle-resolved photoemission spectroscopy". In: *Physical Review B* 92 (2015), p. 224516. DOI: 10.1103/PhysRevB.92.224516.

[131] S. Ichinokura et al. "Superconducting Calcium-Intercalated Bilayer Graphene". In: *ACS Nano* 10.2 (2016), pp. 2761–2765. DOI: 10.1021/acsnano.5b07848.

[132] B. Uchoa and A. H. Castro Neto. "Superconducting States of Pure and Doped Graphene". In: *Physical Review Letters* 98 (2007), p. 146801. DOI: 10.1103/PhysRevLett.98.146801.

[133] M. Foxe et al. "Graphene field-effect transistors on undoped semiconductor substrates for radiation detection". In: *IEEE Transactions on Nanotechnology* 11.3 (2012), pp. 581–587. DOI: 10.1109/TNANO.2012.2186312.

[134] S. Link et al. "Introducing strong correlation effects into graphene by gadolinium intercalation". In: *Physical Review B* 100 (2019), p. 121407. DOI: 10.1103/PhysRevB.100.121407.

[135] C. Bao et al. "Experimental Evidence of Chiral Symmetry Breaking in Kekulé-Ordered Graphene". In: *Physical Review Letters* 126 (2021), p. 206804. DOI: 10.1103/PhysRevLett.126.206804.

[136] P. Rosenzweig et al. "Tuning the doping level of graphene in the vicinity of the van Hove singularity via ytterbium intercalation". In: *Physical Review B* 100 (2019), p. 035445. DOI: 10.1103/PhysRevB.100.035445.

[137] P. Rosenzweig et al. "Overdoping Graphene beyond the van Hove Singularity". In: *Physical Review Letters* 125 (2020), p. 176403. DOI: 10.1103/PhysRevLett.125.176403.

[138] E. Thingstad et al. "Phonon-mediated superconductivity in doped monolayer materials". In: *Physical Review B* 101.21 (2020), p. 214513. DOI: 10.1103/PhysRevB.101.214513.

[139] S. W. Jung et al. "Sublattice Interference as the Origin of σ Band Kinks in Graphene". In: *Physical Review Letters* 116 (2016), p. 186802. DOI: 10.1103/PhysRevLett.116.186802.

[140] C. R. Dean et al. "Boron nitride substrates for high-quality graphene electronics". In: *Nature Nanotechnology* 5.10 (2010), pp. 722–726. DOI: 10.1038/nnano.2010.172.

[141] L. Wirtz et al. "Ab initio calculations of the lattice dynamics of boron nitride nanotubes". In: *Physical Review B* 68.4 (2003), p. 045425. DOI: `10.1103/PhysRevB.68.045425`.

[142] J. Robertson. "Electronic structure and core exciton of hexagonal boron nitride". In: *Physical Review B* 29.4 (1984), p. 2131. DOI: `10.1103/PhysRevB.29.2131`.

[143] C. Elias et al. "Direct band-gap crossover in epitaxial monolayer boron nitride". In: *Nature Communications* 10.1 (2019), pp. 1–7. DOI: `10.1038/s41467-019-10610-5`.

[144] C. C. Hu. *Modern Semiconductor Devices for Integrated Circuits.* 2nd ed. Pearson/Prentice Hall, 2010. Chap. 1. ISBN: 9780136085256.

[145] E. F. Schubert. *Delta-doping of Semiconductors.* 1st ed. Cambridge University Press, 1996. Chap. 1. ISBN: 9780521017961.

[146] E. F. Schubert, J. E. Cunningham, and W. T. Tsang. "Self-aligned enhancement-mode and depletion-mode GaAs field-effect transistors employing the δ-doping technique". In: *Applied Physics Letters* 49.25 (1986), pp. 1729–1731. DOI: `10.1063/1.97229`.

[147] E. F. Schubert et al. "Selectively δ-doped $Al_xGa_{1-x}As$/GaAs heterostructures with high two-dimensional electron-gas concentrations n 2DEG $\geq 1.5 \times 10^{12}$ cm^{-2} for field-effect transistors". In: *Applied Physics Letters* 51.15 (1987), pp. 1170–1172. DOI: `10.1063/1.98722`.

[148] M. R. Sardela Jr., H. H. Radamson, and G. V. Hansson. "Negative differential resistance at room temperature in δ-doped diodes grown by Si-molecular beam epitaxy". In: *Applied Physics Letters* 64.13 (1994), pp. 1711–1713. DOI: `10.1063/1.111813`.

[149] K. D. Hobart et al. "p-on-n Si interband tunnel diode grown by molecular beam epitaxy". In: *Journal of Vacuum Science & Technology B: Microelectronics and Nanometer Structures Processing, Measurement, and Phenomena* 19.1 (2001), pp. 290–293. DOI: `10.1116/1.1339011`.

[150] B. E. Kane. "A silicon-based nuclear spin quantum computer". In: *Nature* 393.6681 (1998), pp. 133–137. DOI: `10.1038/30156`.

[151] M. Fuechsle et al. "A single-atom transistor". In: *Nature Nanotechnology* 7.4 (2012), pp. 242–246. DOI: `10.1038/nnano.2012.21`.

[152] M. Veldhorst et al. "A two-qubit logic gate in silicon". In: *Nature* 526.7573 (2015), pp. 410–414. DOI: `10.1038/nature15263`.

[153]   F. A. Zwanenburg et al. "Silicon quantum electronics". In: *Reviews of Modern Physics* 85 (2013), pp. 961–1019. DOI: `10.1103/RevModPhys.85.961`.

[154]   C. M. Polley et al. "Microscopic four-point-probe resistivity measurements of shallow, high density doping layers in silicon". In: *Applied Physics Letters* 101.26 (2012), p. 262105. DOI: `10.1063/1.4773485`.

[155]   C. M. Polley et al. "Exploring the limits of N-type ultra-shallow junction formation". In: *ACS Nano* 7.6 (2013), pp. 5499–5505. DOI: `10.1021/nn4016407`.

[156]   S. R. McKibbin et al. "Low resistivity, super-saturation phosphorus-in-silicon monolayer doping". In: *Applied Physics Letters* 104.12 (2014), p. 123502. DOI: `10.1063/1.4869111`.

[157]   J. G. Keizer, S. R. McKibbin, and M. Y. Simmons. "The Impact of Dopant Segregation on the Maximum Carrier Density in Si:P Multilayers". In: *ACS Nano* 9.7 (2015), pp. 7080–7084. DOI: `10.1021/acsnano.5b01638`.

[158]   S. V. Kravchenko and M. P. Sarachik. "Metal–insulator transition in two-dimensional electron systems". In: *Reports on Progress in Physics* 67.1 (2003), p. 1. DOI: `10.1088/0034-4885/67/1/R01`.

[159]   F. Mazzola et al. "Determining the electronic confinement of a subsurface metallic state". In: *ACS Nano* 8.10 (2014), pp. 10223–10228. DOI: `10.1021/nn5045239`.

[160]   J. A. Miwa et al. "Direct Measurement of the Band Structure of a Buried Two-Dimensional Electron Gas". In: *Physical Review Letters* 110 (2013), p. 136801. DOI: `10.1103/PhysRevLett.110.136801`.

[161]   J. A. Miwa et al. "Valley splitting in a silicon quantum device platform". In: *Nano Letters* 14.3 (2014), pp. 1515–1519. DOI: `10.1021/nl404738j`.

[162]   M. Cardona and F. H. Pollak. "Energy-Band Structure of Germanium and Silicon: The k·p Method". In: *Physical Review* 142 (1966), pp. 530–543. DOI: `10.1103/PhysRev.142.530`.

[163]   A. J. Holt et al. "Observation and origin of the Δ manifold in Si:P δ layers". In: *Physical Review B* 101 (2020), p. 121402. DOI: `10.1103/PhysRevB.101.121402`.

[164]   D. J. Carter et al. "Electronic structure models of phosphorus δ-doped silicon". In: *Physical Review B* 79 (2009), p. 033204. DOI: `10.1103/PhysRevB.79.033204`.

[165]   S. Lee et al. "Electronic structure of realistically extended atomistically resolved disordered Si:P δ-doped layers". In: *Physical Review B* 84 (2011), p. 205309. DOI: `10.1103/PhysRevB.84.205309`.

[166]   D. J. Carter et al. "Phosphorus δ-doped silicon: mixed-atom pseudopotentials and dopant disorder effects". In: *Nanotechnology* 22.6 (2011), p. 065701. DOI: `10.1088/0957-4484/22/6/065701`.

[167]   H. F. Wilson et al. "Phosphine Dissociation on the Si(001) Surface". In: *Physical Review Letters* 93 (2004), p. 226102. DOI: `10.1103/PhysRevLett.93.226102`.

[168]   O. Warschkow et al. "Phosphine adsorption and dissociation on the Si(001) surface: An ab initio survey of structures". In: *Physical Review B* 72 (2005), p. 125328. DOI: `10.1103/PhysRevB.72.125328`.

[169]   H. F. Wilson et al. "Thermal dissociation and desorption of PH_3 on Si(001): A reinterpretation of spectroscopic data". In: *Physical Review B* 74 (2006), p. 195310. DOI: `10.1103/PhysRevB.74.195310`.

[170]   M. L. Yu, D. J. Vitkavage, and B. S. Meyerson. "Doping reaction of PH_3 and B_2H_6 with Si(100)". In: *Journal of Applied Physics* 59.12 (1986), pp. 4032–4037. DOI: `10.1063/1.336708`.

[171]   Y. Wang, M. J. Bronikowski, and R. J. Hamers. "An atomically resolved STM study of the interaction of phosphine with the silicon (001) surface". In: *The Journal of Physical Chemistry* 98.23 (1994), pp. 5966–5973. DOI: `10.1021/j100074a025`.

[172]   J. G. Keizer et al. "Suppressing Segregation in Highly Phosphorus Doped Silicon Monolayers". In: *ACS Nano* 9.12 (2015), pp. 12537–12541. DOI: `10.1021/acsnano.5b06299`.

[173]   S. R. McKibbin, W. R. Clarke, and M. Y. Simmons. "Investigating the surface quality and confinement of Si:P δ-layers at different growth temperatures". In: *Physica E: Low-dimensional Systems and Nanostructures* 42.4 (2010). 18th International Conference on Electron Properties of Two-Dimensional Systems, pp. 1180–1183. DOI: `10.1016/j.physe.2009.11.111`.

[174] F. Mazzola et al. "The sub-band structure of atomically sharp dopant profiles in silicon". In: *npj Quantum Materials* 5.1 (2020), pp. 1–5. DOI: 10.1038/s41535-020-0237-1.

[175] D.-S. Lin, T.-S. Ku, and T.-J. Sheu. "Thermal reactions of phosphine with Si(100): a combined photoemission and scanning-tunneling- microscopy study". In: *Surface Science* 424.1 (1999), pp. 7–18. DOI: 10.1016/S0039-6028(98)00943-1.

[176] Y. Tsukidate and M. Suemitsu. "Saturated adsorption of PH_3 on Si(100):P and its application to digital control of phosphorus coverage on Si(100) surface". In: *Applied Surface Science* 151.1 (1999), pp. 148–152. DOI: 10.1016/S0169-4332(99)00272-X.

[177] S. R. McKibbin et al. "Investigating the regrowth surface of Si:P δ-layers toward vertically stacked three dimensional devices". In: *Applied Physics Letters* 95.23 (2009), p. 233111. DOI: 10.1063/1.3269924.

[178] M. Chubarov et al. "In-plane X-ray diffraction for characterization of monolayer and few-layer transition metal dichalcogenide films". In: *Nanotechnology* 29.5 (2018), p. 055706. DOI: 10.1088/1361-6528/aaa1bd.

[179] S. Yamashita et al. "Atomic number dependence of Z contrast in scanning transmission electron microscopy". In: *Scientific Reports* 8.1 (2018), pp. 1–7. DOI: 10.1038/s41598-018-30941-5.

[180] N. Karchev. "Magnon exchange mechanism of ferromagnetic superconductivity". In: *Physical Review B* 67 (2003), p. 054416. DOI: 10.1103/PhysRevB.67.054416.

[181] P. A. Lee, N. Nagaosa, and X.-G. Wen. "Doping a Mott insulator: Physics of high-temperature superconductivity". In: *Reviews of Modern Physics* 78 (2006), pp. 17–85. DOI: 10.1103/RevModPhys.78.17.

[182] G. M. Zhang, Z. Y. Lu, and T. Xiang. "Superconductivity mediated by the antiferromagnetic spin wave in chalcogenide iron-based superconductors". In: *Physical Review B* 84 (2011), p. 052502. DOI: 10.1103/PhysRevB.84.052502.

[183] W. Pauli. "Über den Zusammenhang des Abschlusses der Elektronengruppen im Atom mit der Komplexstruktur der Spektren". In: *Zeitschrift für Physik* 31 (Feb. 1925), pp. 765–783. DOI: 10.1007/BF02980631.

[184]   A. S. T. Pires. "The Heisenberg model". In: *Theoretical Tools for Spin Models in Magnetic Systems*. 2053-2563. IOP Publishing, 2021, pp. 1–16. ISBN: 978-0-7503-3879-0. DOI: `10.1088/978-0-7503-3879-0ch1`.

[185]   S. S. Saxena et al. "Superconductivity on the border of itinerant-electron ferromagnetism in UGe_2". In: *Nature* 406.6796 (2000), pp. 587–592. DOI: `10.1038/35020500`.

[186]   C. Pfleiderer et al. "Coexistence of superconductivity and ferromagnetism in the d-band metal $ZrZn_2$". In: *Nature* 412.6842 (2001), pp. 58–61. DOI: `10.1038/35083531`.

[187]   D. Aoki et al. "Coexistence of superconductivity and ferromagnetism in URhGe". In: *Nature* 413.6856 (2001), pp. 613–616. DOI: `10.1038/35098048`.

[188]   Y. Kamihara et al. "Iron-Based Layered Superconductor $La[O_{1-x}F_x]FeAs$ ($x = 0.05 - 0.12$) with $T_C = 26$ K". In: *Journal of the American Chemical Society* 130.11 (2008), pp. 3296–3297. DOI: `10.1021/ja800073m`.

[189]   H. Bruus and K. Flensberg. *Many-Body Quantum Theory in Condensed Matter Physics: An Introduction*. Oxford: Oxford University Press, 2004. ISBN: 9780198566335.

[190]   F. Mazzola et al. "Tuneable electron–magnon coupling of ferromagnetic surface states in $PdCoO_2$". In: *npj Quantum Materials* 7.1 (2022), pp. 1–6. DOI: `10.17630/1914b7df-3421-422a-8697-774a149c7f00`.

[191]   F. Marsiglio, M. Schossmann, and J. P. Carbotte. "Iterative analytic continuation of the electron self-energy to the real axis". In: *Physical Review B* 37 (1988), pp. 4965–4969. DOI: `10.1103/PhysRevB.37.4965`.

[192]   F. Marsiglio. "Pairing and charge-density-wave correlations in the Holstein model at half-filling". In: *Physical Review B* 42 (1990), pp. 2416–2424. DOI: `10.1103/PhysRevB.42.2416`.

[193]   B. Andres et al. "Strong momentum-dependent electron–magnon renormalization of a surface resonance on iron". In: *Applied Physics Letters* 120.20 (2022), p. 202404. DOI: `10.1063/5.0089688`.

[194]   J. Schäfer et al. "Electronic Quasiparticle Renormalization on the Spin Wave Energy Scale". In: *Physical Review Letters* 92 (2004), p. 097205. DOI: `10.1103/PhysRevLett.92.097205`.

[195]   G. R. Stewart. "Measurement of low-temperature specific heat". In: *Review of Scientific Instruments* 54.1 (1983), pp. 1–11. DOI: 10.1063/1.1137207.

[196]   R. J. Birgeneau et al. "Normal Modes of Vibration in Nickel". In: *Physical Review* 136 (1964), A1359–A1365. DOI: 10.1103/PhysRev.136.A1359.

[197]   M. Higashiguchi et al. "Energy band and spin-dependent many-body interactions in ferromagnetic Ni(110): A high-resolution angle-resolved photoemission study". In: *Physical Review B* 72 (2005), p. 214438. DOI: 10.1103/PhysRevB.72.214438.

[198]   N. B. Brookes et al. "Spin waves in metallic iron and nickel measured by soft x-ray resonant inelastic scattering". In: *Physical Review B* 102 (2020), p. 064412. DOI: 10.1103/PhysRevB.102.064412.

[199]   J. F. Cooke, J. A. Blackman, and T. Morgan. "New Interpretation of Spin-Wave Behavior in Nickel". In: *Physical Review Letters* 54 (1985), pp. 718–721. DOI: 10.1103/PhysRevLett.54.718.

[200]   H. G. Hugdal et al. "Magnon-induced superconductivity in a topological insulator coupled to ferromagnetic and antiferromagnetic insulators". In: *Physical Review B* 97.19 (2018), p. 195438. DOI: 10.1103/PhysRevB.97.195438.

[201]   N. Rohling, E. L. Fjærbu, and A. Brataas. "Superconductivity induced by interfacial coupling to magnons". In: *Physical Review B* 97.11 (2018), p. 115401. DOI: 10.1103/PhysRevB.97.115401.

[202]   E. Erlandsen, A. Brataas, and A. Sudbø. "Magnon-mediated superconductivity on the surface of a topological insulator". In: *Physical Review B* 101 (2020), p. 094503. DOI: 10.1103/PhysRevB.101.094503.

[203]   E. Thingstad, E. Erlandsen, and A. Sudbø. "Eliashberg study of superconductivity induced by interfacial coupling to antiferromagnets". In: *Physical Review B* 104 (2021), p. 014508. DOI: 10.1103/PhysRevB.104.014508.

[204]   Q. Liu et al. "Magnetic Impurities on the Surface of a Topological Insulator". In: *Physical Review Letters* 102 (2009), p. 156603. DOI: 10.1103/PhysRevLett.102.156603.

[205]   I. Garate and M. Franz. "Inverse Spin-Galvanic Effect in the Interface between a Topological Insulator and a Ferromagnet". In: *Physical Review Letters* 104 (2010), p. 146802. DOI: `10.1103/PhysRevLett.104.146802`.

[206]   B. Gupta et al. "Effect of substrate polishing on the growth of graphene on 3C–SiC(111)/Si(111) by high temperature annealing". In: *Nanotechnology* 27.18 (2016), p. 185601. DOI: `10.1088/0957-4484/27/18/185601`.

[207]   A. N. Ramanayaka et al. "Towards superconductivity in p-type delta-doped Si/Al/Si heterostructures". In: *AIP Advances* 8.7 (2018), p. 075329. DOI: `10.1063/1.5045338`.

NTNU

Norwegian University of
Science and Technology